MULTISTABLE MORPHING STRUCTURES USING VARIABLE STIFFNESS LAMINATES

Von der der Fakultät für Bauingenieurwesen und Geodäsie
der Gottfried Wilhelm Leibniz Universität Hannover
zur Erlangung des Grades

DOKTOR-INGENIEUR

– Dr.-Ing. –

genehmigte Dissertation
von

AYAN HALDAR
Master of Science in Computational Mechanics

2020

Referent: Prof. Dr.-Ing. habil. R. Rolfes
Leibniz Universität Hannover
Korreferent: Prof. Dr. Olivier Allix,
ENS Paris-Saclay

Tag der Promotion: 09.10.2019

To my parents
and my brother

Abstract

As the concern about climate change grows, more industries and research organizations are stepping up in search of viable solutions. Wind energy is one of the cheapest clean forms of energy, making it an attractive alternative against non-renewable sources. Upscaling of wind turbine has traditionally been considered a means to decrease the cost per kWh, and it remains a trend.

However, with an increase in the size of wind turbine rotor blades, there is a need to conceptualize designs capable of reducing ultimate and fatigue loads. Active trailing edge flap is one such promising concept to alleviate loads in large wind turbine blades. Most existing flap mechanisms have the potential for quick reaction time, but it often involves intricate actuation systems, adding additional weight and complexity. Moreover, it requires a continuous supply of energy input to maintain a particular position of the flap. Multistable variable stiffness (VS) laminates have a great potential in morphing applications primarily due to the existence of multiple stable shapes. The use of VS laminates with curvilinear fiber paths allows one to improve further the performance of multistable laminates as morphing structures.

The principal aim of this thesis is to exploit the properties of multistable VS laminates and apply them to a novel design of morphing trailing edge flap. This requires not only developing numerical and analytical tools, but also a suitable design to integrate VS laminates into a morphing flap. Therefore in this work, a fast semi-analytical tool is developed to predict the stable shapes of VS laminates. In addition, a systematic study is carried out to investigate the variation the curvilinear fiber paths on the stable equilibrium shapes. As a result of these investigations, VS laminates could be classified into families with similar multistable equilibrium positions. This, in turn, is applied to the envisaged design of the morphing flap.

Snap-through, which is a transition from one equilibrium state to another, is a crucial process to characterize multistable laminates in morphing applications. Two different snapping mechanisms are studied, one using concentrated force and the other using piezoelectric actuators. The extension of the aforementioned semi-analytical tool provides insights that reflect the underlying mechanics and characteristics of the snap-through process.

The knowledge gained from the semi-analytical calculations facilitates the design and analysis of more complex multistable rectangular plates. Optimal design of rectangular plates with actuators that leads to maximum out-of-plane displacement but with minimum snap-through voltage is determined. A novel concept of a morphing trailing edge flap with integrated rectangular bistable plates is proposed. In this new concept, the trailing edge deflection is realized by the snap-through of the multistable rectangular plates. The viability of the proposed morphing mechanism is examined using finite element tools.

Keywords: Multistable structure, Morphing trailing edge flap, Variable-stiffness laminate, Snap-through process, Semi-analytical method

Zusammenfassung

Mit zunehmender Thematisierung des Klimawandels vertiefen auch immer mehr Branchen und Forschungseinrichtungen die Suche nach ökologischen Energiequellen. Windenergie ist eine der billigsten sauberen Energieformen und somit eine attraktive Alternative zu nicht erneuerbaren Energien. Das Hochskalieren von Windkraftanlagen gilt klassischerweise als Mittel zur Kostensenkung je Kilowattstunde und ist nach wie vor im Trend.

Mit zunehmender Größe der Rotorblätter von Windkraftanlagen besteht jedoch die Notwendigkeit, Konstruktionen zu entwickeln, die in der Lage sind, Extrem- und Ermüdungslasten zu reduzieren. Die aktive Hinterkantenklappe ist ein vielversprechendes Konzept zur Entlastung großer Rotorblätter von Windkraftanlagen. Die meisten existierenden Klappenmechanismen haben zwar das Potenzial zu einer schnellen Reaktionszeit, und damit verbundener Lastreduktion, sind aber oft mit komplizierten Aktuator-Systemen verbunden, was zu zusätzlichem Gewicht und zunehmender Komplexität führt. Darüber hinaus erfordern sie eine kontinuierliche Energiezufuhr, um eine bestimmte Position der Klappe beizubehalten. Multistabile Laminate mit variabler Steifigkeit (VS) haben ein großes Potenzial bei Morphing-Anwendungen, in erster Linie aufgrund der Existenz mehrerer stabiler Gleichgewichtslagen. Der Einsatz von VS-Laminaten mit kurvenförmigen Faserbahnen ermöglicht es, die Leistungsfähigkeit von multistabilen Laminaten als Morphing-Strukturen weiter zu verbessern.

Das Hauptziel dieser Arbeit ist es, die Eigenschaften von multistabilen VS-Laminaten nutzbar zu machen, und sie bei einem neuartigen Entwurf von Morphing-Hinterkantenklappen anzuwenden. Um dies zu erreichen, bedarf es nicht nur der Entwicklung numerischer und analytischer Werkzeuge, sondern auch eines geeigneten Entwurfes, um die VS-Eigenschaften in eine Morphing-Klappe zu integrieren. Daher wird in dieser Arbeit ein schnelles semi-analytisches Berechnungsverfahren entwickelt, um stabile Gleichgewichtslagen von VS-Laminaten vorherzusagen. Darüber hinaus wird in einer systematischen Studie untersucht, wie sich die stabilen Zustände bei Variation der kurvenförmigen Faserbahnen ändern. Als Ergebnis dieser Untersuchungen wurden Kriterien abgeleitet durch die VS-Laminate in Familien mit gleichartigen multistabilen Gleichgewichtslagen eingeteilt werden können. Dies ist wiederum für den vorgesehenen Entwurf der Morphing-Klappe erforderlich.

Durchschlagen, d. h. der Übergang von einer Gleichgewichtslage zur nächsten, ist ein wesentlicher Prozess bei der Charakterisierung multistabiler Laminate in Morphing-Anwendungen. Zwei unterschiedliche Durchschlagsmechanismen werden hier untersucht, einer mit Hilfe konzentrierter Krafteinleitung, und der andere mit piezoelektrischen Aktuatoren. Das oben genannte semi-analytische Berechnungsverfahren verschafft Einblicke in die zugrundeliegende Mechanik sowie die Eigenschaften des Durchschlagsprozesses.

Die Erkenntnisse aus den semi-analytischen Berechnungen ermöglichen Entwurf und Analyse komplexerer multistabiler Rechteckplatten. Es wird der optimale Entwurf von rechteckigen Platten mit Aktuatoren bestimmt, der zu einer maximalen Verschiebung außerhalb der Ebene führt, jedoch eine minimale Durchschlagspannung erfordert. Ein neuartiges Konzept einer Morphing-Hinterkantenklappe mit integrierten rechteckigen bistabilen Platten wird vorgestellt. In diesem neuen Konzept ist die Auslenkung der Hinterkante durch multistabile Platten realisiert. Die Verifikation des vorgeschlagenen Morphing-Mechanismus wird mittels Finite Elemente-Software erbracht.

Schlagworte: multistabile Struktur, Morphing Hinterkantenklappe, variabler Steifigkeit, Durchslagsprozess, semi-analytisches Berechnungsverfahren

Acknowledgements

This thesis is accomplished at the Institute of Structural Analysis (ISD), Leibniz Universität Hannover. The presented work has been supported by IRTG-1627 Grant from DFG - German Research Foundation and SmartBlades2.0 project funded by BMWi - Federal Ministry for Economic Affairs and Energy.

Many key people have contributed in different ways to the successful completion of this dissertation. First of all, I would like to express my sincere gratitude to my supervisor, Professor Raimund Rolfes, for giving me the opportunity to work on such a new and exciting topic. I am most grateful for his immense support, insights, critical views, and constant reminding to look at things in the bigger context, which has been particularly important for the development of this research. I also thank him for engaging me in teaching and supervising activities, writing project proposals, and giving the freedom to develop my own ideas, which certainly enhanced my scientific, professional, and personal skills.

This work would not have been possible without the constant support and invaluable mentorship of Dr. Eelco Jansen. I am extremely indebted for all his invaluable ideas, incessant help, and countless discussions, even at the most ungodly hours.

An important part of this thesis was initiated during my research stay at the LMT-Cachan. Words cannot express my gratitude and appreciation for Professor Olivier Allix. His priceless supervision and the stimulating discussions during my time in Cachan contributed immensely to this work.

A special place in this acknowledgment should undoubtedly be held for Prof. Paul Weaver, whose insights and ingenuity reflected a substantial part of this thesis. His passion and dedication to research is an inspiration for me. I am truly grateful to both Prof. Weaver and Dr. Alberto Pirrera for hosting me at ACCIS, University of Bristol, and sharing their expertise and ideas. Further, I would like to thank Dr. Rainer Groh for all the useful discussions that helped in understanding and implementing the DQM part.

I express my appreciation to various project partners from the SmartBlades2.0, especially colleagues from DLR: Dr. Johannes Reimenscheider and Dr. Martin Pohl, who helped me to look at the practical perspective of this work.

I am thankful to former colleague Dr. Jose Reinoso; not only for his scientific advice and guidance but for his most encouraging and reassuring words. Special thanks to Dr. Benedikt Daum, with whom I had the pleasure to support the course in Composite Lightweight Structures; and for his numerous insightful and valuable discussions, and his unceasing readiness to help. My sincere thanks to Benedikt Hoffmeister and Marlene Bruns for extending their help and expertise for the optimization part of this work. Furthermore, I take this opportunity to acknowledge the students I had the honor to advise - Anilkumar PM, Janina Moehle, and Class Kleinhoff.

I would like to express my appreciation to my current and former colleagues at ISD, for a cheerful and friendly work atmosphere. Many thanks to Cristina Diaz, Roozbeh Nabavi, Christian Gebhardt, Mehdi Garmabi, Margarita Aktersakaia, Christian Hente, Gerrit Gottleib, Dorian Pache and Tim Rogge, with whom I had spent some wonderful time that I will cherish my whole life. Many thanks to Andreas Ehrmann and Stefan Wernitz for helping me with the German abstract. This acknowledgment is incomplete without mentioning Stavroula Tsiapoki and Sander van den Broek, with whom I had the pleasure to share my office. I sincerely thank for their invaluable support and friendship during the ups and downs of this journey.

I am truly indebted to my friends Prez, Naskar, Ayan Da, Sangeeta Di, Mr. Ja, Swati, Dr. Fau, Bhumika, Aparna, Prajna, and Thirumal. Their friendship and support during this Ph.D. time were priceless. I specially thank Steffi for her continuous moral support and help at every step, and keeping her sanity throughout.

Last but not least, I would like to thank my lovely parents and my brother, Ankit, for their unconditional love and support throughout my entire life, and without whom I could not even imagine to reach this point.

Contents

List of Figures

List of Tables

Nomenclature

Acronyms

CLT	Classical Lamination Theory
ECLT	Extended Classical Lamination Theory
CTE	coefficient of thermal expansion
FEM	Finite element method
SMA	Shape memory alloy
MFC	Macro Fiber Composite
PVDF	polyvinylidene fluoride
TE	Trailing edge
UD	unidirectional
GW	Gigawatt
MW	Megawatt
BTC	Bend-twist coupling
AFC	Active flap control
TRL	Technology readiness level
EU	European union
US	United states
DQM	Differential quadrature method
PMPE	Principle of Minimum Potential Energy
AFP	Automated Fiber Placement
CTS	Continuous Tow Shearing
CMTS	Continuous multi-tow shearing
TFP	Tailored fiber placement
VS	Variable stiffness
MFC	Macro-Fiber Composite
DLR	Deutsches Zentrum für Luft- und Raumfahrt (German Aerospace Center)

Symbols

θ	Fiber Orientation
ϕ, T_0, T_1	Angle parameters for VS laminates
u, v	In-plane displacements
w	Out-of-plane displacements
S	Surface area
ϵ	Total strain vector
ε	Mid-plane strain vector
κ	Curvature vector
N	Membrane stress resultant
M	Moment resultant
N^{th}	Thermal force resultant
M^{th}	Thermal moment resultant
A, B, D	In-plane, coupling and bending stiffness matrices respectively
Π	Total Strain Energy
V	Work due to External Forces
W_T	Total virtual work
$\tilde{\Pi}_d$	Factor to scale the total strain energy
U_d, V_d, W_d	Factors to scale the displacements
q_{ij}	Coefficients of Legendre polynomial
$\tilde{\mathcal{L}}_A$, $\tilde{\mathcal{L}}_B$, $\tilde{\mathcal{L}}_c$	Differential operator
$\boldsymbol{E}$	Factor to scale the mid-plane strains
$\boldsymbol{K}$	Factor to scale the curvatures
ΔT	Difference between the curing and the room temperature

Subscript

0	Mid-plane surface
th	Thermal effects

Superscript

$\sim$	Non-dimensional parameters

1

Introduction

1.1 Background

Over the years, there has been a quest to conceptualize designs relying on continuous and smoother geometrical changes in aerospace structural components. The term "morphing" has been coined to describe this novel strategy which characterizes continuous shape change without any discrete parts moving relative to each other. Structural shape adaptivity or morphing has been a subject of promising research, especially in aircraft wings enabling maneuverability, better fuel efficiency, and multiple mission capabilities. Several morphing aircraft concepts have already been proposed and have matured to types such as the compliant trailing edge flap manufactured by Flexsys Inc. [122], which is capable of achieving a deflection of $\pm 10^\circ$ and twist deferentially up to 1° per foot over the span using an internal electromechanical actuator. Another example is the seamless skin and wing folding elements developed at Lockheed Martin [35].

Apart from morphing aircraft, there is an increasing demand for developing efficient morphing wind turbine rotor blades. Wind energy is the fastest growing renewable energy source, whose usage has increased by a factor of fifty in the last two decades. The worldwide capacity has increased from 7.5 GW in 1997 to 597 GW by the end of 2018. With 87 GW of wind power due to be installed in the next five years, Europe could reach 258 GW of installed capacity by 2022 [221]. In 2018, wind energy increased its capacity more than any other form of power generation in the EU. It accounted for 48% of the total new power capacity installations. What has been observed over the years is that with the growth of the wind energy industry, there has been a steady increase in the size of rotor blades. This is particularly aimed towards reducing the cost per kWh wind power [207]. General Electric Co. (GE) [93] recently announced developing Haliade-X 12 MW offshore wind turbine with a 220 m rotor and 107 m blades, the largest of its kind in the world. It promises to generate 45% more energy than the most powerful wind turbine available in the market.

Following the Betz law, the electrical power P generated by wind turbine blade with radius r at a given wind velocity v, air density ρ and power coefficient c_p is given by:

$$P = \frac{1}{2}\rho\pi r^2 v^3 c_p \tag{1.1}$$

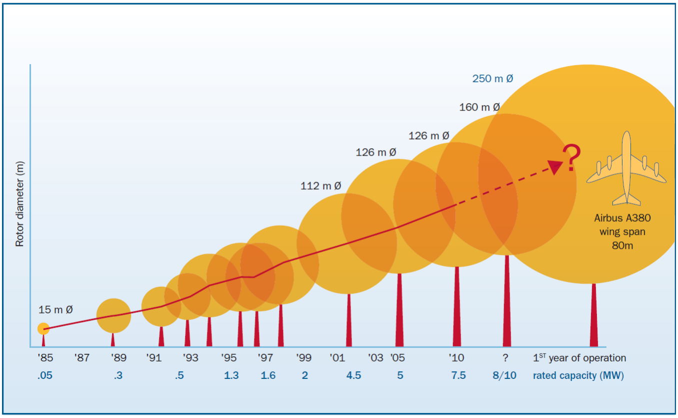

FIGURE 1.1: Trend of growing wind turbine blade size (Courtesy Upwind project report [71]).

It can be seen from Equation 1.1 that upscaling the wind turbine increases the energy production, as the energy yield is directly proportional to the square of the diameter. Wind flow is stronger at larger altitudes, with which more energy can be harvested readily. Unfortunately, increasing the blade size also increases the mass of the blade by r^3, which in turn increases the critical stresses at the root of the blade.

Aerodynamic loads in large rotor blades can be highly variable and fluctuating in nature. Variability is caused by factors like yawning operation, gust, wind shear, and turbulence [95], which increases with altitude. Larger rotor blades can result in an increase in the bending moment at the root of the blades. Additionally, higher loads variability due to the turbulent nature of the wind at higher altitudes can increase fatigue loading. Reducing fatigue loads can lead to a significant reduction in cost, affecting required materials, maintenance costs, and system reliability [13]. Therefore, one of the primary goals in the wind energy industry and the research community is to develop innovative and efficient technologies to reduce ultimate and fatigue loads in large wind turbine systems.

1.2 Morphing mechanisms

Conventional methods like pitching the entire blade from the root can reduce loads to a certain extent [95]. However, due to the high inertia and speed of the blade, rapid actuation in response to aerodynamic loading is quite difficult. Furthermore, local variation of the aerodynamic loading along the length of the blade cannot be controlled by changing the blade pitch. Keeping this in mind, morphing sections capable of rapidly changing shape by suitable actuation techniques provide a better alternative. Several concepts from recent programs and research works for load mitigation can be found in the review papers([13], [112], [127]). Figure 1.2 shows the classification of different morphing mechanisms in smart wind turbine blades. Principally, these concepts fall into either of the two categories: Active and Passive control.

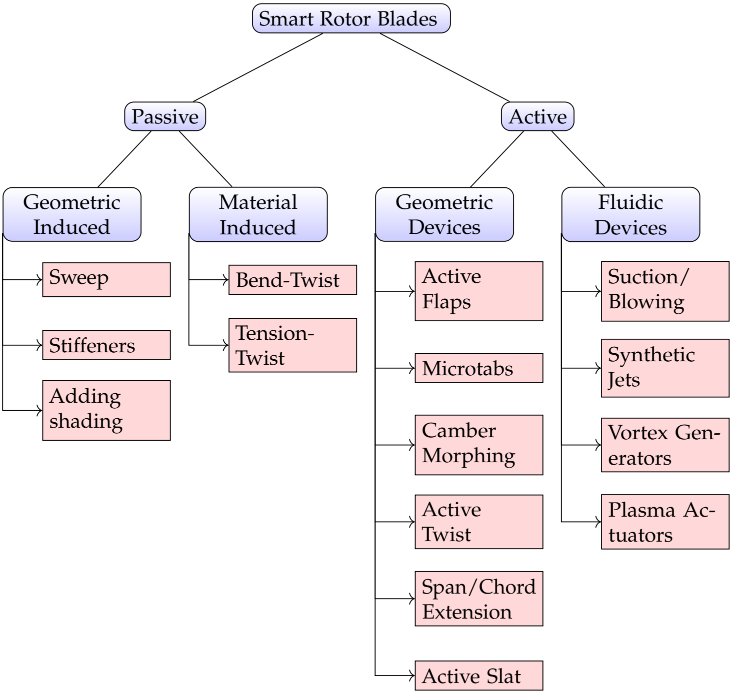

FIGURE 1.2: Classification of morphing mechanisms in smart wind turbine rotor blade.

1.2.1 *Passive control*

Passive control involves mechanisms through which the system responds to certain parameters (e.g., load, pressure) and automatically activates the morphing mechanism when the measured parameters exceed a threshold value. The mechanism is intended to allow variation in the aerodynamic loading, as the angle of attack changes. What makes passive control an attractive option is its simplicity. There is no requirement of any additional mechanical parts or actuators, making it easy to maintain [192]. However, most passive systems lack control and are often open looped, which means, change, or control in the passive system is not possible during operation. This can in-fact have a negative influence on the performance.

Passive systems can be broadly divided into geometry and material based control. Material based passive control involves exploiting the material anisotropy of composite laminates and suitable coupling between different stiffness components. A few examples of material based passive control are through utilizing the Tension-Twist coupling and Bend-Twist coupling [39, 69, 135, 203, 211]. The bend-twist coupling (BTC) exploits the laminate design with bending-twisting stiffness coupling. As the blade bends out of the plane, a twist deformation occurs simultaneously reducing the net aerodynamic loading. Fedorov et al. [68] manifested the BTC effect in wind turbines through experiments and full 3D finite element (FE) simulation.

Geometry based passive systems involve changing the shape of the blade with a certain twist [8] or by introducing an additional structural component, for example stiffeners [96]. The former can be achieved by the concepts of sweep introducted by Liebst [134] and later studied by Zuteck [227] and Larwood [129], where a load reduction of 5%-10% is reported. The load generated by the tip of the blade causes a moment about the pitch axis which in turn assist the tip to twist, resulting in load alleviation. The combination of both geometric and material coupling for passive control can lead to further load reduction as shown in [40].

Passive systems have been researched extensively over the years and have been a part of several research projects. The project *INNWIND* and *SmartBlades* have investigated the BTC concept for large wind turbine blades, to reduce fatigue damage.

1.2.2 *Active control*

Active control, on the other hand, allows a change in the aerodynamic loading by introducing local structural or flow changes. Two types of active controls have been widely investigated, namely fluidic and geometric devices. Geometric devices can alter the flow field around the blade by changing the airfoil profile. Prominent examples for such concepts include the suction/blowing of air, synthetic jets, vortex generators, and plasma actuators.

Blowing of air involves injecting air stream through orifices or slats at specified locations of the blade. On the other hand, suction aims at removing air flow close to the airfoil surface. Both strategies are used to change the pressure gradient to circumvent flow separation. Synthetic jets, on the other hand, consists of a cavity of variable volume controlled by a diaphragm. Plasma actuators create a strong electric field between a pair of electrodes, which ionizes the air molecules. This process accelerates the air molecules in the direction of the flow delaying the transition from laminar to turbulent flow. Fluidic devices have the advantage of faster response time and no requirement of moving mechanical parts.

Apart from fluidic devices, other ways of active control are through geometric devices. Some notable example being microtabs and flaps. Microtabs are devices that protrude outside the trailing edge surface, increasing the chord length by $1-2\%$. However, its position is either 'retracted' or 'extended' and therefore, no intermediate change in the lift coefficient can be achieved.

Active Flap Control (AFC) systems offer easier control and more flexibility than other concepts, especially during unsteady changes in flow state [47]. AFC for wind turbine blades is inspired by the concept of aircraft wing flaps. From the past studies, it can be concluded that it has reached a high TRL (technology readiness level). An extensive review of different concepts of passive as well as the active flow can be found in [13, 23, 62, 112].

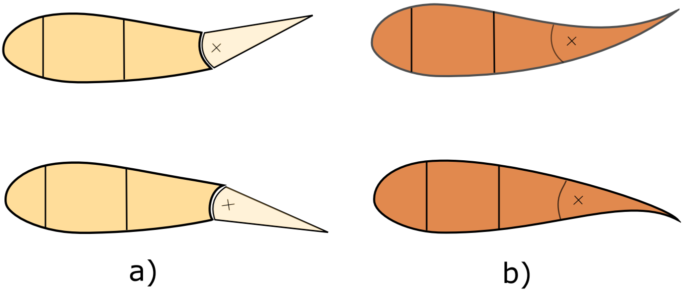

FIGURE 1.3: a) Rigid Flap b) Flexible Flap.

Several studies [9, 13, 132] have shown that fatigue loading can be decreased by employing a fast and distributed active trailing edge flap. As shown in Figure 1.3, flap at the trailing edge can be placed using two different ways: rigid and flexible. Rigid flaps or ailerons are usually hinged and require a moment over the hinge to achieve different configurations. Further, surface discontinuity can trigger noise and stall issues, which are critical design criteria for wind turbines. On the other hand, continuous morphing trailing edge flaps show better effectiveness and lift to drag ratio with a smooth change in the camber [1].

1.3 Past active flap concepts for wind turbine blades

In the last two decades, various projects have been undertaken in collaboration with research institutes and industries, and as a result, several concepts for active flaps have been studied and investigated. Some concepts, have also been experimentally tested with small prototypes in real test conditions. Table 1.1 gives a brief overview of some of the major projects carried out in collaboration with the EU and US.

In the *Smart Rotor* project coordinated by Sandia National Labs, a conventional rigid flap was used and actuated like a small scale aircraft control surface. A 9 m wind turbine blade was used, with the cut-out of the flap extending from 40%

Project	Year of commencement	partners	Flap Concept	Key Features	References
ADAPWING/ **ADAPWING 2**	2003	DTU	Metallic flap with THUNDER actuators (60 cm x 6 cm)	3D numerical studies showed 64% reduction in flapwise root bending moment for 12 m flaps on 33 m blade.	[10, 34]
INDUFLAP/ **INDUFLAP 2**	2011- 2014 2014-2018	DTU Siemens Hydratech Industries Rehau	Controllable Rubber Trailing Edge Flap with pressurized fluid (15 cm) in 1m chord-wise length	Flap required few assembling elements. Optimal blade design for integrated flap, with 1% increase in AEP.	[14, 141, 150]
UPWIND/ **INNWIND**	2006-2011 2012-2017	27 EU partners Coordinated by DTU	Made of carbon fiber laminate, with 3D printed zero Poisson's ratio honeycomb core and a flexible silicone surface. Actuated using SMAs.	Component level innovation integrated to offshore wind turbines. Successful experimental proof achieved on load alleviation with combined flap and pitch control.	[2, 11, 12, 199]
SmartBlades/ **SmartBlades2**	2014-2016 2016-2019	DLR, IWES-Fraunhofer, DLR, ForWind and Industrial partners	Glass fiber structure, actuated by forces. Gaps between stringer and spar was covered with elastomer	Both passive (BTC) and active concepts (Flaps) investigated, with the aim of lab and field measurements.	[152, 156, 170, 180]
AVATAR	2013-2017	11 Research Institutes and 2 Industrial partners. Coordinated by ECN, Netherlands	DU95W180 airfoil equipped with an actuated rigid trailing edge flap with 20% chord	Validated aerodynamic models with and without flow devices in large scale wind turbines. LE/TE flaps and VGs considered as flow device.	[41, 42, 67]
Smart Rotor	2010-2013	Sandia National Labs TU-Delft	Hinged Flap with 10 percent chord	Conventional hinged flaps which the possibility of simple integration and good aerodynamic control authority.	[19, 20, 22]

Table 1.1: A brief overview of major EU and US projects on smart wind turbine blades.

of the chord length at a span length of 7.029 m and linearly expanding to 50% at 8.857m. The load alleviation capabilities were demonstrated using numerical and experimental tests. Further insights into the project could be found in the project report files [18, 21].

The Danish national *ADAPWING* project [10, 34] focused on the numerical and experimental studies of using a Vestas v66 rotor blade (33 m long blade), where different flaps were applied in six different sections, to allow independent control. Using a total of 11 m long flap, it was possible to reduce flap-wise root bending moment by 64%. The wind tunnel experiment carried out on Riso B1-18 pitching blade equipped with morphing trailing edge flap. It is seen that C_L varied about 0.14 for the pitching profile without flap response. The curve with an active flap with pitching resulted in a C_L variation of 0.025 which is a reduction of 82%

As part of *INNWIND* project, a morphing flap comprising of light weight carbon fiber laminate and made of 3D printed zero Poisson's ratio honeycomb core and a flexible silicone surface, was used to conduct an extensive test campaign. The flap was tested on a rotating rig under similar operating conditions as a full scale turbine, using a realistic Reynolds number and turbulent inflow. The test campaign included the effect of both pitching and flap actuation at the same time.

At Risoe (now DTU Wind Energy), the pursuit of technological solutions for active flap control of large wind turbines was initiated back in 2003, with the goal of developing a robust and efficient flap system for large wind turbines. In 2006, DTU patented the so-called Controllable Rubber Trailing Edge Flap (CRTEF), made of flexible elastomer, which deflects when pressurized air or fluid fills in a number of voids in the flap. The concept is simple as no mechanical or moving metal parts were involved. The prototypes were investigated, tested and further developed in collaboration with industry partners like Hydratech Industries (DK) and Rehau (DE), within the *INDUFLAP* project. The flap system with a boom was tested in a real operating condition with real atmospheric turbulent inflow in a testing rig. From the test results, it was reported that a 3° flap deflection gave the change in lift similar to 1° pitch of the whole blade.

The project *AVATAR* was carried out with 11 EU research institutes and two industry partners, coordinated by the Energy Research Center of the Netherlands (ECN). The focus of the project was on studying the aerodynamics of large wind turbines (> 10 MW). Apart from the development of different tools for aerodynamic modelling, a part of the work was focused on aerodynamic studies of flow device with vortex generators and Leading Edge (LE)/ Trailing Edge (TE) flaps, using both numerical and experimental methods.

The project *SmartBlades* focused primarily on four different technologies: a) Passive control using bend-twist coupling b) Active trailing edge flap c) Active leading edge flaps d) Cross-technology topics. The main goal of the project is to validate developed tools and models using wind tunnel and field tests of demonstrators. The cross-technology topics focus on developing new insights for the wind turbine as a whole and investigating the potential and drawbacks of all the other three concepts. The whole project aimed at reaching a higher TRL by building and testing the concepts in a real wind turbine and ultimately facilitating the concepts in the industry. Figure 1.4 shows a prototype of an active trailing edge flap used in the Smartblades project. From various project outputs, continuous morphing trailing edge flap proves to be an attractive option, to achieve load alleviation in large wind turbine blades.

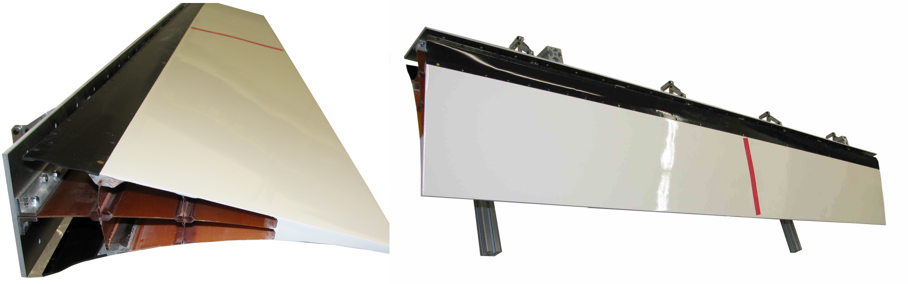

FIGURE 1.4: Prototype of flexible trailing edge [170].

In this and the previous sections, different concepts of morphing mechanisms are discussed for wind turbine applications. Most of the research projects have focused on developing the concept of active flaps. Barlas [13] had pointed out in his review paper that: "It is clear that maximum control authority can be achieved by using trailing edge flaps in combination with mechanically amplified smart material actuation.". A comparison between the lift coefficients of different concepts can be found in Barlas et al. [13]. It has been found that the effect of change in the lift coefficient is significantly higher with using the flaps ($\Delta C_L = 0.4$), than with other devices. However, this study maybe not comprehensive as many new concepts have been introduced in last few years.

1.4 Challenges and motivation

Although many recently developed active control morphing mechanisms have the potential for quick reaction time, it often involves intricate actuation systems. As seen from previous works, conventional actuating systems suffer from severe wear and tear at the junction due to alternating movements during the flap motion, requiring high maintenance. The penalties associated with excess weight, complexity, and cost involved in mechanical actuators hinder such morphing concepts from reaching a high TRL. In compliant morphing mechanisms, a continuous supply of energy input is required to maintain a particular position. Hence, concepts addressing minimum energy requirements is a key challenge in any morphing system.

In this work, to design a light and simple morphing system, the property of multistability is exploited. This is done mainly to enable large deflections with low actuation demand. Multistable structures have great potential in morphing

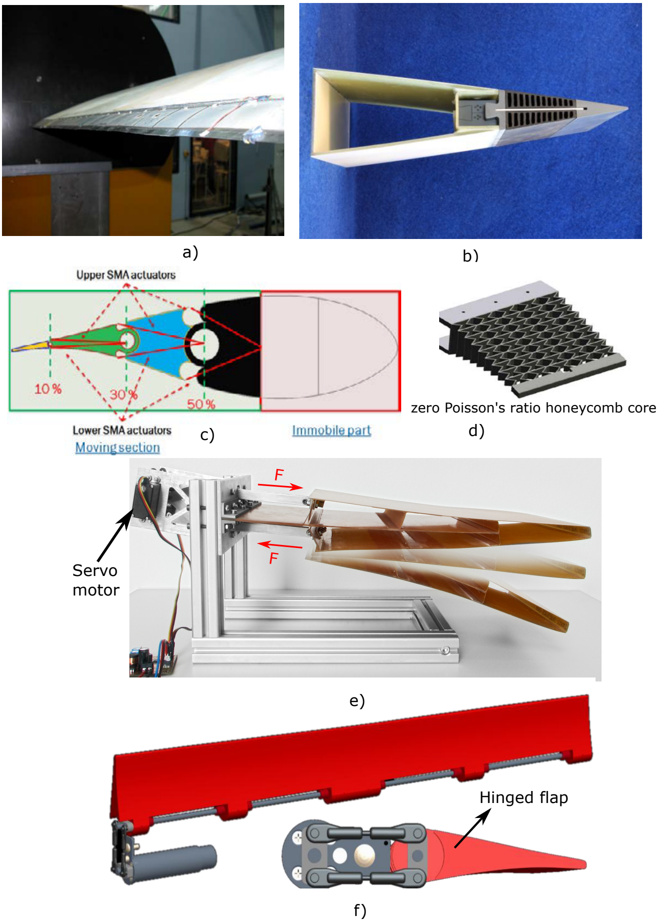

FIGURE 1.5: Different active flap concepts realised in major US and EU projects a) Continuous trailing edge flap morphed using THUNDER actuators, consisting of thin layer of piezoelectric material attached to a metallic substrate (ADAPWING project). b) Controllable Rubber Trailing Edge Flap (CRTEF), made of flexible elastomer, which deflects when pressurized air or fluid fills in a number of voids in the flap (INDUFLAP project) c) Flap with zero Poisson's ratio honeycomb core and a flexible silicone surface, actuated using SMAs, d) showing the 3D printed flap (INDUFLAP project). e) Glass fiber central structure, actuated using electric servo motor with specially designed control unit (SmartBlades project), f) Hinged flap (SmartRotor project).

applications due to their ability to remain in stable equilibrium states without any external force/energy. The multiple stable shapes can correspond to different deflected states in a morphing mechanism. Continuous supply of energy is not required to hold a particular configuration; rather, energy is required to snap from one stable shape to another. The main challenge lies in addressing the inherent conflicting requirements evident in any morphing structure. They are being lightweight, flexible to allow shape changes and at the same time possessing adequate load bearing capabilities. A structure demands a vastly varying internal composition to fulfil such conflicting criteria. Such a design would encompass desired multiple deformation modes with reduced actuation effort.

Variable stiffness (VS) laminates, with spatially varying fiber orientations are promising candidates to be applied in morphing structures. They underlie an active subject of research owing to advanced manufacturing techniques. However, their tailoring capabilities are still not fully exploited for different morphing mechanisms. In particular, combining multistability and VS laminate generated from curvilinear fiber paths is a topic yet to be fully explored. In this regard, the present thesis addresses a systematic investigation on multistable VS laminates, particularly looking at the stable shapes and actuation requirements.

Using active multistable laminates, there is further need to conceptualize a morphing flap design for wind turbine blades. The foremost challenge of including actuators on multistable plates is the chance of losing its multistability. Due to the added stiffness of any actuation system, the multistable laminate might reduce curvature or in extreme cases lose its multistable nature. Therefore there is a need to place the actuators in an optimal manner such that a design is aimed with minimum energy input to trigger snap-through and at the same time maximum out-of-plane displacements.

1.5 Research objectives

From the description of the current state of the art for smart wind turbine rotor blades, as well as the motivation described from the last section, the concept of utilizing multistable VS laminates is quite promising. An adequate understanding and systematic exploration of the multistable VS laminates is still missing in the literature. In this thesis, the following questions are intended to be addressed:

1. How do thin structures change shape in general? Which parameters drive such a process?
2. Can we increase the range of multistable shapes using VS laminates?
3. Is it possible to design multistable composite plates leading to stable shapes with high curvatures but at the same time requiring less force to snap?
4. How realistic is it to change such shapes using actuators?
5. Finally, how can we use multistable laminates in a real morphing application: a morphing trailing edge flap of a wind turbine blade?

The goal of the thesis is to depart from conventional straight fiber laminates and exploit VS laminates as multistable structures. Such laminates are then aimed to be used in potential morphing applications.

In the process of addressing the above-posed questions, we aim to understand the behavior of the multistable VS laminates using analytical as well as numerical tools. One objective will be to develop fast efficient analytical tools to capture the behavior of such laminates with simpler geometry, leading to a better understanding of the behavior of such structures. Numerical tools will also be developed to verify the analytical results, and additionally, tackle more complex geometry. A rectangular plate with VS laminate will be designed to allow both snap-through and snap-back using piezoelectric actuators. This would require an calculating the optimal size and location of the actuators to achieve the most efficient snap-through mechanism. Finally, the objective is to propose a concept where such multistable laminates could be integrated into a morphing wind turbine flap. The concept is aimed at replacing conventional actuator systems with bistable laminates and achieving the ensuing deformations with feasible actuation requirements.

1.6 Outline of the thesis

In this section, a summary of each chapter is highlighted, focusing on the key concepts and methodologies. In this thesis, starting from a fundamental square plate type structure, we progress slowly with each chapter to finally apply the bistable plates into a morphing trailing edge flap. Figure 1.6 illustrates briefly the outline of the thesis. This work not just aims at the practical implications of this concept, but also focuses on the understanding of the behavior of bistable VS laminates.

Chapter-2 begins with an extensive literature review on multistable structures and highlighting different techniques of inducing multistability. Particularly, different analytical, numerical and experimental works on unsymmetric laminate is presented. Different actuation techniques and different concepts on how they have been applied in morphing applications are reviewed as well.

In **Chapter-3**, a theoretical background of different topics is presented that serves as a basis for the content presented in the following chapters. Some fundamental questions are raised. Further, the concept of tow steered laminates is introduced, and a brief description of the differential quadrature method (DQM) is presented.

In **Chapter-4**, lays the foundation of the thesis, where the bistable shapes of VS laminates resulting from the cool-down process from curing temperature are investigated. A semi-analytical framework based on the Rayleigh-Ritz method is developed, which is verified with FE tools. The semi-analytical model is further used to carry out a parametric study. From this study, the families of VS laminates are classified based on the cooled-down multistable shapes. This chapter clearly illustrates the enrichment of the design space possible with VS laminates.

In **Chapter-5**, the VS laminates that yield stable shapes similar to cross-ply laminates are specifically addressed. Such shapes allow fulfilling the requirements imposed by the envisaged morphing application. The semi-analytical approach is further extended to calculate the snap-through loads. A corresponding numerical model is developed to capture in detail the snap-through process for different VS laminates and compare with the semi-analytical model.

Chapter-6 presents a reduced semi-analytical model to calculate the snap-through loads. The total strain energy is decoupled using a semi-constitutive approach so that the stretching and bending energy are calculated separately. By solving the in-plane equilibrium equations and the compatibility equation, the in-plane stress resultants are written in terms of curvatures. The resulting system of PDEs is solved using differential quadrature method. This reduction procedure allows higher order polynomial approximation for the curvatures, with low computational costs. The snap-through mechanisms of different VS laminates are studied.

In **Chapter-7**, piezoelectric actuators are used to realize snap-through as well as snap-back for square unsymmetrical laminate. The semi-analytical model developed in the previous chapter is extended to include the addition of actuators. Two sets of actuators are attached on the top and the bottom surface of the bistable square plate. A two-way morphing mechanism is adopted, where both the actuators are employed simultaneously. The developed semi-analytical results are compared with the numerical results. The VS laminates are identified, which results in low snapping voltages.

Chapter-8 addresses the design of a rectangular bistable plate suitable for embedding in a larger morphing structure. The insights acquired from the previous chapters are used to design this plate, where a part which engenders bistability constitutes either a) cross-ply laminate or b) VS laminate. The dimensions of the plate are designated based on its envisaged integration in a larger morphing flap. The plate is triggered to snap using either force or actuators. The location of the actuators is optimized to satisfy the two objectives a) minimizing the snapping voltages b) maximizing the out-of-plane displacements.

Chapter-9 presents the proposed morphing concept of a wind turbine trailing edge flap. The bistable rectangular plates designed in the previous chapter are embedded at a particular location of the trailing edge flap. A nonlinear FE model was used to simulate the concept. As the bistable plates snapped from one stable to another, the flap deflected at a particular angle.

Chapter-10 summarizes the important findings and conclusions. Additionally, some recommendations for future work are also proposed.

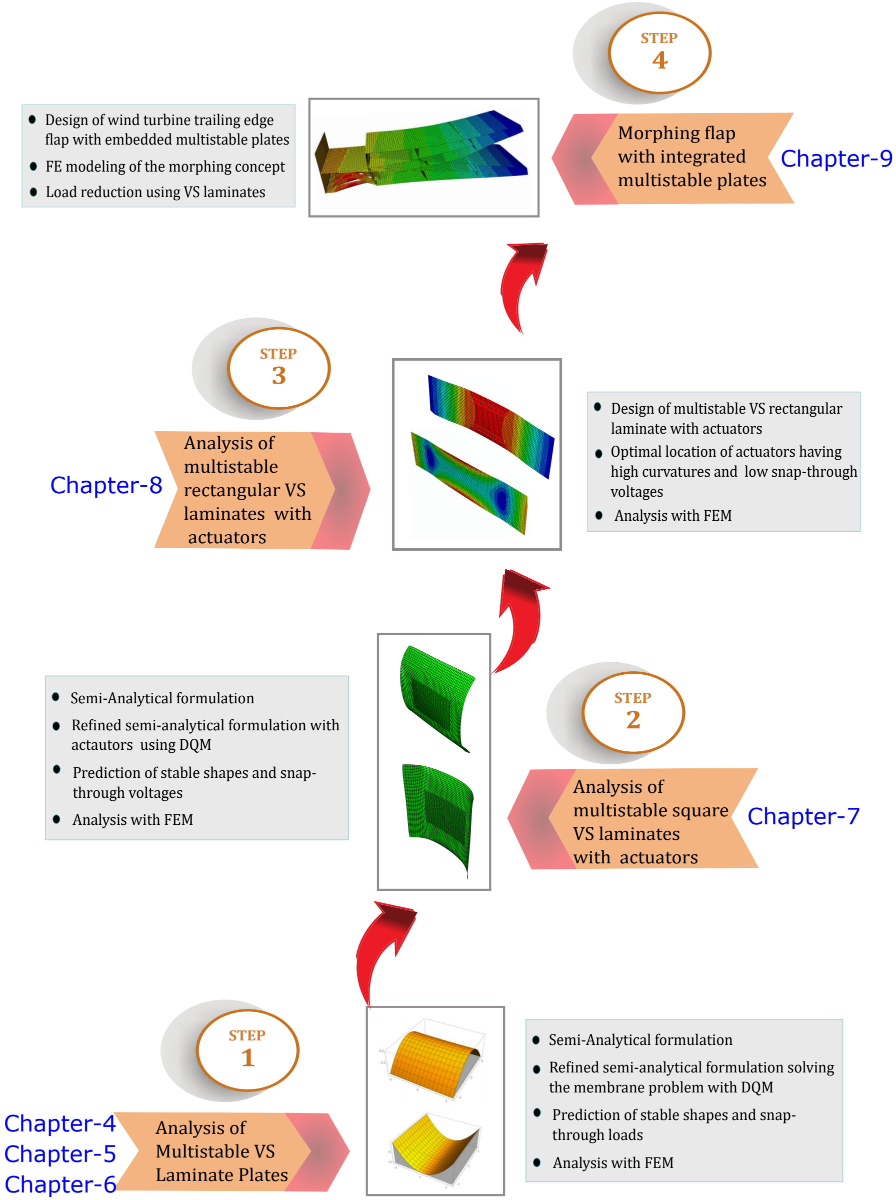

- Design of wind turbine trailing edge flap with embedded multistable plates
- FE modeling of the morphing concept
- Load reduction using VS laminates

- Design of multistable VS rectangular laminate with actuators
- Optimal location of actuators having high curvatures and low snap-through voltages
- Analysis with FEM

- Semi-Analytical formulation
- Refined semi-analytical formulation with actautors using DQM
- Prediction of stable shapes and snap-through voltages
- Analysis with FEM

- Semi-Analytical formulation
- Refined semi-analytical formulation solving the membrane problem with DQM
- Prediction of stable shapes and snap-through loads
- Analysis with FEM

FIGURE 1.6: Brief illustration of the thesis outline.

2

State of the Art

2.1 Introduction to multistable structures

Buckling is traditionally considered as a first step towards failure in slender and thin engineering structures. An alternative perspective is towards the emerging concept of exploiting such geometrically nonlinear behavior to novel multi-functional structures, in other words, advancing from buckliphobia to buckliphilia [177]. The notion of multistability is one such concept that has drawn quite a considerable attention in the last few years due to some of its interesting functionalities in shape changing applications. A multistable structure is characterized by having two or more equilibrium stable shapes in distinct geometrical configurations. Bistable structure, which possesses two stable shapes, is the simplest of the multistable structure. The novel aspect of such a structure is the ability to remain in a particular state without requiring any external energy or force. A certain force/energy is required to snap from one shape to another and vice-versa. The fundamental principle behind the concept of multistability lies in how material anisotropy , geometry or a combination of both develop interaction between bending and stretching energy, inseminating a preferential mode for minimum stored energy [193]. If this potential energy well has multiple local minima, then the structure is deemed to attain any of these corresponding configurations. Some simple examples observed in our day to day life are slap bracelets, contact lens, a spherical cap demonstrated by cutting a tennis ball and many others.

The use of the multistable structure dates back to the 18th century when the clock inventor Harrison invented bimetallic strips [200]. It is commonly used as a component in thermostats and electric devices. The first theoretical description of an elastic multistable structure was first attempted by A.E.H Love to explain why the longitudinal curvature of the spring-steel tape appears to exactly match the transverse curvature [166]. However, he did not succeed and the explanation was offered decades later by Rimrott [181] and later refined solution was reported by Calladine [37]. Though today, we can well describe the functionality of a bistable spring tape, the physics behind it had helped us to construct mathematical models for multistable curved shell structures [73, 74, 108, 109, 126, 193].

Bistability arises particularly either due to the presence of (Figure 2.1 a) initial curvatures, even in isotropic materials, or due to residual stresses arising from material anisotropy (such as unsymmetrical laminates, figure 2.1 b), or the combination of both. Residual stresses can be generated by prestressing isotropic shells, for example as presented in Kebadze et al. [117] (Figure 2.1 c). Kebadze used an analytical model for beryllium–copper cylindrical shells to estimate the curvatures of bistable shells undergoing an elasto-plastic forming process. Symmetric laminates can also be bistable as shown by Daynes et al. [57], with asymmetric prestressing stresses. The prestressing needs to be applied during the laminate curing process, which requires a cumbersome additional setup. Daynes et al. [58] and Li et al. [131] presented hybrid composite laminates with sandwiched metal cores. They are manufactured similar to unsymmetric laminates, but due to the difference in the coefficients of thermal expansion between the metal core and the laminates, the structure exhibited bistability. Chillara et al. [43] studied the snap-through behavior of a bistable composite consisting of two orthogonal mechanically-prestressed laminae with a stress-free isotropic core sandwiched in between (Figure 2.1 d)) . The combination of initial Gaussian curvature and material anisotropy can lead to interesting regimes of tristability for a certain range of material parameters, which was first reported by Vidoli and Maurini [212] and manufactured by Coburn et al. [45].

Bistability can also occur by changing purely local geometrical parameters like by using dimples [78] and corrugations [157, 158] (Figure 2.1 e). By stiffening the shell in one direction, it introduces orthotropy, and with nonlinear changes in geometry leads to multistability. Loukaides [136] showed how honeycomb lattice with isotropic material properties can also exhibit multistability. Recently, origami patterns [60, 65, 214, 225] and krigami [224] have attracted tremendous attention, due to its ability to tune the mechanical properties by controlling the topology of the shell structures. Origami involves developing creases and folds whereas krigami allow cuts. They have inspired to develop metamerials exhibiting multistability capable of shape changing objects from 2D to 3D .

2.2 Different approaches for analyzing multistable laminates

In the past, unsymmetric laminates were often considered undesirable in most engineering applications. This is especially due to the presence of bending-stretching coupling which produced unwanted curvatures with the change in temperature. It is the seminal work of Hyer in 1981, that lead to the paradigm shift of utilizing unsymmetric laminates as useful morphing structures. Hyer presented a study on the deformation shapes of different unsymmetric cross-ply laminates when cooled from curing to room temperature. Hyer found that thin unsymmetrical cross-ply laminate exhibited bistability with two cylindrical shapes when cooled down from curing temperature to room temperature. Contrary to the stigmas associated with

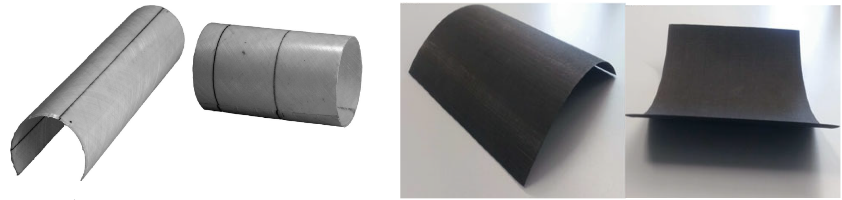

a) Initial curvature

b) Material Anisotropy

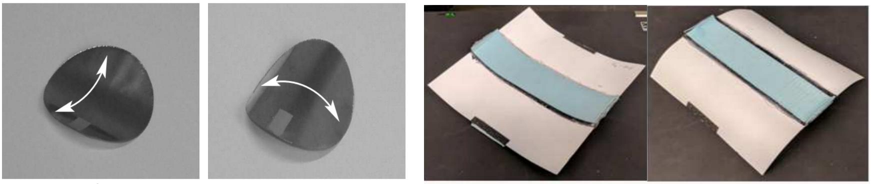

c) Prestess due to Plasticity

d) Elastic Prestress

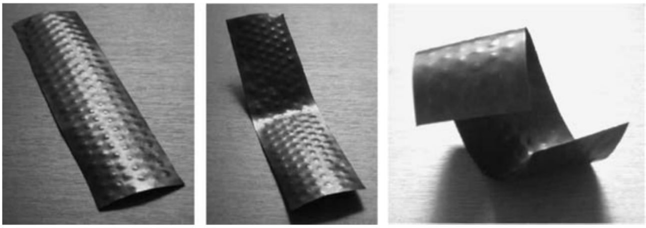

e) Local geometrical patterns

FIGURE 2.1: Different methods of generating multistable structures a) Utilizing gaussian curvature [84], b) Material anisotropy in unsymmetrical cross-ply laminates [91], c) Prestress due to plasticity [196], d) Elastic prestress [43], e) Local geometrical patterns. The picture on left shows multistability in dimpled isotropic shells [194], picture on the right shows multistability in a isotropic corrugated shell [157].

unsymmetrical laminates of having unnecessary warping, Hyer emphasized the potential of utilizing such shapes in an advantageous way.

Different specimens of unsymmetric composite laminates were investigated by Hyer [104]. All of them were cross plies with $[0_2/90_2]$ layup, but having different shapes (shown in Fig. 2.1 a). Bistability in unsymmetric composite laminates is caused due to the difference in thermal properties between the layers, resulting in multiple high deformation modes, thereby accommodating differential expansions within the minimum energy state.

To design multistable components for shape changing applications, it is important that the equilibrium paths are traced accurately up to the post-buckling regimes. Broadly three different approaches have been commonly used in the literature: analytical, semi-analytical and numerical. The analytical solutions, which are closed form and are only possible for certain geometry, load cases, and boundary conditions [73, 74, 84, 108, 142–144, 196]. The semi-analytical approach relies on approximate functions to describe a certain behavior of a structure and has fewer restrictions on the geometry of the structure, as the analytical approach. Finite elements, on the other hand, can be easily applied to any geometry and loading scenarios. The literature review for the semi-analytical and the finite elements, will be covered in the following section, as they are used throughout this work.

2.2.1 *Semi-analytical approach*

Several works on nonlinear vibration, buckling and post-buckling behaviour of composite laminates haven been already been carried out using semi-analytical approaches [33, 110, 111, 123]. In order to study multistable structures, it is of paramount importance that a simple and computationally efficient model is developed. Apart from experimental observations, Hyer calculated the deformation shapes of square unsymmetric laminates using Classical Lamination Theory (CLT). However, Hyer [103] observed that CLT could not predict the cylindrical shapes of the unsymmetrical laminates when cooled from cured temperature to room temperature. CLT predicted the cured shapes of $[0_2/90_2]$ to be saddle-shaped, instead of two cylindrical shapes that were found in the experimental observation. Later, Hyer extended the CLT model with non-linear Von Kármán strains [103]. The following equation depicts the strain-displacement relationship:

$$\epsilon_{xx} = \frac{\partial u}{\partial x} + \frac{1}{2}\left(\frac{\partial w}{\partial x}\right)^2, \quad \epsilon_{yy} = \frac{\partial v}{\partial y} + \frac{1}{2}\left(\frac{\partial w}{\partial y}\right)^2, \quad \gamma_{xy} = \frac{\partial u}{\partial y} + \frac{\partial v}{\partial x} + \frac{\partial w}{\partial x}\frac{\partial w}{\partial y} \tag{2.1}$$

With the additional nonlinear terms, CLT could accurately capture the two cylindrical modes. Interestingly, the model gave three solutions: two stable cylindrical and one unstable saddle shape. The unstable saddle was obviously not detected in the experimental tests. A quadratic approximation for the out of plane displacement w was used as shown in Eq.2.2.

$$w\,(x,y) = \frac{1}{2}\left(ax^2 + by^2\right) \tag{2.2}$$

It can be clearly observed from Eq. 2.2 that the saddle shape occurred when $a = -b$, and cylindrical shape when $a = 0, b \neq 0$ or $b = 0, a \neq 0$. The unknowns a, b were found out using the Rayleigh-Ritz method where the total potential energy was calculated and minimized. Therefore, with just four coefficients, Hyer's model could predict the bistable shapes of the unsymmetrical cross-ply laminates. Hyer [105] improved the previous model by adding increasing polynomial orders to the in-plane displacement terms. Lower order in-plane polynomial functions were previously used for the ease of algebraic calculations. However, only 'even' powers were used as it was assumed that the strain either increased or decreased while moving away from the center of the plate.

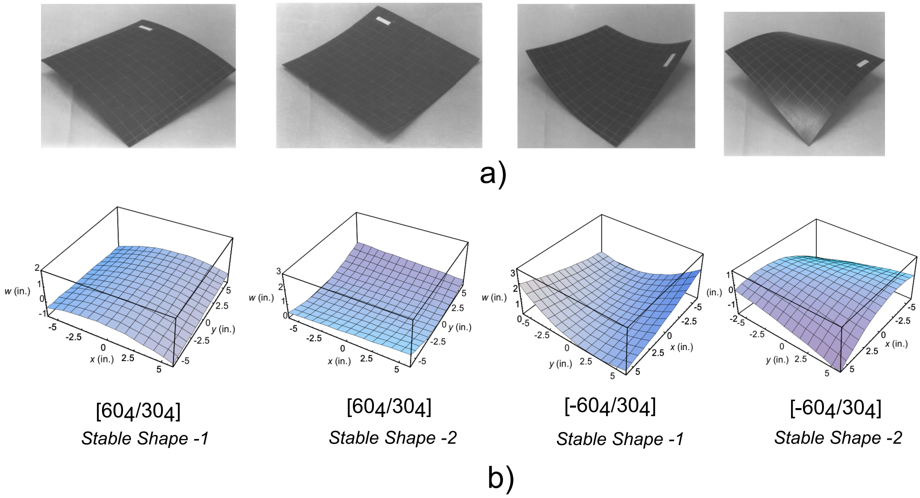

$[60_4/30_4]$ *Stable Shape -1*

$[60_4/30_4]$ *Stable Shape -2*

$[-60_4/30_4]$ *Stable Shape -1*

$[-60_4/30_4]$ *Stable Shape -2*

FIGURE 2.2: (a) Actual shapes obtained for unsymmetrical angle-ply laminates (b) Predicted shapes obtained using semi-analytical method [52].

Dano and Hyer [56] extended the Hyer's model by assuming a polynomial function directly for the strain field and out-of-plane displacement rather than just the displacement field and then calculating the in-plane displacements and stresses. The unknown coefficients were found using the Rayleigh-Ritz Method. Analyzing the obtained results, it was observed that certain terms in the polynomial function always appeared to be zero. It was concluded that all the powers of x and y that summed up to an even number, should be excluded from the polynomial approximation. Taking this into account, the number of coefficients were reduced to fourteen and showed better agreement with FE analysis than previous model of Jung and Hong [115]. The model was more compact than the previously developed models and could accurately capture the curvatures of the stable shapes within a set of polynomial functions, assuming constant uniform curvatures. The Dano-Hyer model also termed as the Extended Classical Lamination Theory (ELCT) was widely considered as 'State-of-the-Art', which was used to perform many further interesting studies ([28, 76]). Figure 2.2 compares the stable shapes of angle-ply laminates with semi-analytical and FE result, showing good agreement. Hufenbach et al. [101] calculated the curvature of the bistable angle-plies and cross-plies for GFRP and CFRP materials with the semi-analytical model from Dano and Hyer and verified them experimentally. The design was successfully applied to novel adaptive multistable composites with integrated smart alloys. The curvatures and principal orientation (results from semi-analytical, FE and experimental) were plotted for cross-plies and angle-plies with the variation of edge length. Various ratios in the composition of $[0_{h1}/90_{h2}]$ were considered, where the ratio of h_1/h_2 varied from 0 to 1 to determine the region of bistability. It was seen that between the ratio 0.3 to 0.7, bistability was preserved and for other ratios there existed only a single saddle monostable shape. Many parameters influence the shape of the laminates, such as the number of layers, relative fiber orientation between the layers and the fiber orientation relative to the laminate coordinate system. Hufenbach also studied variation in the composition of $[0_{h1}/90_{h2}]$ laminate, where the ratio of h_1/h_2 was varied from 0 to 1 to determine the regions of bistability. It was observed that between the ratio 0.3 to 0.7, bistability was preserved and for other ratios there existed only a single saddle monostable shape. Further, Hufenbach and Gude [100] used genetic algorithms for $[0_{h1}/[90_{h2}/[0_{h3}]$ and $[0_{h1}/[90_{h2}/[90_{h3}]$ to determine the stacking sequences and thickness in order to achieve a desired curvature.

Dano-Hyer's model, though produced accurate results, failed to produce a variation of curvature near the free boundaries, as it was based on constant curvature assumption. The polynomial functions used could not predict the stable shapes for complex geometries and ply-layups.

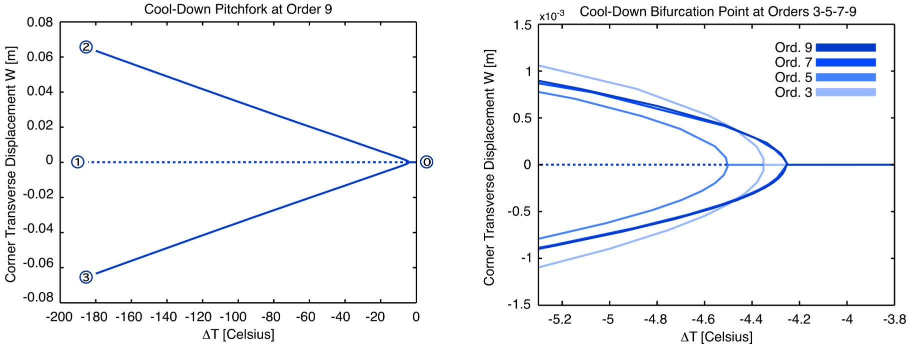

FIGURE 2.3: The figure on the left shows the cool-down bifurcation diagram – Pitchfork obtained with a 9^{th} order polynomial approximation. The plot represents the transverse displacement of the plate corners against the temperature variation. The figure on the right shows the close-up of the pitchfork bifurcation. The bifurcation point moves towards convergence as the order of the polynomial approximation increases. Solid and dashed lines correspond to stable and unstable solutions, respectively [168].

For the first time, a refined higher order polynomial approximation was used by Pirrera et al. [168]. The Ritz method was complemented with continuation techniques based on the path following algorithms. This approach provided a way to explore the design space systematically and parametrically, which was difficult using commercial FE software. Figure 2.3 depicts the cool-down bifurcation diagram obtained from the 9^{th} polynomial functions, which converges to 'pitchfork' bifurcation as the order of the polynomial increases. The change in corner displace-

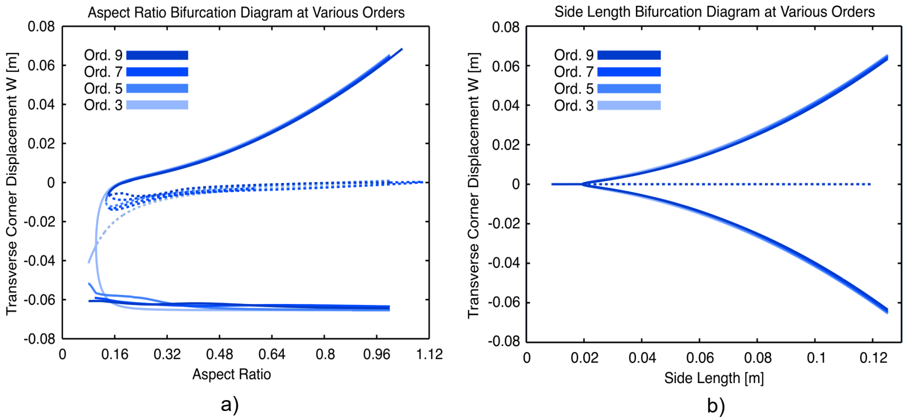

FIGURE 2.4: a) Plot between Aspect ratio v/s corner displacements – As the aspect ratio decreases the solutions reach a turning point and plate loses its bistability b) Plot between side length v/s corner displacements – The plot refers to square plates of various side lengths. As the plates dimensions decreases, the cylindrical solutions become flatter. The saddle-like solution stabilises at the pitchfork, after which the system is no longer bistable. Solid and dashed lines correspond to stable and unstable solutions, respectively [168].

ment with the change in the aspect ratio (Figure 2.4 a)) was also investigated. The pitchfork bifurcation was well observed with higher order polynomials, when the side length of the plate was plotted against the corner displacement (Figure 2.4 b)). As the plate dimension decreased, the structure was no longer bistable and exhibited a single saddle shape. The increased degrees of freedom used in the model provided insights to the complex snap-through process for the first time. It was shown that the kinematic characteristics is well resolved using 3^{rd} order, however the nonlinear behavior like the bifurcation and snap-through required much higher order polynomials. The snap-through load for an unsymmetric cross-ply laminates were computed with a discrepancy of 5% with recpect to the FE result, using 11^{th} order polynomial. Analyses using 11^{th} gave satisfactory description of the nonlinear phenomenon, but at the expense of high computational cost. Pirrera et al. [169] extended the model from flat plates to cylindrical shells. Sander's strain to describe the kinematics, where broader design space was covered with parameters producing larger displacement-to-thickness ratios than observed in Pirrera et al. [168].

2.2.2 *Finite element analysis*

The Finite Element (FE) method has become an indispensable tool to predict the behavior of multistable structures with complex geometrical configurations, and also as a tool for verification with analytical and validation for experimental results. Schlecht and Schulte [185, 186] used finite elements for the first time to calculate the stable shapes of unsymmetric cross-ply laminates using the commercial FE package MARC. Using FE, there is no general restriction regarding laminate geometry and layup description. Moreover, it was shown that FE agreed very well with the experimental values even near the edges, which was rather difficult to attain using simpler analytical tools. However, the principal limitation of FE lies in determining the complete depiction of all the multistable shapes in a single analysis. The nonlinear FE computation of a thermally cured unsymmetric laminate generally renders the unstable solution. Consequently, certain imperfections should be imposed in the form of forces, moments or slight changes in the geometry, to coax the FE to one of the stable shapes. Other stable shapes can be generated by imposing adequate imperfections on the other direction or applying snap-through loads. Further, it often requires fine tuning of parameters in nonlinear incremental algorithms to achieve a converged solution. Due to this encumbered process, FE can be time consuming and computationally expensive.

Tawfik et al. [204, 205] introduced imperfections in the FE simulation, generated from an initial eigenvalue buckling analysis performed on the 'perfect' structure. These resulting eigenmodes were then specified as imperfections for the nonlinear FE analysis. Upon analyzing it with the modified Riks method, one of the stable shapes was found. Once a stable shape was found, a concentrated load was applied to obtain the load-displacement curve, from which the snap-through load was determined. The FE solutions showed a better correlation with experimental values than that of semi-analytical results.

Giddings [75] developed an FE model in ANSYS using solid elements and predicted accurately the cured shapes of bistable composites by including manufacturing imperfections, such as resin rich areas and ply thickness variations. Effects local curvature reversal at the corners due to high through-thickness shear stresses were also predicted well by the FE model.

2.3 Utilizing stiffness variation in multistable laminates

Conventionally, bistable laminates have been developed from prepreg plies with constant stiffness using straight fibers. The laminates that have in-plane variations in the stiffness are particularly interesting as they offer the prospect of easy integration to a larger morphing structure. For instance, Mattioni et al. [148] proposed a piecewise variation of stiffness in the rectangular plate using half of the plate with a symmetric layup and the other half with an unsymmetric layup. As expected, the symmetric part remained flat whereas the adjacent unsymmetric part developed a curvature. The flat part of the plate can be easily clamped to a larger structure, and the unsymmetric bistable part can be used for allowing morphing. Sousa et al. [201] transformed the model from Mattioni et al. [148] and replaced discrete straight fibers with curvilinear fibers (Figure 2.5). This is to ensure fiber continuity between the symmetric and unsymmetric regions (as shown in figure 2.5 a)), and therefore avoiding stress concentrations at the delimiting region.

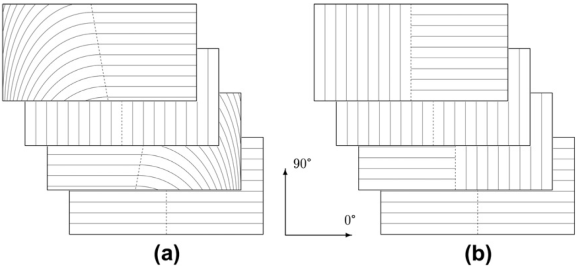

FIGURE 2.5: *(a)* Multistable laminate based on curvilinear fibers (b) Straight fiber laminate based on [148] ([201]).

It is also interesting how new stable shapes can be attained by connecting several unsymmetric laminates. Specific arrangements can lead to more than two stable shapes. Dai et al. [49] achieved three stable configurations of a lattice structure made from unsymmetric cross-ply laminates connected, and these tristable plates were further connected to form 2^N configurations, where N is the number of tristable elements [50]. However, the laminates were connected using bolts, resulting in undesirable local stresses at the connection points. Later, Cui and Santer [48] developed tessellated surfaces combining multiple unsymmetric and symmetric laminates. The single plate with piecewise variation in the layups is manufactured. At the interface, however, the sudden change in the laminate layups lead to stress concentrations. The bistable shapes generated from an example tessellated plate are illustrated in Figure 2.6.

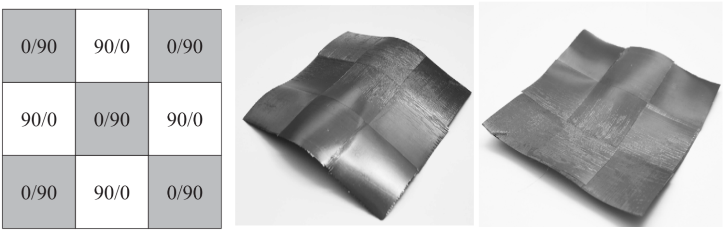

FIGURE 2.6: Two stable configurations of a physical model of the tessellated surface shown on left [48].

Spatial variation in material properties has previously shown to enhance structural performance [210]. With the advancement of tow-placement techniques, it is now possible to manufacture advanced composite structure that allows the fiber orientation to vary continuously throughout the laminate, commonly known as variable stiffness (VS) laminates. This adds an extra dimension to structural tailorability and further increases the design space than the conventional straight fiber composite laminates. Previous studies regarding the mechanical performance of

VS composites demonstrated their higher critical buckling loads in comparison to those of conventional straight fibers. This capability directly stems from their ability to redistribute the pre-buckling stresses [88]. Several semi-analytical and reduced order models were developed to study the enhanced post-buckling behavior of VS composites in comparison to straight fiber laminates [174, 175, 223]. Panesar et al. [162] replaced a narrow region at the center of the laminate $[\pm 45^\circ/0^\circ]$ with curvilinear fibers using tow steering technique, to avoid fiber discontinuity in the $\pm 45^\circ$ interface, as shown in figure 2.7. The FE calculations correlated well with the experimental results, with an error of less than 6.5% in the measurement of the cured stable shapes.

Apart from the works of Sousa et al. [201] and Panesar et al. [162], VS laminates using curvilinear fiber paths were not utilized for generating multistable laminates. The exploitation of VS laminates especially to tailor the stable shapes and the snap-though behaviour is a potential topic yet to be explored.

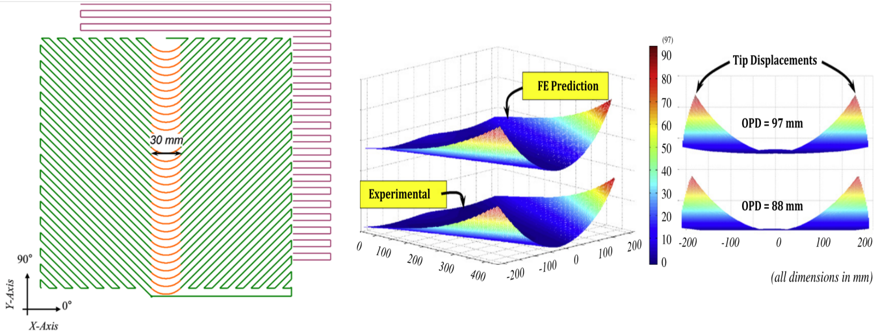

FIGURE 2.7: (*a*) Multistable laminate with a section having curvilinear fibers [162].

2.4 Actuation mechanisms in multistable laminates

As multistable structures are intended to be used in morphing applications, the phenomenon of snapping from one stable state to another and back plays an important role. For instance, if the snapping loads are quite high, morphing action would be difficult to achieve or require a large number of actuators which can be contrary to the weight requirement. Snapping in a bistable structure is a complex phenomenon, which is determined by the interplay between bending and stretching energies. Several methods have so far been proposed to snap from one stable shape to another, such as by using external forces [55, 168], electric current [188], magnetic actuators [137, 195] or induced curvature due to non-mechanical stimuli like temperature and swelling [99, 167]. It has been shown previously that both initial curvature and material parameters are two crucial parameters dictating the snapping process [80, 130]. Here, we discuss three widely used mechanisms to trigger snap-through a) Using mechanical force b) Shape memory alloys (SMAs) c) Piezoelectric actuators.

2.4.1 *Using mechanical force*

The simplest and most intuitive way to trigger snap-through is by simply applying concentrated force. Several numerical as well as experimental studies have been carried out to model and capture this snap-through process. Schlecht und Schulte [185] used an FE program (MARC) to model the snap-through process when a concentrated force was applied to the center of the plate. Consequently the snap-through force was found from an iterative nonlinear analysis. It was observed that for laminate with layup as: $[0^\circ_2/\theta^\circ_2]$ with θ being the fiber orientation angle, the snap-through loads increased monotonically with increasing θ. A similar analysis was also performed on circular laminates. A typical FE program gives the possibility to use arc-length or the Riks method to calculate snap-through loads. Static analysis with artificial stabilization is also often used and is equivalent to a force-controlled method [147, 168, 205].

Potter et. al [172] investigated the process of snap-through experimentally for unsymmetric cross-ply composite plates and found it to be not a single event, but rather two distinct snap-through events. One side of the plate snaps to the second stable shape, ahead of the other side. At the load increases, the curvature in one side of plate flattens followed by development of curvature in the perpendicular plane. This was later confirmed by Pirrera et al. [168] using higher order polynomials. Lamacchia et al. [128] used the Differential Quadrature Method (DQM) to solve the membrane problem and then solved the strain energy only in terms of curvatures. Accurate results were obtained within a relatively small computational cost.

Potter's multi-event snap-through process was further confirmed by the experimental setup reported by Cantera [38] to snap a plate supported at four corner points with a concentrated load at the center. A quarter of the plate was divided into four different regions each having different out-of-plane displacement function. Therefore a piecewise function of out-of-plane was defined that varied with the coordinates and a uniform through thickness was also considered. However, the analytical method resulted in quite complex formulation without having a good correlation with the experimental values.

Until now, all the literature described had considered snapping as a quasi-static process. In reality, snap-through is an instantaneous event and can be therefore modeled as a dynamic process [187]. Diaconu et al. [63] used Hamilton's principle in conjunction with Rayleigh Ritz's analysis to add inertial and damping terms to the model. With the dynamic analysis, there was a reasonable correlation with analytical and FE results, however, the author pointed out further calibration in the values of damping parameters to match the FE and experimental values.

2.4.2 *Shape memory alloys*

Shape memory alloys have this fascinating property of displaying strains when subjected to heat. Buehler and group discovered this property back in 1961, when they stumbled upon a bent-out strip of Nickel-Titannium alloy. One of the initial works to trigger snap-through in multistable composite laminates using SMA wires was performed by Dano and Hyer [51, 55]. An actuation system was developed using shape memory alloy as shown in Figure 2.8. The SMA wire, which is in its pre-strained martensite phase is connected between the two set of supports. As the wire is heated, it changes to the austenite phase, returning to the length it was before pre-straining, and consequently generating enough force to pull the tips of the support and triggering snap-through in the laminate. For triggering snap-back, the same arrangement but on the other side of the laminate is required. However, as can be observed in Figure 2.8, the mechanism seems cumbersome requiring a lot of wires and can have practical issues when applied in larger morphing structures.

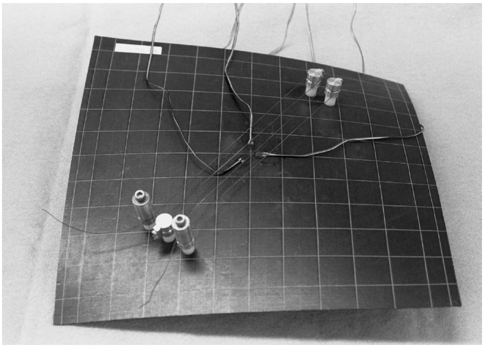

FIGURE 2.8: Arrangement of supports and SMA wires on a $[-60_4/30_4]$ laminate [54].

The semi-analytical model previously devised by Dano and Hyer ([51, 56]) was extended to include the external forces generated from the shape memory alloy wires. Dano and Hyer [52], later extended the model for general layups and off-axis applied forces. Although the model was computationally very efficient and the formulations were relatively simple, there were discrepancies with the experimental values. However, to understand the general behavior of the snap-through process for general unsymmetric laminates, this method provided a good starting point.

Hufenbach et al. [101] designed and manufactured a smart adaptive prototype made of GFRP by actuating it using NiTi wires. These wires were attached to the top and bottom of the laminate surface and were integrated with an electric circuit. A possible switch between two stable deformation modes could be realized by connecting or disconnecting the circuit. Ryu et al. [184] performed finite element analysis of SMA springs attached to the support on the surface of laminates to enable actuation (Fig. 2.9). The springs could be tailored with different design parameters like coil numbers and coil diameter to fulfill the actuation requirements. Various FE simulations were conducted for different cross-ply stacking sequences, however, details about modeling accuracy were not mentioned. Recently, Chillara et al. [44] used SMA actuators to snap prestressed laminates consisting of elastomeric matrix composites, and showed from 3D motion capture tests, the multi-event snap-through phenomenon.

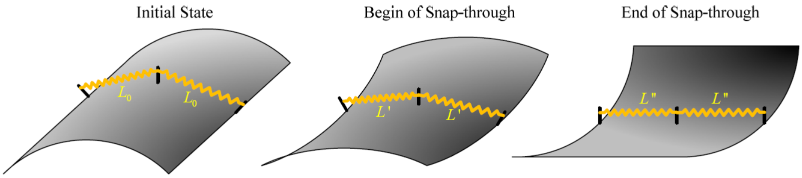

FIGURE 2.9: Snap-through in unsymmetric composite laminate using SMA spring [184].

2.4.3 *Piezoelectric actuators*

Piezoceramic materials are extensively used in the industry as both actuators and sensors due to their interesting properties [217]. These materials possess high stiffness and high response frequency range, which deforms when subjected to an electric field with quick response time. Above all, good availability and affordable prices make them quite attractive in different industrial applications. However, monolithic piezoceramic materials are brittle in nature, making them susceptible to breakage under tensile loads. To overcome this limitation, Macro-fiber composite (MFC) actuators, which are piezoceramics processed in the form of piezocomposites, are considered as a viable replacement.

2.4.3.1 *Triggering snap-through: Experimental and analytical studies*

Schultz and Hyer [189, 191] constructed an unsymmetric bistable laminate with Macro Fiber Composite (MFC) actuators bonded on one side of the plate (Figure 2.10). The bistable laminate was first cured and cooled to room temperature and then bonded to the curved surface of laminate. This is done by placing the laminate and actautors together in a vacuum bag, where the vacuum made the surface of the laminate and actuator pressed against each other. On removing the vacuum bag, the curvature of found to reduced to the added stiffness of the actuator, but still exhibited two stable shapes. As voltage was applied, at 1700 V was required to snap from one stable shape to another. A semi-analytical framework is developed using Rayleigh-Ritz method (using the same steps described in Dano and Hyer [56]), to model the complete process in three steps. This consisted of the cool-down, the bonding, and the actuation process. The results from each step are used in a cumulative sense, to calculate the final potential energy. Based on the experimental results, it is observed that there is a localized reversal of curvature in the region where the actuator is bonded. The Dano-Hyer model could not capture this effect very well due to the constant curvature assumption. However, a higher order displacement function [187, 190] gave better correlation with the experimental results, though it still had large discrepancies between the experimental results and experimental prediction.

Ren [178] analyzed the snap-through phenomenon in cross-ply laminates with piezoelectric actuators, but using a different modelling approach. Ren considered a unified model, where the thermal curing and the actuation processes are combined in a single step. This was particularly aimed at developing a simpler analytical model. This model could be conceived as a process in which both the actuators and the laminate are placed inside the autoclave at the same time, but the curing temperature for each of them are assumed to be different. However, this lead of loss of generalization, and the change in plate shape and the energy at each steps could be not determined step-wise. The relation between the curvatures and the electric field is also studied and is found to be linear in nature. The FE model is also developed and had a good correlation with analytical values. Ren and Par [179] later extended the model for arbitrary lay-up laminates. Compared to cross-ply laminates, it was observed that with the increase in the electric field, in addition to the change in laminate shape, there was also change in principal direction, an observation also reported by Dano-Hyer ([51]).

A simple analytical model considering the bonding of the actuator as well as application of voltage to the actuator was presented by Gude et. al. [81, 82]. To verify the curvatures of the bistable shapes, as well as the snap-through loads, experimental tests were also conducted by the authors. The corresponding FE models for the laminate and the MFC was first developed using solid elements [81]. Later the authors found that the use of shell elements for the actuators and the composite laminate, not only resulted in considerable time saving but also more accurate results. However, the developed semi-analytical formulations resulted in some deviation from the experimental and FE results. They reported that a polynomial function based on six parameters appears to be a precise and efficient approximation, based on the convergence studies on the increasing order of polynomial function. These semi-analytical models described above lacked one important aspect. All of the models consider polynomial expression for in-plane strains $(\epsilon_{xx}, \epsilon_{yy}, \epsilon_{xy})$ or in-plane displacements(u, v) and out-of-plane displacements (w). Although such polynomial functions are chosen in such a way that they satisfy the compatibility equation, they don't necessarily satisfy the in-plane equilibrium equation in a strong sense. Therefore, it is important that the inplane-equilibrium equations are satisfied with reasonable accuracy, to predict the stretching energy and consequently the snap-through voltage accurately.

Fernandes [70] included actuators in the form of inelastic strains and solved the membrane problem, comprising of in-plane equilibrium equations and the compatibility equation. However, the authors didn't include the bonding and the actuation process, and the stiffness of the actuators separately. There is indeed a

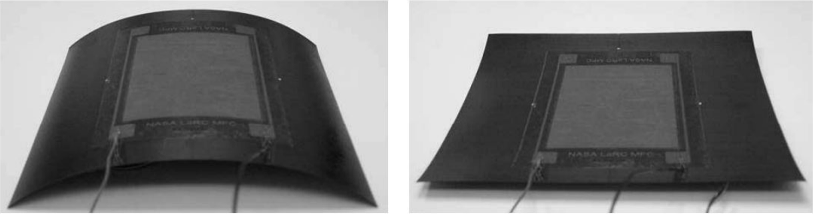

FIGURE 2.10: Bistable composite shell actuated by an piezoceramic actuator [189].

scope here to develop a more robust analytical model which can predict the snap-through voltage accurately with relatively fewer degrees of freedom. The methods followed in the works of [70, 128, 193] can be further extended to include the effect of actuators on the stiffness of the laminate, and at the same time satisfying the equilibrium equations with reasonable accuracy.

One of the major issues of actuating bistable laminates with piezoelectric actuators is the inherent requirement of being compliant and load carrying at the same time [27]. Piezoelectric actuators can be used successfully to change shape only if the bending stiffness of the structure is low, which leads to lower load carrying capacity. By tuning the directional properties (by changing fiber orientation in each ply) of the laminate, it can be possible to resolve this conflicting requirement. Betts et al. [25, 26] presented an optimization study for the design of a bistable laminate with two orthogonal piezoelectric layers to enable efficient snap-through. The formulation optimizes the load carrying capacity subject to a particular deflection and actuation limits, through variation in ply orientation and geometry. With the combined use of positive and negative applied voltages to the top and bottom of piezoelectric layers, a reduction of 33.8% in the total actuation voltage was found.

2.4.3.2 *Two-way actuation mechanisms*

The studies discussed until now have focused on single actuation techniques where a snap-through phenomenon from one stable shape to another was modeled or analyzed. However, it is equally important to devise efficient mechanisms for the snap-back process, especially considering its potential use in morphing applications. There has been little work done so far regarding reverse actuation systems. Portela [171], as well as Bowen et al. [31] considered reverse actuation with a single MFC layer, and reported its infeasibility without the usage of any external weights.

Schultz et al. [188] investigated a self-setting laminate through the combined use of two different MFCs, attaching orthogonal to each other on the two outer surfaces. A successful reverse curvature was achieved but at the cost of considerable high actuation voltages which were outside the operating range of MFCs. This can be solved by using a larger size of MFC if it does not lead to loss in bistability [171].

Tawfik [206] reported the design, analysis, and manufacturing of morphing composites with both MFC and Polyvinylidene Fluoride (PVDF) piezoelectric actuators on both sides of the composite to enable two-way snapping. An FE model was developed to validate the experimental results. As observed by other researchers previously [83, 171, 190], the value of curvatures reduces due to the extra stiffness generated by the actuators. The results obtained using MFC and PVDF were compared and found that MFCs are more suitable to induce snap-through due to its high actuation effectiveness. To generate the same force to generate, the MFC needed thickness of one-third than the PVDF. The authors suggested bonding the actuators by first making it curve and then attaching to the curved shape of the laminate, rather than the traditional method of first forcing the curved laminate to be straight, and then the piezoelectric actuator straight on the surface. Betts [26] performed an optimization study to find the optimized configuration of reverse actuation in a square plate.

At present, the piezoelectric technology looks quite promising for actuating multistable composites, although it has a lower degree of displacement control than SMA wires. Piezoelectric actuators can induce strains (typically $0.1 - 0.4\%$) much smaller than SMAs (8%) [31]. However, piezoelectric actuators have larger maximum operating frequency than the SMA wires (10 kHz for piezoelectric as compared to 10 Hz for SMA wires [220]. SMA wires are slow in response and difficult to integrate, whereas MFCs are faster and easier to integrate into a larger structure due to its layer like construction.

Kim et al [120] introduced a new actuation mechanism termed as shape memory alloy-piezoelectric actuation mechanism or SMAPAS which combines the advantages of both piezoelectric and SMA materials to achieve self-setting bistable composites. To change from first to the second stable shape, a piezoelectric actuator is used for rapid snapping. Whereas, for reverse actuation relatively slow but high strain SMA wires are used. A cantilever beam of $[0/0/90/90]_T$ layup was successfully analyzed to demonstrate the two side actuation mechanism. The piezoelectric actuators required higher voltage, in this case, 1300 V. The SMA wires required a voltage of 11 V with 1 V interval, to induce the shape memory effect and achieve reverse snapping.

The advantages and disadvantages of the actuation methods discussed is summarized in Table 2.1. Although several works have been carried out trigger snap-through in multistable laminates, only few works have successfully demonstrated both snap-through and snap-back which is essential aspect in a morphing application. Further, studies on actuation method in more complex structural components which are more likely to used in larger morphing structure is still missing. It would be challenging to design for instance a rectangular laminate with actuators to allow both snap-through and snap-back. Such laminates can be directly embedded in a larger structure such that realisable morphing mechanisms can be achieved.

Type	Advantages	Disadvantages	Reference
Force	Easy to model No effect on bistable shapes Easy to apply in different directions	Difficult in practical application	[38, 172, 226]
Piezoelectic Actuator	Large operational range Fast response Economical Easy integration	Added additional stiffness Reverse actuation requires two actuators Changes curvature in bistable shapes Lower strain	[53, 83, 154, 188]
SMAs	High Strain Easy to model	Slow response time Difficult to integrate	[44, 51, 184]

TABLE 2.1: Advantages and disadvantages of different actuation methods.

2.5 Morphing structures using multistable elements

Designing and investigation of deployable space structure using bistable mechanisms is an active research field. Iqbal and Pelligrino [108, 109] analyzed a bistable composite slit tubes with application in deployable boom. These concepts were futher extended and investigated by many others [73, 74, 108, 109]. Bistable springs are suitable for deployable structures due to their low cost, high packaging ratio, lightweight and stiffness properties [145].

Over the last decade, several concepts have been investigated to include multistable components for morphing aerofoil. Diaconu et al. [64] explored three different concepts to enable morphing using bistable laminates. Nonlinear FE analyses of different geometries and laminate configurations were performed to analyze the viability of these concepts. The first concept involved attaching two bistable components to form a flap (2.11 a). The stable regions in the flap indicated in figure 2.11 a) are constructed using symmetric laminates and therefore remains flat. The bistable regions consisting of the top and bottom half of the trailing edge is made of unsymmetric laminates, inducing bistability. The symmetric parts should be flexible enough to allow deflections induced in the bistable parts. Figure 2.11 b) shows a morphing trailing edge box which allows for a flap angle of 9° between stable states. In the second concept, a horizontal bistable component is attached along the chord, to allow change in the camber (2.11 c). The leading edge of the bistable plate is clamped at the center of the spar. The other side of the bistable plate is hinged allowing relative movement of the skin during actuation. As the bistable plate is actuated to the other stable shape, the camber of the aerofoil gets changed (2.11 d). In the third concept, a vertical member is attached along with the main spar of the airfoil, as shown in figure 2.11 e). The leading edge is considered to be fixed with the spar. The corner points of the bistable plates can slide along the top and bottom part of the aerofoil. As the bistable plate snapped, all the corner points move towards the leading edge part, causing the top and the bottom part of the trailing edge to slide inside the leading part of the aerofoil. This causes the chord length to be reduced (2.11 f).

The thermal residual stresses in the structure might depend on extreme temperatures, for example, the bistability would be enhanced for cold temperature but on the other hand, might diminish when subjected to high temperatures. Diaconu et al. [64] therefore suggested to use of prestressing to generate residual stresses rather than generating from the thermal curing process, to obviate temperature differences. In all these concepts, the snap-through mechanisms are achieved by applying loads. A complete description of a realistic mechanism to design such morphing concepts is still a subject not addressed in detail.

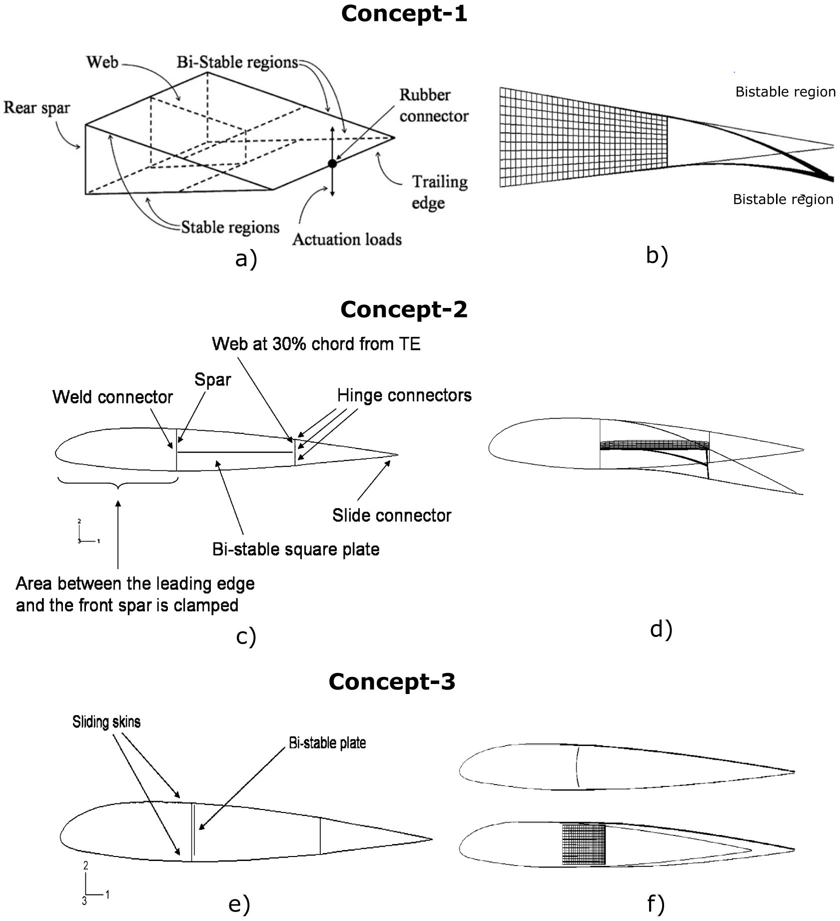

FIGURE 2.11: Morphing trailing edge concept Diaconu et al. [64].

Panesar et al. [161–163] employed bistable tow steered blended laminates to study the behavior of stable states in a trailing edge flap and also found out the optimal fiber direction for maximum out-of-plane displacement and maximum angle of attack. In the optimal results, it was seen that every discrete part of the flap should have a different value of fiber orientation, implying a curvilinear fiber path.

A concept of tip morphing of a winglet using a bistable panel was proposed by Mattioni et al. [149]. The bistable winglet comprised of two parts: outboard section consists of unsymmetric layout $[0_4/90_4]$, whereas the inboard part consisted of a symmetric layup $[0_2/90_4/0_2]$. As the speed of the airplane increased, the bistable part snapped from one stable shape to another resulting in an increased lift.

Daynes [59, 61] presented a novel design to achieve morphing of a helicopter blade flap using prestressed bistable composite laminates. The flap consisted of a stack of six bistable plates with the dimension of 100mm x 100mm, which was clamped at a spar located at 85% of the chord length. The design solution, provided a smooth camber variation unlike conventional hinged control surfaces.

Arrieta et al. [6] utilized the variability of the stiffness in the two bistable shapes of unsymmetric rectangular laminates, for designing a passive morphing systems. Arrieta studied composites with different layups in distinct sections to obtain a straight and a curved stable shapes having different stiffness. Figure 2.12 illustrates an integrated airfoil section with embedded bistable plate. The response of the aerofoil when subjected to a loading upwards is significantly different, when the multistable element adopts either a straight or a curved stable shape. When a 6 N upward load is applied to the aerofoil when the bistable element is in its straight state, it experiences a deflection of 0.64 mm. On the other hand, in an configuration with curved stable shape, it experiences 20 mm deflection, for the same amount of load. This is because the stiffness of the airfoil is lower when the bistable plate is in its curved stable shape, than when it is in the straight configuration. Due to the variability of stiffness between the straight and the curve shape, a noticeable softening of the structure can be achieved. This is also evident from the load-displacement curve of the two configurations, as 2.12 b). Later Kuder et al. [124] extended the work, by considering the pressure distribution emanating from the aerodynamic loads. This was performed by considering a weak static aeroelastic coupling using XFOIL.

2.6 Conclusions

In this chapter, a literature review was presented, highlighting important works on unsymmetric composite laminates. A plethora of work has been reported on analytical, numerical and experimental investigations of multistable laminates. A brief background of different methodologies like semi-analytical and FE methods used in the context of calculating the stable shapes and the snap-through loads have been described. The complexity of predicting the snapping phenomenon for such

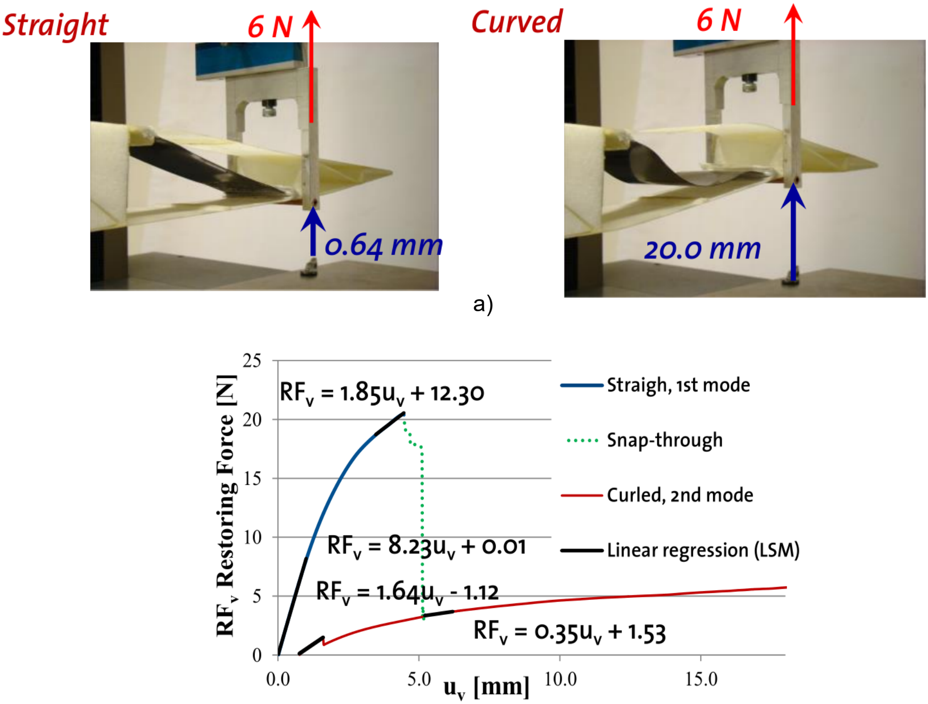

a)

b)

FIGURE 2.12: a) Passive concept utlizing stiffness variability in the different stable shapes of a multistable composite rectangular laminate b) The resulting load-displacement curve displaying the different stiffness properties, when the multistable element is in its curved state and in its straight stable shape ([5]).

structures both analytically and using numerical methods was well highlighted, with some recent literature focusing on improved reduced methods.

The idea of varying stiffness properties along the plane of a laminate has lead to interesting observations. Some concepts like varying the layups of the composite plate in a piecewise manner can lead to shapes which are easy to embed in a morphing structures. Different bistable elements when joined with others can produce more than two stable shapes. Varying the fiber orientation spatially is an attractive option for tailoring structural properties in a composite plate. However, there are only few published works on multistable structures utilizing curvilinear fiber paths. A systematic investigation especially using fast and reasonably accurate tools is required to understand the factors influencing the multistable property in such laminates. Such tools should provide a platform to conduct optimization studies.

Devising appropriate and effective actuation mechanisms are vital for applying multistable laminates in morphing structures. In this review, three actuation strategies were discussed, namely using concentrated loads, SMAs and piezoelectric actuators. Piezoelectric actuators like MFC have been widely employed in actuating composite structures, especially due to its large operation range, fast response and easy integration due to its laminate type structure. To fully realize the bistable characteristics of unsymmetric laminates, both snap-through and snap-back have been studied. Only few works till now have successfully demonstrated both snap-through and snap-back. There is indeed a scope to investigate and design multistable elements having different shapes and layups, to allow both snap-through and snap-back using appropriate size and placement of actuators.

Finally, few morphing applications utilizing multistable laminates are discussed. While some concepts are active in nature, where actuation loads are applied at particular locations, others employ bistable laminates for passive concepts, making use of stiffness variability in the two stable states. Although, a large number of active morphing concepts utilizing multistable properties have been published till date, very few concepts take into account a realistic and detailed actuation mechanism. Further, most of the studies are found to be still in a conceptual phase. The current state of the art lacks a fully functional prototype, where a careful design of multistable laminates has been carried out to achieve a particular morphing mechanism. A detailed numerical and experimental study is therefore required with appropriate loading and boundary conditions to study the feasibility of concepts utilizing bistable laminates. The concept of variable stiffness laminates offering structural tailoring is a topic yet to relished to its full extend. Few works on using VS laminates to generate multistable structures have shown promising morphing applications, and therefore more attention is needed to study such laminates.

3

Theoretical background

3.1 Shape changing structures

3.1.1 *Introduction*

As we enter the age of advanced materials, we aim not only to seek materials with exceptional mechanical properties but also look for ways to control them [209]. We look for materials that can morph or change shape as we want. With the onset of *4-D* printing technology, it is now possible to change *3-D* printed structures into other shapes over time, triggered by external stimuli like temperature, light, voltage or even water [176, 208]. The simplicity and effectiveness of such concepts have always inspired engineers and designers to develop innovative reconfigurable and morphing structures.

However, it is quite a challenge to develop tools for structures undergoing large deformations and at the same time made up of highly anisotropic materials. The first step towards such an endeavour is to understand the fundamental parameters governing such structures. In this section, we delve a bit into the mechanics of multistable unsymmetric laminate, study some examples from the literature and revisit the fundamentals. At the end, we seek to answer the following questions:

1. How does bistability arise in a heated unsymmetrical laminate plate, and why?
2. Which parameters effect such bistable plates, and how?

3.1.2 *Why do objects change shape?*

This is not the first time this question has been posed, for engineers and physicists have raised and addressed such problems for decades. It is, however, no surprise that the resurgence of such concepts has come in parallel with the emergence of new adaptive engineering technologies. Over the last decade, there has been a proportionate amount of work dealing with different concepts to allow shape changing capabilities, especially in the mechanical and aerospace industry to develop efficient engineering systems. Several concepts, including mechanical and non-mechanical stimuli, have been proposed until now to trigger changes in shape, such as applying temperature, swelling and prestressing. Certainly, a lot of the concepts have been inspired by observing nature. There are plenty of examples from nature involving shape changing process instantiating new ideas of efficient engineering design [133]. One notable example of shape changing phenomena is the snapping of insectivorous plant *Dionaea muscipula*, commonly known as Venus Flytrap. Fortella et al. [72] demonstrated the importance of the interplay between geometry and material properties in understanding the snapping behavior of the plant. Based on the concept, a flytrap inspired robot was designed with bistable cross-ply laminate [121].

To allow easy change in shape, any structure needs to be soft, either from a material point of view or geometrically [98]. Soft materials like rubber or gel, allowing large displacements before reaching the material failure limit, whereas slender or thin structures are soft in the geometrical sense allowing buckling. Deflection in a thin plate or shell type structure is governed by the storage and release of total potential energy, which can be decomposed into bending and stretching components. The stretching energy which accounts for the in-plane deformation is linear in thickness t of the plate, whereas the bending energy accounts for the curvatures, which is cubic with t. The following equation shows the energy components of a Kirchhoff-Love thin plate:

$$\Pi_{tot} = \underbrace{A\int_{\Omega}\epsilon^2 dxdy}_{\substack{\text{Stretching Energy}\\ \Pi_s}} + \underbrace{D\int_{\Omega}\kappa^2 dxdy}_{\substack{\text{Bending Energy}\\ \Pi_b}} \tag{3.1}$$

For an isotropic plate, the value of the stretching stiffness is given by $A = \frac{Et}{1-\nu^2}$ and bending stiffness by $D = \frac{Et^3}{12(1-\nu^2)}$. Here Ω refers to the area of the plate. By scaling the bending and the stretching energies, it can be seen that the ratio $\frac{\Pi_b}{\Pi_s} \approx t^2(\frac{\kappa}{\epsilon})^2$ (as $\Pi_b \propto t^3$ and $\Pi_s \propto t$). Considering the structure very thin, this ratio can be very small. The bending energy for such structure is always less than the stretching energy, favouring pure bending deflections than with stretching involved [98]. The low energy requirement of a pure bending problem, attributes to various experiences we deal with in everyday life. A paper sheet for example can be rolled very easily to a cylindrical or conical shape involving pure bending rather than deforming into a sphere, involving stretching. Similarly, a thin rod when compressed bends to take a curved buckled shape.

3.1.3 *Gauss's theorema egregium*

At the heart of understanding the link between geometry and elasticity, lies the famous theorem given by Gauss in the, 'Theorema Egregium' of his *Disquisitiones generates circa superficies curvas* (general investigations of curved surfaces), published in 1827.

Before delving into Gauss's theorem, we first define what developable structures are. As we showed in the last section, pure bending deformations involving no stretching or no mid-plane strains can lead to energetically favorable deformations. Such deformations involving no stretching are called *isometric* deformations, and can lead to *developable* surfaces.

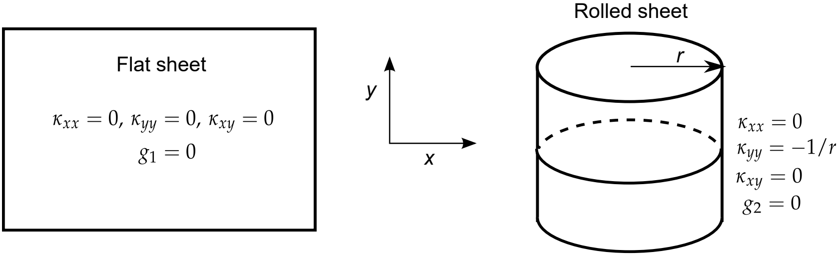

FIGURE 3.1: No change in gaussian curvature when a flat sheet is rolled into a cylindrical shape ($\Delta g = g_1 - g_2 = 0$). The values g_1 and g_2 corresponds to the Gauss curvature of the flat and the rolled sheet respectively.

The Gauss theorem says that for any developable deformation, gaussian curvature which is defined as $\Delta g = \kappa_{xx}\kappa_{yy} - \kappa_{xy}^2$, remains unchanged. This is valid if the structure is not cut or crumbled. Here, κ_{xx}, κ_{yy} and κ_{xy} are the components of the curvature vector. This implies directly that if the change in the Gaussian curvature of any resultant deformation is non-zero, it comes at the cost of some stretching. Figure 3.1 shows how the gauss curvature is preserved for a flat plate undergoing bending to form a cylindrical roll. As the net change in the gaussian curvature is zero, there is no stretching involved.

As discussed in Calladine et al. [36] and Mansfield [142], for small in-plane strains, the change in the gaussian curvature and the mid-plane strains are related using the following compatibility equation:

$$\frac{\partial^2 \varepsilon_{yy}}{\partial x^2} + \frac{\partial^2 \varepsilon_{xx}}{\partial y^2} - \frac{\partial^2 \varepsilon_{xy}}{\partial x \partial y} = \Delta g = \det \kappa \tag{3.2}$$

Here, ε_{xx}, ε_{xx} and ε_{xy} are the component of mid-plane strains. κ refers to the curvatures. Eq. 3.2 shows the fundamental compatibility equation that links the in-plane strains with the curvatures.

3.2 Mechanics of adaptive multistable composites

3.2.1 *Role of bending and stretching*

Although unsymmetrical laminates do contain stiffness coupling terms, one can easily decouple the effective stretching and bending energy from the total potential energy, as will be shown in the subsequent chapters. Following the same argument presented in the previous section, when subjected to a temperature difference, the unsymmetric bistable plates tend to follow the bending mode as it is more energetically favorable than involving stretching. Uniform heating of an unsymmetrical laminate plate warps into a cylindrical shape when cooled down, and not spherical shape, which might be more intuitive, due to uniform heating. Cylindrical configurations are isometric to the initial straight plate, as both have zero Gaussian curvatures. On the other hand, a spherical shape has a non-zero Gaussian curvature and would be manifested at the cost of stretching energy, making it energetically less favorable.

We explore a bit further on how the bending and the stretching energy varies with different fiber orientation and understand its influence on the stable shapes and the snap-through loads. We revisit examples, previously been studied by Diaconu et al. [63], where a systematic study on variation of fiber orientation angle is conducted, the corner displacement of the resulting shape and the snap-through loads are determined. We use the model described in Lamacchia et al. [128], to determine the ratio of bending and the stretching energies for some laminate layups, as we apply an increasing load to snap.

Let's compare first the stable shapes of the different bistable laminates. It is clear from previous studies as well as experiments conducted by Dano and Hyer [52] that the direction of the curvatures depends on the fiber orientation angle. For example, $[0^\circ_4/90^\circ_4]$ exhibits curvature along one of the axes of the plate, whereas $[-45^\circ_4/45^\circ_4]$ cools down as shapes with 45° angle from the plate axes (as depicted in figure 3.2). However, in order to quantify the magnitude of curvatures, we use the principal curvatures K_1, K_2 and the direction of the principal curvature ϕ to describe the resultant shapes of the bistable laminate. The principal curvature direction can be found using the following relation:

$$\begin{aligned} K_1 &= \frac{\kappa_x + \kappa_y}{2} + \sqrt{\left(\frac{\kappa_x - \kappa_y}{2}\right)^2 + \left(\frac{\kappa_{xy}}{2}\right)^2} \\ K_2 &= \frac{\kappa_x + \kappa_y}{2} - \sqrt{\left(\frac{\kappa_x - \kappa_y}{2}\right)^2 + \left(\frac{\kappa_{xy}}{2}\right)^2} \\ \Phi &= \frac{1}{2}\tanh\left(\frac{\kappa_{xy}}{\kappa_x - \kappa_y}\right) \end{aligned} \tag{3.3}$$

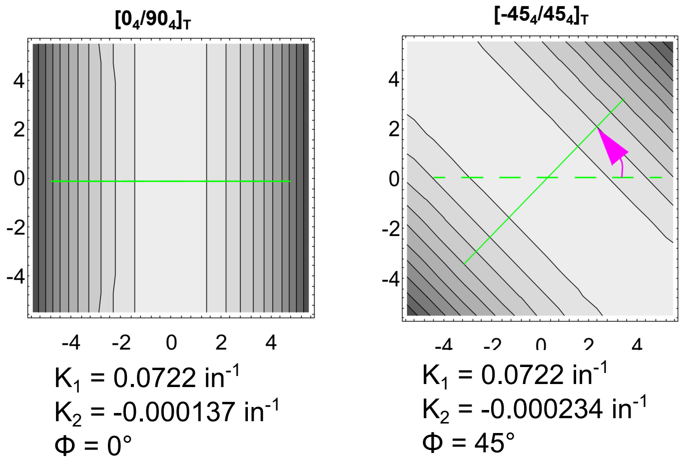

FIGURE 3.2: Principal curvature K_1, K_2 and the direction of the principal curvature Φ using a 4^{th} order Legendre polynomial. For laminates whose fiber angle differences are same, exhibits similar major principal curvatures K_1. The angle of the principal curvature is 0° for $[0^\circ_4/90^\circ_4]$ laminate, and 45° for $[-45^\circ_4/45^\circ_4]$ [52]. The values of K_1, K_2 and Φ can be determined from Eq. 3.3.

From previous works of Dano and Hyer [52] and Diaconu et al. [64], it can be observed that the principal curvatures of the generated stable shapes (calculated using Eq. 3.3), are proportional to the difference in the magnitude of the fiber orientation angle between each layer. It is maximum when the angle between the fibers is maximum.

The snap-loads of $[-45^\circ_4/45^\circ_4]$ are higher than $[0^\circ_4/45^\circ_4]$, as more energy needs to be expended in order to snap a bistable laminate with larger principal curvature. However, laminates with the same difference of the fiber angle between the layers, like $[0^\circ_4/90^\circ_4]$ and $[-45^\circ_4/45^\circ_4]$, have the same principal curvatures, but still different snap-through loads. This is particularly due to the differences in the bending and the stretching energies. Figure 3.3 shows the change in the ratio of bending and stretching energy, as the load increases to trigger snap-through. It can be observed from the figure that the snap-through of $[-45^\circ_4/45^\circ_4]$ occurs a bit before that of $[0^\circ_4/90^\circ_4]$ laminate. As the load is applied, the curvatures reduce, and so the bending energies. However, the stretching energy increases with increase in load, and becomes maximum just at the limit point. At the limit point, as the plate becomes flatter, the curvatures approach zero and the bending energy becomes minimum here. This can also be confirmed by the increase in Gaussian curvature as the load increases from Figure 3.4, which in turn increases the stretching energy. Due to difference in the layups, resulting in different bending and stretching stiffness, the rate of decrease in $[-45^\circ_4/45^\circ_4]$ is faster than $[0^\circ_4/90^\circ_4]$, leading to an earlier snap-through in $[-45^\circ_4/45^\circ_4]$.

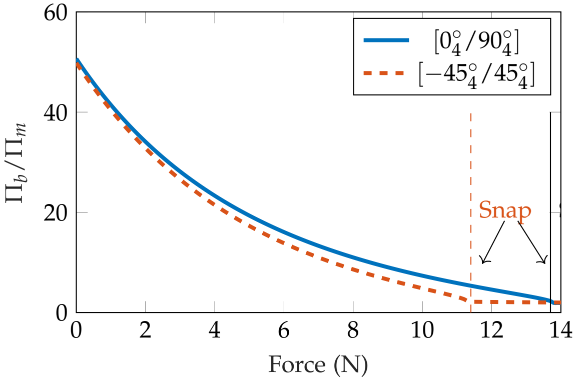

us

FIGURE 3.3: Change in the ratio of the Bending and Membrane energies, as we progress from one stable shape to the snap-through process.

At this stage we can conclude two points:

1. The direction of the principal curvature depends on the fiber orientation angles. The magnitude of principal curvatures depends on the difference in the angle between the plies.

2. The snap-through loads depend particularly on two factors: the curvature of the stable configuration, which depends on the difference in the magnitude of the difference between the angle orientation. Secondly, if two laminates have the same difference in the fiber angles, like $[0^\circ/90^\circ]$ and $[-45^\circ/45^\circ]$, it is the bending and the stretching energies that influences the limit point where snap-through occurs.

It must be noted that from Figure 3.3, the stretching energies at the stable equilibrium state for both $[0^\circ_4/90^\circ_4]$ and $[-45^\circ_4/45^\circ_4]$ are quite lower than the respective bending energies. During the stable equilibrium configuration, both $[0^\circ_4/90^\circ_4]$ and $[-45^\circ_4/45^\circ_4]$ have a ratio $\Pi_b/\Pi_m > 50$. Therefore, assumptions of inextensibility, can be a good approximation if one needs to calculate the cured shapes. However, it is clear from Figure 3.3 that as we approach towards the limit point, the bending energy decreases (due to flattening of the plate leading to reduction in the curvatures), and the stretching energy increases. This is also supported from figure 3.4, where the gauss curvature (therefore stretching energy) increases as the applied force is increased till snap-through is encountered. Therefore, accurate estimation of stretching energy can be an important factor for predicting the snap-through loads.

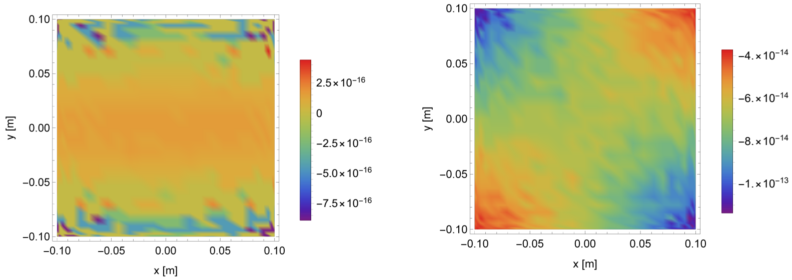

(a) at $F = 0N$

(d) at $F = 0N$

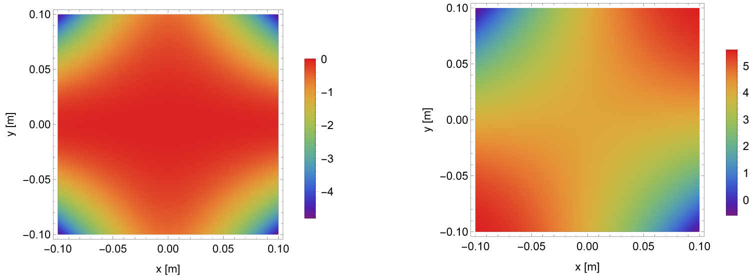

(b) at $F = 5N$

(e) at $F = 5N$

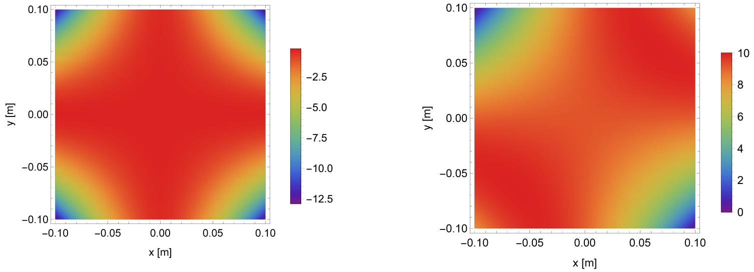

(c) At snap-through

(f) At snap-through

FIGURE 3.4: Change in the Gaussian curvature as the force is increased until snap-through. a), b) and c) shows the transition for laminate $[0^\circ_4/90^\circ_4]$, and d),e) and f) for laminate $[-45^\circ_4/45^\circ_4]$. The legend shows the change in the Gaussian curvature.

3.2.2 *Principle of minimum potential energy*

Unsymmetric laminates under the effect of temperature undergo nonlinear deformations, and therefore a subject of non-linear stability. Such problems can be solved using energy methods, with the help of FE or semi-analytical techniques. We therefore start by writing the total potential energy as:

$$\Pi = \Pi^{int} + \Pi^{ext} \tag{3.4}$$

The internal energy is also called deformation energy or strain energy and the external energy corresponds to the work of body forces and surface tractions.

According to the Principle of Minimum Potential Energy (PMPE), any conservative system develops into a configuration that minimizes the total potential energy. Any admissible variation of $\delta\Pi$ causes no change in the energy Π as shown below:

$$\delta\Pi = \delta(\Pi^{int} + \Pi^{ext}) = 0. \tag{3.5}$$

The first variation of the PMPE leads to the virtual work principle, where the material law and the kinematic equations are identically satisfied, and the equilibrium equations are satisfied in the integral sense (weak sense).

The second variation, indicates if the system is stable or unstable. The following relation holds if :

$$\delta^2\Pi \begin{cases} > 0, & \text{if stable equilibrium} \\ = 0, & \text{if neutral equilibrium} \\ < 0, & \text{if unstable equilibrium} \end{cases} \tag{3.6}$$

Eq. 3.6 indicates, whether the structure is in stable, unstable or neutral equilibrium.

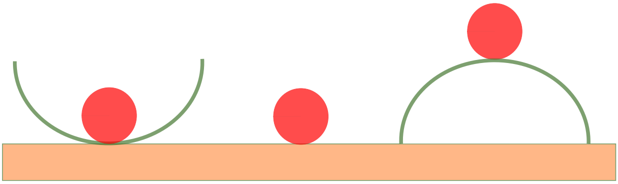

FIGURE 3.5: Equilibrium configurations

As described in Jones et al. [114], an equilibrium state or configuration is stable if, upon every small perturbation, the structure results in a deformation within the vicinity of the equilibrium state and returns back to its original position. The unstable state, on the other hand, moves completely to a new state of deformation and doesn't return back to the original state. If a small perturbation doesn't cause

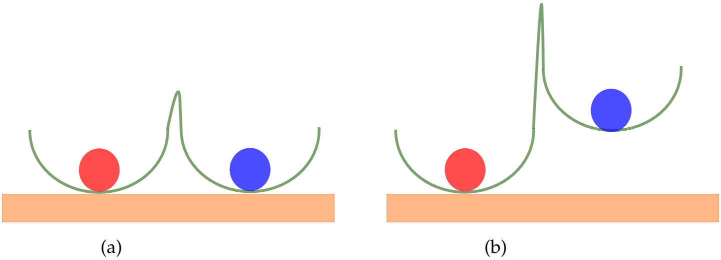
(a) (b)

FIGURE 3.6: Potential energy well for multistable structures with a) similar energy levels b) different energy levels.

instability but also doesn't come back to the original position, then this state is neutrally stable. All three cases can be illustrated in Figure 3.5, where the left figure is the unstable state, the center being the neutral state and the right image corresponds to an stable state.

If the potential energy well not just consists of a single minimum, but rather multiple minima (Figure 3.6), it corresponds to multistability. On applying an external force, the structure can move from one equilibrium state to another. The force is not necessarily small and within the vicinity of the equilibrium state. Both energy states in a multistable system can be the same leading to symmetric potential energy wells (Figure 3.6). In such a case, the structure is equally likely to exhibit any one of the stable shapes. If the potential energy wells have a difference in the energy levels, it can lead to asymmetric multistability. The state with lower energy is likely to occur naturally. The other state can be reached by expending a certain amount of energy.

3.3 Fiber steering to manufacture VS laminates

In addition to geometry, material properties also play an important role in the behavior of multistable structures. Fiber steering allows in-plane tailoring in a smooth and continuous manner.

With the advent of new fiber placement technologies [120, 139, 202, 222], spatial variation in the fiber orientation angle can be achieved by placing the fiber in a curvilinear fashion within the plane of each composite lamina. This technique adds an extra dimension to structural tailorability and further increases the design space of laminated composites exhibiting multistable behavior compared to conventional straight fiber composite laminates. It also allows further exploiting the anisotropic nature of composite laminates which is a well known driving factor for creating multistable structures and designing efficient morphing mechanisms [125].

A considerable amount of work has been carried out on the mechanical behavior of such composite laminates, showing a clear advantage in mechanical performance. The initial idea of introducing curvilinear fibers was proposed by Hyer et al. [106, 107], where a laminated square plate with a central circular hole was investigated using curvilinear fiber paths. Gürdal and Olmedo [86] adopted a linear variation of fiber paths and showed significant improvements in the buckling performance by stiffness tailoring using curvilinear fibers. Later, Gürdal [87] also adopted fiber trajectories with constant curvature based on the definition of circular arcs. Several semi-analytical and reduced order models were developed to study the enhanced postbuckling behavior of VS composites in comparison to straight fiber laminates [174, 175, 223]. The enhanced postbuckling behavior of VS composites was also demonstrated by Wu et al. [223] and Coburn et al. [46] for plates with different boundary conditions under uniform edge-compression and in-plane shear loadings [175].

Nonlinear variations of fiber angle have also been adopted by several researchers to enhance the design space, for example using Lagrange polynomials [46, 85, 223], Bezier curves [164], B-Splines [153, 155] and Lobatto polynomial [3, 197]. However, manufacturability constraints should be considered for any proposed fiber path, to avoid fiber breakage and wrinkling when steering with a small curvature radius. Some recent works have elucidated the effect of manufacturing constraints on optimal designs of VS laminates [32, 138, 165].

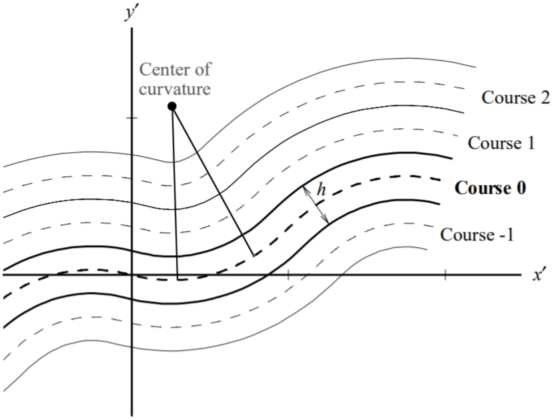

Figure 3.7: Configuration for $0\langle -15^\circ | 45^\circ \rangle$ parallel method ply.

There are commonly two ways in which the fiber trajectories can be defined: the parallel and the shifted method, shown in Figure 3.7 and Figure 3.8 respectively.

In the parallel method, the fiber paths are constructed from the reference fiber path by moving it parallelly. It is more advantageous to use the parallel method, as this leads to no tow overlapping and gaps (3.7). Using the shifted method, the fiber paths are constructed by moving the reference fiber path at a constant distance in a particular axis (y' in Figure 3.7). Using this method, it is much easier to manufacture, as the fiber paths can be defined easily using a simple definition. However, shifted

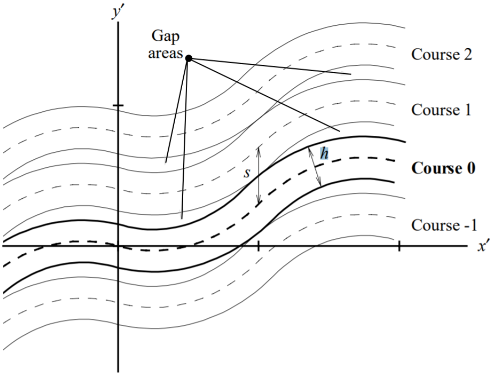

FIGURE 3.8: Shifted configuration for $0\langle -15|45\rangle$ ply with zero overlap.

method can lead to tow drops and overlaps (Figure 3.8). In this work, we follow the shifted method. There are different techniques to manufacture variable stiffness laminates with inplane stiffness variability.

3.3.1 *Advanced manufacturing techniques*

Different advanced manufacturing techniques are used to produce spatial variation in the stiffness using curvilinear fiber paths. Some of the widely used manufacturing techniques to achieve in-plane fiber steering are :

Automated Fiber Placement (AFP) [88] utilizes a robotic fiber placement head to the place tows of slit tape prepregs along curved paths over the plane of the plate. The prepregs are heated shortly after the deposition. A special roller is then used to compact the fibers into the substrate. AFP is known for its fast production, especially manufacturing larger, complex structures. The AFP technique can lead to tow overlaps and gaps in order to cover the whole surface when the shifted method is used. For this reason, AFP has the option of cutting and restarting the tow placement to eliminate gaps and overlaps. The tows are bent when the fibers are steered at particular radius. At the minimum turning radius, the fibers at the inner radius of tow start buckling out-of-plane, reducing the laminate quality. The minimum turning radius of the tow path is typically prescribed by the manufacturer of the AFP machine. As reported in Blom et al. [30], a typical value for the minimum turning radius for a 32 tow course with 3.175 mm wide tows is 635 mm (25 in). Waldhart recommended a turning radius of 12 in from the use of the tow placement machine used by the Boeing Defense and Space Group in Philadelphia.

Tailored Fiber Placement (TFP) [77, 146, 182, 202] technology developed at the Leibniz Institute of Polymer Research Dresden uses standard embroidery technique. The machines deposit and stitch continuous fiber roving material onto a base material. It is finally fixed onto the base material by a zigzag double lock stitch with upper and lower thread. Several optimal fiber paths were manufactured and tested to show the capabilities of the technology. The advantage of this technology is that fiber paths with even very small radius is producible.

Continuous Tow Shearing (CTS) [119], presented a novel fiber placement technique where typically dry tows are placed utilizing their shear deformation characteristics. In AFP, the tows were placed using their in-plane bending deformations. The fibers get packed together but increase the local thickness of the substrate as the fibers are steered. This creates a variable stiffness in the thickness direction as well, which is important to be accounted for when they are modeled. This manufacturing technique reduces process-induced defect and the fibers are placed in a more accurate fiber path than AFP. However,the process much slower than the AFP. Continuous multi-tow shearing (CMTS) [118] is an extended version of CTS, where multiple tows are laid down at the same time, making the process much faster.

3.3.2 *Fiber path definition*

In this study, instead of straight fiber, a curvilinear fiber path definition for the composite laminate is employed. Although different ways exist to vary the fiber path in a curvilinear pattern, the linear variation of the fiber orientation angle proposed by Gürdal et al. [88] is considered in this work. Such linear variation is more practical than nonlinear variations due to its adaptability to manufacturing constraints, and also useful in building simpler analytical models.

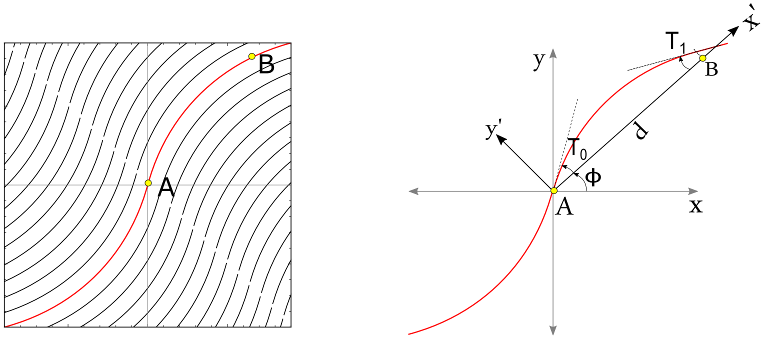

FIGURE 3.9: Parameters defining the curvilinear fiber path [88].

The fiber orientation angle θ is defined as follows:

$$\theta(x') = \begin{cases} \phi + \frac{(T_0 - T_1)x'}{d} + T_0, & \text{for } -d \leq x' \leq 0 \\ \phi + \frac{(T_1 - T_0)x'}{d} + T_0, & \text{for } 0 \leq x' \leq d \end{cases} \tag{3.7}$$

where

$$x' = x\cos\phi + y\sin\phi \tag{3.8}$$

Here, the fiber orientation linearly varies from angle T_0 at Point A to angle T_1 at Point B (Eq. 3.9). The points A and B are separated by a distance d on the x' axis, referred as the characteristic length on the x' axis (Fig. 3.9). The angle parameters T_0 and T_1 are defined with respect to the x' and y' axes, which are rotated by angle ϕ with respect to the reference Cartesian coordinate axes (Fig. 3.9). The value d can be determined from the coordinates of point $A(X_0, Y_0)$ and $B(X_1, Y_1)$ where the angles T_0 and T_1 are defined.

In Fig. 3.9, the fiber marked in red is the reference fiber path. All the other fiber paths can be generated by shifting the reference fiber path in the y' direction (known as the shifted fiber method [215]). Although the fiber is changing its orientation along x' direction, if viewed from the perspective of Cartesian coordinate axes, the fiber orientation is a function of x and y: $\theta = \theta(x, y)$. The standard notation to define a particular VS laminate with the above-mentioned three parameters is as follows: $\phi\langle T_0|T_1\rangle$. Throughout this work, point A is considered at the center, and point B is considered at the corner. Therefore, the fiber angle T_0 is defined as the angle at the center of the plate, and T_1 is defined as the angle at the edge of the plate.

3.4 Differential quadrature method (DQM)

The differential quadrature method is a numerical technique to solve differential equations with initial and boundary valued problems, with relatively lower computational efforts. This method have been used in this work, and its implementation will be discussed in Chapter 6. In DQM, the problem is particularly solved at certain grid points, with higher order polynomial interpolation functions to obtain precise solutions. This method was first proposed by Bellman in 1970s, and consequently was applied successfully in different engineering problems. Bert and Malik [24] in a review paper provided an extensive overview with a variety of problems, pointing out its convergence rates with increasing polynomial orders, and sampling grid points. Through different problems, they illustrate their potential over low-order finite difference and finite element method in terms of computational efficiency and accuracy. Low order techniques usually require higher discretized points as compared to DQM.

DQM can be similar to finite differences (FD) and collocation methods, and there are certain differences. In FD , the unknown function is approximated locally using lower order interpolating polynomials. On the other hand, DQM is a global method, where the computation at any given point depends not only on information at neighbouring points, but on information from the entire domain. In the collocation point method, finite-dimensional space of test functions (usually polynomials up to a certain degree) and a number of points in the domain (called collocation points) is chosen. This approach requires the differential equation to be satisfied exactly at the collocation points. The derivatives required in the differential equations are then carried out at the chosen collocation points. In Chebyshev collocation method, the base function is first approximated by Chebyshev poynomial, and then the grid points are determined based on base function. In DQM, we first specify the grid point distribution, and then construct the base polynomial function on the basis of the coordinates of the grid points [198]. By chosing certain certain polynomial functions for the weighing coefficients in the DQM, an equivalence between the DQM and collocation method can be derived [17].

DQM can be applied directly to solve any system of differential equations with boundary conditions. Raju et al. [175] successfully solved the buckling and post-buckling of variable angle tow laminates under in-plane shear loading using DQM, and proved DQM to be an effective tool especially for analyzing simple geometries without any discontinuities.

3.4.1 *One-dimensional domain*

Gauss quadrature is a widely used method to numerically integrate a continuous function over a particular domain. The main idea is to approximate an integral by summing the product of the function at certain nodal points with a particular weight.

$$\int_a^b g(x)dx \approx \sum_{j=1}^{N} w_j g(x_j) \tag{3.9}$$

Using the same idea, Bellman et al. [16] introduced the derivative of a function $g(x)$ in 1-D space from $[-1,1]$ by a weighted sum of the function at certain grid points over the entire domain. It is assumed that the function $g(x)$ is continuous and differentiable at this domain. This can be written as follows:

$$\begin{aligned} \frac{dg(x_i)}{dx}|_{x=x_i} &\approx \sum_{j=1}^{N} a_{ij}^{(1)} g(x_j), \quad \text{for } i = 1,2,.....N \\ \frac{d^2g(x_i)}{dx^2}|_{x=x_i} &\approx \sum_{j=1}^{N} a_{ij}^{(2)} g(x_j), \quad \text{for } i = 1,2,.....N, \end{aligned} \tag{3.10}$$

where $a_{ij}^{(1)}$ and $a_{ij}^{(2)}$ are the weighting coefficients for the first and the second order derivatives. Here N refers to the number of grid points.

There are several ways in which grid points can be defined. A non-uniform grid distribution as given by Chebyshev-Gauss-Lobatto points (depicted in figure 3.10) is used in this work to avoid oscillations occurring at the edges due to Runga's phenomenon [183]. The grid distribution is given as follows:

$$X_i = \frac{1}{2}\left[1 - \cos\left(\frac{i-1}{N-1}\pi\right)\right], \tag{3.11}$$

where i is the number of grid points from 1 to N. The weighting functions can be found using Lagrange interpolation polynomials as test functions, as described in Quan and Chang [173], Shu [198]. For the 1^{st} order derivative of the function $g(x)$, the off-diagonal terms of the weighting coefficient are defined as:

$$a_{ij}^{(1)} = \frac{M^{(1)}(x_i)}{M^{(1)}(x_j)(x_i - x_j)}, \quad \text{for } i \neq j, \tag{3.12}$$

where

$$M^{(1)}(x_i) = \prod_{j=1, j\neq i}^{N} (x_i - x_j) \tag{3.13}$$

For diagonal terms, the weighting coefficients can be written as:

$$a_{ii}^{(1)} = - \sum_{j=1, j\neq i}^{N} a_{ij}^{(1)}, \tag{3.14}$$

For the higher order derivatives (r^{th} derivative), the off-diagonal terms can be given by the following recurrence relationship:

$$a_{ij}^{(r)} = r \left(a_{ij}^{(r)} a_{ii}^{(r-1)} - \frac{a_{ij}^{(r-1)}}{x_i - x_j} \right), \tag{3.15}$$
$$\text{for } i, j = 1, 2, ..., N; \quad r = 2, 3, ..., N-1$$

and for the diagonal terms, the weighting coefficients are:

$$a_{ii}^{(r)} = - \sum_{j=1, j\neq i}^{N} a_{ij}^{(r)}, \tag{3.16}$$

3.4.2 *Extension to multi-dimensional domain*

The concepts described in the previous section, can be easily extended to the multi-dimensional case. For the sake of simplicity, and for the relevance to this work, a 2-D rectangular domain is considered, with $N \times M$ grid points. The derivative of a function $g(x, y)$ can be written as follows:

$$\left.\frac{dg}{dx}\right|_{x=x_i, y=y_j} \approx \sum_{k=1}^{N} a_{ik}^{(1)} g(x_k, y_j), i = 1, 2, ...N \tag{3.17}$$

$$\left.\frac{dg}{dy}\right|_{x=x_i, y=y_j} \approx \sum_{k=1}^{M} b_{jk}^{(1)} g(x_i, y_k), i = 1, 2, ...M$$

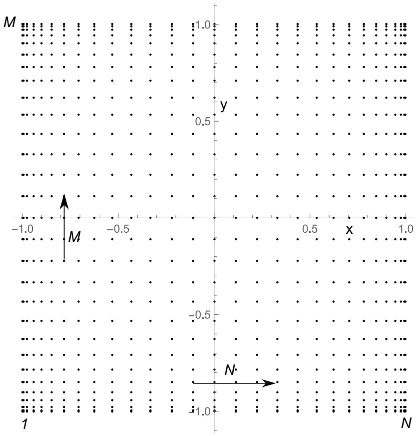

FIGURE 3.10: Non-uniform Chebyshev–Gauss–Labotto DQM grid point distribution in two-dimension.

where the weighting coefficients for the first derivative in x is represented by $a_{ij}^{(1)}$, and in y in represented by $b_{ij}^{(1)}$. They can be written as:

$$a_{ij}^{(1)} = \frac{M^{(1)}(x_i)}{M^{(1)}(x_j)(x_i - x_j)}, \quad \text{for } i \neq j, \tag{3.18}$$

$$a_{ii}^{(1)} = -\sum_{j=1, j\neq i}^{N} a_{ij}^{(1)} \quad \text{for } i = 1, 2, ...N,$$

$$b_{ij}^{(1)} = \frac{P^{(1)}(y_i)}{P^{(1)}(y_j)(y_i - y_j)}, \quad \text{for } i \neq j, \tag{3.19}$$

$$b_{ii}^{(1)} = -\sum_{j=1, j\neq i}^{M} b_{ij}^{(1)} \quad \text{for } i = 1, 2, ...M,$$

where,

$$M^{(1)}(x_i) = \prod_{j=1, j\neq i}^{N} (x_i - x_j), \quad P^{(1)}(y_i) = \prod_{j=1, j\neq i}^{M} (y_i - y_j) \tag{3.20}$$

Similarly, using the recursive formula used for 1-D (Eq. 3.16), we extend the relationships to 2-D.

$$a_{ij}^{(r_x)} = r_x \left(a_{ij}^{(r_x)} a_{ii}^{(r_x-1)} - \frac{a_{ij}^{(r_x-1)}}{x_i - x_j} \right), \tag{3.21}$$

$$\text{for } i,j = 1,2,...,N; \quad r_x = 2,3,...,N-1$$

$$a_{ii}^{(r_x)} = - \sum_{j=1, j\neq i}^{N} a_{ij}^{(r_x)}, \quad \text{for } i = 1,2,.....N \tag{3.22}$$

$$b_{ij}^{(r_y)} = r \left(b_{ij}^{(r_y)} b_{ii}^{(r_y-1)} - \frac{b_{ij}^{(r_y-1)}}{y_i - y_j} \right), \tag{3.23}$$

$$\text{for } i,j = 1,2,...,M; \quad r_y = 2,3,...,M-1$$

$$b_{ii}^{(r_y)} = - \sum_{j=1, j\neq i}^{M} b_{ij}^{(r_y)}, \quad \text{for } i = 1,2,.....M \tag{3.24}$$

Here $a_{ij}^{(r_x)}$ are the weighting coefficients for the $(r_x)^{th}$ order of derivative of $g(x,y)$ at the point (x_i, y_j) with respect to x, and $b_{ij}^{(r_y)}$ are the weighting coefficients for the $(r_y)^{th}$ order of derivative of $g(x,y)$ at the point (x_i, y_j) with respect to y. Therefore, this satisfies the following:

$$\left.\frac{d^{r_x} g}{\partial x^{r_x}}\right|_{x=x_i, y=y_j} \approx \sum_{k=1}^{N} a_{ik}^{(r_x)} g(x_k, y_j) \tag{3.25}$$

$$\left.\frac{d^{r_y} g}{\partial y^{r_y}}\right|_{x=x_i, y=y_j} \approx \sum_{k=1}^{M} b_{jk}^{(r_y)} g(x_i, y_k),$$

$$\text{for } i = 1,2,...,N; \quad j = 1,2,...,M;$$

$$r_x = 2,3,...,N-1; \quad r_y = 2,3,...,M-1$$

This can be further written down in a more simplified notation using matrices. Eq. 3.26 can be written in a generic form as:

$$\begin{aligned}\left.\frac{d^{r_x} g}{\partial x^{r_x}}\right|_{x=x_i, y=y_j} &\approx \sum_{k=1}^{N} a_{ik}^{(r_x)} g(x_k, y_j) \\ &= \begin{pmatrix} a_{11}^{(r_x)} & a_{12}^{(r_x)} & \cdots & a_{1n}^{(r_x)} \\ a_{21}^{(r_x)} & a_{22}^{(r_x)} & \cdots & a_{2n}^{(r_x)} \\ \vdots & \vdots & \ddots & \vdots \\ a_{N1}^{(r_x)} & a_{N2}^{(r_x)} & \cdots & a_{NM}^{(r_x)} \end{pmatrix} \cdot \begin{pmatrix} g_{11} & g_{12} & \cdots & g_{1n} \\ g_{21} & g_{22} & \cdots & g_{2n} \\ \vdots & \vdots & \ddots & \vdots \\ g_{N1} & g_{N2} & \cdots & g_{NM} \end{pmatrix} \\ &= A_{(r_x)} g \end{aligned} \tag{3.26}$$

Similarly the $(r_y)^{th}$ derivative can be written as:

$$\left.\frac{d^{r_y} g}{\partial y^{r_y}}\right|_{x=x_i, y=y_j} \approx \sum_{k=1}^{M} b_{jk}^{(r_y)} g(x_i, y_k) = B_{(r_y)} g \tag{3.27}$$

3.5 Conclusions

In this chapter, the fundamental question on how objects change shape is addressed. The role of bending and stretching energies in thin structures is highlighted. In thin structures, the bending energy is lower than the stretching energy, making the bending process more favorable to stretching. The gauss theorem is described that links the in-plane strains with the curvatures using the compatibility equation. Some examples from the literature were revisited, on how the ratio of bending and stretching energies changes when a concentrated load is applied until snap-through is triggered. With increasing load, the ratio of the bending and stretching energies reduces as the plate becomes flatter.

Different parameters are also identified, that influence the bistable shapes and the snap-through loads in the unsymmetric laminates. The direction of the principal curvature of the bistable shapes depend on the fiber orientation angle, and the value of the curvatures depends on the difference in the angle between the plies. The snap-through loads depend on a) the curvature of the bistable shapes and b) bending and stretching energies of the VS laminates.

4

Multistable shapes of VS laminates

4.1 Introduction

[1] As we discussed in the previous chapter, using advanced tow placement techniques, it is possible to manufacture composite structures that allow the fiber orientation to vary continuously throughout the laminate. So far, only limited work has been carried out to generate multistable structures using VS laminates. Moreover, these works are limited to just FE analysis of the cool-down of the process. An analytical or a semi-analytical model to predict the multistable shapes of thermally cured unsymmetric VS composites is still missing.

The current chapter aims primarily at the following two objectives. First, a semi-analytical model is developed to calculate the stable shapes of VS composites as a result of the cool-down process from the curing temperature. The underlying foundation of the method is based on the earlier works of Dano and Hyer [56]. The VS laminate is defined by a linear variation of the curvilinear fibers as proposed by Gürdal et al. [88]. FE calculations are further carried out to verify the obtained semi-analytical solutions.

Second, the design space for multistable plates is explored using VS laminates. A potential enrichment of the design space is demonstrated by the use of VS laminates. The explored design space reveals a wide range of stable shapes. A parametric study is conducted to demonstrate the relationship between the angle parameters that describe a VS laminate and the cured stable shapes in terms of corner displacement, curvatures, and principal curvature direction.

4.2 Semi-analytical approach to determine stable shapes

An unsymmetric VS square plate of side length L and total thickness t is considered. All the plies of the laminate have equal thicknesses. The fiber orientation is varied

---

[1] This chapter is based on the journal publication: Haldar et al. [92]

linearly, as described in chapter 3, section 3.3.2. The laminate which is initially flap, upon cooling from curing to room temperature, exhibits two curved stable shapes. The cool down shape of different straight fiber laminates are depicted in Fig. 2.2 Neither external mechanical forces nor hygroscopic effects are accounted for in the analysis. Using a semi-analytical approach the stable shapes of different unsymmetrical VS laminates are determined.

The Extended Classical Laminate Theory (ECLT) described in Dano and Hyer [56] is extended to VS laminates. It should also be noted that the **ABD** matrix varies along the coordinates of a plate.

4.2.1 *Governing equations*

The following equations systematically derive the total potential energy for an assumed polynomial out-of-plane displacement and strain field (described later in Section 4.2.2) and follows the Rayleigh-Ritz approach to determine the coefficients of the displacement functions.

A material point in the deformed configuration can be expressed as $\mathbf{x} = \mathbf{X} + \mathbf{u}$, where $\mathbf{u}(u, v, w)$ denotes the displacement vector in the x, y and z direction. $\mathbf{x}$, $\mathbf{X}$ identify the position vectors in the undeformed and in the reference configuration, respectively. The components of the displacement vector are defined accordingly as:

$$u(x,y,z) = u_0(x,y) - z\frac{\partial w_0}{\partial x}, \quad v(x,y,z) = v_0(x,y) - z\frac{\partial w_0}{\partial y}, \quad w(x,y,z) = w_0(x,y) \tag{4.1}$$

where the subscript 0 identifies the mid-plane displacements.

The total strain component ϵ includes non-linear von Kármán strains under the assumption of small strain and moderate rotation, and is given by:

$$\epsilon_{xx} = \frac{\partial u}{\partial x} + \frac{1}{2}\left(\frac{\partial w}{\partial x}\right)^2, \quad \epsilon_{yy} = \frac{\partial v}{\partial y} + \frac{1}{2}\left(\frac{\partial w}{\partial y}\right)^2, \quad \gamma_{xy} = \frac{\partial u}{\partial y} + \frac{\partial v}{\partial x} + \frac{\partial w}{\partial x}\frac{\partial w}{\partial y}. \tag{4.2}$$

Eq. 4.2 shows the non-linear strain displacement relationship. By inserting Eq. 4.1 into Eq. 4.2, the strain relations can be rearranged as:

$$\boldsymbol{\epsilon} = \begin{bmatrix} \epsilon_{xx} \\ \epsilon_{yy} \\ \gamma_{xy} \end{bmatrix} = \begin{bmatrix} \varepsilon_{xx} \\ \varepsilon_{yy} \\ \varepsilon_{xy} \end{bmatrix} + z \begin{bmatrix} \kappa_{xx} \\ \kappa_{yy} \\ \kappa_{xy} \end{bmatrix} = \begin{bmatrix} \frac{\partial u_0}{\partial x} + \frac{1}{2}\left(\frac{\partial w_0}{\partial x}\right)^2 \\ \frac{\partial v_0}{\partial y} + \frac{1}{2}\left(\frac{\partial w_0}{\partial y}\right)^2 \\ \frac{\partial u_0}{\partial y} + \frac{\partial v_0}{\partial x} + \frac{\partial w_0}{\partial x}\frac{\partial w_0}{\partial y} \end{bmatrix} + z \begin{bmatrix} -\frac{\partial^2 w_0}{\partial x^2} \\ -\frac{\partial^2 w_0}{\partial y^2} \\ -2\frac{\partial^2 w_0}{\partial x \partial y} \end{bmatrix} = \boldsymbol{\varepsilon} + z\boldsymbol{\kappa}, \tag{4.3}$$

where $\boldsymbol{\varepsilon}$ and $\boldsymbol{\kappa}$ represent the mid-plane strain and curvature vector respectively. The stress-strain relation for a particular layer k, with accounting for the thermal effects can be written in the global coordinate system as:

$$\boldsymbol{\sigma} = \begin{bmatrix} \sigma_{xx} \\ \sigma_{yy} \\ \sigma_{xy} \end{bmatrix}^{(k)} = \begin{bmatrix} \bar{Q}_{11}(x,y) & \bar{Q}_{12}(x,y) & \bar{Q}_{16}(x,y) \\ \bar{Q}_{12}(x,y) & \bar{Q}_{22}(x,y) & \bar{Q}_{26}(x,y) \\ \bar{Q}_{16}(x,y) & \bar{Q}_{26}(x,y) & \bar{Q}_{66}(x,y) \end{bmatrix}^{(k)} \left(\begin{bmatrix} \epsilon_{xx}(x,y) \\ \epsilon_{yy}(x,y) \\ \gamma_{xy}(x,y) \end{bmatrix} - \Delta T \begin{bmatrix} \alpha_{xx}(x,y) \\ \alpha_{yy}(x,y) \\ 2\alpha_{xy}(x,y) \end{bmatrix}^{(k)} \right) \tag{4.4}$$

where ΔT refers to the difference between the curing temperature and the room temperature. It should be noted that for VS composites, the components of the reduced stiffness matrix ($\bar{\mathbf{Q}}$) and the coefficients of thermal expansion vary with the coordinates of the plate.

Integrating the stress-strain relation over the thickness, it is possible to rewrite Eq. 4.4 in terms of the force and moment resultants

$$\begin{bmatrix} \mathbf{N} \\ \mathbf{M} \end{bmatrix} = \begin{bmatrix} \mathbf{A}(x,y) & \mathbf{B}(x,y) \\ \mathbf{B}(x,y) & \mathbf{D}(x,y) \end{bmatrix} \begin{bmatrix} \boldsymbol{\varepsilon} \\ \boldsymbol{\kappa} \end{bmatrix} - \begin{bmatrix} \mathbf{N}^{th} \\ \mathbf{M}^{th} \end{bmatrix} \tag{4.5}$$

where **N** and **M** are the vectors containing the resultant forces and moments respectively. **A**, **B** and **D** represent the in-plane, coupling and bending matrices respectively. The main difference between the formulation used in a typical straight fiber laminate and the one corresponding to VS composites are the terms present in the **A**, **B** and **D** matrices. These are constants for straight fibers while they vary as a function of spatial coordinates in case of VS composites as shown in Eq. 4.5. The resultant quantities with the superscript *th* in Eq. 4.5 are denoted as the thermal forces. As the reduced stiffness $\bar{\mathbf{Q}}$ matrix is a function of the x and y coordinates, but independent of the z coordinate, the entries of the matrices **A**, **B** and **D** can simply be calculated as:

$$\begin{aligned} \left[A_{ij}(x,y), B_{ij}(x,y), D_{ij}(x,y)\right] &= \int_{-t/2}^{t/2} \bar{Q}_{ij} \left[1, z, z^2\right] \mathrm{d}z \\ &= \sum_{k=1}^{N_{ply}} \bar{Q}_{ij}^{(k)}(x,y) \left[z_{k+1} - z_k, z_{k+1}^2 - z_k^2, z_{k+1}^3 - z_k^3\right] \end{aligned} \tag{4.6}$$

where N_{ply} identifies the total number of plies for each laminate configuration.

The value of $\bar{Q}_{ij}^{(k)}$ can also be written as a function of invariants of orthotropic material U_i [66, 88].

$$\begin{aligned}
\bar{Q}_{11} &= U_1 + U_2\cos\left[2\theta\left(x,y\right)\right] + U_3\cos\left[4\theta\left(x,y\right)\right] \\
\bar{Q}_{12} &= U_4 - U_3\cos\left[4\theta\left(x,y\right)\right] \\
\bar{Q}_{22} &= U_1 - U_2\cos\left[2\theta\left(x,y\right)\right] + U_3\cos\left[4\theta\left(x,y\right)\right] \\
\bar{Q}_{66} &= U_5 - U_3\cos\left[4\theta\left(x,y\right)\right] \\
\bar{Q}_{16} &= \frac{1}{2}U_2\sin\left[2\theta\left(x,y\right)\right] + U_3\sin\left[4\theta\left(x,y\right)\right] \\
\bar{Q}_{26} &= \frac{1}{2}U_2\sin\left[2\theta\left(x,y\right)\right] - U_3\sin\left[4\theta\left(x,y\right)\right]
\end{aligned} \tag{4.7}$$

The **ABD** matrix can be written in terms of the material invariants, details can be seen in the Appendix-A. This splitting of stiffness coefficients $\bar{Q}_{ij}$ in terms of invariants makes the computations much faster and avoids higher powers of trigonometric terms in the formulation. This is especially suitable for this work where the fiber orientation angle depends on the spatial coordinates of the plate. The response of the laminated structure is determined by means of the Minimum Potential Energy Theorem, where the potential energy of the structure in the absence of external mechanical actions is given by:

$$\begin{aligned}
\Pi = \int_{-L/2}^{L/2}\int_{-L/2}^{L/2} \Bigg(\frac{1}{2} \begin{bmatrix} \boldsymbol{\varepsilon} \\ \boldsymbol{\kappa} \end{bmatrix}^T \begin{bmatrix} \mathbf{A}(x,y) & \mathbf{B}(x,y) \\ \mathbf{B}(x,y) & \mathbf{D}(x,y) \end{bmatrix} \begin{bmatrix} \boldsymbol{\varepsilon} \\ \boldsymbol{\kappa} \end{bmatrix} - \\
\begin{bmatrix} \mathbf{N}^{th}(x,y) \\ \mathbf{M}^{th}(x,y) \end{bmatrix}^T \begin{bmatrix} \boldsymbol{\varepsilon} \\ \boldsymbol{\kappa} \end{bmatrix} \Bigg) \mathrm{d}x\, \mathrm{d}y
\end{aligned} \tag{4.8}$$

4.2.2 *Kinematics*

As a consequence of varying fiber orientation, VS composites can experience notable twisting curvatures. Wu [222] showed that for asymmetric variable stiffness laminates, when cooled down from cure to room temperature, exhibit shapes quite close to cylindrical shapes. Therefore, the kinematic field should be accordingly defined in the displacement field in order to capture such deformation patterns. The kinematic field proposed by Dano and Hyer [51] is therefore considered in this study which accounts for both the bending and the twisting curvature in its kinematic description. Particularly, the mid-plane strains are approximated as the following set of complete polynomials:

$$\begin{aligned}
\varepsilon_{xx}^0 &= c_1 + c_2x^2 + c_3y^2 + c_4xy \\
\varepsilon_{yy}^0 &= c_5 + c_6x^2 + c_7y^2 + c_8xy \\
w_0 &= \frac{1}{2}(c_9x^2 + c_{10}y^2 + c_{11}xy)
\end{aligned} \tag{4.9}$$

As suggested in [56], the corresponding polynomial for mid–plane strains needs to contain only powers of x and y that add to an even number, as other terms tend to be zero. In addition, c_9, c_{10} and c_{11} equal to the negative of curvatures in x and y directions and the negative of twist curvature, respectively.

$$\kappa_{xx} = \frac{\partial^2 w_0}{\partial x^2} = -c_9, \; \kappa_{yy} = \frac{\partial^2 w_0}{\partial y^2} = -c_{10}, \; \kappa_{xy} = 2\frac{\partial^2 w_0}{\partial x \partial y} = -c_{11} \tag{4.10}$$

It is important that the assumed strain and displacement fields satisfy the compatibility equation of a curved surface, as discussed in the previous chapter (Eq. 3.2):

$$det\,\kappa := \kappa_{xx}\kappa_{yy} - \kappa_{xy}^2 = \frac{\partial^2 \varepsilon_y}{\partial x^2} + \frac{\partial^2 \varepsilon_x}{\partial y^2} - 2\frac{\partial^2 \varepsilon_{xy}}{\partial x \partial y} \tag{4.11}$$

The in-plane strain components and the out-of-plane displacement are assumed, such they result in constant curvatures. Using Eq. 4.12 in the expression for extensional strains ε_x^0, the in-plane displacements can be computed as:

$$u_0(x,y) = \int \left[\varepsilon_{xx}^0 - \frac{1}{2}\left(\frac{\partial w^0}{\partial x}\right)^2 \right] dx + c_{12}y + c_{13}y^3 \tag{4.12}$$

$$v_0(x,y) = \int \left[\varepsilon_{yy}^0 - \frac{1}{2}\left(\frac{\partial w^0}{\partial y}\right)^2 \right] dy + c_{15}x + c_{14}x^3 \tag{4.13}$$

$$\tag{4.14}$$

In order to remove rigid body motion from the assumed displacement field, the first order terms of the variable x and y are needed to be equated, which results in $c_{15} = c_{12}$. The shear strain can simply be calculated from the expression:

$$\gamma^0 = \frac{\partial u^0}{\partial y} + \frac{\partial v^0}{\partial x} + \frac{\partial w^0}{\partial y}\frac{\partial w^0}{\partial x} \tag{4.15}$$

Based on the previous developments, it can be seen that the coefficients from c_1 to c_{14} correspond to the set of unknowns, which are determined using the Rayleigh–Ritz method.

4.2.3 *Rayleigh-Ritz approach*

The Rayleigh-Ritz method can be applied using Eq. 4.8 as starting point, minimizing the potential energy of the structure ($\delta\Pi = 0$). The displacements depend on a certain number of unknowns denoted as c_i (i = 1, nn being the total number of unknowns) that need to be determined. For a particular ΔT, the total potential energy can be expressed in terms of unknowns c_i as shown in Eq. 4.16 .

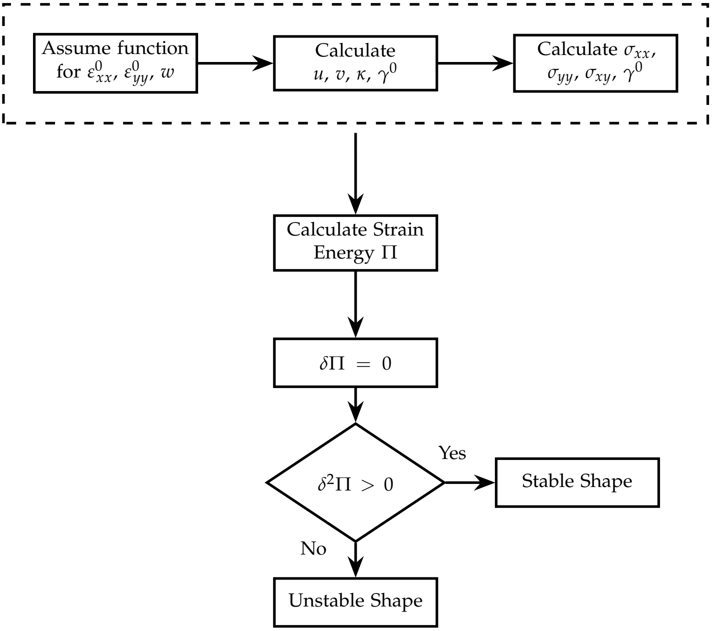

FIGURE 4.1: Flowchart of the semi-analytical framework.

$$\Pi \approx \Pi_N(\mathbf{c}),\ \mathbf{c} = \{c_i\},\ \text{i=1, ..., nn} \tag{4.16}$$

In order to calculate the final deformed shapes of the multistable unsymmetric laminates as it is cooled down from its curing temperature to the room temperature ($\Delta T < 0$), the principle of minimum potential energy is used. This results in a set of a highly non-linear system of equations (Eq. 4.17) solved using the Newton-Raphson technique.

$$\frac{\partial \Pi_N(\mathbf{c})}{\partial c_i} = \mathbf{0} \tag{4.17}$$

The stability of the solution is evaluated by means of the construction of the Jacobian matrix $\mathbf{J}$, that reads:

$$\mathbf{J} = \frac{\partial^2 \Pi_N}{\partial c_i \partial c_j}; \quad \text{i,j=1, ..., nn} \tag{4.18}$$

An equilibrium configuration is stable, if and only if the corresponding Jacobian matrix Eq. 6.32 is positive definite. All the symbolic computation described were accomplished using the routines written in *Mathematica*.

The scheme of the semi-analytical formulation to calculate the stable shapes of the laminates is depicted in figure 4.1.

4.3 Finite-element analyses

Geometrically nonlinear FE analyses are performed in `ABAQUS`^{TM} using 2304 four-node quadrilateral shell elements (S4R) with uniform thermal loading applied throughout the plate. The plate is allowed to cool down from curing temperature to room temperature, resulting in a curved configuration. In a FE simulation, the curvilinear fiber path of the VS composite gets approximated as a linear piecewise function due to discretization (Fig. 4.2). Each element assumes a constant, straight fiber orientation which is equal to the fiber angle at the element centroid using Eq. 3.9. Therefore, within each individual elements, the fiber orientation is constant but varies from one element to the other in a linearly piecewise manner. It is obvious that, the higher the number of element, the better is the curved fiber approximation. It should be noted that with this assumption, the **A**, **B** and **D** matrices are constant for each element. Mesh convergence studies were carried out, and a particular mesh size was chosen to achieve a good compromise between the computational time and the precision of the solution. With the aim of imposing initial geometrical imperfections in the finite element model, the method introduced by Tawfik [205] is used (see also [29]). In this method, a linear eigenvalue analysis is initially performed on the VS composites. Through this analysis, various eigenmodes are numerically estimated for the given temperature difference. These eigenmodes are subsequently applied as an imperfection to the real composite laminates resulting in one of the post–bifurcation stable state. It should be noted that the number and magnitude of the chosen eigenmodes to perturb the nominal geometry of the specimen have a strong influence on the numerical results, in general leading to different equilibrium states. This method proves to be especially useful for VS composites since it is difficult to estimate the stable shapes beforehand, as it can be accomplished for straight fiber composite panels.

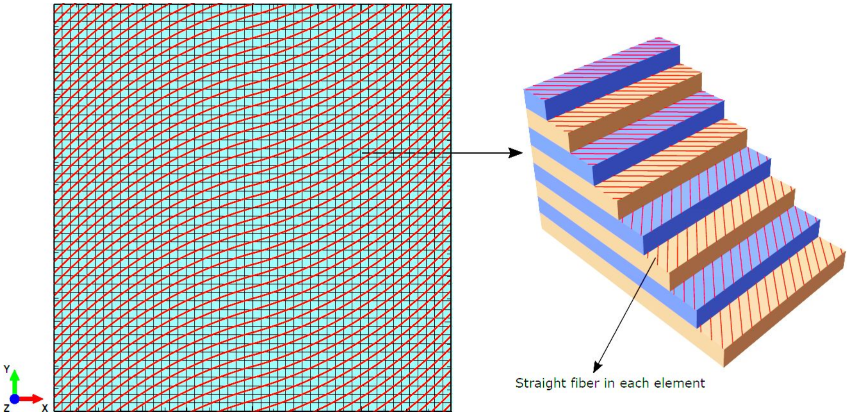

FIGURE 4.2: FE modeling of variable stiffness composites.

Once the imperfections are applied, geometrically non-linear static analysis for each VS configuration is performed in `ABAQUS`$^{\text{TM}}$. A certain damping factor is introduced to reduce the local instabilities when convergence is not achieved. However, it should not be chosen too high as this results in inaccurate solutions. The artificial damping equal to 10^{-7} is found to be appropriate upon some preliminary FE computations and lead to solutions without deteriorating the accuracy of the solution. In particular, damping forces are added in the form of:

$$F_d = d\mathbf{M}^* v \tag{4.19}$$

where d is the damping factor, $\mathbf{M}^*$ is the artificial mass matrix, v is the vector for nodal velocities. The damping force vector is added to the global equilibrium equations as follows:

$$F_{ext} - F_{int} - F_d = 0 \tag{4.20}$$

where F_{ext} and F_{int} are the external and the internal force vectors.

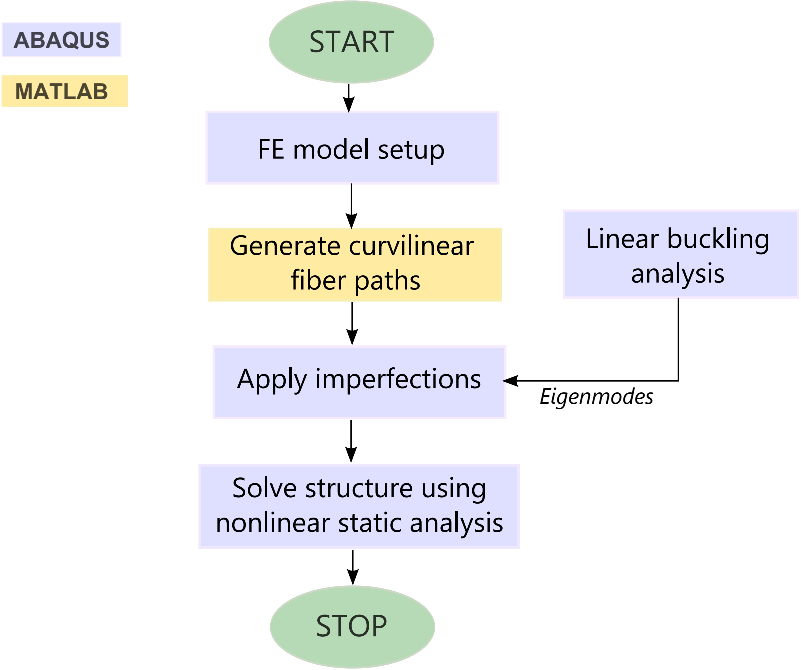

FIGURE 4.3: Scheme of the FE analysis.

A temperature difference of curing and room temperature is applied on the investigated composite plate. Upon the nonlinear static FE analysis, the plate cooled down to one of the stable shape. The other stable configurations could

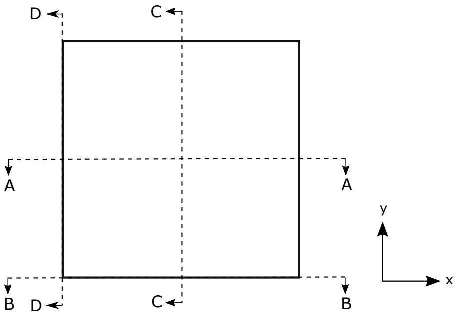

Figure 4.4: Test model geometry and sections analyzed.

easily be found by applying a force in the center of the plate or running the finite element analysis with other eigenmodes as initial imperfections. The solution can be identified as stable or unstable by checking the eigenvalues in the tangent stiffness matrix. The solution is unstable if one of the eigenvalues is zero or negative. The complete scheme of the FE analysis is illustrated in figure 4.3.

4.4 Comparison of FE and semi-analytical results

The multistable shapes of VS composite subjected to thermal loading (with temperature difference $\Delta T = 280°\text{F}/137.77°\text{C}$) are calculated using the semi–analytical approach as described in Section 4.2. The corresponding results are compared with the FE simulations following the modeling guidelines outlined in Section 4.3. Geometry and material of the plate are chosen identical to the numerical example given by Dano and Hyer [51]. The laminates studied are square and have a length L equal to 11.5 in, with eight layers each of 0.005 in-thick plies of graphite-epoxy prepreg. The material properties at ply-level are given as:

$$\begin{aligned} E_1 &= 27.77 \times 10^6\,\text{psi},\ E_2 = 1.27 \times 10^6\,\text{psi},\ G_{12} = 1.03 \times 10^6\,\text{psi} \\ \nu_{12} &= 0.335,\ \alpha_1 = 0.345 \times 10^{-6}/°\text{F},\ \alpha_2 = 15.34 \times 10^{-6}/°\text{F} \end{aligned} \tag{4.21}$$

Type	ϕ	T_0	T_1	Layup
Straight	0	± 45	± 45	$[-45_4/45_4]_T$
VS-1	0	± 30	± 45	$[0\langle -30\vert -45\rangle_4/0\langle 30\vert 45\rangle_4]_T$
VS-2	0	± 15	± 45	$[0\langle -15\vert -45\rangle_4/0\langle 15\vert 45\rangle_4]_T$
VS-3	0	± 0	± 45	$[0\langle 0\vert -45\rangle_4/0\langle 0\vert 45\rangle_4]_T$

Table 4.1: Fiber orientation and layup data for the investigated VS laminates.

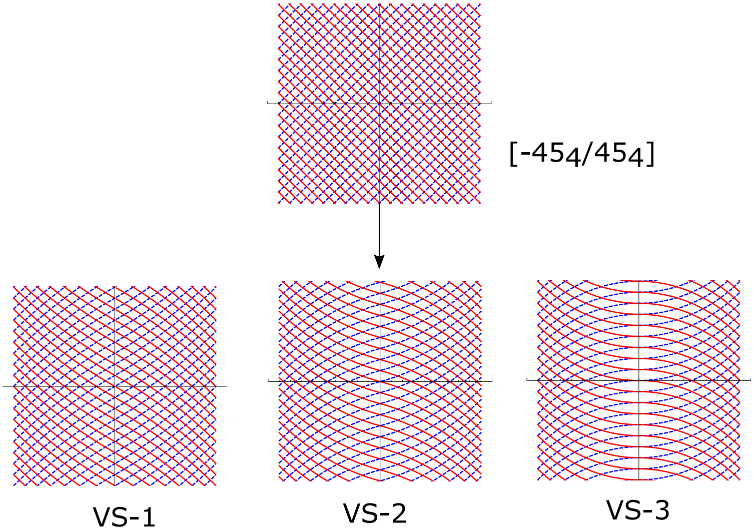

FIGURE 4.5: VS laminates constructed from straight fiber configuration $[-45_4{}^\circ/45_4{}^\circ]$. Layups of the VS laminate can be referred in Table 4.1.

The VS laminates herein investigated have a layup of $[0\langle -T_0| - T_1\rangle_4$ $/0\langle T_0|T_1\rangle_4]_{\mathrm{T}}$ and are constructed on the basis of the reference straight fiber configuration $[-45_4{}^\circ/45_4{}^\circ]$. For all the VS composites, the angle at the edge of the plate (T_1) is kept constant and equals to 45°, but the angle at the center (T_0) is varied from 0° to 45°. In this section, the value of ϕ is considered to be zero. The preliminary results to validate the current approach are compared with the example presented by Dano and Hyer [56] for straight fibers, obtaining exact agreement.

The stable shapes obtained from the semi-analytical and FE results are compared for three different VS laminates, namely VS-1, VS-2 and VS-3. The layup configurations for each of the VS laminates can be found in Table 4.1. It can be seen that the fiber concentration is more localized at the edges and decreases at the center. This distribution clearly makes the plate stiffer at the edges.

The current VS composite laminates generated two stable solutions for each particular configuration. Fig. 4.6 shows the out-of-plane displacement for both stable shapes at room temperature. The FE results (dotted line) are superimposed over the semi–analytical solutions (solid line) to depict the differences. Analyzing the data in more detail, it can be observed that for the VS-1 and VS-2 composites, the FE and the semi–analytical predictions show satisfactory agreement with very small differences near the edges (Fig. 4.6 a-4.6 d). This contrasts with the results corresponding to the configuration VS-3, which presents larger discrepancies with respect to the FE solutions (Fig. 4.6 e-f). The two stable shapes of VS-1, VS-2 and VS-3 are depicted in Figure 4.6 after cooling down to room temperature. In this

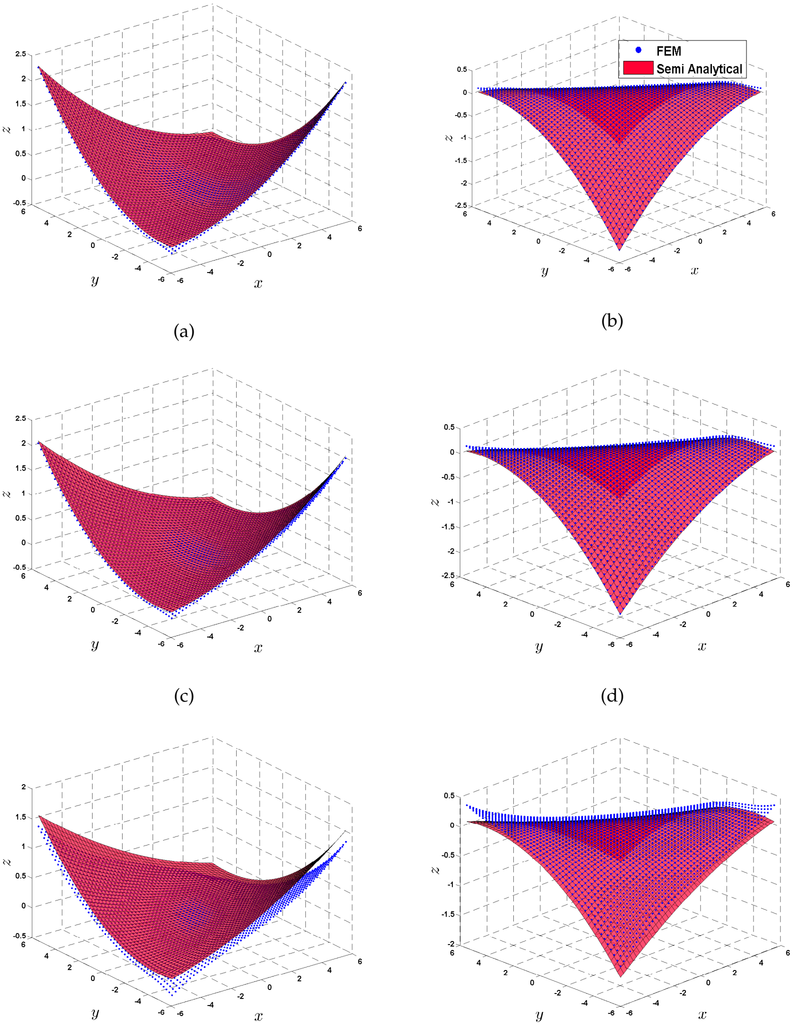

(a) (b) (c) (d) (e) (f)

FIGURE 4.6: Comparison of predicted bistable shapes between semi–analytical and FE results for different VS composites for Case I. a,b) VS-1, c,d) VS-2 and e,f) VS-3. The left and right hand side shows the two stable shapes. Refer to Table 4.1 for the layout details.

figure, it can be seen that the stable FE configurations do not present a constant curvature throughout the plate domain, featuring reverse curvature near the edges.

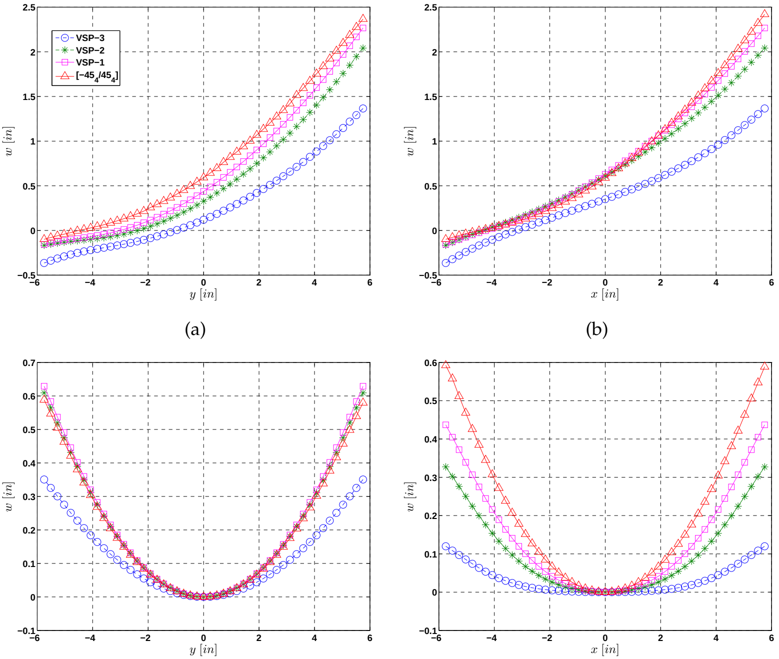

(a) (b)

(c) (d)

FIGURE 4.7: Out of plane displacements using FE for Case I at different sections a) Section D-D ($x = -L/2$), b) Section B-B ($y = -L/2$), c) Section C-C ($x = 0$), d) Section A-A ($y = 0$). The sections are defined in Fig. 4.4.

To closely analyze this edge effect, out-of-plane displacement results of a stable shape from FE analysis are plotted for different sections at Section A-A ($y = 0$), Section B-B ($y = -L/2$), Section C-C ($y = 0$) and Section D-D ($x = -L/2$) as shown in Fig. 4.4. In figures 4.7 a) and 4.7 b), it can be seen clearly that significant reverse curvatures are developed around the corner. Such development of reverse curvatures was previously reported also for straight fibers, where it is more prominent in the proximity of the corner points [75, 185]. They showed that the locations where reversal of curvature occurred coincided with the locations with maximum interlaminar shear stresses. To fulfill the stress-free conditions at the free edges, additional shear stresses develop at the corner. Such reversal in curvatures are also observed in the FE results of the VS laminates, quite prominently in case of VS-3. However, since the semi–analytical method considered in the current study only assumes constant curvatures, it is not able to capture such edge effects.

As the difference between the value of T_0 and T_1 increases, the discrepancy between FE and semi-analytical result for the corner displacement increases too.

For VS-1 and VS-2, the semi-analytical and FE results for out-of-plane displacement agrees well with discrepancies less than 2%. However, for VS-3 laminates, out-of-plane displacements at the corners shows discrepancies of as high as 14% between the semi-analytical and FE results. This is primary due to the formation of localized reverse curvature near the corners as visualized in figure 4.6e and 4.6f. Although the corner displacements from semi-analytical results differed with FE, the overall shape was captured well. If we are interested in determining the general stables shapes and its influence with change in the curvilinear fiber paths, the fast semi-analytical tool proves to a reasonable option.

4.5 Parametric studies on the variation of VS angle parameters using semi-analytical approach

In order to present a more comprehensive analysis, a parametric study of the multistable shapes of unsymmetric square VS composite is conducted using the semi–analytical method. The angle parameters T_0 and T_1 vary from 0° to 90° with a step of 7.5° angle. As the specimen under investigation is a square panel and the loading is uniform throughout the plate, it is irrelevant whether the variation of the fiber angle is along the x–axis or the y–axis. The parametric study is conducted for layup $[\phi\langle -T_0| -T_1\rangle_4/\phi\langle T_0|T_1\rangle_4]_T$, with two different values of ϕ being considered: $\phi = 0^\circ$ and $\phi = 45^\circ$.

Figs. 4.8 and 4.9 depict the relation of curvature κ_x, κ_y and κ_{xy} with changing angle parameters T_0 and T_1 for $\phi = 0^\circ$ and $\phi = 45^\circ$, respectively, whereas Fig. 4.10 shows the maximum out-of-plane displacement (corner displacement) and the principal curvature direction for $\phi = 0^\circ$ and $\phi = 45^\circ$. The principal curvature direction Φ is computed according to the following expression (as reported in Dano and Hyer [56]):

$$\Phi = \frac{1}{2}\arctan\left(\frac{\kappa_{xy}}{\kappa_x - \kappa_y}\right) \tag{4.22}$$

The values of Φ are added or subtracted with $\pi/2$, in order to obtain a consistent larger magnitude of the principal curvature. It should be noted that all these plots depict one of the stable shapes. The description of the other stable shapes will be described later in this chapter. The thicker blue dashed curve in all the plots denotes the results from the straight fiber laminates. A family of curves corresponding to different values of T_0 and T_1 is plotted for VS panels. Each curve is generated by varying the value of T_0 from 0° to 90° for a given value of T_1 as labeled in the figure. Moreover, the intersection between straight fiber laminates and the VS laminates denote the points where T_0 and T_1 are equal. It can be seen that values for straight fiber composite vary from laminates with layup $[-7.5_4/7.5_4]$ to $[-82.5_4/82.5_4]$. At $\theta = 0^\circ$ and $\theta = 90^\circ$, the straight fiber laminate becomes unidirectional and thus is monostable and remains flat. VS laminates with values $T_1 = 7.5^\circ$, $T_0 = 0^\circ$; $T_1 = 82.5^\circ$, $T_0 = 90^\circ$ and $T_1 = 90^\circ$, $T_0 = 82.5^\circ$ with both $\phi = 0^\circ$ and 45° also remain monostable after curing and thus are not included in all the following figures.

4.5.1 *Case I: $\phi = 0°$*

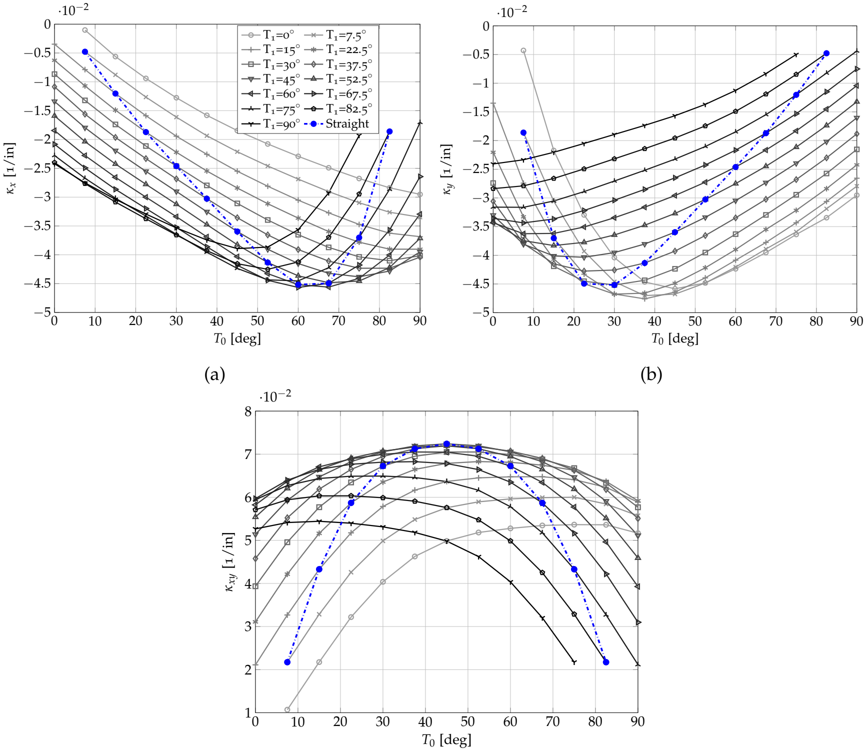

(a)

(b)

(c)

FIGURE 4.8: a) κ_x versus T_0 b) κ_y versus T_0 c) κ_{xy} versus for VS laminates with $\phi = 0°$. Each line represents a family of VS laminates with the same values of T_1.

Fig. 4.8 shows the curvatures of one of the stable shapes with parameter $\phi = 0°$. The values of curvature for other stable shape yield:

$$\kappa_x^{II} = -\kappa_x^{I},\ \kappa_y^{II} = -\kappa_y^{I},\ \kappa_{xy}^{II} = \kappa_{xy}^{I} \tag{4.23}$$

Analyzing the curvature diagrams for $\phi = 0°$ (Fig. 4.8), it can be seen that for the values for straight fibers with $T_0 = T_1 = 45°$, the curvatures κ_x and κ_y are equal, which complies with the results obtained by [56, 179]. According to Ren [179] and based on the present results, it can be seen that for straight fibers with $[-\theta_4/\theta_4]_T$, the curvature values are limited to the one shown by the blue dashed line. On the other hand, VS laminates offer a very rich design space with both higher and lower values of curvatures than those obtained with straight fibers.

For straight fibers, the maximum curvature κ_x of 0.0451 in^{-1} is obtained for $T_0 = T_1 = 60°$ (also reported in [159]), whereas for VS laminates, the maximum κ_x of 0.0456 in^{-1} is obtained for $T_0 = 67.5°,\ T_1 = 60°$ and also for VS composite $T_0 = 60°,\ T_1 = 67.5°$. Similarly, the maximum κ_y for straight fibers is shown by $T_0 = T_1 = 30°$ where $\kappa_y = 0.0451\ \text{in}^{-1}$, whereas for VS composites, the maximum κ_y is obtained from $T_0 = 37.5°,\ T_1 = 15°$ with $\kappa_y = 0.0475\ \text{in}^{-1}$. The maximum value of κ_{xy} in case of straight fibers is obtained from $T_0 = T_1 = 45°$ which is equal to 0.0724 in^{-1}. The maximum value of κ_{xy} for VS composites is obtained for the case of $T_0 = 45°$ and $T_1 = 37.5°$. Therefore, with VS composites, slightly higher values of curvatures can be obtained.

Further, it can be seen that for a given value of curvature, say κ_x, there are several VS composite options generating different values of κ_y and κ_{xy} in contrast to only one set of curvature values with straight fiber composites. For example, when κ_x results in $-0.03\ \text{in}^{-1}$, the straight fiber laminate exhibits κ_y as $-0.041\ \text{in}^{-1}$ and κ_{xy} as $-0.07\ \text{in}^{-1}$. However, it is possible to achieve other values of κ_y and κ_{xy} with the same value κ_x in case of VS composites. To mention a few, laminate with $T_1 = 60°, T_0 = 22.5°$ and $T_1 = 82.5°, T_0 = 75°$ both exhibit $\kappa_x = 0.03\ \text{in}^{-1}$ but at the same time show different values of κ_y as $-0.003\ \text{in}^{-1}$ and $-0.0084\ \text{in}^{-1}$ and κ_{xy} as $-0.068\ \text{in}^{-1}$ and $0.032\ \text{in}^{-1}$ respectively.

Additionally, the study proves that in certain VS laminates, κ_y can be greater than κ_{xy} (for example: $T_0 = 22.5°,\ T_1 = 0°$), which is not possible in angle plies with straight fibers where the twisting curvatures are always dominating.

With regard to the plate deflection (Fig. 4.10a), it can be seen that for straight fibers, the maximum out-of-plane displacement is achieved for a $[-45_4°/45_4°]$ laminate with $w = 2.386$ in, which also verifies the results obtained by Dano and Hyer [56]. However, the maximum out-of-plane displacement is displayed by VS with the angle parameters: $T_0 = 52.5°,\ T_1 = 37.5°$ and $\phi = 0°$, having a value of 2.39 in, which is slightly higher than the maximum value corresponding to straight fibers composites.

A bistable configuration with an equal value of κ_x and κ_y is only possible in the straight fiber laminate $[-45_4/45_4]$. This bistable shape has a principal curvature of 45° as also observed in Dano and Hyer [56]. However, there can be many options in VS composites in which the curvatures κ_x and κ_y are equal. From Fig. 8.7a), it is observed that the values of κ_x and κ_y are almost equal when $T_0 + T_1 = 90°$, though the magnitude of curvatures can vary in the respective VS laminates.

4.5.2 *Case II: $\phi = 45°$*

A similar study is conducted for $\phi = 45°$, where the coordinate system for all layups is rotated with 45° from the Cartesian coordinate. Fig. 4.9 shows the curvatures

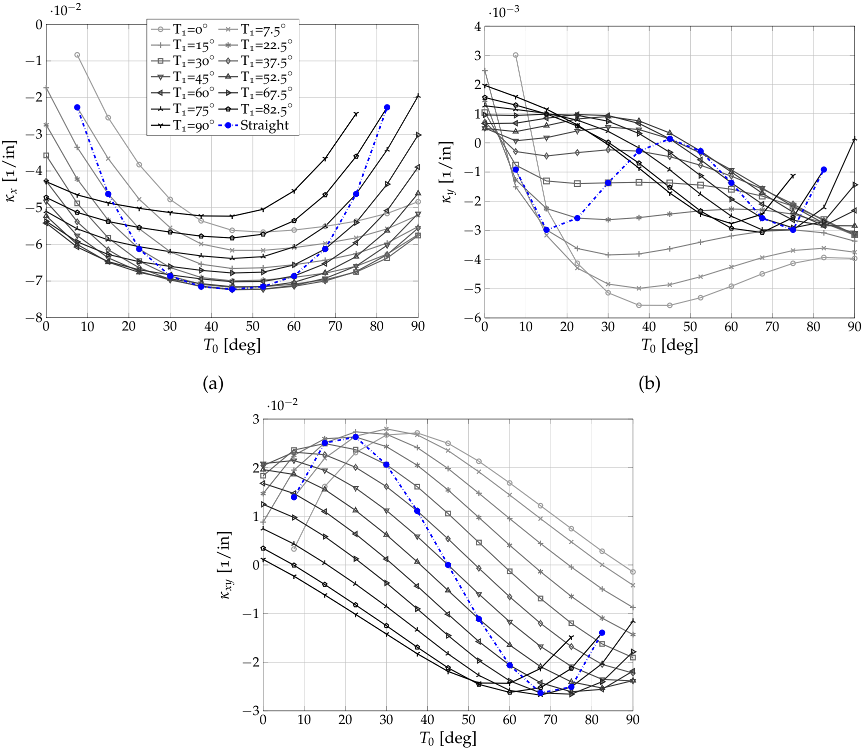

(a)

(b)

(c)

FIGURE 4.9: Parametric study of curvatures as a function of T_0 and T_1 for $\phi = 45°$. a) κ_x versus T_0 b) κ_y versus T_0 c) κ_{xy} versus T_0. Each line represents a family of VS laminates with the same values of T_1.

of one of the stable shapes with different T_0 and T_1 values. The curvatures of the second stable shape are related to that of the first one by the following:

$$\kappa_x^{II} = -\kappa_y^{I},\ \kappa_y^{II} = -\kappa_x^{I},\ \kappa_{xy}^{II} = -\kappa_{xy}^{I} \tag{4.24}$$

From Fig. 4.9, it can be seen that with straight fibers, a cylindrical shape is obtained only when $T_0 = T_1 = 45°$ (which is equivalent to $[0_4/90_4]$) where the value of twisting curvature κ_{xy} is equal to zero. On the other hand, with VS laminates there can be several possibilities from which cylindrical shapes can be generated, with diverse range of curvature values. For example, VS laminates with angle parameters as: $T_1 = 75°$, $T_0 = 15°$; $T_1 = 37.5°$, $T_0 = 52.5°$ also cools down as cylindrical shapes. It is observed that all the values of T_0 and T_1 which satisfies $T_0 + T_1 = 90°$ leads to cylindrical shapes after cooling down to room temperature. However, the twisting curvature κ_{xy} has a definite value in contrast to the cylindrical configuration attained

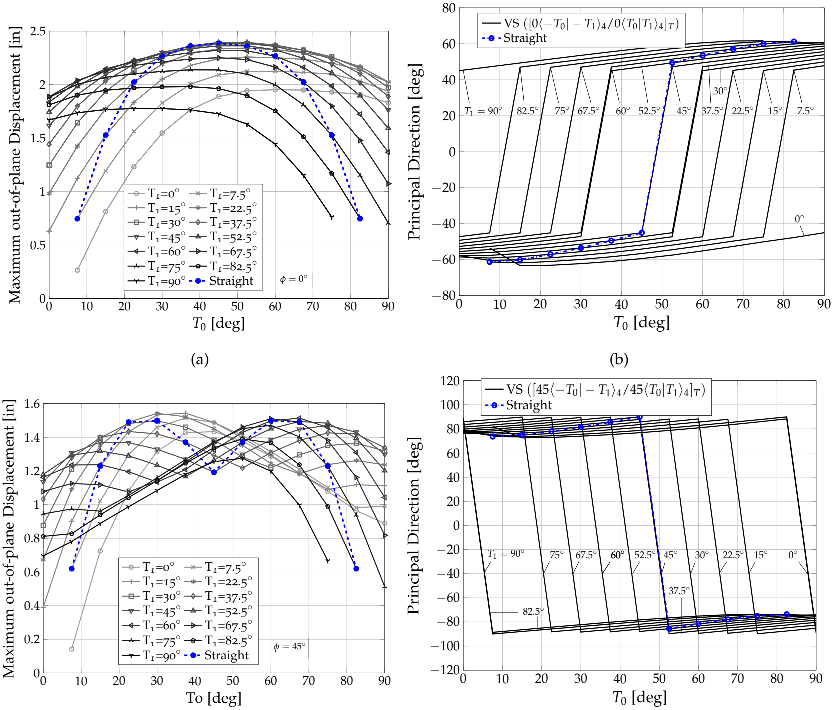

(a) (b) (c) (d)

FIGURE 4.10: Parametric study of out-of-plane displacement and the direction of the principal curvature as a function of T_0 and T_1 a) Maximum out-of-plane displacement versus T_0 for $\phi = 0°$ b) Direction of principal curvature Φ for $\phi = 0°$ c) Maximum out-of-plane displacement versus T_0 for $\phi = 45°$ d) Direction of principal curvature Φ for $\phi = 45°$. Each line represents a family of VS laminates with the same values of T_1.

from the straight fiber with $[0_4/90_4]$, where the twisting curvature is zero. For all the VS laminates leading to cylindrical configuration, the value of κ_{xy} is positive with $T_0 < T_1$, zero at $T_0 = T_1$ and negative with $T_0 > T_1$. The same trend is also followed by the direction of the principal curvature, which is naturally affected by the value of κ_{xy} (see Eq. 4.22). As seen from Fig. 4.10d, the transition from positive to negative direction of the principal curvature occurs at 90°, when the VS laminates attain a cylindrical shape.

Certain VS laminates with cylindrical multistable shapes have also higher out-of-plane displacements than the straight fiber configuration. For example: VS laminate with $T_0 = 60°$, $T_1 = 30°$ (Fig. 8.7c) has a corner displacement of 1.22 in, whereas the straight fiber configuration $[0_4/90_4]$ ($T_0 = T_1 = 45°$) has a corner displacement of 1.19 in (Fig. 4.10c). Similarly, when using VS laminates, lower values of corner displacements for cylindrical multistable shapes can also be achieved.

Fig. 8.7 illustrates several stable shapes that can be attained by changing the angle parameters in VS composites. From a qualitative point of view, this parametric study reveals the rich design space of multistable shapes generated using VS laminates, with a wide range of curvatures and maximum corner displacements, and with the corresponding different principal curvature directions.

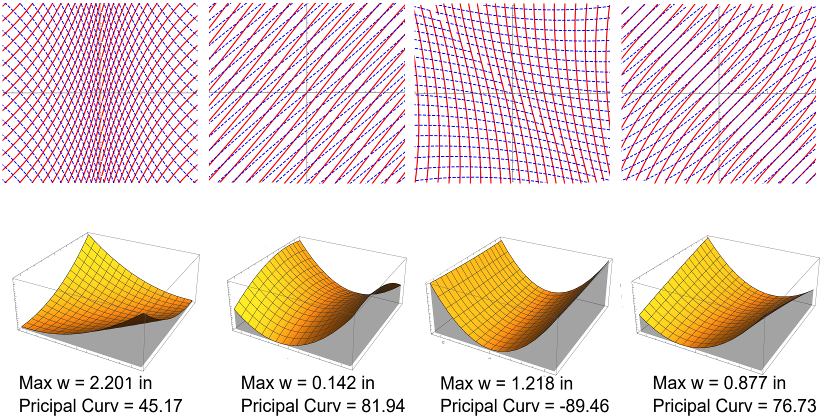

FIGURE 4.11: Predicted multistable shape of laminates with different curvilinear fiber paths. a) $[0\langle -75|-15\rangle_4/0\langle 75|15\rangle_4]_T$, b) $[45\langle -7.5|0\rangle_4/45\langle 7.5|0\rangle_4]_T$, c) $[45\langle -60|-30\rangle_4/45\langle 60|30\rangle_4]_T$, d) $[45\langle -0|-30\rangle_4/45\langle 0|30\rangle_4]_T$.

4.6 Conclusions

In this study, a semi-analytical method based on the Rayleigh-Ritz approach is used for calculating the thermally induced multistable behavior of unsymmetric laminates with curvilinear fiber paths. The developed technique proved to be an efficient and a relatively simple tool, providing estimations for all the stable shapes for the unsymmetric VS composite plates. The reliability of the semi–analytical results is examined by means of corresponding FE models, where curvilinear fibers were defined discretely at each element.

Certain VS laminate were analyzed to compare the stable shapes obtained from FE and semi-analytical results. Higher discrepancies are observed at the corner and edges with an increasing difference between T_0 and T_1 values. However, the fast semi-analytical tool provided a good overall picture of the stable shapes. Discrepancies around the corners and edges do not play an important role, when this tool is used to classify VS laminates into families with similar multistable equilibrium positions. Taken this point into account, it was further used for conducting parametric studies.

A variation of out-of-plane displacements and the principal curvatures of the stable shapes are observed with the change in variable stiffness angle parameters

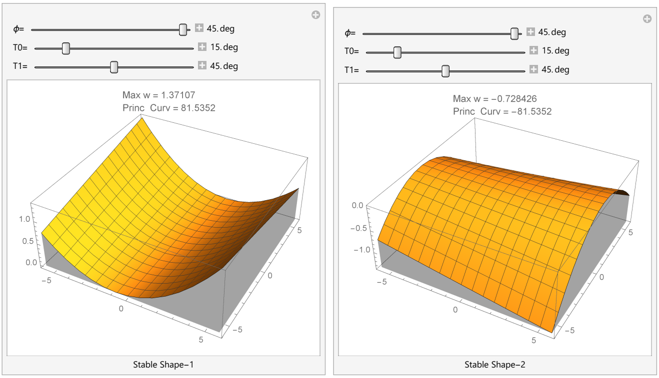
ϕ= 45.deg
T0= 15.deg
T1= 45.deg

Max w = 1.37107
Princ Curv = 81.5352

ϕ= 45.deg
T0= 15.deg
T1= 45.deg

Max w = −0.728426
Princ Curv = −81.5352

FIGURE 4.12: The plot represents a parametric study of the multistable shapes of different VS composites.This interactive plot consists of three sliders : ϕ, T_0 and T_1. The study is performed for two different ϕ a) 0° and b) 45°, in which the values of T_0 and T_1 are varied from 0° to 90°. The study reveals the different multistable shapes that can generated using VS composites. For certain parameters the shape doesn't show up which indicates that the structure is mono-stable.

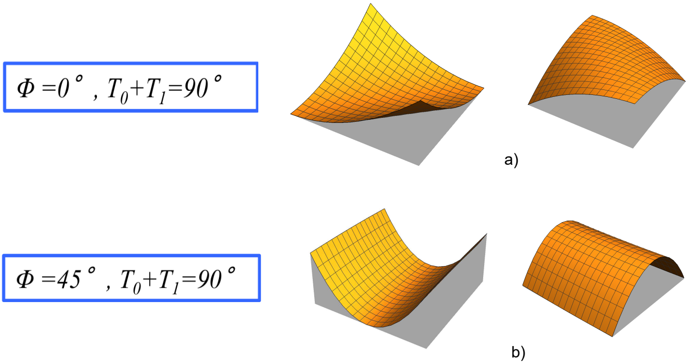

FIGURE 4.13: Family to VS laminates resembling unsymmetric laminates generated from a) $[0^\circ_n/90^\circ_n]$ b)$[-45^\circ_n/45^\circ_n]$.

(T_0, T_1 and ϕ). It is also shown that many different stable shapes can be attained by changing the VS angle parameters. Many VS composites can cool-down to the same stable shapes but might have different curvature values. Certain families of VS laminate were observed which yield similar bistable shapes as the cross-ply laminate $[0_n{}^\circ/90_n{}^\circ]$ and angle ply laminate $[-45_n{}^\circ/45_n{}^\circ]$. As shown in Figure 4.13, bistable laminates generated from the family of VS laminate satisfying $\phi = 0^\circ$ and $T_0 + T_1 = 90^\circ$ yielded similar shapes as the angle ply laminate $[-45_n/45_n]$, whereas the family of VS laminate satisfying $\phi = 45^\circ$ and $T_0 + T_1 = 90^\circ$ yielded shapes similar to the ones obtained from cross-ply laminate $[0_n/90_n]$. This is particularly because of the average fiber orientation on a VS laminate ply equals to a corresponding straight fiber laminate ply. For instance, the average angle in each ply of VS laminate family : $[\phi\langle -T_0| - T_1\rangle_4/\phi\langle T_0|T_1\rangle_4]_T$ is equal to $[0^\circ/90^\circ]$, for the VS laminates satisfying $\phi = 45^\circ$ and $T_0 + T_1 = 90^\circ$. Therefore, the bistable shapes of such VS laminates resemble the shapes of a [0/90] cross-ply laminate. This is for the first time that such alternatives were recognized where similar bistable shapes as straight fiber laminate could be obtained.

The parametric study clearly proves the rich design space of VS laminates in generating multistable structures. VS composite is therefore advantageous in the design process, giving the designer more room to tailor the fiber orientations than straight fiber laminates. Different curvatures and out-of-plane displacements in the multistable structure can be achieved as required.

5

Snapping of multistable VS square laminates

5.1 Introduction

[1] In order to characterize a multistable laminate, it is important to study its snap-through behavior. The transition from one stable solution to the other stable configuration can be achieved through mechanical actions, as is the case of the present investigation.

In the previous chapter, we classified the VS laminates into two families: $\phi = 0^\circ$ and $T_0 + T_1 = 90^\circ$ and other one $\phi = 45^\circ$ and $T_0 + T_1 = 90^\circ$. In this work, we investigate further on the VS laminate family satisfying $\phi = 45^\circ$ and $T_0 + T_1 = 90^\circ$, particularly looking at the snapping behavior. This family yields bistable shapes similar to unsymmetric cross-ply laminates, which are particularly interesting for the morphing application we will be addressing in the later chapters.

The semi-analytical framework introduced in the previous chapter gave a good prediction on the bistable shapes of different VS laminates. The revealed rich design space disclosed configurations that can be suitable for any specific morphing application. To design a morphing system with multistable elements, it is crucial that the snap through loads are calculated in an efficient yet accurate manner. So the question we ask at this point is: How well does this semi-analytical formulation capture the snap-through process?

To address this, we extend the formulations from the previous chapter and rewrite the total energy by including the contribution of external energy (in the form of applied force). Subsequently, the finite element model is developed to compare the semi-analytical results. We take an example from the literature [63], where a detailed investigation on the snap-through loads has been reported. Taking this example as a reference, we construct VS laminate based on the family satisfying $\phi = 45^\circ$ and $T_0 + T_1 = 90^\circ$. The snap-through phenomenon for a few VS laminates from this group is studied featuring in detail the transition phases involved during

---

[1] This work presented in this chapter is based on the published book chapter: Haldar et al. [91]

the snap-through process. Some discussions are made on why the snap-through differs even for VS laminates with similar bistable shapes.

5.2 On the snap-through process

5.2.1 *Semi-analytical formulation*

The cool-down from the curing temperature to working or room temperature leads to the generation of one of the stable shapes. Snap-through from one stable shape to another can be achieved using actuators, shape-memory alloys or simply a mechanical force. In this chapter, a concentrated force is applied at each corner of the plate to facilitate snap-through. Therefore, the external force contribution due to these concentrated forces to the virtual energy equation can be written as:

$$\delta V = F_x.\delta u + F_y.\delta v + F_z.\delta w \tag{5.1}$$

As the force is applied at the z-direction, the components $F_x = F_y = 0$. The values of the displacement fields can be directly computed using the kinematic relation described in Section 4.2.2 . Substituting Eq. 4.9 in Eq. 5.1, one obtains:

$$\delta V = \frac{L^2}{8} F_z \left(\delta c_9 + \delta c_{10} + \delta c_{11}\right) \tag{5.2}$$

Accordingly, the modified virtual work principle with the external force contribution V and internal strain energy Π can be written as follows:

$$\delta W_T = \delta\Pi - \delta V = 0 \tag{5.3}$$

$$\frac{\partial W_T(\mathbf{c})}{\partial c_i} = 0 \tag{5.4}$$

$$\begin{gathered}\left(\frac{\partial\Pi_N}{\partial c_9} - \frac{L^2}{8}F_z\right)\delta c_9 + \left(\frac{\partial\Pi_N}{\partial c_{10}} - \frac{L^2}{8}F_z\right)\delta c_{10} + \left(\frac{\partial\Pi_N}{\partial c_{11}} - \frac{L^2}{8}F_z\right)\delta c_{11} \\ + \cdots\cdots \frac{\partial\Pi_N}{\partial c_i}\delta c_i = 0\end{gathered} \tag{5.5}$$

This results in a set of highly non-linear system of equations (Eq. 6.31) which are solved using the Newton-Raphson technique. Finally, the stability of the solution is evaluated by means of the construction of the Jacobian matrix **J**, that reads:

$$\mathbf{J} = \frac{\partial^2 W_T}{\partial c_i \partial c_j}, \text{ i,j=1, ..., nn} \tag{5.6}$$

An equilibrium configuration is stable, if and only if the corresponding Jacobian matrix Eq. 5.6 is positive definite.

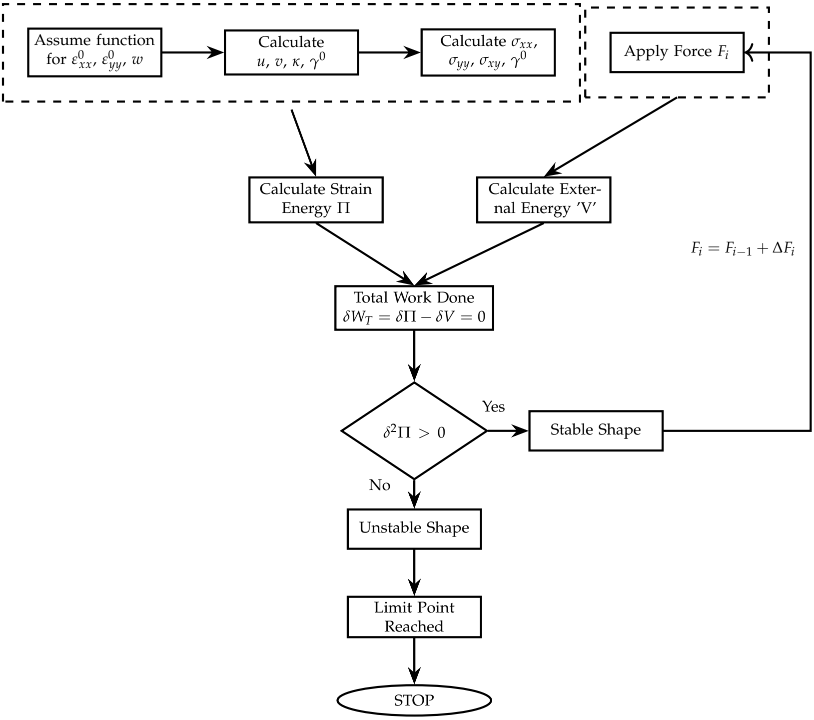

FIGURE 5.1: Flowchart of the semi-analytical framework to calculate the snap-through loads.

The two stable shapes obtained after the cool down process can be first obtained by setting the value of the applied force to zero. The snap-through force can subsequently be found by gradually increasing the values of the applied force until a single solution is found. The scheme of the semi-analytical formulation is shown in figure 5.1.

5.2.2 *Finite element analysis*

A finite element model is developed to simulate the nonlinear snap-through process. We verify the snap-through loads calculated using semi-analytical results with FE model. Further, using the FE model, the deformation modes are determined as the load is increases until it reaches the limit point. We use mechanical forces applied at the center to trigger snap-through. All the described steps are well illustrated in Figure 5.2, where the transition between stable shapes is depicted. The FE procedure is divided into different steps, as described below:

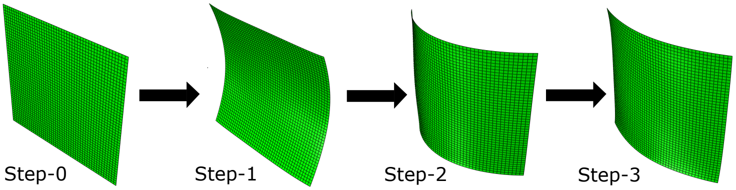

FIGURE 5.2: Performed steps in the FE analysis.

1. After identifying the first stable configuration resulting from the cool-down process (Step-1 in Fig. 5.2), the snap-through phenomenon is investigated by changing the boundary conditions of the FE simulation from the cool-down step. In particular, the displacements along the 'z' direction are restrained at the corner nodes. Additionally, the center node is restrained from translation motion in 'x' and 'y' direction and rotation motion in the 'z' direction.

2. The second step involves application of an external load. A concentrated force is applied at the center node of the obtained cured shape. This force should be greater than the required snap-through force so that the analysis crosses the limit point (Step-2 in Fig. 5.2).

3. Subsequently, at the final stage, the applied load is removed from the center node, so that the plate comes to equilibrium and returns to the second stable shape (Step-3 in Fig. 5.2).

In the semi-analytical method, the forces were applied at the corner points, whereas in the FE model the loads are applied at the center point. This is particularly because in the semi-analytical formulation, the assumed strain and the displacement fields assume a boundary condition of fixed center in the cool-down process. The same boundary condition is maintained during the snap-through process. Changing the boundary conditions, means assuming new function for the strain and displacement fields, which is cumbersome in case of the semi-analytical method. However, this is rather simple in the case of FE modelling where the boundary conditions can be changed within the analysis steps. Both applying loads at the corners or at the center of the plate yields same results in FE analyses.

5.3 Comparison of semi-analytical and FE results

5.3.1 *Determining stable shapes*

We first model the cross-ply laminate investigated in Diaconu et al. [63], and investigate VS laminates exhibiting similar bistable shapes. The laminates studied are square and have a length L equal to 200 mm, with eight layers each of 0.131mmthick plies of graphite-epoxy prepreg. The material properties at ply-level are given as:

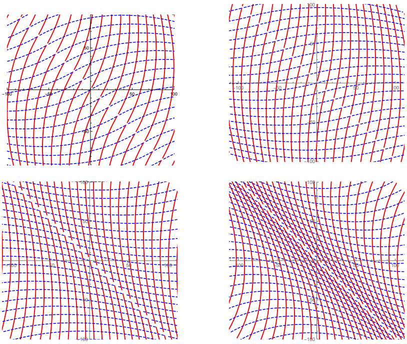

FIGURE 5.3: Investigated VS composites a) VS-1 b) VS-2 c) VS-3 d) VS-4. All of them yield cylindrical bistable shapes similar to unsymmetric cross-ply laminate.

$$\begin{aligned} E_1 &= 164\,\text{GPa},\ E_2 = 12\,\text{GPa},\ G_{12} = 4.6\,\text{GPa} \\ \nu_{12} &= 0.3,\ \alpha_1 = -1.8\times10^{-8}/^\circ\text{C},\ \alpha_2 = 3\times10^{-5}/^\circ\text{C} \end{aligned} \tag{5.7}$$

The layup data and the values of angle parameters ϕ, T_0 and T_1 of the investigated VS laminates are given in Table 5.1. The investigated VS laminate are illustrated in Fig. 5.3. As reported in the previous chapter, all the VS composites satisfying $\phi = 45^\circ$ and $T_0 + T_1 = 90^\circ$ lead to cylindrical bistable shapes with low twisting curvatures, similar to that obtained from cross-ply laminates. The investigated VS composites are then compared with $[0_4/90_4]$ straight fiber laminate, which generates a similar shape as seen in [63].

In this chapter, we focus only on $\phi = 45^\circ$ VS laminate. This is particularly keeping into consideration the morphing application described in the later chapters. The

Type	ϕ	T_0	T_1	Layup
Straight	45	±45	±45	$[0_4/90_4]_T$
VS-1	45	±15	±75	$[45\langle15\vert75\rangle_4/45\langle-15\vert-75\rangle_4]_T$
VS-2	45	±30	±60	$[45\langle30\vert60\rangle_4/45\langle-30\vert-60\rangle_4]_T$
VS-3	45	±60	±30	$[45\langle60\vert30\rangle_4/45\langle-60\vert-30\rangle_4]_T$
VS-4	45	±75	±15	$[45\langle75\vert15\rangle_4/45\langle-75\vert-15\rangle_4]_T$

TABLE 5.1: Fiber orientation and layup data for the investigated straight cross-ply and various VS composites

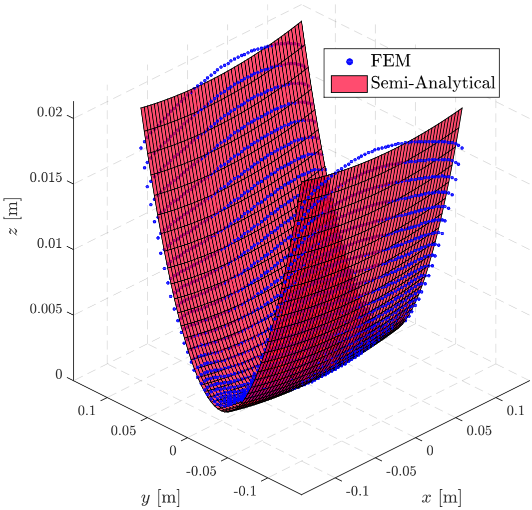

Figure 5.4: Comparison of a stable shape calculated using finite element and semi-analytical methods for VS laminate with $T_0 = 60°$, $T_1 = 30°$, $\phi = 60°$.

stable shapes obtained from FE analysis are compared with the semi-analytical results (Fig. 5.4).

However, as observed in Fig. 5.4, the discrepancies are higher at the corner points. Table 5.2 shows the out-of-plane displacements at the corner points and the center edges of the square laminate for the first and second stable shape. For the FE analysis, these corresponds to the out-of-plane displacement at step-1 and step-3. The difference between the FE and semi-analytical results at the corners is 13.9% in case of the straight fiber cross-ply, 21.8% for VS-1, 18.7% for VS-2, 11.9% for VS-3 and 10.5% for VS-4. At the edge point $x = L_x/2$, $y = 0$, laminates exhibit discrepancies of 1.4% for the straight cross-ply, and 8.8% for VS-1, 8.6% for VS-2, 1.3% for VS-3 and 2.8% for VS-4. The overall comparison shows good agreement between semi-analytical and FE results. Therefore, it can be observed that the differences are lower at the edges of the plate than the corner points.

The analysis is complemented through performing a comparison between different stable configurations for several VS laminates. Fig. 5.5(a) compares the FE result of the two stable shapes of the straight fiber cross-ply laminate 5.5. Fig.5.5(b) depicts the two stable shapes of VS-1 where the value of $T_0 < T_1$, whereas Fig.5.5(c) depicts the two stable shapes of VS-4 where the value of $T_0 > T_1$ computed using the FE analysis. Based on these results, it is observed that the straight fiber cross-ply

Laminate	$[0_4/90_4]_T$	VS-1	VS-2	VS-3	VS-4
Displ. at $(L_x/2, L_y/2)$					
Analytical					
w_1	−21.07	−16.15	−18.23	−21.65	−19.73
w_2	21.07	16.15	18.23	21.65	19.73
FEM					
w_1	−18.5	−13.26	−15.36	−19.34	−17.86
w_2	18.5	13.26	15.36	19.34	17.86
Displ. at $(0, L_y/2); (L_x/2, 0)$					
Analytical					
w_1	−21.20	−16.75	−19.09	−20.54	−18.48
	0.13	0.54	0.55	−0.76	−1.17
w_2	−0.13	−0.54	−0.55	0.76	1.17
	21.20	16.75	19.09	20.54	18.48
FEM					
w_1	−21.90	−15.39	−17.58	−20.82	−19.02
	−0.08	−2.84	−1.88	1.18	1.53
w_2	0.08	2.84	1.88	−1.18	−1.53
	21.90	15.39	17.58	20.82	19.02

Table 5.2: Out-of-plane displacements for the adjacent corners of cross-ply and VS plates using FE and semi-analytical method (in –*mm*).

exhibits a uniform distribution of out-of-plane displacement at the center region of the plate. However, VS-1 and VS-4 shows non-uniform curvature at the center region of the plate. In order of further analyze the distribution of out-of-plane displacements at the center region of the plate, a graph is constructed which depicts the value of out-of-plane displacement of the first stable shape against the x-axis (Figure 5.6). For the straight fiber cross-ply, the value of out-of-plane displacement does not vary much along the x-axis. On the other hand, for VS-1 laminate, the value of out-of-plane displacement varies from zero at the center of the plate to negative values at the edge of the plate. This results in a dip at the center of the plate. Such local deformation makes the plate conducive to snap-through to the second stable shape. An opposite effect is observed for the laminate VS-4, where values of out-of-plane displacement changes from zero at the center to positive values of out-of-plane displacement at the edges, making it unfavorable for the snap-through process.

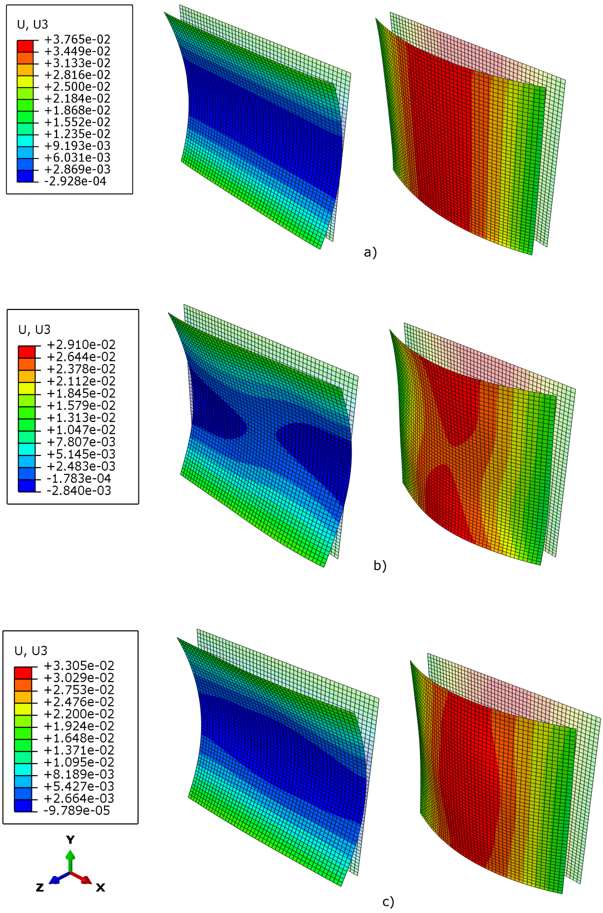

FIGURE 5.5: Two stable shapes of a) straight fiber cross-ply and b) VS laminate with $T_0 < T_1$ (VS-1) c) VS laminate with $T_0 > T_1$ (VS-4) calculated using FEM.

Laminate	$[0_4/90_4]_T$	VS-1	VS-2	VS-3	VS-4
Analytical	54.4	33.6	38.0	92.0	106.0
FEM	36.8	25.7	20.2	71.0	76.4

TABLE 5.3: Comparison of snap-through loads for various VS laminates and straight fiber laminate.

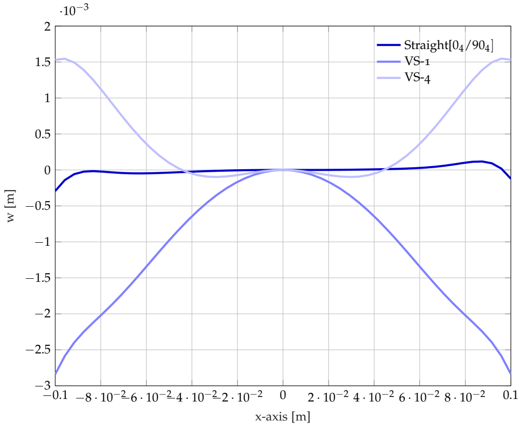

Figure 5.6: Plot of out-of-plane displacement with x-axis. The graph shows the formation of local curvatures in VS composites.

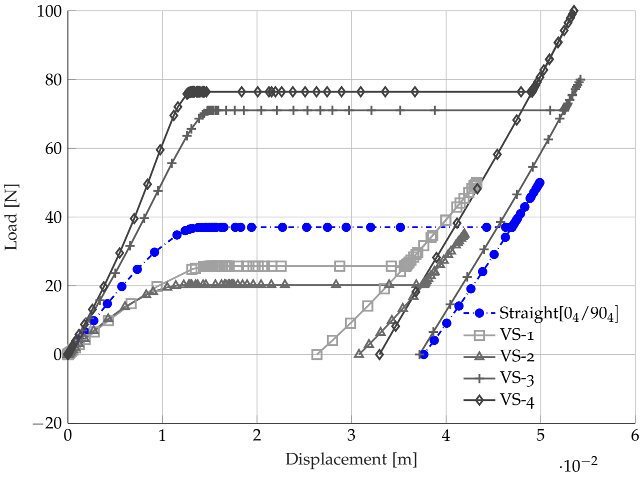

Figure 5.7: Stabilised load–displacement diagram obtained from FE calculations, depicting snap-through phenomenon.

5.3.2 *Calculation of snap-through loads*

The first stable shape is generated when the laminate is cooled from curing to room temperature. In order to snap from this stable shape to another, a certain load is applied at the center of the plate. As described in section 6.4.3 a geometrically nonlinear FE calculation was carried out in ABAQUS to simulate the snap-through process. The snap-through is a dynamic process and requires a stabilization tech-

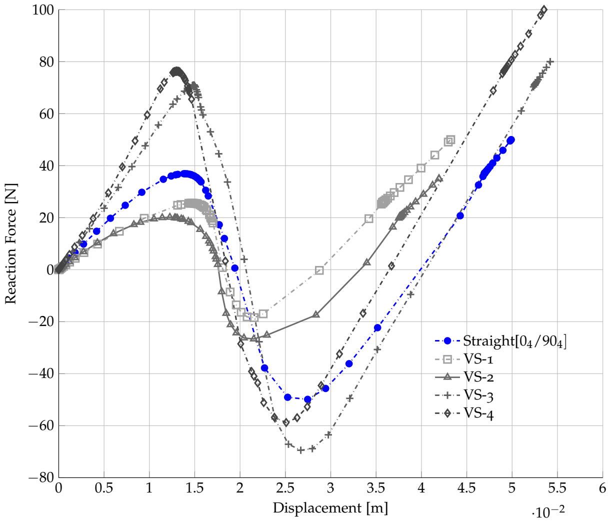

FIGURE 5.8: Reaction force-displacement diagram obtained from FE calculations showing the intermediate unstable path.

nique to damp the local instabilities. Therefore, numerical stabilization is introduced in the form of viscous forces when instabilities are detected at the stiffness matrix of the system. This method is equivalent to the load-controlled test performed in experiments.

The out-of-plane displacement at the center of the plate is measured at each load increment of all the VS laminates and the straight fiber cross-ply. The resultant load-displacement curve is shown in Figure 5.7. It can be seen that with the applied load, the structure deforms elastically featuring linear load-displacement curves. Once the critical point is detected, the structure snaps from one stable shape to another.

The snap-through force can be directly determined from the load-displacement curve. It can be observed from the figure that among all the laminates investigated, VS-4 requires the maximum snap-through force (76.5 N) followed by VS-3 (71.0 N), VS-1 (25.7 N) and VS-2 (20.2 N). The straight fiber cross-ply $[0_4/90_4]$ requires a snap-through force of 36.8 N. This value of can be verified from the previous calculation carried out by Diaconu et al. [63]. It can be observed that laminate VS-2 has 45% lower snap-through forces than the straight cross-ply laminate, with a just 14% lower out-of-plane displacement. Figure 5.8 depicts the variation of the reaction forces at the corners of the plate and the out-of-plane displacement. Through this curve, the unstable equilibrium path after the limit point can also be observed.

The snap-through forces calculated from the semi-analytical approach is compared with FE results in Table 5.3. Analyzing these data, significant deviations between

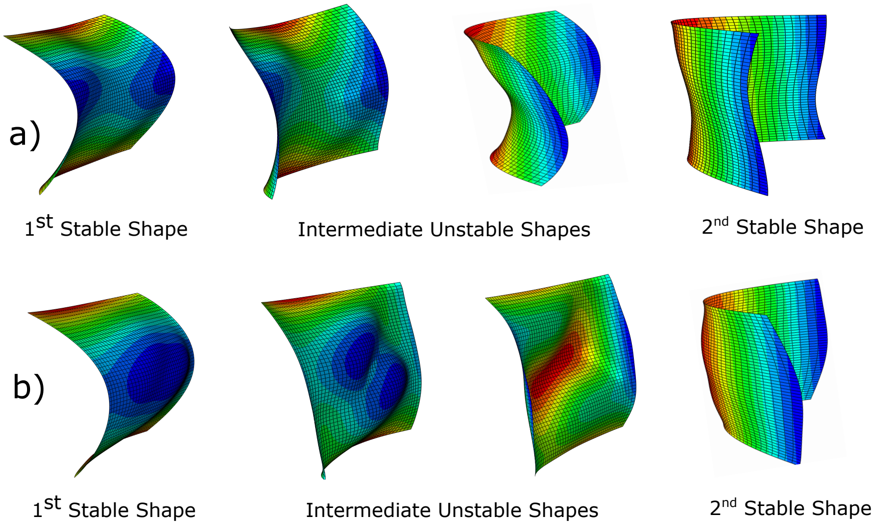

FIGURE 5.9: Transition from one stable shape to another when subjected to concentrated force at the center of the VS plates with a) $T_0 < T_1$ b) $T_0 > T_1$.

the FE and the semi-analytical predictions can be observed. These differences are attributed to the development of complex intermediate unstable shapes during the snap-through process. However, such complex, unstable geometries cannot be captured using the current semi-analytical procedure since this model restricts the plate to deform only within the cylindrical modes, which is incorrect as observed in the FE analysis.

Figure 5.9 shows an exaggerated picture of the snap-through process for VS-1 ($T_0 < T_1$) and VS-4 ($T_1 < T_0$) involving complex intermediate shapes prior to snap-through. This figure also illustrates the formation of a dip at the center of VS-1 laminate as described in Section 5.3 favoring the snap-through process. It therefore requires a lower external force for the transition between stable shapes. On the other hand, VS-4 laminate shows a bulge at the center of the plate making the snap-through process unfavorable. This leads to higher snap-through forces for VS-4. A similar argument can be made for VS-2 and VS-3 laminates.

From this study, an important aspect of using VS composite as a multistable structure can yet be noticed. Due to a large design space owing to huge tailoring options, VS composites possess the capability to allow large out-of-plane displacement with lower snap-through loads than the straight fiber laminates. Multistable VS composites can be thus used in morphing applications enabling large deflections with lower snap-through forces than what is achieved using conventional straight fiber laminates.

5.4 Conclusions

The semi-analytical formulation introduced in the previous chapter is extended to included snap-through loads. A family of VS laminates satisfying the condition: ϕ=45° and $T_0 + T_1$=90° is investigated. All of them generated a bistable cylindrical shape similar to that produced from a cross-ply laminate. Using both semi-analytical and FE methods, the snap-through loads were determined. The predicted value of snap-through loads had significant deviations from the FE results. Unlike any straight fiber laminate, the VS laminate exhibited local deformations at the center region of the plate. The stable shape of VS-1 and VS-2 had a dip in a direction favorable for the snap-through phenomenon, whereas VS-3 and VS-4 had a bulge at the center counteracting the snap-through process.

Local deformations occurring in VS composites near the center of the plate and deviation at the edges are not accurately captured by the semi-analytical method as it assumes uniform curvatures. Finite element computations can handle such complexities and can accurately predict local phenomena, due to a more significant number of degrees of freedom. Due to the development of complex intermediate unstable shapes during the snap-through process, the current semi-analytical method yields deviations in comparison to the FE predictions of the snap-through forces. Such differences are attributed to the fact that the proposed semi-analytical model restricts the plate to deform only within the modes having uniform curvatures. This is found to be incorrect as observed in the FE analysis. To capture such local deformations, higher order polynomial expansions are needed to describe the displacements.

Based on the non-linear FE analysis, it was observed that the snap-through force varies with different VS composites. The snap-through forces were much higher for VS-3 and VS-4 laminates, where the fibers are more concentrated at the center of the plate. The VS-1 and VS-2, on the other hand, required lower snap-through forces than the straight fiber cross-ply with a marginal reduction of corner displacements. Such VS composites can advantageously be embedded as a component in a larger structure to achieve morphing, with low snap-through forces.

6

Determining snap-through loads in multistable VS laminates using reduced semi-analytical model

---

6.1 Introduction

[1] Thermally induced bistable shapes of unsymmetric laminates often result in a narrow range of shapes limiting its use in different applications. As we observed in chapter 4, VS laminates could be used to generate a broader range of stable shapes than that of straight fiber laminates.

Due to their vast augmented design space, VS laminates offer tremendous freedom to tailor material parameters in such a way that the snapping behavior can also be tailored. Such capabilities were revealed for the first time in the previous chapter.

In the previous chapter, it was also observed that the semi-analytical formulation predicted the snap-through loads with significant deviations. FE proves to be an accurate tool but requires high computational cost, which may not be suitable for optimization or parametric studies where large number of calculation are required. Additionally, it is not possible to capture all the stable solution in a single analysis using FE. Prior knowledge of the bistable shapes might be required to apply the imperfections in such a way that solution converges to one of the stable shapes.

To design VS bistable plates for morphing application, a fast and sufficiently accurate analytical tool is required to study their snap-through behavior. The semi-analytical method used in the previous chapter could be directly used to increase the polynomial order. This can improve snap-through load predictions but comes at the expense of high computational costs, which hinders the purpose of the semi-analytical formulation. Therefore, we seek a suitable reduction strategy to reduce the number of unknowns in the semi-analytical formulation derived in the last

---

[1] This chapter is based on the conference proceeding: Haldar et al. [90]

chapter, such that the snap-through loads are calculated in a fast and yet reasonably accurate manner.

Vidoli et al. [213], in his seminal paper, showed that the number of unknowns required for describing the in-plane strains could be eliminated by solving the so-called membrane problem separately. The membrane problem consists of the compatibility equation and the in-plane equilibrium equations. This procedure requires expressing the in-plane stress resultants in terms of the curvatures. The curvatures are directly calculated from the assumed out-of-plane displacement functions as already mentioned in chapter 4, Eq. 4.10. For elliptical shapes, it has been shown previously by Seffen [193] that a direct closed-form solution can be obtained for the resulting partial differential equations (PDEs) . However, for any other generic shape, it requires solving a set of PDEs using a numerical method, which we focus in this work.

Vidoli et al. [213] emphasized on the importance of solving the PDEs accurately, to determine consequently the stretching energy, which has a crucial role in describing the behavior of the bistable laminates. Lamacchia et al. [128] solved such a system of PDEs using the Differential Quadrature Method (DQM). The stretching energy was estimated with reasonable accuracy. Vidoli, on the other hand, had rearranged the equations such that it could be solved with finite elements similar to a standard elasticity problem.

Both these formulations required to decouple the bending and stretching parts of the total strain energy, using a semi-inverse constitutive relationship. To reduce the number of unknowns, the in-plane stress resultants are expressed once and for all in terms of curvatures and thermal strains using the compatibility equation and the constitutive relations. The total energy is then expressed as a function of just curvatures and thermal strains. Therefore, using this strategy the number of unknowns used for the Rayleigh-Ritz method can be drastically reduced when compared to the semi-analytical method described in the previous chapter. In this approach, we need to describe just the out-of-plane displacement or the curvature field. On the other hand, the semi-analytical method described in the previous chapter, required both in-plane strain and out-of-plane displacement field to be defined.

Lamacchia et al. [128] showed that the snap-through loads for a cross-ply laminate could be solved accurately using this approach, where the partial differential equations are solved using DQM. In this work, we extend this work and apply it to VS laminates. A single robust framework is developed, where the analytical expressions are not needed to be derived separately for different orders of polynomial functions.

This chapter is organized into the following sections. Section 6.2 describes the adopted curvilinear fiber trajectory, defining the necessary modifications in the fiber angle parameters. The following Section 6.3 describes briefly the adopted methodology followed by its non-dimensional form in Section 6.4. The membrane problem, where the in-plane stresses are calculated numerically using DQM, is described in Section 6.5. Section 6.6 describes the results obtained from the analytical model which are compared with the results obtained from the FE model. The snap-through loads, as well as the out-of-plane displacements, are calculated in a parametric study described in Section 6.7 for the family of VS laminates. Finally, concluding remarks can be found in Section 6.8.

6.2 Variable stiffness model

In this paper, the bi-linearly fiber variation proposed by Gürdal et al. [88], as used in the previous chapters is modified to a smoother nonlinear fiber variation at the center of the laminate as shown in Figure 6.1. The original linear variation by Gürdal et al. [88] imposed a symmetric fiber path around the centroid of the laminate, which led to a non-differentiable function at this point. Figure 6.2 shows the plot for the second derivative of the B_{11} component with respect to y in the non-dimensional space, for the linear Gürdal's model. The figure on the left shows the exact derivative and that on the right shows the derivative with DQM discretization (DQM was introduced in chapter-3, section: 3.4). It is quite evident that the linear model results in a discontinuity on double differentiation, due to which the DQM fails to determine the correct value. For the nonlinear variation, the fiber orientation angle θ for the reference fiber path is defined as follows:

$$\theta(x') = \phi + \frac{(T_1 - T_0)}{d} \frac{a|x'|^3}{1 + a(x')^2} + T_0 \tag{6.1}$$

where

$$x' = x \cos\phi + y \sin\phi. \tag{6.2}$$

In comparison to the linearly varying fiber angle in the model introduced by Gürdal et al. [88], an additional parameter a is introduced (Eq. 6.1), which adds nonlinearity to the variation of fiber orientation angle at the center of the plate. Therefore, the fiber angle variation defined here is similar to the typical linear variation but with a smoother nonlinear transition of fiber angle at the center of the plate. With such variation, the derivatives of the components of the stiffness matrix, for example as shown in Figure 6.3 shows less difference when calculated analytically (6.3 a) and numerically (6.3 b). A smoother transition between the fiber orientation obviates numerical errors pertaining to differentiation of the fiber orientation angle θ near the center of the plate. This is because the discontinuity in the first derivative of the bi-linear function is eliminated by using a continuous varying function. The difference in the double derivative of B_{11} between the bilinear fiber variation and nonlinear variation is clearly reduced.

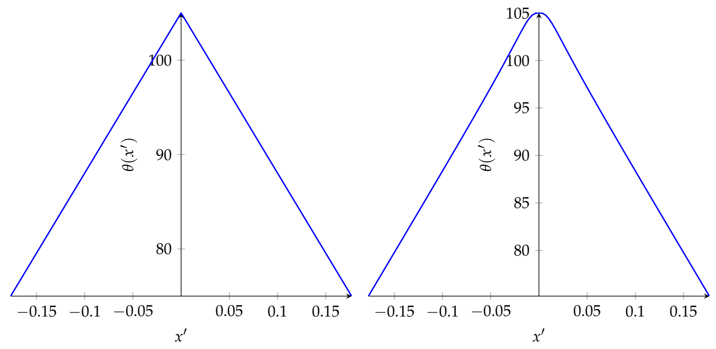

FIGURE 6.1: Variation of fiber angle for $[45\langle 15|75\rangle]$ a) Bilinear Variation ([88]), b) Nonlinear Variation with $a = 1000$.

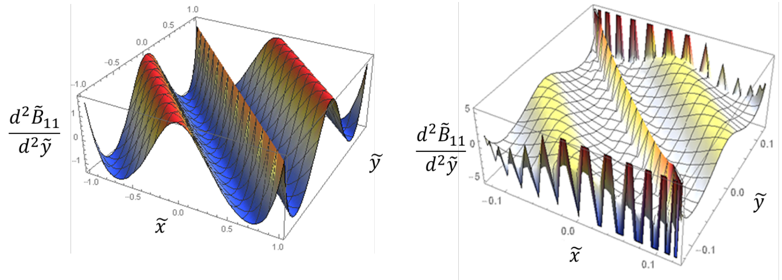

Exact Derivative

Derivative using DQM

FIGURE 6.2: Comparison between double derivative of a component $\tilde{B_{11}}$ with $\tilde{y}$ for linear variation of angle in $[45\langle 15|75\rangle_4/45\langle -15|-75\rangle_4]_T$. There is clear difference in the derivatives between the analytical derivative and when calculated using DQM. Here $\tilde{x}$ and $\tilde{y}$ refers to the axes of the plate in a non-dimensional scale.

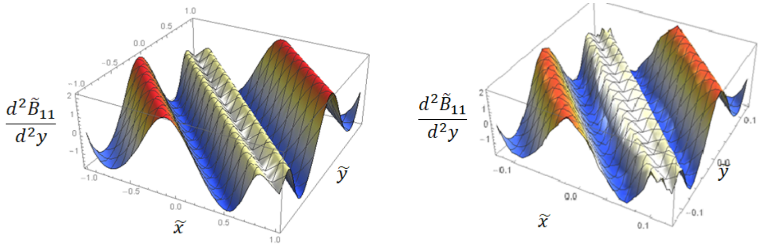

Exact Derivative

Derivative using DQM

FIGURE 6.3: Comparison between double derivative of a component $\tilde{B_{11}}$ with $\tilde{y}$ for a non-linear variation of angle in $[45\langle 15|75\rangle_4/45\langle -15|-75\rangle_4]_T$ with $a = 1000$. Here $\tilde{x}$ and $\tilde{y}$ refers to the axes of the plate in a non-dimensional scale.

6.3 Theoretical development

6.3.1 *Kinematic description*

In the work presented here, all assumptions from Classical Laminate Plate Theory (CLPT) are considered to hold. A material point in the deformed configuration can be expressed as $\mathbf{x} = \mathbf{X} + \mathbf{u}$, where $\mathbf{u}(u, v, w)$ denotes the displacement vector in the x, y and z direction, whereas $\mathbf{x}$, $\mathbf{X}$ identify the position vectors in the deformed and in the undeformed reference configuration, respectively. The components of the displacement vector are defined as [113]:

$$u(x,y,z) = u_0(x,y) - z\frac{\partial w_0}{\partial x}, \quad v(x,y,z) = v_0(x,y) - z\frac{\partial w_0}{\partial y}, \quad w(x,y,z) = w_0(x,y)\,, \tag{6.3}$$

where the subscript 0 identifies the mid-plane displacements. The multistable laminate undergoes large displacements. The strain components with moderate rotations are sufficient enough to capture the deformation during the cool-down process. The strain components include nonlinear von Kármán strains under the assumption of small strains and moderate rotations and follows the CLPT kinematics. They are defined as:

$$\epsilon_{xx} = \frac{\partial u}{\partial x} + \frac{1}{2}\left(\frac{\partial w}{\partial x}\right)^2, \quad \epsilon_{yy} = \frac{\partial v}{\partial y} + \frac{1}{2}\left(\frac{\partial w}{\partial y}\right)^2, \quad \gamma_{xy} = \frac{\partial u}{\partial y} + \frac{\partial v}{\partial x} + \frac{\partial w}{\partial x}\frac{\partial w}{\partial y} \tag{6.4}$$

which shows the nonlinear strain-displacement relationships. By inserting Eq. (6.3) into Eq. (6.4), the strain relations can be rearranged as:

$$\boldsymbol{\epsilon} = \begin{bmatrix} \epsilon_{xx} \\ \epsilon_{yy} \\ \gamma_{xy} \end{bmatrix} = \begin{bmatrix} \varepsilon_{xx} \\ \varepsilon_{yy} \\ \varepsilon_{xy} \end{bmatrix} + z \begin{bmatrix} \kappa_{xx} \\ \kappa_{yy} \\ \kappa_{xy} \end{bmatrix} = \begin{bmatrix} \frac{\partial u_0}{\partial x} + \frac{1}{2}\left(\frac{\partial w_0}{\partial x}\right)^2 \\ \frac{\partial v_0}{\partial y} + \frac{1}{2}\left(\frac{\partial w_0}{\partial y}\right)^2 \\ \frac{\partial u_0}{\partial y} + \frac{\partial v_0}{\partial x} + \frac{\partial w_0}{\partial x}\frac{\partial w_0}{\partial y} \end{bmatrix} + z \begin{bmatrix} -\frac{\partial^2 w_0}{\partial x^2} \\ -\frac{\partial^2 w_0}{\partial y^2} \\ -2\frac{\partial^2 w_0}{\partial x \partial y} \end{bmatrix} = \boldsymbol{\varepsilon} + z\boldsymbol{\kappa}, \tag{6.5}$$

where $\boldsymbol{\varepsilon}$ and $\boldsymbol{\kappa}$ represent the mid-plane strain and curvature vectors, respectively.

6.3.2 *Calculation of total energy*

We already discussed in chapter-3 about the role of bending and stretching energies in thin shape-changing structures. In this formulation, we decompose the total strain energy into the bending and stretching contributions. The total strain energy can be expressed as:

$$\begin{aligned}\Pi =&\frac{1}{2}\int_S\left[\boldsymbol{\varepsilon}^T\boldsymbol{A}(x,y)\boldsymbol{\varepsilon}\right]dS+\int_S\left[\boldsymbol{\varepsilon}^T\boldsymbol{B}(x,y)\boldsymbol{\kappa}\right]dS+\\ &\frac{1}{2}\int_S\left[\boldsymbol{\kappa}\boldsymbol{D}(x,y)\boldsymbol{\kappa}\right]dS-\int_S\boldsymbol{N}^{th}\boldsymbol{\varepsilon}dS-\int_S\boldsymbol{M}^{th}\boldsymbol{\kappa}dS\,,\end{aligned}\tag{6.6}$$

where the superscript ^{T} denotes vector transpose, N^{th} and M^{th} represent stresses and moments associated with thermal effects, respectively and dS refers to the surface element. As the laminate is unsymmetric, the presence of non-zero B-matrix causes a coupling between bending and stretching.

Using the semi-inverse constitutive relations, the strains can be written in terms of curvatures and stress resultants as follows:

$$\boldsymbol{\varepsilon}=\boldsymbol{A}^*(\boldsymbol{N}+\boldsymbol{N}^{th})+\boldsymbol{B}^*\boldsymbol{\kappa}\,.\tag{6.7}$$

The bending and the membrane part of total strain energy can then be decoupled and written as:

$$\begin{aligned}\Pi=&\overbrace{\frac{1}{2}\int_S\left[\boldsymbol{N}^T\boldsymbol{A}^*(x,y)\boldsymbol{N}\right]dS}^{\text{Stretching Energy}}+\overbrace{\frac{1}{2}\int_S\left[\boldsymbol{\kappa}^T\boldsymbol{D}^*(x,y)\boldsymbol{\kappa}\right]dS}^{\text{Bending Energy}}\\ &-\frac{1}{2}\int_S\left[(\boldsymbol{N}^{th})^T\boldsymbol{A}^*(x,y)\boldsymbol{N}^{th}\right]dS-\int_S\left[(\boldsymbol{N}^{th})^T\boldsymbol{B}^*(x,y)\boldsymbol{\kappa}\right]dS\\ &-\int_S\left[(\boldsymbol{M}^{th})^T\boldsymbol{I}\boldsymbol{\kappa}\right]dS\,,\end{aligned}\tag{6.8}$$

with

$$\begin{aligned}\boldsymbol{A}^*&:=\boldsymbol{A}^{-1}\\ \boldsymbol{B}^*&:=-\boldsymbol{A}^{-1}\boldsymbol{B}\\ \boldsymbol{D}^*&:=\boldsymbol{D}-\boldsymbol{B}^T\boldsymbol{A}^{-1}\boldsymbol{B}\,,\end{aligned}\tag{6.9}$$

where I is the unit matrix. $\boldsymbol{N}$ and $\boldsymbol{M}$ are the vectors containing the resultant forces and moments respectively. This formulation as shown by Lamacchia et al. [128], clearly reveals the independent contribution of bending and stretching parts of the total strain energy. The minimization of Eq. 6.8 reveals the equilibria in the admissible space of in-plane and out-of-plane displacement.

6.3.3 *Calculation of the membrane energy*

Compatibility of a shallow shell relates the in-plane strains and the curvatures [37, 142].

$$\mathcal{L}_A(\varepsilon)=\frac{\partial^2\varepsilon_{yy}}{\partial x^2}+\frac{\partial^2\varepsilon_{xx}}{\partial y^2}-\frac{\partial^2\varepsilon_{xy}}{\partial x\partial y}=\det\kappa=\kappa_{xx}\kappa_{yy}-\kappa_{xy}^2/4\,,\tag{6.10}$$

where $\det \kappa$ denotes the Gaussian curvature. Note that the plate studied in this work is initially flat and therefore the value of initial curvature is considered to be zero. The in-plane equilibirum equation can be written as:

$$\operatorname{div} \boldsymbol{N} = 0 \quad \text{on } S, \qquad \boldsymbol{N}.\boldsymbol{n} = 0 \quad \text{on } \partial S\,, \tag{6.11}$$

where $\boldsymbol{n}$ refers to the normal of the plate and ∂S refers to its boundary. By combining both the compatibility Eq. 6.10 and the in-plane equilibrium Eq. 6.11, the in-plane forces can be expressed in terms of the curvatures, without the need to introduce separate polynomial functions for the membrane problem. From the semi-constitutive relation in Eq. 6.7, the in-plane strains can be written in terms of stresses and curvatures as:

$$\mathcal{L}_A(\boldsymbol{A}^*\boldsymbol{N}) = \det \boldsymbol{\kappa} - \mathcal{L}_A\left(\boldsymbol{A}^*\boldsymbol{N}^{th} + \boldsymbol{B}^*\boldsymbol{\kappa}\right) := f \quad \text{on } S\,, \tag{6.12}$$

where the term $\mathcal{L}_A(\boldsymbol{A}^*\boldsymbol{N}^{th} + \boldsymbol{B}^*\boldsymbol{\kappa})$ is non-zero for VS laminates.

It is important therefore to solve the set of differential equations accurately, with a good estimation of the in-plane forces. The importance of reducing the degrees of freedom by solving the membrane problem only once, was previously shown by Vidoli [213] and Lamacchia et al. [128]. The membrane problem can be solved by applying DQM to Eq. 6.11 and Eq. 6.12, where the individual terms are converted into DQM matrices of weighting coefficients, which are solved over a Chebyshev-Gauss-Lobatto mesh grid. It is non-uniform grid. As discussed in the review paper of Bert and Malik [24], DQM solutions deliver more accurate results with non-uniform grid space.

6.4 Non-dimensional formulation

6.4.1 *Scaling of strain and curvature components*

To minimise the ill-conditioning of the nonlinear model, a non-dimensionalisation procedure is performed, with $(\tilde{\ })$ representing the non-dimensionalised form. In this section, all the components are defined in the dimensionless form. The coordinate axis is defined as $x = L_x\tilde{x}$ and $y = L_y\tilde{y}$ and therefore the displacement vectors are:

$$u = U_d\tilde{u}, v = V_d\tilde{v}, w = W_d\tilde{w}\,. \tag{6.13}$$

Further, the strain components can therefore be written in dimensionless quantities as:

$$\varepsilon = \boldsymbol{E}\tilde{\varepsilon}, \boldsymbol{\kappa} = \boldsymbol{K}\tilde{\boldsymbol{\kappa}}\,, \tag{6.14}$$

where:

- $2L_x$ and $2L_y$ are the side lengths of the plate along the Cartesian axes,

- U_d, V_d, W_d are defined as [128, 168] :

$$
\begin{aligned}
U_d &= \frac{1}{L_x}\sqrt{A_{11}^* A_{22}^* D_{11}^* D_{22}^*} \\
V_d &= \frac{1}{L_y}\sqrt{A_{11}^* A_{22}^* D_{11}^* D_{22}^*} \\
W_d &= \sqrt[4]{A_{11}^* A_{22}^* D_{11}^* D_{22}^*}
\end{aligned}
\tag{6.15}
$$

- The in-plane strains and curvatures can be scaled using **E** and **K**, as given below:

$$
\begin{aligned}
E_{xx} &= \frac{1}{2}\frac{W_d^2}{L_x^2}, E_{yy} = \frac{1}{2}\frac{W_d^2}{L_y^2}, E_{xy} = \frac{W_d^2}{L_x L_y} \\
K_{xx} &= -\frac{W_d}{L_x^2}, K_{yy} = -\frac{W_d}{L_y^2}, K_{xy} = -2\frac{W_d}{L_x L_y}
\end{aligned}
\tag{6.16}
$$

The thermal forces and the moments can be scaled as: $\boldsymbol{N}^{th} = \tilde{\boldsymbol{N}}^{th}\tilde{\tau}$ and $\boldsymbol{M}^{th} = \tilde{\boldsymbol{M}}^{th}\tilde{\tau}$. Here, $\tilde{\tau}$ is defined as:

$$
T - T_{ref} = \Delta T_0 \tilde{\tau}\,,
\tag{6.17}
$$

where T to the current temperature, T_{ref} is the curing temperature and ΔT_0 is the difference between curing and room temperature. The thermal force resultants $\tilde{\boldsymbol{N}}^{th}$ and the moment results $\tilde{\boldsymbol{M}}^{th}$ can be written as:

$$
\begin{aligned}
\tilde{\boldsymbol{N}}^{th} &= \sum_{k=1}^{n_{ply}} \int_{z_k}^{z_{k+1}} \boldsymbol{Q}_k\left(x,y\right)\boldsymbol{\alpha}_k\left(x,y\right)\Delta T dz \\
\tilde{\boldsymbol{M}}^{th} &= \sum_{k=1}^{n_{ply}} \int_{z_k}^{z_{k+1}} \boldsymbol{Q}_k\left(x,y\right)\boldsymbol{\alpha}_k\left(x,y\right)\Delta T z dz\,.
\end{aligned}
\tag{6.18}
$$

$\boldsymbol{Q}_k$ refers to the reduced stiffness matrix whereas $\boldsymbol{\alpha}_k$ corresponds to the coefficient of thermal expansion transformed in the laminate coordinate for the k^{th} layer.

Legendre polynomials are used to describe the out-of-plane displacements w, from which the curvature fields are calculated. The following definition of w is used:

$$
\tilde{w}(x,y) = \sum_{i=0}^{n}\sum_{j=0}^{n} q_{ij} P_i(x) Q_j(y)\,,
\tag{6.19}
$$

The terms $P_i(x)$ and $Q_j(y)$ are defined as:

$$\begin{aligned} P_i(x) &= \sum_{k=0}^{l} \binom{l}{k} \binom{-l-1}{k} \left(\frac{1-x}{2}\right)^k , \\ Q_j(y) &= \sum_{k=0}^{l} \binom{l}{k} \binom{-l-1}{k} \left(\frac{1-y}{2}\right)^k . \end{aligned} \tag{6.20}$$

For a $2n$-order polynomial, there are $(n+1)^2$ different combinations of shape functions $P_i(x)Q_j(y)$ multiplied with q_{ij} unknown parameters. With this approximation of the out-of-plane displacement $\tilde{w}$, the membrane problem is re-written in dimensionless form, where the in-plane stresses resultants can be expressed in terms of the unknown coefficients q_{ij} defining $\tilde{w}$.

6.4.2 *Calculation of non-dimensional strain energy*

The compatibility equation in the non-dimensional form reads as:

$$\frac{1}{2}\frac{\partial^2 \tilde{\varepsilon}_{yy}}{\partial \tilde{x}^2} + \frac{1}{2}\frac{\partial^2 \tilde{\varepsilon}_{xx}}{\partial \tilde{y}^2} - \frac{\partial^2 \tilde{\varepsilon}_{xy}}{\partial \tilde{x}\partial \tilde{y}} = \det \tilde{\kappa} = \tilde{\kappa}_{xx}\tilde{\kappa}_{yy} - \tilde{\kappa}_{xy}^2 . \tag{6.21}$$

Introducing the operator $\tilde{\mathcal{L}}_A$ which is defined as:

$$\tilde{\mathcal{L}}_A = \left[\frac{1}{2}\frac{\partial^2}{\partial \tilde{y}^2}, \frac{1}{2}\frac{\partial^2}{\partial \tilde{x}^2}, -\frac{\partial^2}{\partial \tilde{x}\partial \tilde{y}} \right] , \tag{6.22}$$

Eq. 6.12 can be written in the dimensionless form as:

$$\tilde{\mathcal{L}}_{\mathcal{A}}(\tilde{\boldsymbol{N}}) = \tilde{\kappa}_{xx}\tilde{\kappa}_{yy} - \tilde{\kappa}_{xy}^2 - \tilde{\mathcal{L}}_{\mathcal{A}}(\boldsymbol{E}^{-1}\boldsymbol{A}^{-1}\tilde{\boldsymbol{N}}^{th}\tilde{\tau}) + \tilde{\mathcal{L}}_{\mathcal{A}}(\tilde{\boldsymbol{B}}^{*}\tilde{\boldsymbol{\kappa}}) := \tilde{f} . \tag{6.23}$$

The in-plane equilibrium equations can be written as:

$$\begin{aligned} \left(\frac{1}{L_x}\tilde{\mathcal{L}}_B(\boldsymbol{A}\boldsymbol{E}\tilde{\boldsymbol{N}}) + \frac{1}{L_y}\tilde{\mathcal{L}}_C(\boldsymbol{A}\boldsymbol{E}\tilde{\boldsymbol{N}}) \right) &= 0 \quad \text{on } \tilde{S} \in [-1,1] \\ \tilde{\boldsymbol{N}}.\boldsymbol{n} &= 0 \quad \text{on } \partial\tilde{S} , \end{aligned} \tag{6.24}$$

where $\tilde{\mathcal{L}}_B$ and $\tilde{\mathcal{L}}_C$ are defined as:

$$\tilde{\mathcal{L}}_B = \begin{bmatrix} \frac{\partial}{\partial \tilde{x}} & 0 & 0 \\ 0 & 0 & \frac{\partial}{\partial \tilde{y}} \end{bmatrix} , \qquad \tilde{\mathcal{L}}_C = \begin{bmatrix} 0 & 0 & \frac{\partial}{\partial \tilde{y}} \\ 0 & \frac{\partial}{\partial \tilde{y}} & 0. \end{bmatrix} \tag{6.25}$$

From Eq. 6.23 and Eq. 6.24, it is possible to write the in-plane stress resultant $\tilde{N}$ in terms of the curvatures $\tilde{\kappa}$ at each point of the DQM grid. Consequently, the strain energy in its non-dimensional form is:

$$\tilde{\Pi} = \int_{-1}^{1}\int_{-1}^{1}\left(\frac{1}{2}\tilde{\boldsymbol{N}}^T\tilde{\boldsymbol{A}}^*\tilde{\boldsymbol{N}} + \frac{1}{2}\tilde{\boldsymbol{\kappa}}^T\tilde{\boldsymbol{D}}^*\tilde{\boldsymbol{\kappa}} - \frac{1}{2}\tilde{\tau}\tilde{\boldsymbol{A}}^{th}\tilde{\tau} - \tilde{\tau}\tilde{\boldsymbol{B}}^{th}\tilde{\boldsymbol{\kappa}} - \tilde{\tau}\tilde{\boldsymbol{D}}^{th}\tilde{\boldsymbol{\kappa}}\right) d\tilde{x}d\tilde{y}\,, \tag{6.26}$$

where the non-dimensional material parameters are defined as:

$$\begin{aligned}
\tilde{\boldsymbol{A}}^* &= \frac{L_xL_y}{\Pi_d}\boldsymbol{E}^T\boldsymbol{A}^*\boldsymbol{E}, \quad \tilde{\boldsymbol{B}}^* = \boldsymbol{E}^{-1}\boldsymbol{A}^{-1}\boldsymbol{B}\boldsymbol{K}, \quad \tilde{\boldsymbol{D}}^* = \frac{L_xL_y}{\Pi_d}\boldsymbol{K}^T\tilde{\boldsymbol{D}}\boldsymbol{K} \\
\tilde{\boldsymbol{A}}^{th} &= \frac{L_xL_y}{\Pi_d}\left(\tilde{\boldsymbol{N}}^{th}\right)^T\boldsymbol{A}^*\tilde{\boldsymbol{N}}^{th}, \quad \tilde{\boldsymbol{B}}^{th} = \frac{L_xL_y}{\Pi_d}\left(\tilde{\boldsymbol{N}}^{th}\right)^T\boldsymbol{B}^*\boldsymbol{K}, \\
\tilde{\boldsymbol{D}}^{th} &= \frac{L_xL_y}{\Pi_d}\left(\tilde{\boldsymbol{M}}^{th}\right)^T\boldsymbol{K}\,,
\end{aligned} \tag{6.27}$$

and

$$\Pi_d = \mathrm{tr}\left(\begin{bmatrix}\mathbf{E} & \mathbf{0}\\ \mathbf{0} & \mathbf{K}\end{bmatrix}\begin{bmatrix}\mathbf{A} & \mathbf{B}\\ \mathbf{B} & \mathbf{D}\end{bmatrix}\begin{bmatrix}\mathbf{E} & \mathbf{0}\\ \mathbf{0} & \mathbf{K}\end{bmatrix}\right) \tag{6.28}$$

is a parameter used to scale the total strain energy ([168]).

6.4.3 *Calculation of energy due to external force component*

In Chapter 5, we have described the inclusion of external force in the total energy. Following the same approach, the contribution of the external forces are added in the virtual work equation as:

$$\delta\tilde{V} = \tilde{F}_z.\delta\tilde{w}\,, \tag{6.29}$$

where $\tilde{F}_z$ is the non-dimensionalized external force applied at the corners of the bistable plate. As the assumed out-of-plane displacement function satisfies the clamped center point. This boundary condition is preserved even when the snap-through process is modeled. Therefore, the loads are applied at the corners and not at the center. The principle of virtual work is written in non-dimensional form as:

$$\delta\tilde{W}_T = \delta\tilde{\Pi} - \delta\tilde{V} = 0\,, \tag{6.30}$$

where $\delta\tilde{W}_T$ is the scaled total virtual work, $\delta\tilde{\Pi}$ is the first variation of the scaled strain energy and $\delta\tilde{V}$ refers to the scaled work done by the applied forces.

The unknowns of the displacement field can be easily found using the Rayleigh-Ritz method. At $\delta\tilde{W}_T = 0$, the minimization of the total energy gives the stable equilibrium shapes.

$$\frac{\partial\tilde{W}_T(q_{ij})}{\partial q_{ij}} = 0\,. \tag{6.31}$$

This results in a highly nonlinear system of equations (Eq. (6.31)) which are solved using the Newton-Raphson method. Finally, the stability of the computed equilibrium (stable or unstable) is evaluated by means of the construction of the Hessian **H**, which reads:

$$\mathbf{H} = \frac{\partial^2 \tilde{W}_T}{\partial q_{ij} \partial q_{kl}}, \; i,j,k,l = 0, ..., n \tag{6.32}$$

where n is the order of the Legendre polynomial. The value of the applied force is gradually increased until a single solution is found. This is the point where the plate snaps from one stable shape to another. An equilibrium configuration is stable, if and only if the corresponding Hessian matrix (Eq. (6.32)) is positive definite.

6.5 DQM formulation of the in-plane equilibrium and compatibility conditions

To solve the system of differential equations resulting from the compatibility equation and in-plane equilibrium equations, the Differential Quadrature Method (DQM) [198] is applied in this work. The partial derivatives of a function $g(x, y)$ in matrix form can be written as, as described in Chapter 3:

$$\begin{aligned} \frac{\partial g}{\partial x} &= P_x g, \quad \frac{\partial g}{\partial y} = g P_y^T, \quad \frac{\partial^2 g}{\partial x \partial y} = P_x g P_y^T \\ \frac{\partial^2 g}{\partial^2 x} &= Q_x g, \quad \frac{\partial^2 g}{\partial^2 y} = g Q_y^T, \quad \frac{\partial^4 g}{\partial^2 x \partial^2 y} = Q_x g Q_y^T, \end{aligned} \tag{6.33}$$

where P, Q are the DQM coefficients for the first- and second-order partial derivatives with respect to x and y.

The right hand side of Eq. 6.23 can be written in the expanded form as:

$$\begin{aligned} \tilde{f} = \tilde{\kappa}_{xx}\tilde{\kappa}_{yy} - \tilde{\kappa}_{xy}^2 + \frac{1}{2}\Big(&\tilde{B}_{11}^*\tilde{\kappa}_{xx,yy} + \tilde{B}_{12}^*\tilde{\kappa}_{yy,yy} + \tilde{B}_{13}^*\tilde{\kappa}_{xy,yy} + \tilde{\kappa}_{xx}\tilde{B}_{11,yy}^* + \tilde{\kappa}_{yy}\tilde{B}_{12,yy}^* \\ &+ \tilde{\kappa}_{xy}\tilde{B}_{13,yy}^* + \tilde{B}_{21}^*\tilde{\kappa}_{xx,xx} + \tilde{B}_{22}^*\tilde{\kappa}_{yy,xx} + \tilde{B}_{23}^*\tilde{\kappa}_{xy,xx} + \tilde{\kappa}_{xx}\tilde{B}_{21,xx}^* + \tilde{\kappa}_{yy}\tilde{B}_{22,xx}^* \\ &+ \tilde{\kappa}_{xy}\tilde{B}_{23,xx}^*) - \Big(\tilde{B}_{31}^*\tilde{\kappa}_{xx,xy} + \tilde{B}_{32}^*\tilde{\kappa}_{yy,xy} + \tilde{B}_{33}^*\tilde{\kappa}_{xy,xy} + \tilde{\kappa}_{xx}\tilde{B}_{31,xy}^* + \tilde{\kappa}_{yy}\tilde{B}_{32,xy}^* \\ &+ \tilde{\kappa}_{xy}\tilde{B}_{33,xy}^*\Big) + \Big(\tilde{B}_{11,y}^*\tilde{\kappa}_{xx,y} + \tilde{B}_{12,y}^*\tilde{\kappa}_{yy,y} + \tilde{B}_{13,y}^*\tilde{\kappa}_{xy,y} + \tilde{B}_{21,x}^*\tilde{\kappa}_{xx,x} + \tilde{B}_{22,x}^*\tilde{\kappa}_{yy,x} \\ &+ \tilde{B}_{23,x}^*\tilde{\kappa}_{xy,x} - \tilde{B}_{31,x}^*\tilde{\kappa}_{xx,y} - \tilde{B}_{32,x}^*\tilde{\kappa}_{yy,y} - \tilde{B}_{33,x}^*\tilde{\kappa}_{xy,y} - \tilde{B}_{31,y}^*\tilde{\kappa}_{xx,x} - \tilde{B}_{32,y}^*\tilde{\kappa}_{yy,x} \end{aligned}$$

$$\begin{aligned}
&- \tilde{B}^{*}_{33,y}\tilde{\kappa}_{xy,x}\Big) - \frac{1}{2}\Big(\Gamma_{11}\tilde{N}^{th}_{xx,yy} + \Gamma_{12}\tilde{N}^{th}_{yy,yy} + \Gamma_{13}\tilde{N}^{th}_{xy,yy} + \tilde{N}^{th}_{xx}\Gamma_{11,yy} + \tilde{N}^{th}_{yy}\Gamma_{12,yy} \\
&+ \tilde{N}^{th}_{xy}\Gamma_{13,yy} + \Gamma_{21}\tilde{N}^{th}_{xx,xx} + \Gamma_{22}\tilde{N}^{th}_{yy,xx} + \Gamma_{23}\tilde{N}^{th}_{xy,xx} + \tilde{N}^{th}_{xx}\Gamma_{21,xx} + \tilde{N}^{th}_{yy}\Gamma_{22,xx} \\
&+ \tilde{N}^{th}_{xy}\Gamma_{23,xx}\Big) + \Big(\Gamma_{31}\tilde{N}^{th}_{xx,xy} + \Gamma_{32}\tilde{N}^{th}_{yy,xy} + \Gamma_{33}\tilde{N}^{th}_{xy,xy} + \tilde{N}^{th}_{xx}\Gamma_{31,xy} + \tilde{N}^{th}_{yy}\Gamma_{32,xy} \\
&+ \tilde{N}^{th}_{xy}\Gamma_{33,xy}\Big) - \Big(\Gamma_{11,y}\tilde{N}^{th}_{xx,y} + \Gamma_{12,y}\tilde{N}^{th}_{yy,y} + \Gamma_{13,y}\tilde{N}^{th}_{xy,y} + \Gamma_{21,x}\tilde{N}^{th}_{xx,x} + \Gamma_{22,x}\tilde{N}^{th}_{yy,x} \\
&+ \Gamma_{23,x}\tilde{N}^{th}_{xy,x} - \Gamma_{31,x}\tilde{N}^{th}_{xx,y} - \Gamma_{32,x}\tilde{N}^{th}_{yy,y} - \Gamma_{33,x}\tilde{N}^{th}_{xy,y} - \Gamma_{31,y}\tilde{N}^{th}_{xx,x} - \Gamma_{32,y}\tilde{N}^{th}_{yy,x} \\
&- \Gamma_{33,y}\tilde{N}^{th}_{xy,x}\Big),
\end{aligned} \tag{6.34}$$

where $\mathbf{\Gamma} = (\boldsymbol{AE})^{-1}$.

Eq. 6.34 is a fourth-order elliptic partial differential equation in terms of the out-of-plane displacement w, which is expressed in terms of the curvatures. It also represents the additional terms arising in case of VS laminates. Eq. 6.34 involves terms containing multiples of the unknown coefficient q_{ij} that are expensive to handle analytically. To increase the computational efficiency, especially for higher order polynomials, a strategy is applied to separate the unknown coefficients from the rest of the expression in Eq. 6.34. The curvatures $\tilde{\kappa}_{xx}$, $\tilde{\kappa}_{yy}$ and $\tilde{\kappa}_{xy}$ can be rearranged in the form:

$$\tilde{\kappa}_{xx} = \mathbb{K}_{x}q, \tilde{\kappa}_{yy} = \mathbb{K}_{y}q, \tilde{\kappa}_{xy} = \mathbb{K}_{xy}q \tag{6.35}$$

Here, $\mathbb{K}_x$,$\mathbb{K}_y$ and $\mathbb{K}_{xy}$ are the vectorized form of matrices containing the coefficients of q_{ij} for $\tilde{\kappa}_{xx}$, $\tilde{\kappa}_{yy}$ and $\tilde{\kappa}_{xy}$ at each DQM grid point. The vector q refers to the vector containing the parameters q_{ij} as defined in Eq. 6.20 . By the definition of the curvatures presented in Eq. 6.35, it is possible to easily separate the unknown terms q_{ij} from its constant coefficient, and therefore avoid involving calculations with unknowns, which ultimately, increases the computationally efficiency.

On the basis of the combination of the unknown coefficients q_{ij}, $\tilde{f}$ can be separated in the following way:

$$\tilde{f} = \mathbf{F_1}q \otimes q + \mathbf{F_2}q + \mathbf{F_3}\,, \tag{6.36}$$

where $\otimes$ is the Kronecker delta product. Such separation of the variable combination can allow one to avoid symbolic calculations and lead to much faster computations. To systemically depict Eq. 6.34 in DQM representation, vectorization is performed on all the matrix components. If $\boldsymbol{A}$, $\boldsymbol{B}$, $\boldsymbol{X}$ and $\boldsymbol{C}$ are the given matrices, the equation $\boldsymbol{AXB} = \boldsymbol{C}$ can be written as $\left(\boldsymbol{B}^{T} \otimes \boldsymbol{A}\right) X = C$. To convert $\mathbf{F_1}$, $\mathbf{F_2}$ and $\mathbf{F_3}$ into the vectorized form, the Kronecker and the Hadamard products are applied to Eq. 6.34, and can be rearrranged in the form of Eq. 6.36. The definition of Kronecker Delta product and the Hadamard product can be found in Appendix A. The term $\mathbf{F_1}$ can be written as:

$$\mathbf{F_1} = (\mathbb{K}_x \otimes \mathbb{K}_y - \mathbb{K}_{xy} \otimes \mathbb{K}_{xy}). \tag{6.37}$$

The above equation can be derived by rearraging the terms of Eq. 6.34 and writing it in the form of Eq. 6.36.

The terms $\mathbf{F_2}$ can be written in the vectorized form as:

$$\begin{aligned}
\mathbf{F_2} = \frac{1}{2} \Big(& \left(\vec{B}^*_{11} \otimes \vec{J}\right) \circ \left(I_y \otimes Q_y\right) \mathbb{K}_x + \left(\vec{B}^*_{12} \otimes \vec{J}\right) \circ \left(I_y \otimes Q_y\right) \mathbb{K}_y \\
+ & \left(\vec{B}^*_{13} \otimes \vec{J}\right) \circ \left(I_y \otimes Q_y\right) \mathbb{K}_{xy} + \left(\vec{B}^*_{11,yy} \otimes \vec{J}\right) \circ \left(I_y \otimes \mathbb{K}_x\right) \\
+ & \left(\vec{B}^*_{12,yy} \otimes \vec{J}\right) \circ \left(I_y \otimes \mathbb{K}_y\right) + \left(\vec{B}^*_{13,yy} \otimes \vec{J}\right) \circ \left(I_y \otimes \mathbb{K}_{xy}\right) \\
+ & \left(\vec{B}^*_{21} \otimes \vec{J}\right) \circ \left(Q_x \otimes I_x\right) \mathbb{K}_x + \left(\vec{B}^*_{22} \otimes \vec{J}\right) \circ \left(Q_x \otimes I_x\right) \mathbb{K}_y \\
+ & \left(\vec{B}^*_{23} \otimes \vec{J}\right) \circ \left(Q_x \otimes I_x\right) \mathbb{K}_{xy} + \left(\vec{B}^*_{21,xx} \otimes \vec{J}\right) \circ \left(\mathbb{K}_x \otimes I_x\right) \\
+ & \left(\vec{B}^*_{22,xx} \otimes \vec{J}\right) \circ \left(\mathbb{K}_y \otimes I_x\right) + \left(\vec{B}^*_{23,xx} \otimes \vec{J}\right) \circ \left(\mathbb{K}_{xy} \otimes I_x\right)\Big) \\
+ \Big(& \left(\vec{B}^*_{11,y} \otimes \vec{J}\right) \circ \left(I_y \otimes P_y\right) \mathbb{K}_x + \left(\vec{B}^*_{12,y} \otimes \vec{J}\right) \circ \left(I_y \otimes P_y\right) \mathbb{K}_y \\
+ & \left(\vec{B}^*_{13,y} \otimes \vec{J}\right) \circ \left(I_y \otimes P_y\right) \mathbb{K}_{xy} + \left(\vec{B}^*_{21,x} \otimes \vec{J}\right) \circ \left(I_y \otimes P_x\right) \mathbb{K}_x \\
+ & \left(\vec{B}^*_{22,x} \otimes \vec{J}\right) \circ \left(I_y \otimes P_x\right) \mathbb{K}_y + \left(\vec{B}^*_{23,x} \otimes \vec{J}\right) \circ \left(I_y \otimes P_x\right) \mathbb{K}_{xy}\Big) \\
- \Big(& \left(\vec{B}^*_{31} \otimes \vec{J}\right) \circ \left(P_x \otimes P_y\right) \mathbb{K}_x + \left(\vec{B}^*_{32} \otimes \vec{J}\right) \circ \left(P_x \otimes P_y\right) \mathbb{K}_y \\
+ & \left(\vec{B}^*_{33} \otimes \vec{J}\right) \circ \left(P_x \otimes P_y\right) \mathbb{K}_{xy} + \left(\vec{B}^*_{31,xy} \otimes \vec{J}\right) \circ \left(K_x \otimes I_x\right) \\
+ & \left(\vec{B}^*_{32,xy} \otimes \vec{J}\right) \circ \left(\mathbb{K}_y \otimes I_x\right) + \left(\vec{B}^*_{33,xy} \otimes \vec{J}\right) \circ \left(K_{xy} \otimes I_x\right) \\
+ & \left(\vec{B}^*_{31,x} \otimes \vec{J}\right) \circ \left(I_y \otimes P_y\right) \mathbb{K}_x + \left(\vec{B}^*_{32,x} \otimes \vec{J}\right) \circ \left(I_y \otimes P_y\right) \mathbb{K}_y \\
+ & \left(\vec{B}^*_{33,x} \otimes \vec{J}\right) \circ \left(I_y \otimes P_y\right) \mathbb{K}_{xy} + \left(\vec{B}^*_{31,y} \otimes \vec{J}\right) \circ \left(I_y \otimes P_x\right) \mathbb{K}_x \\
+ & \left(\vec{B}^*_{32,y} \otimes \vec{J}\right) \circ \left(I_y \otimes P_x\right) \mathbb{K}_y + \left(\vec{B}^*_{33,y} \otimes \vec{J}\right) \circ \left(I_y \otimes P_x\right) \mathbb{K}_{xy}\Big) \ ,
\end{aligned} \tag{6.38}$$

where $\circ$ is the Hadamard product. The vector $\vec{B}^*_{ij}$ is generated by stacking the components of $\tilde{B}^*$ over the grid points of the two-dimensional domain in a column-wise manner. $\vec{J}$ refers to a row vector defined as: $[1, 1, ..., 1]_{1 \times ng}$, where $ng = ng_x \times ng_y$ representing the total number of grid points. I_x and I_y are identity matrices whose sizes depend on the number of grid points in x and y direction, respectively.

The $\mathbf{F_3}$ matrix does not contain any terms of unknown coefficient q_{ij}, and therefore no vectorization is required.

$$\begin{aligned}\mathbf{F_3} = & -\frac{1}{2}\Big(\Gamma_{11}\tilde{N}^{th}_{xx,yy} + \Gamma_{12}\tilde{N}^{th}_{yy,yy} + \Gamma_{13}\tilde{N}^{th}_{xy,yy} + \tilde{N}^{th}_{xx}\Gamma_{11,yy} + \tilde{N}^{th}_{yy}\Gamma_{12,yy} \\ & + \tilde{N}^{th}_{xy}\Gamma_{13,yy} + \Gamma_{21}\tilde{N}^{th}_{xx,xx}\Gamma_{22}\tilde{N}^{th}_{yy,xx} + \Gamma_{23}\tilde{N}^{th}_{xy,xx} + \tilde{N}^{th}_{xx}\Gamma_{21,xx} + \tilde{N}^{th}_{yy}\Gamma_{22,xx} \\ & + \tilde{N}^{th}_{xy}\Gamma_{23,xx}\Big) + \Big(\Gamma_{31}\tilde{N}^{th}_{xx,xy} + \Gamma_{32}\tilde{N}^{th}_{yy,xy} + \Gamma_{33}\tilde{N}^{th}_{xy,xy} + \tilde{N}^{th}_{xx}\Gamma_{31,xy} \\ & + \tilde{N}^{th}_{yy}\Gamma_{32,xy} + \tilde{N}^{th}_{xy}\Gamma_{33,xy}\Big) - \Big(\Gamma_{11,y}\tilde{N}^{th}_{xx,y} + \Gamma_{12,y}\tilde{N}^{th}_{yy,y} + \Gamma_{13,y}\tilde{N}^{th}_{xy,y} \\ & + \Gamma_{21,x}\tilde{N}^{th}_{xx,x} + \Gamma_{22,x}\tilde{N}^{th}_{yy,x} + \Gamma_{23,x}\tilde{N}^{th}_{xy,x} - \Gamma_{31,x}\tilde{N}^{th}_{xx,y} - \Gamma_{32,x}\tilde{N}^{th}_{yy,y} \\ & - \Gamma_{33,x}\tilde{N}^{th}_{xy,y} - \Gamma_{31,y}\tilde{N}^{th}_{xx,x} - \Gamma_{32,y}\tilde{N}^{th}_{yy,x} - \Gamma_{33,y}\tilde{N}^{th}_{xy,x}\Big)\ ,\end{aligned} \tag{6.39}$$

From Eq. 6.23, the force vector can also be expressed as:

$$\tilde{N} = \tilde{\mathcal{L}}_{\mathcal{A}}^{-1}\tilde{f} = \quad \widetilde{\mathbf{N}}_{\mathbf{1}} q \otimes q + \widetilde{\mathbf{N}}_{\mathbf{2}} q + \widetilde{\mathbf{N}}_{\mathbf{3}} \tag{6.40}$$

where the introduced coefficient matrices corresponds to:

$$\widetilde{\mathbf{N}}_{\mathbf{1}} = \tilde{\mathcal{L}}_{\mathcal{A}}^{-1}\left(\mathbf{F_1}\right), \quad \widetilde{\mathbf{N}}_{\mathbf{2}} = \tilde{\mathcal{L}}_{\mathcal{A}}^{-1}\left(\mathbf{F_2}\right), \quad \widetilde{\mathbf{N}}_{\mathbf{3}} \quad = \tilde{\mathcal{L}}_{\mathcal{A}}^{-1}\left(\mathbf{F_3}\right) \tag{6.41}$$

Calculation of Membrane Energy

The calculated in-plane forces from Eq. 6.40 can be substituted back into Eq. 6.26 to calculate the total potential energy. The membrane energy part can be written as:

$$\tilde{\Pi}_{mem} = \int_{-1}^{1}\int_{-1}^{1}\frac{1}{2}\tilde{\boldsymbol{N}}^T\tilde{\boldsymbol{A}}^*\tilde{\boldsymbol{N}}d\tilde{x}d\tilde{y}. \tag{6.42}$$

Similar to the differential form, all integration operations on a set of discrete points can be replaced by a matrix multiplication operation. The approach explained by White et al. [216] is adopted in this work to solve the integrals involved in Eq. 6.42.

In a concise manner, Eq. 6.42 can be written as:

$$\tilde{\Pi}_{mem} = \mathbf{P}q \otimes q \otimes q \otimes q + \mathbf{Q}q \otimes (q \otimes q) + Rq \otimes q + \mathbf{S}q + \mathbf{T}. \tag{6.43}$$

Here the coefficients $\mathbf{P}$,$\mathbf{Q}$,$\mathbf{R}$, $\mathbf{S}$ and $\mathbf{T}$ can be correspondingly found from substituting Eq. 6.40 in Eq. 6.42. The derived terms of $\mathbf{P}$,$\mathbf{Q}$,$\mathbf{R}$,$\mathbf{S}$ can be found in Appendix B. They can be rearranged and written in terms of the components of the $\tilde{\boldsymbol{A}}^*$ matrix and $\widetilde{\mathbf{N}}_{\mathbf{1}}$, $\widetilde{\mathbf{N}}_{\mathbf{2}}$ and $\widetilde{\mathbf{N}}_{\mathbf{3}}$. The other component of the total strain energy, namely, the bending energy and the energy due to thermal loads can be calculated in a straight-forward manner using Eq. 6.26.

6.6 Semi-analytical results

In this section, a square laminate with a length L equal to 200 mm, with four layers each of 0.131mm-thick plies of graphite-epoxy prepreg is studied. The plate is subjected to a temperature difference of $\Delta T = -180^\circ$ from curing temperature to room temperature. The material properties at ply-level are given as:

$$\begin{aligned} E_1 &= 161\,\text{GPa},\ E_2 = 11.38\,\text{GPa},\ G_{12} = 5.17\,\text{GPa} \\ \nu_{12} &= 0.3,\ \alpha_1 = -1.8 \times 10^{-8}/^\circ\text{C},\ \alpha_2 = 3 \times 10^{-5}/^\circ\text{C}. \end{aligned} \tag{6.44}$$

In the semi-analytical approach, the membrane problem is solved using a Chebyshev-Lobatto DQ grid of 29×29 nodes. This size of DQ grid is decided based on a convergence study, finding a balance between sufficient accuracy and computational effort. An increasing order of Legendre polynomials is used to describe the out-of-plane displacements. Similar to Chapter 4 and 5, the investigated VS laminates belong to a family where $\phi = 45^\circ$ and $T_0 + T_1 = 90^\circ$ (Table 6.1).

The work presented by Pirrera et al. [168] is considered as a benchmark for comparison of the results obtained for straight fiber laminates. It was shown previously by Pirrera et al. [168] as well as Diaconu et al. [63] that the snap-through event involves very complex intermediate unstable shapes where higher order polynomial functions are required to capture the snap-through loads accurately. Recently, Groh et al. [79] found further modes near the bifurcation point containing regions of both stable and unstable parts.

In this study, the out-of-plane corner displacement and the snap-through loads are determined using different polynomial orders starting from $n = 2$ to $n = 5$. To verify the semi-analytical model, a nonlinear FE analysis is performed to compare the results using the formulated approach. A total of 96×96 four-node quadrilateral shell elements (S4R) were used in the commercial FE software `ABAQUS`$^{\text{TM}}$ to model the cool-down process. The details of the FE procedure can be found in Chapter 5, Section 5.2.2. It has to be emphasized that the present work, not just concerns on comparing the semi-analytical and FE results, but also focuses on understanding how the snap-through loads vary for different VS laminates. Using a fast and

Type	ϕ	T_0	T_1	Layup
Straight	45	45	45	$[0_2/90_2]_T$
VS-1	45	± 15	± 75	$[45\langle 15\vert 75\rangle_2/45\langle -15\vert -75\rangle_2]_T$
VS-2	45	± 30	± 60	$[45\langle 30\vert 60\rangle_2/45\langle -30\vert -60\rangle_2]_T$
VS-3	45	± 60	± 30	$[45\langle 60\vert 30\rangle_2/45\langle -60\vert -30\rangle_2]_T$
VS-4	45	± 75	± 15	$[45\langle 75\vert 15\rangle_2/45\langle -75\vert -15\rangle_2]_T$

TABLE 6.1: Fiber orientation and layup data for the investigated straight cross-ply and various VS laminates.

relatively accurate tool will help us to gain a better understanding of the snap-through process in VS laminates.

The results can be divided particularly into three parts. Four different VS laminates with increasing value of T_0 are investigated and compared with a straight fiber laminate, $[0_2/90_2]$, which can alternatively be written as $T_0 = T_1 = 45°$ and $\phi = 45°$. The layups of the investigated VS laminates are reported in Table 6.1. In the first part, the corner displacements are reported for the investigated VS laminates and compared with the corresponding FE results. It has also been shown how the accuracy improves with increasing order of Legendre polynomials. In the second part, the in-plane stress resultants solved using DQM are plotted and compared with the corresponding FE results. The load displacement curves are plotted and the snap-through loads are determined for different VS laminates in the third part. Further, a parametric study is conducted where the value of T_0 is incremented by 5°, with T_1 satisfying $T_1 = 90 - T_0$ and $\phi = 45°$. The tailoring capabilities of the VS laminates are discussed by comparing snap-through loads and the corner displacements.

6.6.1 *Determination of out-of-plane displacements*

Table 6.2 shows the initial corner displacement of one of the stable shapes for four different VS laminates. It can be observed that for all cases, the correlation between FE and the analytical results improves as the order of the Legendre polynomials increases. With $n = 5$, the maximum difference between the FE and the analytical results is 4.4% for VS-1, 4.3% for VS-2, 2.9% for VS-3 and 6.9% for VS-4. The corner displacements of the $[0_2/90_2]$ laminate at all the corners are equal. However, only the diagonally opposite sets of corner are equal and the other corners not equal in case of VS laminates.

A detailed comparison of how the stable shapes vary for different VS laminates along the section $x = 0$ is shown in Figure 6.4a. The difference in the results between the analytical and the FE results is plotted in Figure 6.4b. The figure shows a good agreement between FE and the analytical model with $n = 4$, where only at the edges the difference becomes higher. A similar graph is also plotted for the orthogonal section $y = 0$. Some undulations for VS laminates can be found in the profile section $x = 0$. Such undulations in the profile can be due to local differences in the

T_0	T_1	$n = 2$		$n = 3$		$n = 4$		$n = 5$		FE	
		w_1	w_2	w_1	w_2	w_1	w_2	w_1	w_2	w_1	w_2
15	75	0.06034	0.03474	0.05019	0.03849	0.04912	0.03808	0.04944	0.03799	0.04813	0.03639
30	60	0.06700	0.05081	0.06433	0.05200	0.06334	0.05100	0.06319	0.05150	0.06080	0.04937
60	30	0.06631	0.05175	0.06581	0.05211	0.06452	0.05021	0.06450	0.05022	0.06270	0.04950
75	15	0.06156	0.03411	0.05314	0.03858	0.053212	0.03413	0.05315	0.03365	0.04970	0.03200

TABLE 6.2: Corner displacements: w_1 at $x = L_x/2, y = L_y/2$ and w_2 at $x = -L_x/2, y = L_y/2$ in (m) with increasing polynomial order and $n_x = n_y = 29$.

generated residual stresses in the plate due to variation in the material parameters at each point of the plate. However, such profile sections can also affect how the structures snap-through, as observed previously in Chapter 5.

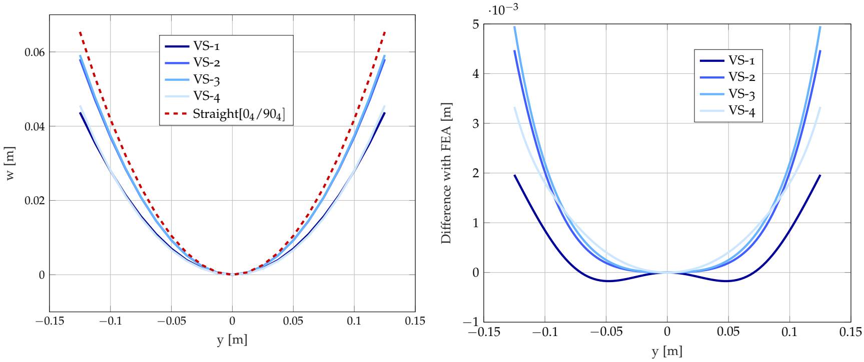

(a)

(b)

FIGURE 6.4: a) Out-of-plane displacement (w) results from the semi-analytical method at the section $x = 0$ and b) its difference with FE results

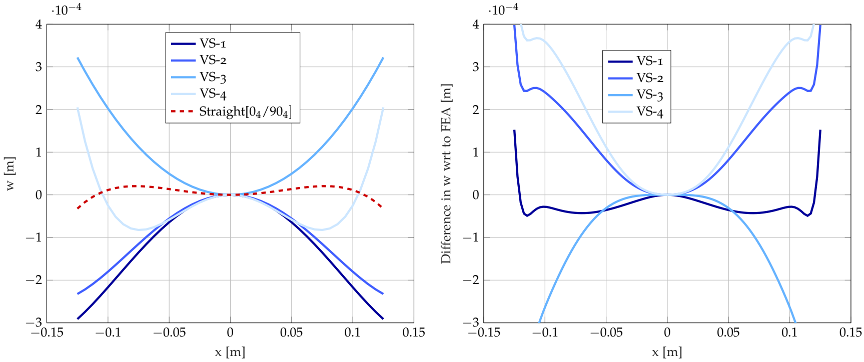

(a)

(b)

FIGURE 6.5: a) Out-of-plane displacement (w) results from the semi-analytical method at the section $y = 0$ and b) its difference with FE results.

6.6.2 *Determination of the in-plane stresses*

In the present formulation, it is important that the in-plane stress resultants are calculated accurately, as this affects directly the membrane energy and consequently, the calculation of the snap-through loads. The in-plane stress resultants calculated from the differential equation resulting from the coupled compatibility and the in-plane equilibrium equations (Eq. 6.12) is found to a have a closed form analytical solution for generic elliptic planform [193]. Hamouche et al. [94] claimed that multiplying the solution from the elliptic planform with a correction factor can provide a sufficiently good estimation of the in-plane stresses and the membrane energy for rectangular shaped plates. The in-plane stress resultants, as described in Section 6.4.2, can be calculated by solving the in-plane equilibrium equations and the compatibility equation, which in our case is solved using the aid of DQM. Figure 6.6 shows the variation of in-plane stress resultants across the plate planform obtained using the formulation described in this paper (left side) and compared with the corresponding FE results (right side) for the VS-3 laminate using a 5^{th} order polynomial. A good correlation is obtained in predicting the in-plane stresses of the laminate. However, due to limited degrees of freedom used in the semi-analytical method, some differences can be observed.

6.6.3 *Calculation of Snap-through loads*

It has been previously reported [51, 63] that assuming constant curvatures in analytical models can lead to high discrepancies in the calculation of snap-through loads. Similar observations are also reported for VS laminates in chapter 5. The snap-through event generally involves intermediate complex shapes and therefore requires a higher-order polynomial function to characterize the shape. In our formulation, solving the membrane problem separately, not only poses the model with fewer number of unknowns as now the in-plane stress resultants can be written in terms of curvatures but also allows correct evaluation of the membrane energy. Table 6.3 shows the prediction of snap-through loads with different polynomial orders and compares the results with a nonlinear FE analysis. It can be noticed that with an increase in the polynomial order, a convergence could be reached. With $n = 5$, a good level accuracy is reached with a difference between FE and analytical results of $4 - 6\%$ for VS laminates.

Figure 8.5 shows the difference in the snap-through loads by plotting the load-displacement curves of the studied VS laminates. It can be observed that with the applied load, the structure deforms elastically featuring linear load-displacement curves. Once the limit point is detected, the structure snaps from one stable shape to another. The snap-through load of the cross-ply laminate $[0_2/90_2]$ compares well with the values reported by Lamacchia et al. [128]. It is clear from the figure that changes in the curvilinear fiber configuration can lead to a difference in the snap-through loads. VS-1 shows the lowest snap-through loads, followed by VS-4, VS-2, and VS-3. The constant cross-ply $[0_2/90_2]$ shows the highest snap-through load.

It is observed that laminate VS-2 has 45% lower snap-through force than the straight cross-ply laminate, with 14% lower out-of-plane displacement. It can therefore be observed that with VS laminates, there can be an immense possibility to

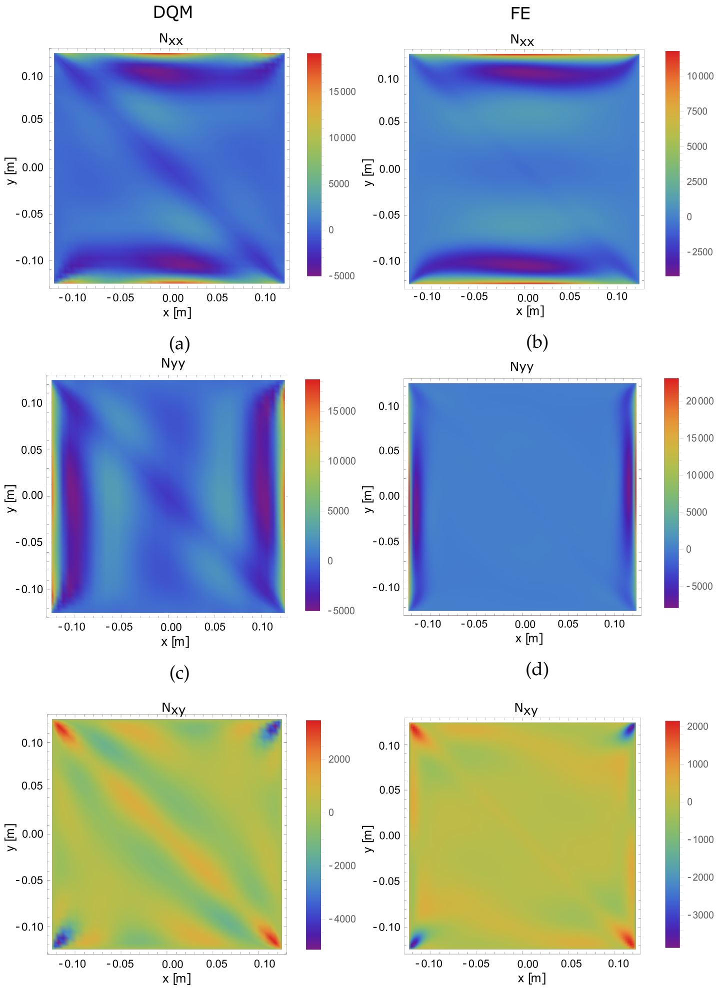

(a) (b)

(c) (d)

(e) (f)

FIGURE 6.6: Comparison of the in-plane stress resultants N_{xx},N_{yy} and N_{xy} ($[N/m]$) between DQM (a,c,e) and FE (b,d,f) for VS-3.

tailor the snap-through loads without much change in the shape of the bistable laminate. Such snap-through tailoring makes VS laminates a promising alternative to be used in efficient morphing systems.

To determine the complete load-displacement curve, a nonlinear finite element analysis was conducted in `ABAQUS`$^{\text{TM}}$ using both static analysis (with stabilization) and the Riks method. The static analysis is equivalent to a force-controlled test.

T_0	T_1	$n = 2$	$n = 3$	$n = 4$	$n = 5$	FE
15	75	1.97	1.91	1.39	1.31	1.23
30	60	3.36	3.24	2.75	2.64	2.46
60	30	6.22	5.56	3.31	3.29	3.17
75	15	4.66	4.20	2.15	1.90	1.79
45	45	4.98	4.32	3.97	3.65	3.35

TABLE 6.3: Snap-through loads–in (N) for different VS laminates with increasing order n of Legendre polynomial function and comparison with FE.

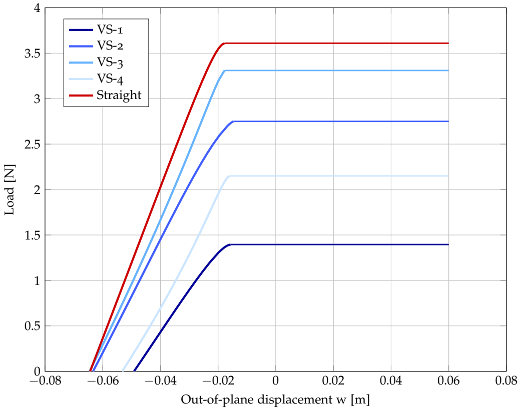

FIGURE 6.7: Load displacement curve from semi-analytical model with 4^{th} order legendre polynomial.

However, additional fictitious viscous forces are added during the stabilization process to damp the instabilities and improve convergence. *The Static- Riks* in general corresponds to the arc-length method. Figure 6.8 shows the load-displacement curve for VS-3 showing *Static-stabilize* in red and "Riks" method in blue. The snap-through forces obtained from both methods compare well with each other. The Riks method shows the complexity of the unstable path attained during the snap-through event. The existence of several unstable equilibria close to each other makes it very difficult to trace the unstable path using the adopted semi-analytical approach. Especially for higher orders, where the convergence of roots becomes more sensitive to each parameter of the Legendre polynomial, it can be time-consuming and difficult to determine the unstable path. However, with a 3^{rd} order Legendre polynomial approximation for the out-of-plane displacement, one of the unstable paths could be traced for VS-1. The load-displacement curve for this laminate is shown in Figure 6.9, where the dotted line represents the unstable path. The figure also shows how the equilibrium shape changes at different steps of the load-displacement curve, starting from a stable configuration and leading to the snap-through event, where unstable shapes are illustrated followed by the second stable shape.

It is also interesting to note that different VS laminates have a different preferential mode of snapping. For example, Figure 6.10a shows the stable equilibrium shape of VS-1 in the initial state and Figure 6.10b shows the shape just before snapping. Similarly, the initial stable shape for VS-4 can be seen in Figure 6.10c and the stable configuration before snapping in Figure 6.10d. Although the initial shapes of VS-1 and VS-4 (Figure. 6.10b and Figure. 6.10c respectively) are similar, both of the laminates snap in different modes. This can be compared with the initial shape and the shape before snapping for the constant stiffness $[0_2/90_2]$ laminate, as illustrated in Figure 6.10e and Figure 6.10f respectively. A distinct difference on how the different VS laminates snap can be observed. Such difference in the snapping mechanism attributes to such difference in the snap-through loads.

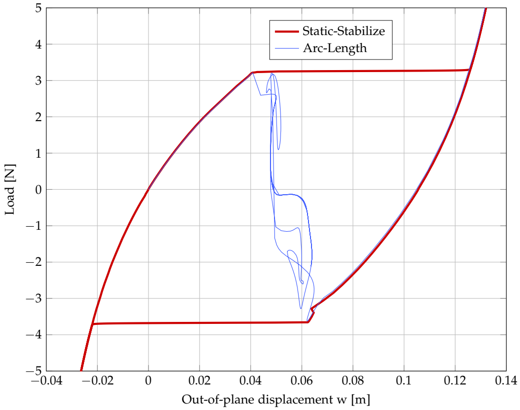

FIGURE 6.8: Load-displacement curve obtained for VS-3 using Finite Elements. The curve in red refers to the curve obtained using load-controlled tests (Static-Stabilize) and the curve in blue refers to the curve from the arc-length method (Static-Riks).

6.7 Parametric study on different VS laminates

As the variable stiffness laminate defined for this work depends on three different parameters ϕ, T_0 and T_1, there can be different possibilities to construct VS laminate layups belonging to the family $\phi = 45^\circ$ and $T_0 + T_1 = 90^\circ$. Therefore, a parametric study is required to understand the effect of the VS angle parameters on the corner displacements and the snap-through loads. The main aim of this investigation is to explore VS fiber configurations that have lower snap-through loads but at the same time give higher corner displacements when compared to constant stiffness unsymmetric cross-ply laminates. The same geometry and material property are

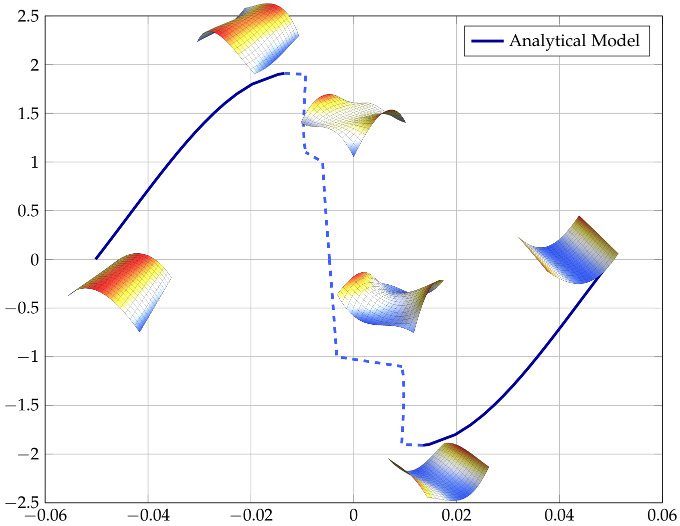

FIGURE 6.9: Analytical load-displacement diagram showing the intermediate unstable path for VS-1 with $n = 3$.

considered as in Section 6.6. It must be noted that for this particular family of VS laminate, $\phi = 45°$ and $T_0 = 90°$ corresponds to the straight fiber laminates $[0_2/90_2]$.

A parametric study is conducted where the value of T_0 is incremented by 5°. It can be observed from Figure. 6.11 that certain VS laminates have lower snap-through loads but a small difference in corner displacement than the $[0_2/90_2]$ laminate. For example, improvement in design of a morphing system can be achieved by using a VS laminate with $T_0 = 65°$, where the snap-through loads are 18.65% lower but with 4.1% difference in maximum corner displacement from the constant stiffness $[0_2/90_2]$ laminate. For certain designs, this could preferable over VS-2 laminate, where there was 45% reduction in snap-through loads, but at the same time, there was 18% reduction in the out-of-plane displacement.

6.8 Conclusions

In this chapter, the concept of VS using curvilinear fiber paths was explored to tailor the snap-through loads of bistable laminates. A robust and computationally efficient formulation was derived, to calculate the snap-through loads of VS laminates. A strategy is proposed to separate the unknown coefficients of the out-of-plane displacement with the known vectorized terms arising from the DQM form of the compatibility and in-plane equilibrium differential equations. This process leads to a computationally efficient scheme to determine the snap-through loads. A

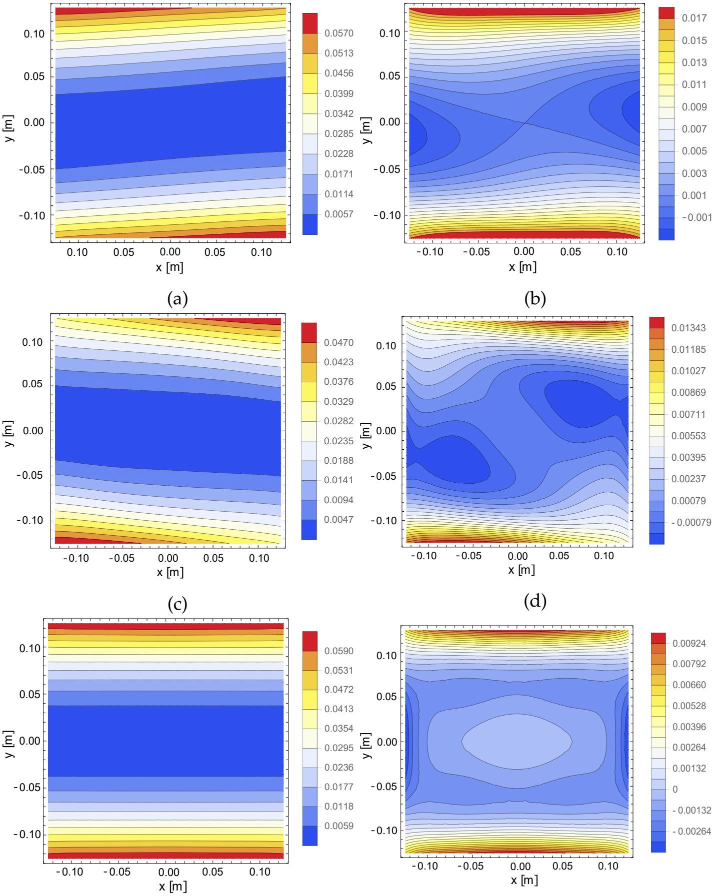

(a) (b)

(c) (d)

(e) (f)

Figure 6.10: a) Initial contour plot of the bistable plate VS-1 with variable stiffness b) Contour plot just before snap-through event for VS-1 with variable stiffness c) Initial contour plot of the bistable plate VS-4 with variable stiffness d) Contour plot just before snap-through event for VS-4 with variable stiffness e) Initial contour plot of the bistable plate with constant stiffness $[0_2/90_2]$ f) Contour plot just before snap-through event for constant stiffness $[0_2/90_2]$. The contours represent the out-of-plane surface position [m].

corresponding FE model was developed to compare the results of the formulated analytical method for a family of VS laminates satisfying $\phi = 45^\circ$ and $T_0 + T_1 = 90^\circ$. The corresponding cross-ply straight fiber laminate is used as a benchmark to quantify the performance of the VS laminates.

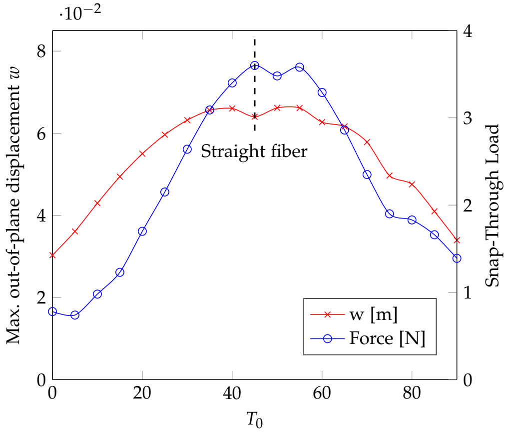

Figure 6.11: Parametric study performed on the family $\phi = 45^\circ$ and $T_0 + T_1 = 90^\circ$ to investigate the effect of VS angle parameter T_0 on the snap-through loads and the corner displacements.

The out-of-plane displacement at different sections and the corner points of four different VS laminates are calculated with the formulated analytical approach and compared with FE results. With the increasing order of Legendre polynomials, the comparison with FE results improves. The solutions are then compared with the reference constant stiffness laminate: $[0_2/90_2]$. As the formulation focuses on solving the membrane energy with sufficient accuracy, the in-plane stress resultants solved using the aid of DQM are plotted on the plane of the plate and compared using the in-plane stress resultants obtained from the FE results. The snap-through loads of the investigated VS laminates are also calculated with increasing orders of Legendre polynomials. At $n = 5$, good convergence is reached with the results obtained from FE analysis. The load-displacement curves are plotted for different VS laminates and the straight fiber laminate. It is observed that the laminate VS-2 has 45% lower snap-through force than the straight cross-ply laminate, with just 14% lower out-of-plane displacement. It is interesting to observe that different VS laminates have a different preferential mode of snapping. It is the interplay between the bending and the stretching energies as well as the presence of local undulations in the initial stable shape that leads to the difference in the snap-through loads.

The tailoring concept is further explored by conducting a parametric study, where the value of T_0 is incremented by 5° with $T_1 = 90 - T_0$ and $\phi = 45^\circ$. It is observed that with VS laminates, there can be an immense possibility to tailor the snap-through loads without much change in the bistable mode shapes. For example, in the studied example, the performance can be improved using $T_0 = 65^\circ$. With such VS laminate, the snap-through loads are lower but with a minimal difference in the out-of-plane displacements, when compared with an equivalent cross-ply laminate.

Such snap-through tailoring makes VS laminates a promising choice in efficient morphing systems.

7

Analysis of multistable VS laminates with actuators

7.1 Introduction

The application of force to trigger the snap-through process might be restrictive for many practical applications. A morphing system with integrated bistable elements might not have enough space to allow a mechanism with concentrated force. An ideal solution would be to attach actuators on the top and bottom surface of the laminate to trigger snap-through and snap-back. In this chapter, the modeling steps to include Macro Fiber Composite (MFC) actuators on the laminate surface are described. The analytical model derived in the previous section is extended to include the effects of the MFC actuators. In this chapter the same VS as well as straight composite layups are investigated, but including the actuators. A square plate is considered as studied by Schultz et al. to verify the models.

When the voltage is applied to the actuators, it generates strains in the longitudinal and transverse directions. The difference in the strains between the actuator and the laminate causes the laminate to bend and eventually snap-through to the other stable shape. Similarly, a snap-back can also be achieved using another set of MFCs placed on the other side of the plate. Experimental data from the literature pertaining to the snap-through and snap-back of a cross-ply laminate is used to verify the model. The snapping voltages are likewise calculated for various VS laminates, using both analytical and FE models.

7.2 Macro-Fiber Composite Actuator

7.2.1 *Background*

Macro-Fiber Composite Actuator (MFC) developed by NASA is a low-cost piezoelectric fiber composite device. It typically consists of piezoceramic fibers such as lead zirconate titanate (PZT), embedded in an epoxy matrix, and sandwiched between Kapton sheets layered with copper interdigitated electrodes, for structural actuation (Figure 7.1). The piezoceramic fibers exhibit a high strain per unit electric field, or so-called the piezoelectric coefficient. When the voltage is applied, the direction of poling and the actuation is the same as the direction of the piezoceramic fiber. Depending on the polarity of the voltage, the electrode fibers extend or contract, generating in-plane strains. These are then transferred through the adhesive layer as shear stress to the laminate.

MFCs show fast actuation response and easier integration to a large structure as compared to SMAs [188, 189]. Mechanisms proposed for SMAs are somewhat cumbersome [52]. The advantage of MFC actuators over discrete mechanical actuators is the transmission of stresses over the whole surface through shear loads, rather than at discrete points. The MFC actuators can be placed over an active surface or can also be integrated inside a structure. An overview of the MFC manufacturing process can be found in William et al. [219] and the complete assembly process in Williams et al. [218].

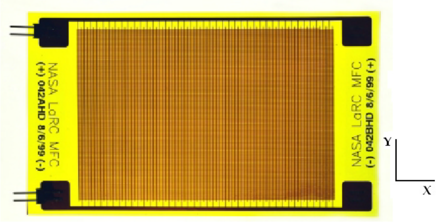

Figure 7.1: Macro Fiber Composite Actuator [217].

Based on the poling direction, the MFC actuators typically works in two different operational modes, the d_{31} and the d_{33}, as shown in Figure 7.3. Here 1-2-3 refers to the direction of the local material coordinate system x_1-x_2 and x_3, as shown in figure 7.3.

In d_{11} or the P_1 mode, the piezoelectric fibers are oriented parallel to the applied electric field and the poling direction (toward axis x_1). On the other hand, in d_{31} or P_2 mode, the applied electric field (toward axis x_3) is perpendicular to the fibers. Both the concepts is illustrated in figure 7.3.

The d_{11} type creates an inhomogeneous electric field, where even a small fracture in the electrodes can lead to total failure. The electric field is relatively homogeneous in d_{31} type, and fracture in the electrodes can lead to a partial reduction in the

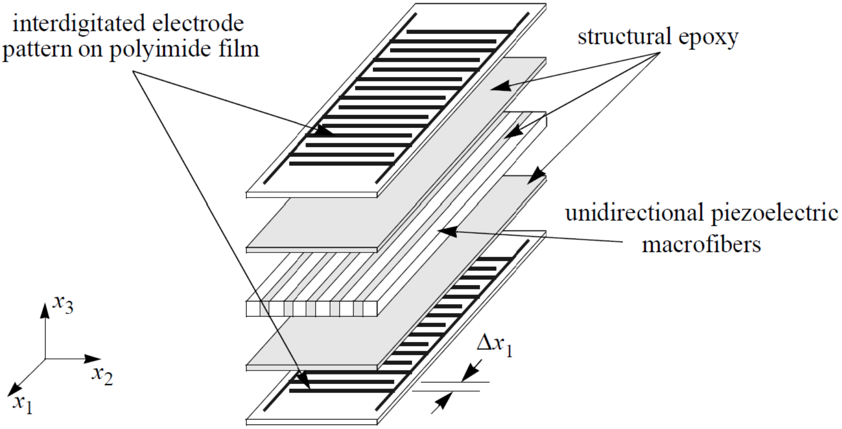

FIGURE 7.2: Exploded view of Macro Fiber Composite Actuator [217].

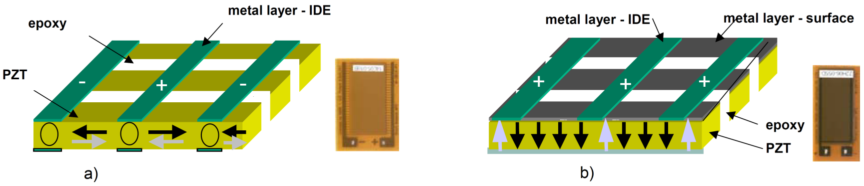

FIGURE 7.3: Macro Fiber Composite Actuator a) d_{11} effect b) d_{31} effect.

generated strain. However, the d_{11} type can produce 2-3 times higher strains than the d_{31} type, with higher operating voltages. The operating limits of the MFC actuators of d_{11} type produced by Smart Materials GmbH are 1500 V and -500 V [140].

In this work, we are particularly interested in exploiting the d_{11} effect to achieve snap-through. We consider a simplified constitutive relation of the piezoelectric actuators, where the three-dimensional constitutive law is simplified to an orthotropic plane-stress type relation. The voltage is applied in the x_1 direction which in turn produces strains ε_{11}^V, ε_{22}^V and ε_{12}^V. Schultz et al. [188] studied the strain-voltage relationship of MFC actuators, which is typically nonlinear. However, for simplicity, it is fair to assume a linear strain-voltage relationship. Therefore the terms d_{11} and d_{12} (arising due to Poisson's effect) are assumed to have constant values. Table 7.1 shows the material properties of a typical MFC actuator [188].

The strains in the actuator in terms of the piezoelectric constant d_{11} and d_{12} on applying a voltage ΔV can be expressed as:

Engineering constant	Identification
E_1	28.6 GPa
E_2	13.1 GPa
v_{12}	0.29
G_{12}	4.03 GPa
d_{11}	$428\mu\varepsilon/(kV/mm)$
d_{12}	$-214\mu\varepsilon/(kV/mm)$
Δx_1	0.5×10^{-3}
t	0.290 mm

Table 7.1: Characteristic properties of MFC actuators [188].

$$\begin{aligned} \varepsilon_{11}^{V} &= d_{11}\frac{\Delta V}{\Delta x_1} \\ \varepsilon_{22}^{V} &= d_{12}\frac{\Delta V}{\Delta x_1} \\ \gamma_{12}^{V} &= 0 \end{aligned} \tag{7.1}$$

Here Δx_1 refers to the spacing of the electrodes.

7.2.2 *Application in shape-changing bistable laminates*

The MFC actuators do not span the entire plane of the laminate. Instead, the actuators are placed as patches on the laminate surface. The electrodes in the proposed MFC model are aligned along the longer side of the laminate to get maximum strain change effects in the FE Model. In this work, we use two layers of the bonded MFC, one on the top and the other on the bottom surface of the laminate (Figure 7.4). The use of two MFC actuators enhances the performance of triggering both snap-through and snap-back as described in Schultz et al. [188]. One patch has a size of $85mm \times 57mm$, with 0° electrode fiber angle whereas the other has a size of $57mm \times 85mm$, with 90° electrode orientation. The thickness of commercially available MFC actuators is usually around 0.29 mm. The alignment of the MFC actuators largely depends on the principal axes of the cool-down cylindrical shape. The actuator with a positive voltage is placed on the inner surface of the curvature, whereas the actuator with negative voltage is placed on the outer surface. The smaller edge of the inner actuator is aligned parallel to the straight edge of the curved bistable laminate. This is depicted in figure 7.5. Upon several conducted studies, this alignment provided the best actuation authority, and therefore is proposed in the rest of this work.

A square laminate of length 135 mm is considered in this study. For smaller laminate sizes, the plate loses bistability, and for larger plates, the actuators are not able to snap the active bistable laminate. The geometry and material data are in reference to the work presented in Schultz et. al. [188], with which we first verify our model.

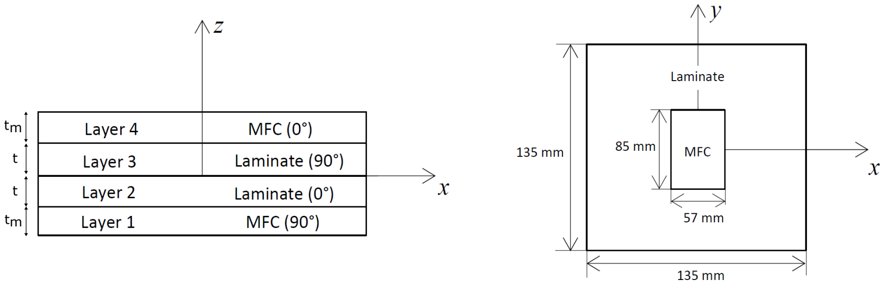

FIGURE 7.4: Laminate- MFC alignments.

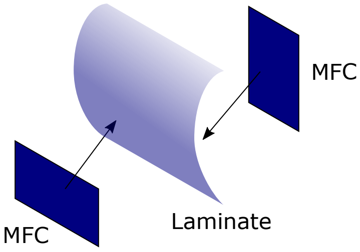

FIGURE 7.5: Representative laminate- MFC alignments.

7.3 Methodologies to model laminate-actuator system

7.3.1 *Semi-analytical approach*

The semi-analytical framework derived from the previous chapter is extended to include the effect of the MFC actuators. The ease of modeling MFC actuators in a semi-analytical framework is mainly due to its fiber composite-like structure. As mentioned earlier, the piezoelectric electrodes can be treated very well like fibers in composite laminates embedded in a polymer-based resin.

The modeling approach of bistable plates with MFC actuators is divided into three different phases in equivalence to the experimental procedure. Firstly, the unsymmetric laminate is cooled down from curing temperature to warp into one of the cylindrical shapes. In this step, we use the Rayleigh-Ritz method, where the internal residual stresses and the two stable shapes are determined. The next step involves bonding the actuators on the laminate surface. The bonding procedure leads to stress discontinuities through the thickness, as the actuators are stressed to attain the same curvature as the laminate. Finally, in step-3, the MFCs are actuated by applying a suitable voltage to trigger snap-through to the other stable shape.

Step 1: Cool-Down Process

The first step involves cooling down of the unsymmetric laminate from curing temperature to room temperature.

We assume the same expression for $\tilde{w}$ as shown previously in Eq. 6.19 and Eq. 6.20. As described in the previous chapter in Eq. 6.8, the total potential energy can be written as:

$$\begin{aligned}\Pi = & \frac{1}{2}\int_S \left[\boldsymbol{N}^T \boldsymbol{A}^*(x,y)\boldsymbol{N}\right] dS + \frac{1}{2}\int_S \left[\boldsymbol{\kappa}^T \boldsymbol{D}^*(x,y)\boldsymbol{\kappa}\right] dS \\ & - \frac{1}{2}\int_S \left[(\boldsymbol{N}^{th})^T \boldsymbol{A}^*(x,y)\boldsymbol{N}^{th}\right] dS - \int_S \left[(\boldsymbol{N}^{th})^T \boldsymbol{B}^*(x,y)\boldsymbol{\kappa}\right] dS \\ & - \int_S \left[(\boldsymbol{M}^{th})^T \boldsymbol{I}\boldsymbol{\kappa}\right] dS\,, \end{aligned} \tag{7.2}$$

where all the terms have been defined previously in Section 6.3. The same steps are followed as described in Section 6.4.2 to calculate the in-plane stress resultants in terms of the curvatures using the compatibility equation and the in-plane equilibrium equations. The resultant differential equation is solved using DQM as shown in section 6.5.

Step 2: Bonding with Actuator

The next step involves the process of bonding the actuators to the laminate surface. One way to achieve this is by using epoxy as adhesive, as explained in Schultz et al. [191]. First, the epoxy is spread over the surface of the actuator and the laminate. The actuator is then carefully centered and taped to the laminate. The laminate and the actuators are then sealed inside a vacuum bag, and the vacuum is drawn. After 48 hours, as the epoxy cures, the actuator is bonded to the laminate surface.

Another technique, as described by Schultz et al. [188] is by flattening the bistable laminate first and then bonding it with the straight MFC actuators. The bistable laminate is kept flattened until the adhesive cures. An external load has to be additionally applied to hold the laminate flat.

Both manufacturing processes yield similar results, leading to a reduced curvature of the laminate-actuator structure. In this work, we consider the first bonding approach, as it is relatively easier to model in the semi-analytical framework.

During the epoxy curing process, the actuators follow the same curvature as the laminate, due to the common contact surface. Until the adhesive is fully cured, the actuators and the laminate can slip relative to each other. Due to this reason, the mid-plane strains at the actuators becomes zero. The total strains on the actuators, therefore, can be expressed just in terms of curvatures. Following the same approach as described in Step-1, we calculate the stable shapes of the bonded laminate-actuator system using the Rayleigh-Ritz approach.

The total strains of the laminate in this step are given by:

$$\boldsymbol{\varepsilon} = \boldsymbol{\epsilon}^{(2)} + z\boldsymbol{\kappa}^{(2)}, \tag{7.3}$$

and the total strains in the actuators are:

$$\boldsymbol{\varepsilon}^{m} = z\boldsymbol{\kappa}^{(2)} \tag{7.4}$$

Here the subscript denotes the step number, which is, in this case 2. Calculating the stresses at the top and the bottom layer of the MFC.

$$\boldsymbol{\sigma}^{m0} = \boldsymbol{Q}^{m0}\boldsymbol{\varepsilon}^{m}, \quad \boldsymbol{\sigma}^{m90} = \boldsymbol{Q}^{m90}\boldsymbol{\varepsilon}^{m} \tag{7.5}$$

$$Q^{m0} = E_0^{m0}\begin{bmatrix} 1 & \nu^m & 0 \\ \nu^m & \beta^m & 0 \\ 0 & 0 & \rho^m \end{bmatrix}, \quad Q^{m90} = E_0^{m90}\begin{bmatrix} \beta^m & \nu^m & 0 \\ \nu^m & 1 & 0 \\ 0 & 0 & \rho^m \end{bmatrix} \tag{7.6}$$

are the Q-matrix for the top and bottom MFCs respectively. Q^{m0} has 0° electrode fiber angle and Q^{m90} has 90°. The total potential energy of the top and bottom layer of the MFC is equal to:

$$\begin{aligned} \Pi^m = & \int_{L_x^{m0}/Lx}^{-L_x^{m0}/Lx}\int_{L_y^{m0}/Ly}^{-L_y^{m0}/Ly}\int_{t}^{t^m+t}\left(\frac{1}{2}(z\boldsymbol{\kappa})^T\boldsymbol{Q}^{m0}(z\boldsymbol{\kappa})\right) \\ & + \int_{L_x^{m90}/Lx}^{-L_x^{m90}/Lx}\int_{L_y^{m90}/Ly}^{-L_y^{m90}/Ly}\int_{-t^m-t}^{-t}\left(\frac{1}{2}(z\boldsymbol{\kappa})^T\boldsymbol{Q}^{m90}(z\boldsymbol{\kappa})\right) \end{aligned} \tag{7.7}$$

On integrating in the thickness direction, we get:

$$\begin{aligned} \Pi^m = & \frac{1}{6}\int_{L_x^{m0}/Lx}^{-L_x^{m0}/Lx}\int_{L_y^{m0}/Ly}^{-L_y^{m0}/Ly}\left((\boldsymbol{\kappa})^T\boldsymbol{Q}^{m0}(\boldsymbol{\kappa})\left((t^{m0}+t)^3 - t^3\right)\right)dxdy \\ & + \frac{1}{6}\int_{L_x^{m90}/Lx}^{-L_x^{m90}/Lx}\int_{L_y^{m90}/Ly}^{-L_y^{m90}/Ly}\left((\boldsymbol{\kappa})^T\boldsymbol{Q}^{m90}(\boldsymbol{\kappa})\left((-t^3) - (-t - t^{m90})^3\right)\right)dxdy \end{aligned} \tag{7.8}$$

Here t_m and t are the thickness of an MFC layer and a laminate layer respectively.

Combining Eq. 7.2 and Eq. 7.8, the total energy of the combined laminate and MFC system can be written as:

$$\Pi^{tot} = \Pi + \Pi^{m} \tag{7.9}$$

Applying Rayleigh-Ritz, the curvatures $\kappa_{xx}{}^{(2)}$, $\kappa_{yy}{}^{(2)}$ and $\kappa_{xy}{}^{(2)}$ are found from solving the resultant system of equations. It should be noted that the total energy of the laminate system is a function of the updated curvatures $\kappa^{(2)}$, due to the addition of the MFCs. Subsequently, the in-plane stresses and the in-plane strains in the MFCs can be calculated using Eq. 7.4 and Eq. 7.5. For the laminates, the in-plane stress resultants can be calculated using the following relation:

$$\mathcal{L}_A(\boldsymbol{A}^*\boldsymbol{N}^{(2)}) = \det\boldsymbol{\kappa}^{(2)} - \mathcal{L}_A\left(\boldsymbol{A}^*\boldsymbol{N}^{th} + \boldsymbol{B}^*\boldsymbol{\kappa}^{(2)}\right) := f \quad \text{on}\, S\,, \tag{7.10}$$

where the term $\mathcal{L}_A(\boldsymbol{A}^*\boldsymbol{N}^{th} + \boldsymbol{B}^*\boldsymbol{\kappa}^{(2)})$ is non-zero for VS laminates. And consequently, the in-plane strains in the laminate can be expressed using the following relation:

$$\boldsymbol{\epsilon}^{(2)} = \boldsymbol{A}^*\left(\boldsymbol{N}^{(2)} + \boldsymbol{N}^{th}\right) + \boldsymbol{B}^*\boldsymbol{\kappa}^{(2)} \tag{7.11}$$

Step 3: Actuation

Once the bonding is accomplished, the next step is to actuate the laminate-actuator system. As the voltage is applied to the MFC actuators, the generated electric field creates strains. However, by this step, the adhesive is already cured and therefore there is no slipping occurring between the actuators and the laminate. The strains in the MFC actuator can be written as:

$$\boldsymbol{\varepsilon}^{(3)} = \boldsymbol{\epsilon}^{(3)} + z\boldsymbol{\kappa}^{(3)}, \tag{7.12}$$

The stresses at the top and the bottom MFC layers are given as:

$$\begin{aligned}(\boldsymbol{\sigma}^{m0})^{(3)} &= \boldsymbol{Q}^{m0}\left(\boldsymbol{\varepsilon}^{(3)} - \boldsymbol{\varepsilon}^{(2)} - \boldsymbol{\varepsilon}^{(V0)}\right), \\ (\boldsymbol{\sigma}^{m90})^{(3)} &= \boldsymbol{Q}^{m90}\left(\boldsymbol{\varepsilon}^{(3)} - \boldsymbol{\varepsilon}^{(2)} - \boldsymbol{\varepsilon}^{(V90)}\right)\end{aligned} \tag{7.13}$$

Here $^{(3)}$ refers to the curvature generated at this step, where voltages are applied at the MFCs. $\varepsilon^{(V_0)}$ and $\varepsilon^{(V_{90})}$ are the strains generated by the applied voltage at the top and the bottom actuator respectively. The term $\epsilon^{(2)}$ is the mid-plane strain of the laminate generated in the previous step, during the bonding process (as calculated using Eq. 7.11). As no mid-plane strains in the actuators existed in Step-2, the component $\epsilon^{(2)}$ should be subtracted from the total actuator strains in this step. Due to this reason, a strain discontinuity can be found in the strain profile of the laminate-MFC structure. Schultz et al. [187] also noted a similar observation and so did Gude et al. [83]. The value of the strains can be found by using Eq. 7.1.

$$\Pi^{mA} = \Pi^{m0} + \Pi^{m90} \tag{7.14}$$

The total potential energy of the actuators can be split into the contribution of MFCs on the top and the bottom. The MFCs at the top and the bottom of the laminate is denoted from now on as $m0$ and $m90$ respectively.

$$\begin{aligned}\Pi^{mA} = &\int_{S^{m0}} \int_{t}^{t^m+t} \left(\frac{1}{2} \left(\boldsymbol{\varepsilon}^{(3)} \right)^T (\boldsymbol{\sigma}^{m0})^{(3)} dz dS^{m0} \right) + \\ &\int_{S^{m90}} \int_{-t^m-t}^{-t} \left(\frac{1}{2} \left(\boldsymbol{\varepsilon}^{(3)} \right)^T (\boldsymbol{\sigma}^{m90})^{(3)} dz dS^{m90} \right)\end{aligned} \tag{7.15}$$

Substituting Eq. 7.12 and 7.13 in Eq. 7.15. This could be further simplified as:

$$\begin{aligned}\Pi^{mA} = &\int_{S^{m0}} \int_{t}^{t^m+t} \left(\frac{1}{2} \left(\boldsymbol{\epsilon}^{(3)} + z\boldsymbol{\kappa} \right)^T \boldsymbol{Q}^{m0} \left(\boldsymbol{\epsilon}^{(3)} - \boldsymbol{\varepsilon}^{(2)} + z\boldsymbol{\kappa}^{(3)} - \boldsymbol{\varepsilon}^{(V0)} \right) dz dS^{m0} \right) + \\ &\int_{S^{m90}} \int_{-t^m-t}^{-t} \left(\frac{1}{2} \left(\boldsymbol{\epsilon}^{(3)} + z\boldsymbol{\kappa}^{(3)} \right)^T \boldsymbol{Q}^{m90} \left(\boldsymbol{\epsilon}^{(3)} - \boldsymbol{\varepsilon}^{(2)} + z\boldsymbol{\kappa} - \boldsymbol{\varepsilon}^{(V90)} \right) dz dS^{m0} \right)\end{aligned} \tag{7.16}$$

In this step, the total strains in the laminate-actuator system are calculated from:

$$\boldsymbol{\epsilon}^{(3)} = (\boldsymbol{A}^c)^*(\boldsymbol{N} + \boldsymbol{N}^{th}) + (\boldsymbol{B}^c)^*\boldsymbol{\kappa}, \tag{7.17}$$

where $(\boldsymbol{A}^c)^*$ and $(\boldsymbol{B}^c)^*$ is calculated for the entire laminate-actuator system.

Expressing strains in terms of in-plane stress resultants and integrating over the thickness, the strain energies of each actuators can be written in the form as:

$$\begin{aligned}\Pi^{mi} = \int_{S^{mi}} \Bigg[&\frac{1}{2} \left(\boldsymbol{\epsilon}^{(3)} \right)^T \boldsymbol{A}^{mi} \boldsymbol{\epsilon}^{(3)} + \left(\boldsymbol{\epsilon}^{(3)} \right)^T \boldsymbol{B}^{mi} \boldsymbol{\kappa}^{(3)} + \frac{1}{2} \left(\boldsymbol{\kappa}^{(3)} \right)^T \boldsymbol{D}^{mi} \boldsymbol{\kappa}^{(3)} \\ &- \left(\boldsymbol{\epsilon}^{(3)} \right)^T \left(\boldsymbol{N}^{(Vi)} + \boldsymbol{N}^{(2i)} \right) - \left(\boldsymbol{\kappa}^{(3)} \right)^T \left(\boldsymbol{M}^{(Vi)} + \boldsymbol{M}^{(2i)} \right) \Bigg]\end{aligned} \tag{7.18}$$

where $i = 0$ is for the top actuator and $i = 90$ for the bottom and $S^{m0} \in [(-L_x^{m0}, L_x^{m0}), (-L_y^{m0}, L_y^{m0})]$ and $S^{m90} \in [(-L_x^{m90}, L_x^{m90}), (-L_y^{m90}, L_y^{m90})]$.

The terms used Eq. 7.17 and 7.18 have the usual meaning as shown below:

$$\begin{aligned}
\boldsymbol{A}^{m0} &= \int_{t}^{t^m+t} \boldsymbol{Q}^{m0} dz, \quad \boldsymbol{A}^{m90} &&= \int_{-t^m-t}^{-t} \boldsymbol{Q}^{m90} dz \\
\boldsymbol{B}^{m0} &= \int_{t}^{t^m+t} \boldsymbol{Q}^{m0} z dz, \quad \boldsymbol{B}^{m90} &&= \int_{-t^m-t}^{-t} \boldsymbol{Q}^{m90} z dz \\
\boldsymbol{D}^{m0} &= \int_{t}^{t^m+t} \boldsymbol{Q}^{m0} z^2 dz, \quad \boldsymbol{D}^{m90} &&= \int_{-t^m-t}^{-t} \boldsymbol{Q}^{m90} z^2 dz
\end{aligned}$$

and

$$\begin{aligned}
\boldsymbol{A}^c &= \sum_{k=1}^{n_{ply}} \int_{z_k}^{z_{k+1}} \boldsymbol{Q}_k\left(x, y\right) dz + A^{m0} + A^{m90} \\
\boldsymbol{B}^c &= \sum_{k=1}^{n_{ply}} \int_{z_k}^{z_{k+1}} \boldsymbol{Q}_k\left(x, y\right) z dz + B^{m0} + B^{m90} \\
\boldsymbol{D}^c &= \sum_{k=1}^{n_{ply}} \int_{z_k}^{z_{k+1}} \boldsymbol{Q}_k\left(x, y\right) z^2 dz + D^{m0} + D^{m90}
\end{aligned}$$

The following relationship holds for the laminate-actuator system as well:

$$\begin{aligned}
(\boldsymbol{A}^c)^* &:= (\boldsymbol{A}^c)^{-1} \\
(\boldsymbol{B}^c)^* &:= -(\boldsymbol{A}^c)^{-1}\boldsymbol{B} \\
(\boldsymbol{D}^c)^* &:= \boldsymbol{D} - (\boldsymbol{B}^c)^T (\boldsymbol{A}^c)^{-1} \boldsymbol{B^c} \,,
\end{aligned} \tag{7.19}$$

The in-plane force and the moment resultants due to the applied voltage on the top and bottom actuators can be written in the following form:

$$\begin{aligned}
\boldsymbol{N}^{V0} &= \int_{t}^{t^m+t} \boldsymbol{Q}^{m0} \boldsymbol{\varepsilon}^{(V0)} dz \\
\boldsymbol{M}^{V0} &= \int_{t}^{t^m+t} \boldsymbol{Q}^{m0} \boldsymbol{\varepsilon}^{(V0)} z dz \\
\boldsymbol{N}^{V90} &= \int_{-t^m-t}^{-t} \boldsymbol{Q}^{m90} \boldsymbol{\varepsilon}^{(V90)} dz \\
\boldsymbol{M}^{V90} &= \int_{-t^m-t}^{-t} \boldsymbol{Q}^{m90} \boldsymbol{\varepsilon}^{(V90)} z dz
\end{aligned}$$

The value of $\boldsymbol{\varepsilon}^{(V0)}$ and $\boldsymbol{\varepsilon}^{(V90)}$ can be found using the Eq. 7.1. Here, $V0$ and $V90$ represents the voltage applied on the top and the bottom actuator respectively. Similarly, the in-plane force and the moment resultants due to the strains from the previous step can be written in the following form:

$$
\begin{aligned}
\boldsymbol{N}^{2-0} &= \int_{t}^{t^m+t} \boldsymbol{Q}^{m0}\boldsymbol{\epsilon}^{(2)} dz \\
\boldsymbol{M}^{2-0} &= \int_{t}^{t^m+t} \boldsymbol{Q}^{m0}\boldsymbol{\epsilon}^{(2)} z dz \\
\boldsymbol{N}^{2-90} &= \int_{-t^m-t}^{-t} \boldsymbol{Q}^{m90}\boldsymbol{\epsilon}^{(2)} dz \\
\boldsymbol{M}^{2-90} &= \int_{-t^m-t}^{-t} \boldsymbol{Q}^{m90}\boldsymbol{\epsilon}^{(2)} z dz
\end{aligned}
$$

The value of $\boldsymbol{\epsilon}^{(2)}$ can be found using Eq. 7.11.

It should be noted that for Eq. 7.16, the in-plane strains $\varepsilon^{(3)}$ and $\varepsilon^{(2)}$ have to be calculated in a DQ grid of the MFC part. This can be done by interpolating the strains from the laminate DQ grid to that of MFCs DQ grid. Both the MFCs have different geometry, and therefore different DQ grids are assigned for the individual MFCs. Therefore the following steps are followed to do so.

The inplane strains $\epsilon^{(2)}$ are first calculated using Eq. 7.11 and interpolated in DQ grid in the region S^{m0} ranging from $[-L_x^{m0}/Lx, L_x^{m0}/Lx]$, $[L_y^{m0}/Ly, L_y^{m0}/Ly]$ for the top MFC (with 0° electrode orientation) and in the region S^{m90} ranging from $[-L_x^{m90}/Lx, L_x^{m90}/Lx]$, $[L_y^{m90}/Ly, L_y^{m90}/Ly]$ for the bottom MFC (with 90° electrode orientation). The stresses and strains are then substituted in the total energy of the actuators, which reads in the following form as:

$$
\Pi^{tot} = \Pi + \Pi^{mA} \tag{7.20}
$$

Applying Rayleigh-Ritz, the curvatures $\kappa_{xx}{}^{(3)}$, $\kappa_{yy}{}^{(3)}$ and $\kappa_{xy}{}^{(3)}$ are found from solving the resultant system of equations, after minimization of the total energy function for a particular applied voltage. An iterative procedure is followed, where the voltages are successively increased in the actuators to trigger snap-through and subsequently snap-back. Snap-through occurs at a point the resulting system of equations yield an unstable solution. Figure 7.6 shows the complete scheme.

7.3.2 *Numerical approach*

A geometrically nonlinear FE model is established for the previously described three steps. During preliminary studies, two different nonlinear approaches were evaluated: the arc-length method (rik's analysis) and static analysis with stabilization (static stabilization). The arc-length was computationally expensive and required fine tuning of the involved parameters, and therefore was not suitable for this study, and therefore static with stabilization was used to perform the numerical study.

The objective of the numerical analysis is to determine the snapping voltages for a multistable laminate-actuator system. The curvillinear fiber paths of the VS laminate is modelled in a piecewise way as described previously in Section 4.3. An FE model is developed consisting of the two MFCs and the laminate. One MFC

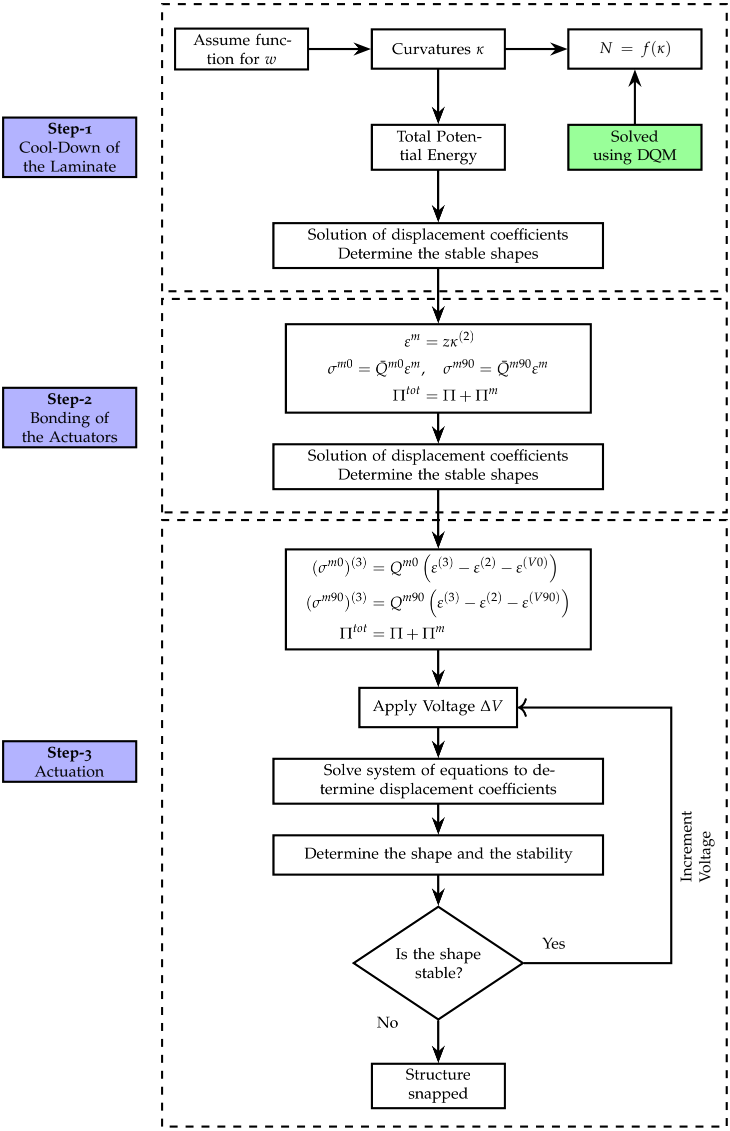

FIGURE 7.6: Flowchart of the semi-analytical framework

is placed on the top and the other on the bottom of the laminate. The MFCs are rectangular in shape. The fiber orientation of the top actuator is orthogonal to that of bottom actuator. The laminate and the MFCs are both modeled using 4-noded

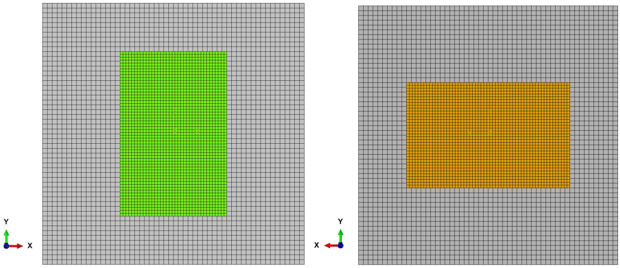

FIGURE 7.7: a) Finite element mesh with the laminate actuator system. a) MFC actuator bonded on the top of the laminate. b) MFC actuator bonded on the bottom of the laminate.

quadrilateral general purpose *S4R* type shell elements. A finer mesh is used for the actuators. A `TIE` type constraint is used to connect the laminate (master surface) with the actuator (slave surface), constraining all degrees of motion. The following steps describe a methodology to bond the actuators on the laminate and trigger snap-through by applying a voltage. The steps are illustrated in figure 7.8.

1. **Eigenvalue Analysis**: An linear eigenvalue analysis is performed on the perfect geometry, to obtain the eigenmodes.

2. **Cool-Down Step**: The obtained eigenmodes are introduced as imperfections to the investigated composite plate. A geometrically nonlinear FE analysis is performed with static analysis with external stabilization technique to obtain a converged solution. The boundary conditions are set by fixing the center of the plate. A predefined temperature difference is applied to simulate the cool-down from curing to room temperature. The structure cools down into one of the curved stable shapes due to the induced residual stresses.

3. **Addition of Actuators**: The next step involves the addition of the actuators in the laminate system. Previous experimental procedures have shown that the actuators are added once the laminate cools down to room temperature. Therefore, to follow the experimental procedure, it is essential to simulate the bonding of the actuators after the laminate is cooled down. Once the actuators are bonded, the curvature of the cured laminate changes due to the added stiffnesses of the actuators. However, in a commercial FE software, the geometry is instead defined at the very beginning of the analysis, and additional geometrical instances are not trivial to be added in between the steps. Therefore, a method proposed by Portela et al. [171] is employed where temperature dependent elastic properties are defined for the actuators. At the initial curing temperature (180°), a very low stiffness value of the actuators is considered. Once it reaches room temperature, the actuators retain its actual stiffness properties. In this way, the actuators remain deactivated until the laminate cools down till room temperature is reached.

4. **Application of Voltage for Snap-Through**: The next step involves applying a voltage to the actuators in the form of a temperature field. An equivalent thermal coefficient for free strain per volt value is calculated and applied to create the actuation effect. With the increase in voltage, the laminate snaps from the first stable shape to the second.

5. **Removal of Voltage**: It is also important to check if the bistability is retained when the voltages are removed from the actuators. Once the voltages are removed, the structure should remain in second stable shape, or else bistability might be lost due to the added actuators.

6. **Application of Voltage for Snap-Back**: Similar to the snap-through process, the snap-back is carried out from second stable shape to the first stable shape. This is carried out by changing the polarity of the actuators.

7. **Removal of Voltage**: At the end, all voltages are removed, to check if the plate stays in the first stable shape.

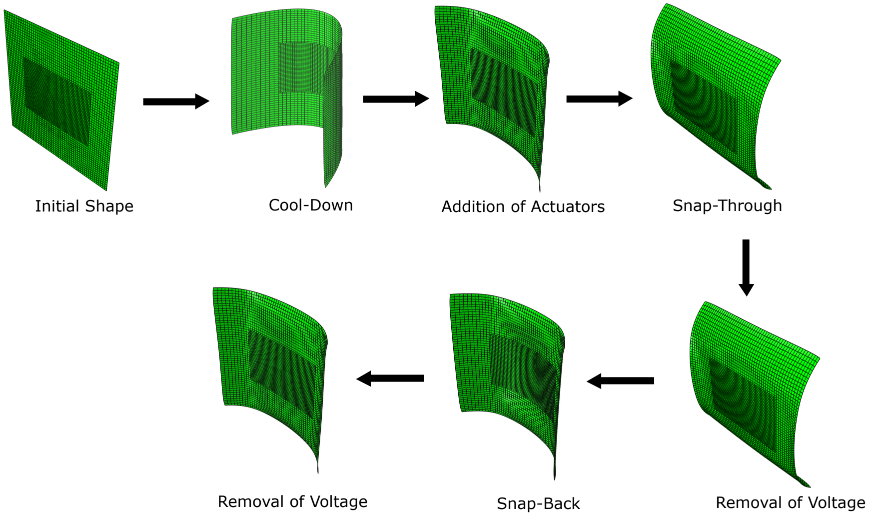

Figure 7.8: Steps for snap-through and snap-back.

7.4 Semi-analytical results and discussion

7.4.1 *Validation and verification*

As a first step, the numerical and the analytical model is validated with the experiments conducted by Schultz. et. al. [188] on a unsymmetric cross-ply laminate.

Schultz et al. demonstrated both snap-through and snap-back of an unsymmetric cross-ply laminate experimentally for the first time. Previous attempts to achieve both snap-through and snap-back were unsuccessful, and often required additional weights to snap ([171, 206].

In Schultz et al., a 135 by 135 mm [0/90] unsymmetric composite base laminate is used, with a total thickness of 0.3 mm. Two MFC actuator patches with a thickness of 0.3 mm each are used at the center of the plate, as shown in Figure 7.7. This resulted in a laminate configuration: $[0^{MFC}/90/0/90^{MFC}]$. The size of the MFC actuators is chosen to be 85 mm × 57 mm. The actuators are aligned in such a way that the piezoelectric fibers are parallel to the longer edge of the actuator (85 mm). The mechanical and thermal properties of the laminate and the MFC used in this work are given in Table 7.1 and Table 7.2.

Engineering constant	Identification
E_1	140 GPa
E_2	13 GPa
v_{12}	0.3
G_{12}	6.6 GPa
G_{13}	6.6 GPa
G_{23}	6.6 GPa
α_1	-0.8×10^{-6}
α_2	29×10^{-6}
t	0.149 mm

TABLE 7.2: Characteristic properties of Laminates (Schultz et al. [188]).

Schultz et al. adopted a novel approach to trigger snap-through and reset back to the original configuration. Schultz used both the actuators simultaneously to trigger snap-through and reset back. With this approach, maximum actuation capabilities could be utilized for both the actuators. Figure 7.9 shows the voltage cycle for the top (or first) and the bottom (or second) actuators. Such voltage cycle is chosen in the study, as it uses the maximum recommended positive as well as negative voltages. It must be noted that Schultz reached even higher voltages (1900 V) than prescribed for MFC actuators (1500 V) by the manufacturers [140].

Although the experimental results gave a good insight into the morphing capabilities of bistable laminates using actuators, the analytical model presented by Schultz et al. [188] failed to predict accurate snapping behavior. The polynomials assumed to describe the in-plane displacement fields, as well as the out-of-plane displacement, were insufficient to capture the complex snap-through process. This is in line with the observations on snap-through loads made previously in section where lower order polynomial could be capture the snap-through loads. Following

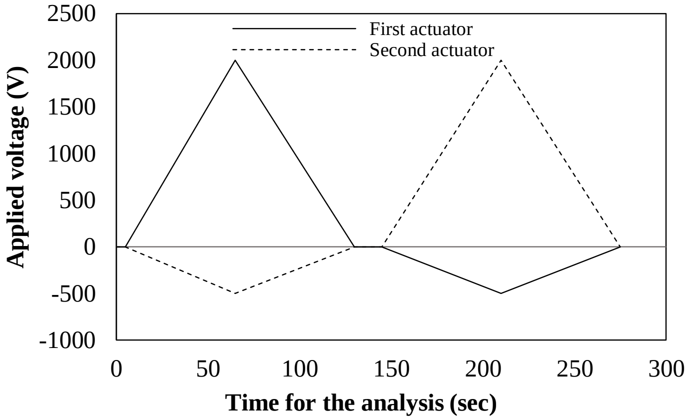

Figure 7.9: Applied voltage increment on MFC actuators [188].

the same reason as discussed in Chapter 5, higher order polynomial functions are required for estimating the snap-through voltages within reasonable accuracy.

We thereby solve the same problem using the formulated refined semi-analytical model described in section 7.3.1. The difference in the shape before and after adding the actuators is illustrated in figure 7.10. These figures have been obtained from a 4^{th} order Legendre polynomial. It is clear from the figure that the curvature reduces as the actuators are added to the laminate, due to the added stiffness.

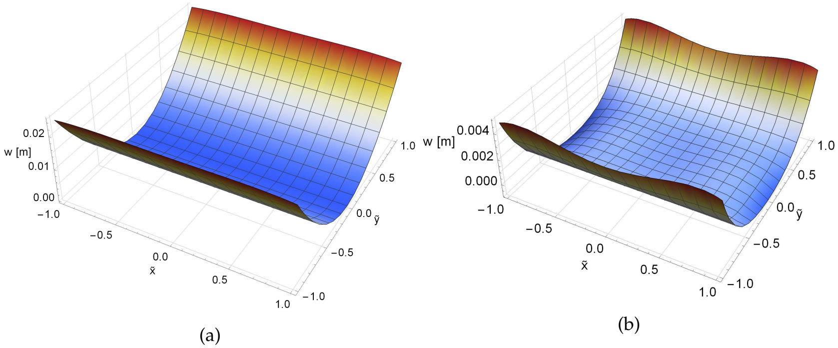

(a)

(b)

Figure 7.10: a) Stable shape without MFC b) Stable shape with MFC. Both shapes are obtained using the semi-analytical formulation with 4^{th} order polynomial approximation.

A comparison between a stable shape obtained after bonding of the actuators (as described in Step:2 Section 7.3.1) between the semi-analytical results with (a) 2^{nd}

order Legendre polynomial b) 4th order Legendre polynomial) and the FE results (c)) in Figure 7.11.

The cooldown shape of a MFC added laminate is compared with the results obtained from semi-analytical ($n = 2$ and $n = 4$) and FE method. Local reversal of the curvatures can be observed at certain portions of the plate from the FE results, and are captured well with the shape obtained from the 4th order polynomial. The result from the 2nd order polynomial is not able to capture such local deformations.

Based on a preliminary study, 4th order polynomial was found to be a good balance between computational costs and accuracy (when compared to FE). Investigations hereafter are therefore carried out using 4th order polynomial approximations for the out-of-plane displacements.

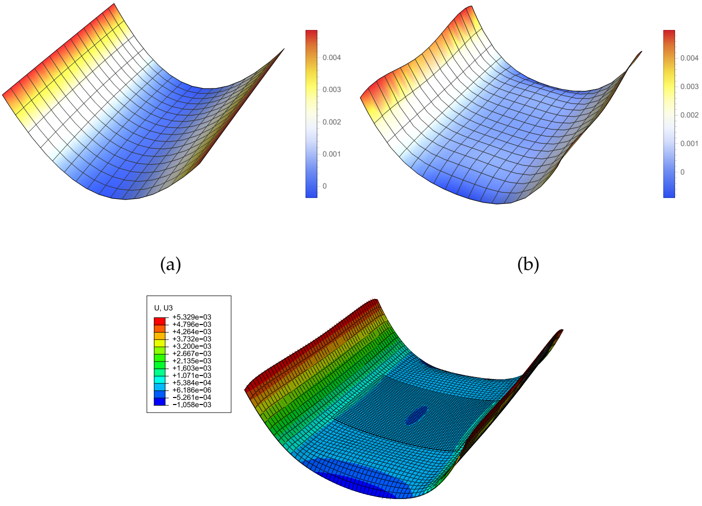

(a)

(b)

(c)

FIGURE 7.11: a) Stable shape with MFC using Legendre polynomial order $n = 2$, b) Stable shape with MFC using Legendre polynomial order $n = 4$ c) Stable shape with MFC using FE.

The voltages are applied on top and bottom actuators to first trigger snap-through and then snap-back. For the snap-through process, the voltage is increased from 0 V to a positive polarity on the top actuator, whereas simultaneously a negative voltage is applied on the bottom actuator. With each increment of the applied positive voltage, 0.25 times the negative voltage is increased.

The experimental results obtained by Schultz are depicted in figure 7.12. Fig. 7.12 a) shows the plot between the x-component of the strain measured on top MFC actuator, with the voltage applied on the top actuator. Similarly, Fig. 7.12 b) shows the plot between the x-component of the strain with the voltage applied to the bottom actuator. Upon examining both the plots, it is seen that a positive voltage

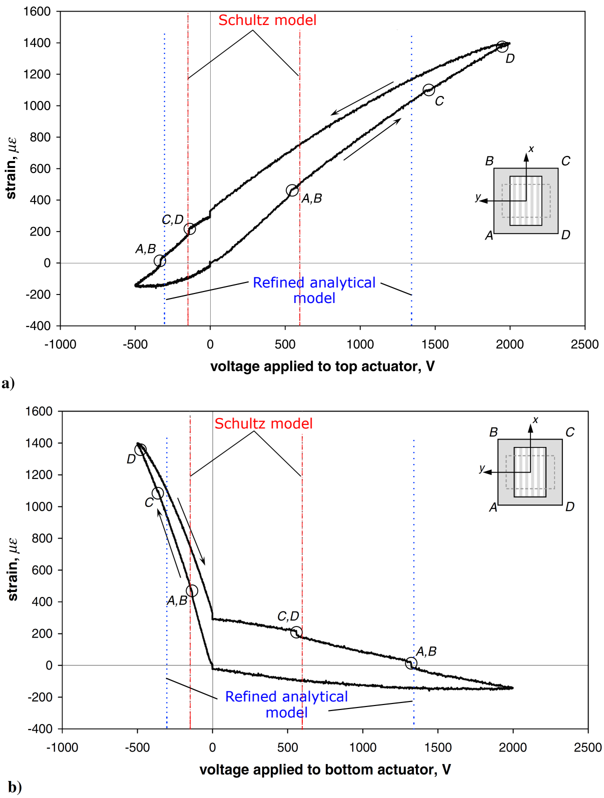

a)

b)

FIGURE 7.12: Comparison of the analytical results with 4^{th} order legendre polynomial and the experimental results reported in [188]. The figure also illustrates the improvement of the refined analytical model over the model described in same work of Schultz.

is initially applied at the top actuator, and at the same time a negative voltage is applied at the bottom actuator. This simultaneous application of the voltage on both actuators acts harmoniously to bend the laminate resulting in a snap to the other stable shape. This can also be visualized from the FE steps shown in Fig. 7.8.

In the experiments conducted by Schultz et al., it is shown that the snap-through is not a single event. This means that all the corners of the laminate does not snap at the same time. In figure 7.12, the letters A, B, C, and D denote the four corners of the square laminate. During the snap-through process, the first set of corners (A and B) changed their curvature when a voltage of 500 V is applied at the top actuator. Corner C and subsequently corner D snaps when the voltage on the top actuator crosses 1500 V and at 1900 V respectively. For switching back from second to first stable shape, only two snapping events were observed. At 500 V applied at the bottom actuator, the corners C and D snapped and later at 1300 V, the corners A and B snapped.

In this chapter, this experimental process is modeled using the described semi-analytical approach (section 7.3.1). A 4^{th} Legendre polynomial is used to define the out-of-plane displacement w. From the semi-analytical calculations, the snap-through (from first tp second shape) occurred when the top and bottom actuators had a voltage of 1344 V and -336 V respectively. The model from Schultz et al. [188] which is based on uniform curvature assumption, predicted the snap-through voltage to occur at 597 V applied at the top actuator, and -149 V applied at the bottom. This is a significant improvement over the predictions from Schultz's model. The difference between the new refined semi-analytical results v/s semi-analytical results obtained in Schultz et al. is also depicted in Fig. 7.12. Both the semi-analytical approaches yielded same snap-through voltages, but with opposite polarity, when switching from first shape to second and vice-versa. The voltage displacement curve for the top and bottom actuator is depicted in Fig.7.13 and 7.14 respectively.

Additionally, finite element simulations are also carried out following the steps described in section 7.3.2. The obtained voltage-displacement curve for the top and bottom actuator for the $[0/90]$ laminate is shown in figure 7.13 and figure 7.14, respectively. From the FE simulation, the plate snaps when 1584 V is applied on the top actuator and -396 V on the bottom. For switching back to initial shape, a similar voltage-displacement plot is obtained, but with the opposite polarity. This is particularly due to the

Both semi-analytical and FE results show the same magnitude of snapping voltage when switching from first to second shape and vice-versa. It is contrary with the experimental observations, where different voltages were recorded when switching from first to second shape and vice-versa. Ideally, due to the symmetry of the investigated problem, both voltages should have the same magnitude. A different snap-through voltage arose in the experiment, perhaps due to experimental errors. Even a small eccentricity in placing the actuators at the center can result in differences between the two snapping voltages.

7.4.2 *Calculation of snap-through and snap-back voltages in VS laminates*

In this section, VS laminates, as discussed in the previous chapter is analyzed using the derived analytical formulation and as well as FE approach.

As seen in the section 7.4.1, the refined semi-analytical results agreed reasonably well with the FE as well as the experimental results. In this section, we use the semi-analytical method to conduct a parametric study on different VS laminates. We calculate the snap-through voltages as well as the maximum out-of-plane displacements. The results for a set of different VS laminates are plotted in figure 7.15. With a morphing application in mind, we seek for VS laminates which results in high out-of-plane displacements and with the snapping voltages within the

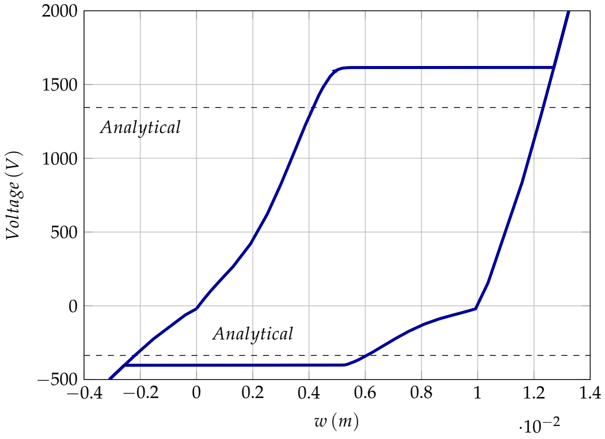

FIGURE 7.13: Voltage displacement curve of the top actuator using FE analysis. The line shows the analytical solution using legendre polynomial of order $n = 4$.

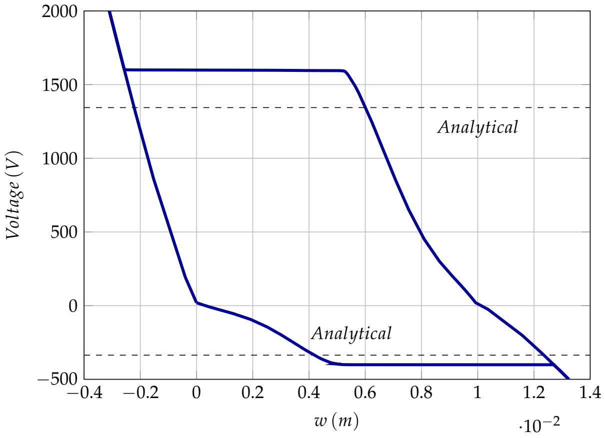

FIGURE 7.14: Voltage displacement curve of the bottom actuator using FE analysis. The line shows the analytical solution using legendre polynomial of order $n = 4$.

operating limits. It must be noted that all the investigated VS laminates, belongs to the family $\phi = 45^\circ$, and $T_0 + T_1 = 90^\circ$.

From figure 7.15, two favorable options have been found satisfying for our objective. They are $T_0 = 60^\circ$ and $T_0 = 75^\circ$ (marked in red circle). As, $T_0 = 75^\circ$ has a higher maximum out-of-plane displacement than $T_0 = 60^\circ$, with the snapping voltage within the operational limits of the MFC actuator. The snap-through voltage

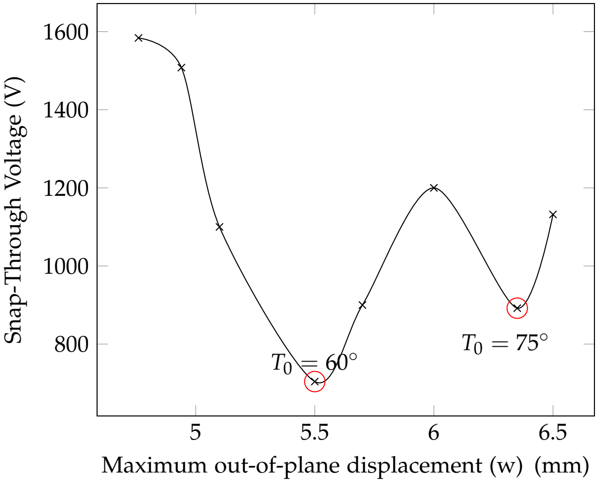

FIGURE 7.15: Parametric study to calculate snap-through voltages and out-of-plane displacements for different VS laminates. The points marked indicate VS laminates with preferable design. Both of them require low voltage for snap-through and show high out-of-plane displacement.

of $T_0 = 75°$ is found to be 892 V. On the other hand, straight-fiber laminate required 1584 V to snap.

It must be noted that all the corner points of VS laminates did not exhibit the same out-of-plane displacements. For example, the two opposite corners of VS laminate $[45\langle -75| -15\rangle/45\langle 75|15\rangle]$ showed an out-of-plane displacement of 6.37 mm and 3.36 mm. In straight fiber laminate, all corner points showed an out-of-plane displacement of 4.76 mm.

The multiple snap-through events, as noticed in the experiments for straight fiber laminates, could also be captured in the FE analysis of VS laminates. As shown in figure 7.16, one set of opposite corner points first snaps followed by the other set. In Fig. 7.16b, the opposite corners A and C snaps, followed by the corners B and D. This is in contrast with what was observed for straight fiber laminates shown in the Section 7.4.1, where the first adjacent set of corner points snapped (A and B) followed by the rest (C and D).

7.5 Conclusions

In this chapter, the analytical formulation described in chapter-6 is extended to include actuators. Further, a numerical model is developed to verify the analytical model. Both models comprise of three steps: the cool-down of the laminate, the bonding of the actuators on the laminate and finally the application of voltages to allow snap-through and snap-back. The models are first validated by the ex-

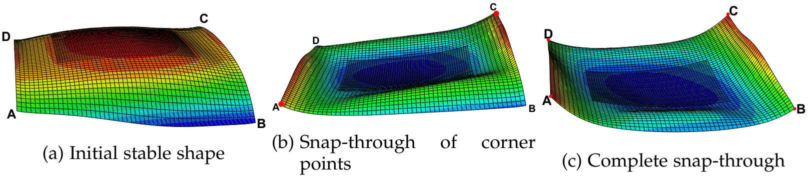

(a) Initial stable shape (b) Snap-through of corner points (c) Complete snap-through

Figure 7.16: Figure showing the intermediate multiple snap-through process VS$[45\langle -75| -15\rangle/45\langle 75|15\rangle]$, where initially opposite corners A and C snap and consequently lead to complete snap-through.

perimental approach presented by Schultz et al. [188], which was conducted for a cross-ply laminate. The proposed analytical model, using 4^{th} order Legendre polynomial showed significant improvements over the predicted values using the uniform curvature model presented by Schultz.

A parametric study was further carried out using the semi-analytical approach, to calculate the snapping voltage and the maximum out-of-plane displacements for several VS laminates. The tailoring capabilities using VS laminates for reducing snapping voltages can be well substantiated from the obtained results. As it was observed in the previous chapter that certain VS laminates yielded similar bistable shapes as cross-ply laminates, but with lower snap-through loads. In this chapter, we observed similar outcomes. For example, $[45\langle -75| -15\rangle/45\langle 75|15\rangle]$ lead to 43.6% decrease in snap-through voltages, with in-fact higher maximum out-of-plane displacements than straight fiber laminate. As the snapping mechanism using a concentrated mechanical force and using actuators are different, the same VS laminates demonstrated a different trend in load/voltage reduction. We conducted a parametric study to calculate the snap-through loads for a range of VS laminates in chapter-6 and snap-through voltages in this chapter. The VS laminates demonstrating the lowest snap-through loads did not necessarily show the lowest snap-through voltages.

The semi-analytical tools discussed in Chapter-4, 5, 6 and 7 facilitated the understanding of the multistable behaviour of VS laminates. This allowed us not just to understand the underlying mechanics but also to advance into designing and analysing more complex structures. From the basic understanding that we gained from the semi-analytical tools, the next step is to analyse structures with more complex layups and geometries using numerical tools.

8

Analysis of Bistable VS Rectangular Plate with Actuators

8.1 Introduction

Relying on the extensive analysis of VS laminates using semi-analytical and FE approach in the preceding chapters, we progress towards exploring the capabilities of such multistable laminates in the envisaged morphing concept. In this chapter, we design a rectangular bistable plate that would later be integrated into a morphing trailing edge flap (Chapter 9).

A rectangular composite plate with a layout of seven distinct sections is adopted [7]. It exhibits two stable shapes: curved and straight. Such a particular layup is used because both the stable shapes lead to straight edges, which is crucial for embeddability in a larger structure. The central section of the rectangular plate consists of a unsymmetrical laminate, engendering bistability in the whole plate. The behavior of the plate is also studied by replacing the central section with VS laminates.

Insights obtained from previous investigations (chapter-6 and chapter-7) in the snap-through process of both using mechanical force and actuators serve as a basis for this study. An analytical treatment for such a plate with distinct sections having different layups is complicated as the resulting displacement field is quite inhomogeneous. Therefore, the numerical tools developed in the previous chapters are extended to analyze such multistable rectangular plates. The numerical tools are investigated for two actuation mechanisms: a) by applying mechanical forces b) by using actuators. In both these cases, numerical methods have been verified with previously derived semi-analytical approaches.

Applying a concentrated mechanical force to snap is a relatively straightforward task, but adding actuators is rather challenging. For a square plate analyzed in the previous chapter, we saw the MFC actuators were placed at the center of the plate. The top actuators were placed orthogonally with respect to the bottom actuator. However, unlike the square plate, the two stable shapes of the rectangular plates

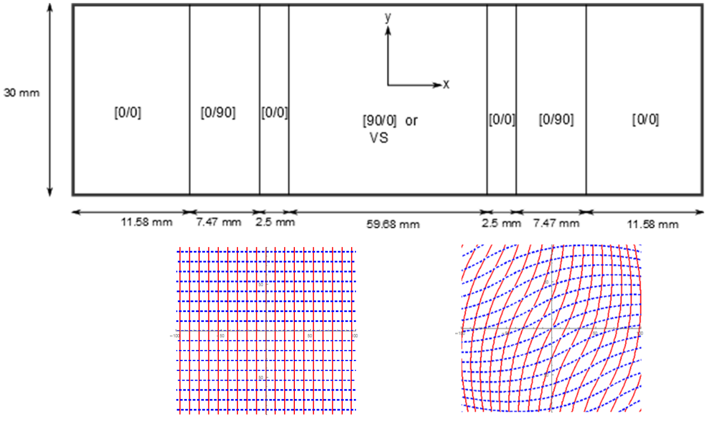

Straight Fibers

Curvilinear Fibers

FIGURE 8.1: Layout of the multistable rectangular plate.

are not similar. The actuators located at the center of the plate were found not ideal for triggering snap-through.

Parameters such as the size and location of the actuators play a crucial role in influencing the snap-through process. Larger actuators can increase the stiffness of the plate to such an extent that it can lead to even loss of bistability. Smaller actuators, on the other hand, cannot generate enough strain to trigger snap-through. Furthermore, placing the actuators at specific locations allows the most effective actuation authority.

To address such intricate dependencies, we make use of an extensive parametric study and consequently an optimization algorithm to calculate the optimal size and position of the actuators. Due to a large number of design variables, we disjointly conduct the optimization process for the two snap-through process (Shape-1 → Shape-2 and Shape-2 → Shape-1). The optimal location of the actuators for the straight fiber laminate plate as well as for the plate constituting a part with VS laminate is found out and compared.

8.2 Layout of the multistable rectangular plate

The structural layout of the multistable laminate is chosen such that the edges of the two stable shapes remain significantly straight, allowing embeddability in a larger structure. Designs with curved bistable edges can result in unfavorable moments when clamped, leading to a loss in curvatures or even in bistability. The layout suggested by Arrieta et al. [7] serves as a basis for the design of the plate chosen in this study. The length of the rectangular plate is chosen depending on the location it is embedded. The same aspect ratio of the whole plate and the ratio of the internal sections is maintained as Kuder et al. [125]. Kuder et al. had conducted an extensive parameteric study on the aspect ratio and the internal sizing of such plates.

The geometry of the investigated rectangular plate is illustrated in Figure 8.1. As observed in the figure, the plate comprises of different sections with two layers of carbon fiber reinforced polymer prepregs, having orientations of 0° and 90°. The central part of the plate, which initially constituted of $[0°/90°]$ plies in Arrieta's model, is additionally analyzed for VS laminates. The thickness of each laminate ply is chosen to be 0.124 mm, which was decided after a series of investigations.

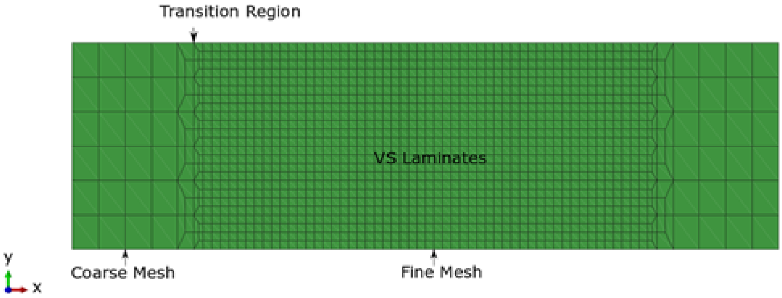

FIGURE 8.2: Adopted mesh for the rectangular bistable plate.

8.3 Numerical model

The finite element modeling of VS laminates in general requires a fine mesh size to accurately describe the curvilinear fiber paths (as shown in Chapter 4). However, as mentioned earlier, this rectangular bistable plate is designed to be integrated into a larger morphing structure. Usually, to reduce computational costs, a larger structure requires a coarser mesh scheme, when compared to a bistable VS plate. In order to integrate the bistable plate with the flap, the nodes from the flap should overlap with the nodes at the embedded bistable plate. Otherwise, it can lead to numerical issues at the contact points. A coarse mesh in the bistable VS plate can lead to an inaccurate description of the curvilinear fiber paths. Therefore, a meshing technique is adopted in the bistable plate where the mesh size changes from coarse at the edge (matching with the flap mesh size) to fine at the center part of the plate consisting of curvilinear fibers (Figure 8.2). Additionally, there is a transition region, as shown in Figure 8.2, where suitable connectivity of the mesh is adopted to allow consistent transfer of stresses between the coarse and the fine mesh. The connection between the flap and the bistable plates is further described in the next chapter.

A static nonlinear finite element analysis is carried out to simulate the cool-down process of the bistable plate, from curing to room temperature. Suitable damping was introduced when necessary for convergence. A total of 3648 four-node quadrilateral S4R shell elements are used to discretize the plate. The material properties of the laminate can be found in below:

$$\begin{gathered} E_1 = 161\,\text{GPa},\ E_2 = 10\,\text{GPa},\ G_{12} = 4.4\,\text{GPa} \\ \nu_{12} = 0.3,\ \alpha_1 = -1.8 \times 10^{-8}/^\circ\text{C},\ \alpha_2 = 3 \times 10^{-5}/^\circ\text{C} \end{gathered} \tag{8.1}$$

A temperature difference of $\Delta T = 140^\circ$ is applied to induce residual thermal stresses, resulting in two stable shapes, when cooled from curing to room temperature.

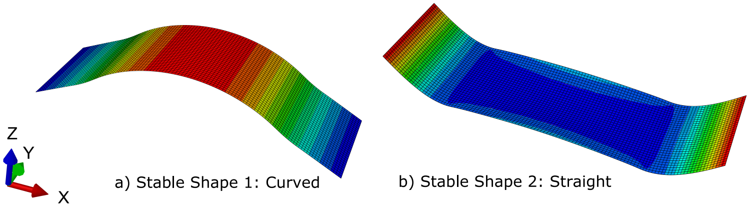

a) Stable Shape 1: Curved

b) Stable Shape 2: Straight

Figure 8.3: Stable shapes of the multistable laminates.

As shown in Fig. 8.3, the designed rectangular plate yields two stable shapes. As the plate cools down from the curing to room temperature ($20^\circ C$), it exhibits a curved stable shape. This rectangular plate shows an asymmetric multistability, as discussed in chapter 3 (figure 3.6). The curved stable shape has a lower energy state, and therefore occurs naturally after the cool-down process. Using a snapping mechanism, the second straight stable shape is obtained. It can be observed from 8.3, that the edges are straight in both stable shapes and no significant curvatures occur near the edges.

Similar shapes are also obtained using the rectangular plate comprising of the VS laminates. Figure 8.4 shows a comparison of the two stable shapes between the straight fiber laminate and the VS laminates. The curved stable shapes are depicted in Figure 8.4a and the straight stable shapes in Figure 8.4b. As observed in the figure, the cool-down stable shapes obtained from different VS laminates and straight fiber laminate are similar to each other, with small differences in the out-of-plane displacements. As the laminate VS-1 do not exhibit bistability, it is not included in the plots. All of these VS laminates belong to the family: $\phi = 45^\circ$ and $T_0 + T_1 = 90^\circ$. This confirms our observations from previous chapters, where such square laminates have been shown to yield similar shapes as cross-ply laminates.

8.4 Analysis of actuation mechanisms

Shapes of the multistable laminates can be changed either using mechanical forces or by applying voltages in actuators. There are certain advantages and disadvantages to both mechanisms. Applying mechanical force does not have any effect on the

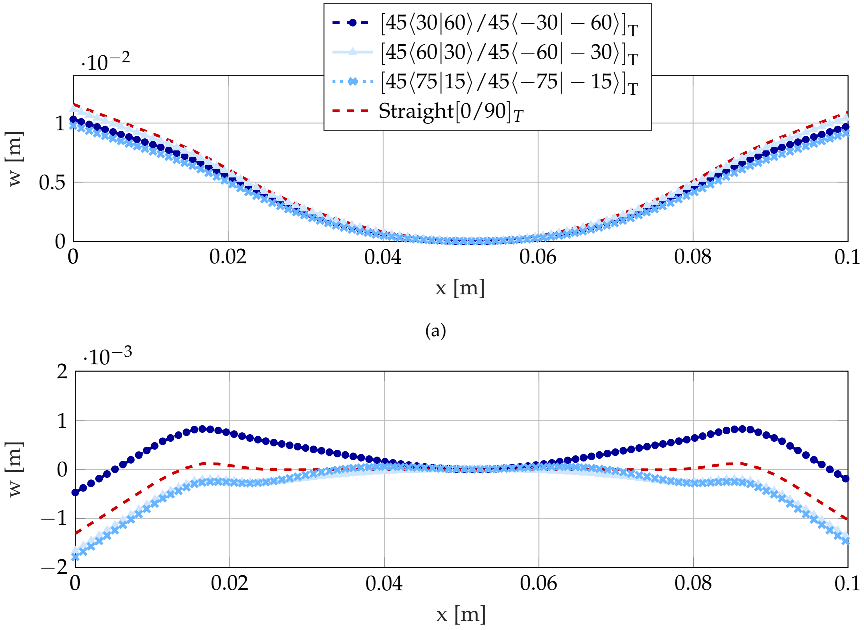

(a)

(b)

FIGURE 8.4: Out-of-plane displacement (w) at the section $y = 0$ for a) curved stable shape b) straight stable shape. Coordinate system can be found in Fig. 8.1.

stable shapes of the plates, and is therefore advantageous in retaining the actual multistable shapes of the plate. However, mechanisms involving mechanical force could be cumbersome to adopt on the multistable plates integrated in a flap. Actuators, on the other hand, can be easily integrated into the multistable plates and accomplish morphing. However, due to the added stiffness, they can lead to significant reduction of the curvature of the multistable plates. This can have a depreciating effect on the tip deflection of the trailing edge flap.

Complementing our studies on bistable square laminates from previous chapters, we carry out the snapping mechanism using two approaches a) applying force and b) using MFC actuators. A non-linear FE model is developed to investigate the snap-through using the two approaches. The following steps are performed in the FE framework:

1. Cool-down of the embedded bistable rectangular plate from curing to room temperature. During this process, the rectangular plate changes into one of the bistable shapes due to the generation of residual stresses.

2. A force on the center node of the plate or voltage on the actuators is applied, to trigger snap-through and snap-back.

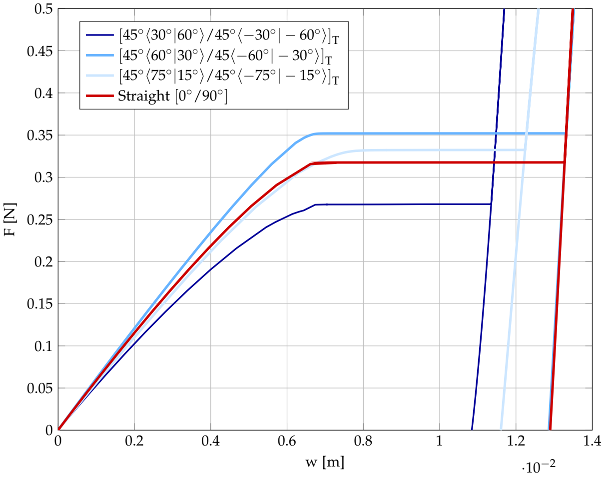

FIGURE 8.5: Load-displacement curve on applying a concentrated force at the center of the plate.

3. The applied force/voltage is removed so that the plate remains in the other stable shape.

8.4.1 *Applying mechanical force*

Figure 8.5 shows the load-displacement plot for different VS laminates and the straight fiber laminate using force controlled method with stabilization technique (for details on the FE technique refer section 4.3. It is observed that certain VS laminates have lower snap-through loads than straight fiber laminates. The laminate VS-2 shows the lowest snap-through force requirement among the investigated plates. If compared to straight fiber laminate, there is a reduction in the snap-through load of 15.7%.

8.4.2 *Applying voltage through MFC actuators*

As previously discussed in chapter 7, MFC actuators are more suitable to accomplish morphing of bistable plates in a realistic scenario. However, unlike square plates, the rectangular plates manifest two very different bistable shapes (figure 8.3). This makes the task to design the actuators, quite challenging. The size and location of the actuator play a crucial role in the snap-through process, and on the bistable nature of the plate.

The size of the actuators plays a crucial role in the snap-through process and on the multistable nature of the plate. Larger MFC patches can add additional stiffness

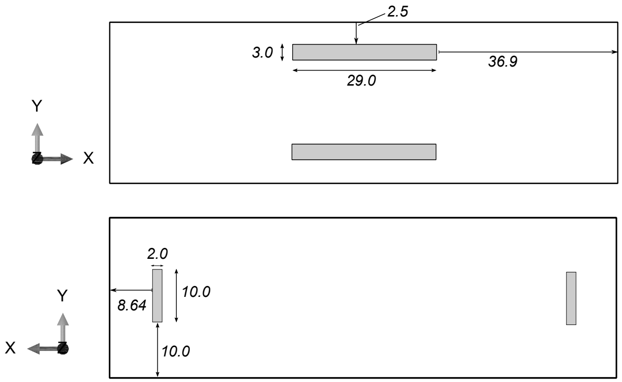

FIGURE 8.6: Arrangement of the MFC patches in multistable rectangular plate for snap-through and snap-back, as result of a parametric study. This is referred as 'Design-A'.

and thus reduce the principal curvatures of the stable shapes. In severe cases, the plate can completely lose bistability, which is undesirable. Smaller actuators, on the other hand, cannot generate enough strain to trigger snap-through. This contradictory requirement is aptly described in Portela et al. [171], where only a small design region is present that can lead to successful snap-through without the loss of bistability. Additionally, it has been observed from previous studies [4] that it is not just the size but also the location of the actuators that play a vital role in the snapping process. Therefore, to solve these conflicting requirements, there is an apparent need for optimization.

However, to reduce the number of design variables for the optimization problem, a parametric study is conducted to fix the size of the actuators following the approach described in [4]. Different sizes of actuators are investigated in search of solutions that lead to two-way snap-through but without the loss of multistability. With each test size the location of the actuators are varied from center to the edge of the multistable plate. A suitable design is found where a total of four actuators are used, two on the top and two on the bottom of the rectangular plate. The size and location of the actuators found are illustrated in figure 8.6. The size of the actuator used is 29 mm × 3 mm for the top actuators and 10 mm × 2 mm for the bottom actuators (as shown in figure 8.6). This is referred hereafter as 'Design-A'. Using this particular size and location of the actuators, the multistable nature of the plate was retained and lead successfully two-way snap-through.

Figure 8.7 illustrates all the steps involved in an FE analysis of this rectangular plate with 'Design-A'. The initial plate, when subjected to the thermal load, cools to a curved stable shape. Once the actuators are added, as expected, the curvature is reduced (depicted as stable shape-1 in figure 8.7). The application of voltage triggers snap-through. When the voltage is removed, the plate rests back to the straight stable shape (depicted as stable shape-2 in figure 8.7), affirming the multistable nature of the plate.

However, Design-A required high snap-through loads, which are outside the operating range prescribed for MFCs. To further reduce the snap-through loads, an optimization is required to calculate the location of the actuators that can trigger snap-through within the prescribed operating range.

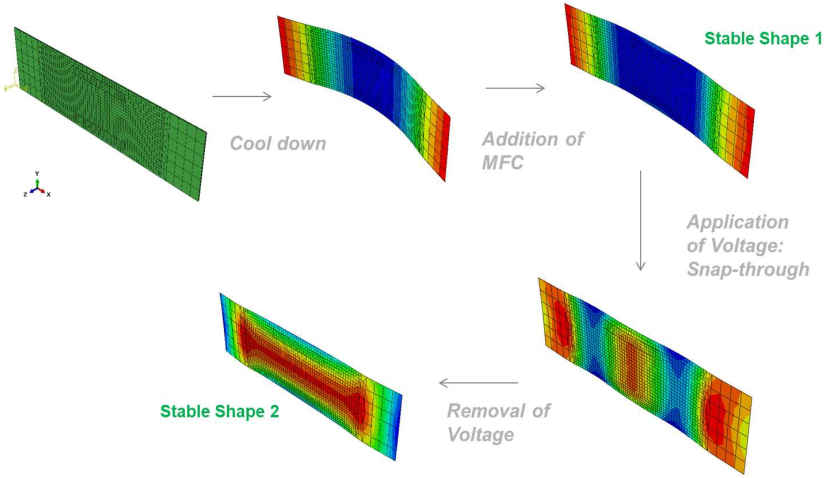

Figure 8.7: Stable shapes of the multistable laminates with MFC actuators for snap-through and snap-back.

8.5 Optimization of actuated bistable laminates

Although from 'Design-A', actuators lead to snap-through and snap-back without the loss of bistability, the voltages required are found to be outside the operating range of the actuators (+1500 V to -500 V). It is observed that it is not only the size of the actuators but also the location, that influence the curvature of the bistable shapes as well as the snapping voltages. From the parametric study in the previous section, a suitable size of the actuators was already found. The same size of the actuators is used, but now calculate the optimal location of the actuators using a derivative-free optimization scheme.

From the parametric study in the previous section, a suitable size of the actuators is already found. In this section, an optimization scheme is presented to calculate the optimal location of the actuators. An ideal optimization problem would consist of design variables as coordinates of the corner points for all the actuators. With this, a full design space can be covered considering all feasible size, location, and inclination of the actuators with respect to the coordinate axes. However, this would

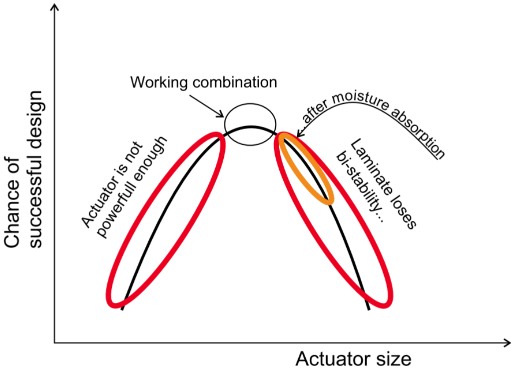

Figure 8.8: Conflicting design requirements of MFC actuated bistable plate. (Portela et al. [171].)

result in a large number of associated design variables that can inherently make the optimization problem difficult to converge. To simplify the given problem, suitable generalizations are considered. We assume a) the top actuators are aligned parallel to the x axis b) the bottom actuators are aligned parallel to the y axis c) the two top actuators are placed symmetrically (both with respect to x any y axis), and so are the bottom actuators.

The optimization problem is solved first a) for single objective optimization, where the objective is to maximize the out-of-plane displacements, b) multi-objective optimization where both objectives of minimizing snap-through voltages and maximizing out-of-plane displacements are considered.

8.5.1 *Single objective optimization*

As a first step, we solve the optimization problem with the objective of maximizing out-of-plane displacements. In other words, we find the minimization for the negative of the out-of-plane displacements. We solve the scalar, bounded, unconstrained, non-linear and derivative-free optimisation problem:

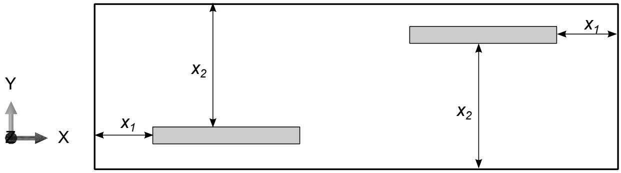

Figure 8.9: Design variables for the optimization of the top acuators.

$$\text{minimise } f(\boldsymbol{x}) \text{ for } \boldsymbol{x} \in \mathbb{R}^n, \tag{8.2}$$

where f is the scalar objective function and the vector $\boldsymbol{x}$ comprises n design variables. The design variables are the position of the top actuators (as depicted in figure 8.9), which are bounded by the edge of the rectangular plate. The bottom actuators are not considered in this section for the optimization process. The position of the bottom actuators is adopted, as shown in figure 8.6. The positioning of the actuators is assumed to be symmetrical with respect to x and y axis. The space of the design variables is bound to the volume of a hypercube:

$$\boldsymbol{x}_{\text{lb}} \leq \boldsymbol{x} \leq \boldsymbol{x}_{\text{ub}}, \tag{8.3}$$

where $\boldsymbol{x}_{\text{lb}}$ and $\boldsymbol{x}_{\text{ub}}$ are the lower and upper bounding vectors. In this work, we do not consider any constraints to the optimisation problem.

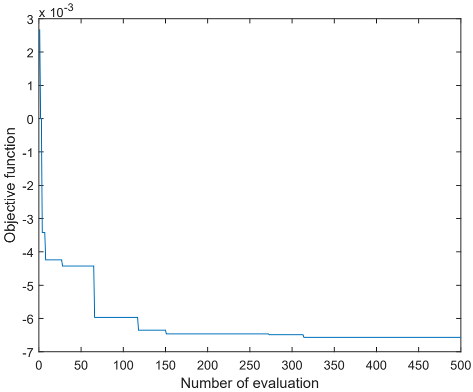

FIGURE 8.10: Convergence of the single-objective optimization scheme. The algorithm converges to the optimal solution at around 320 evaluations.

The global pattern search algorithm optimization scheme is an approach within the class of deterministic, derivative-free global algorithm. This is used to achieve a global optimization where the used algorithm tracks the number of T globally best coordinates. This can be interpreted much like the population size in a meta-heuristic algorithm: Small populations tend to local convergence with few objective function evaluations, whereas large populations tend to explore the design variable space more globally, but also lead to more objective function evaluations. In each iteration, the list of globally best coordinates - the so-called 'hall of fame' $\boldsymbol{H}$ - is updated and sampling is continued using the current set of best coordinates. The first sampling point for this scheme is always at the center of the variable design space. When the objective function is evaluated for a coordinate $\boldsymbol{x}$, the result $y = f(\boldsymbol{x})$ is stored in a

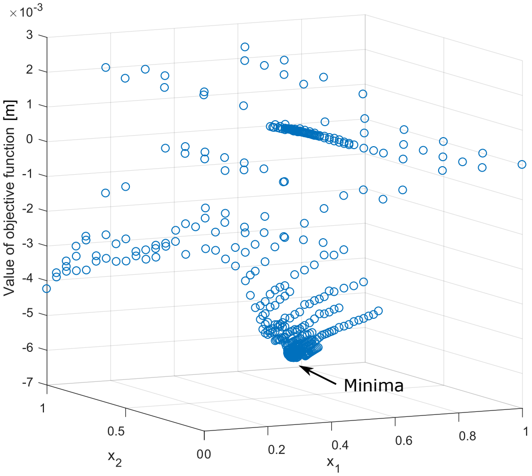

Figure 8.11: The design variable space showing all sampling points computed during optimization run.

cache which prevents redundant evaluations of the objective function. The detailed discussion on the optimization algorithm lies outside the scope of this work and therefore, is not discussed here. Further details on the optimization scheme could be found in [97]. Figure 8.10 shows the convergence behavior of the optimization scheme. It reaches a converged solution after 320 iterations. Figure 8.11 illustrates the design variable space showing all the sampling points computed during the optimization run. A clear minimum can be observed from the figure where a large number of evaluations have been carried out, where convergence occurred.

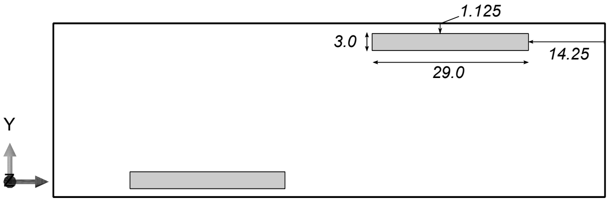

Figure 8.12: Optimal location of the top actuators with the single objective of maximum out-of-plane displacement (All units in mm). With such a layout of actuators, a maximum displacement of 6.7 mm was achieved. All measurements shown in the figure are in *mm*.

Figure 8.12 shows the optimal location of the top actuators, resulting in a maximum out-of-plane displacement. In comparison with the initial design (Design A), which had an out-of-plane displacement of 2.9 mm whereas, the optimal configura-

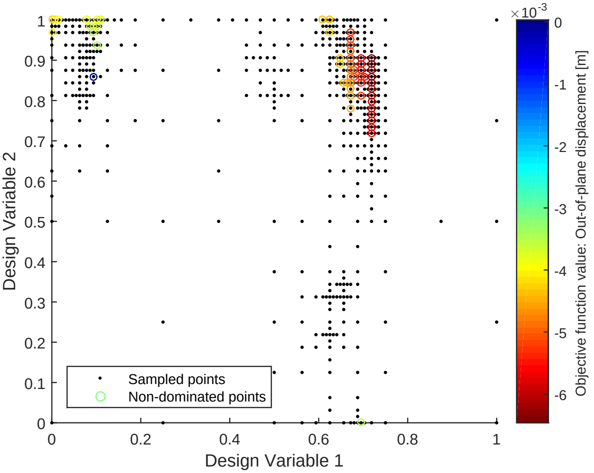

FIGURE 8.13: The plot shows the design space of the problem as the optimizer progresses towards the optimal solution. The design variable 1 and 2 refers to the scaled x and y coordinate of the actuators for this problem. The investigated plate comprises of straight cross-ply laminates. The clustered points in red depict the points leading to maximum out-of-plane displacements, which conforms with the optimal point found for the single objective function shown in the figure 8.11.

tion has an out-of-plane displacement of 6.7 mm. Figure 8.10 shows the convergence behavior of the optimization scheme. It reaches a converged solution after 320 iterations. Figure 8.11 illustrates the design variable space showing all the sampling points computed during the optimization run. A clear minimum can be observed from the figure.

However, higher out-of-plane displacements came at the cost of higher snap-through voltages. The snap-through voltage for Design A and the optimal design is $2950V$ and $4906V$ respectively. However, both of them are outside the operating limit of the actuators. Therefore, it is important that in the optimization problem, the snap-through and snap-back voltages are also considered as objectives.

8.5.2 *Multi-objective optimization*

As a next step, we extend the optimization scheme to a multi-objective formulation. We not only prescribe the out-of-plane displacements as the objective function but also include the snapping voltages. We employ a multi-objective global pattern search algorithm, which is an extension of the previously described deterministic algorithm, with the following objectives a) minimize the snapping voltages b)

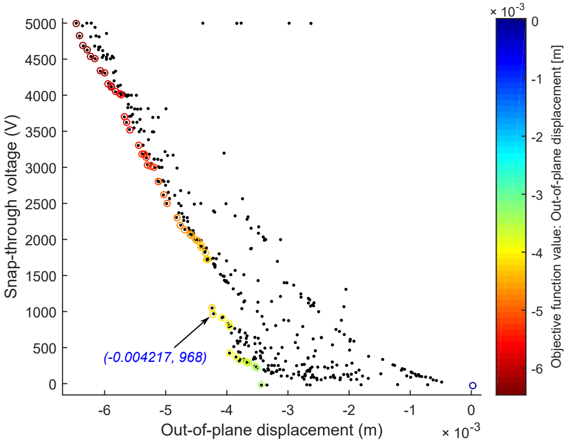

FIGURE 8.14: Depiction of the pareto-front in the multi-objective optimization problem for the bistable plate comprising of straight cross-ply laminates. The indicated point shows the best trade-off satisfying both the objective functions.

maximize the out-of-plane displacements. The scalar, bounded, unconstrained, non-linear and derivative-free optimisation problem can be written as follows:

$$\text{minimise } \boldsymbol{f}(\boldsymbol{x}) \qquad \text{for } \boldsymbol{f} \in \mathbb{R}^m, \boldsymbol{x} \in \mathbb{R}^n, \tag{8.4}$$

where $\boldsymbol{f}$ is the m-dimensional objective function and $\mathbf{x}$ comprises n design variables. The space of the design variables is bounded to the volume of a hypercube:

$$\boldsymbol{x}_{\text{lb}} \leq \boldsymbol{x} \leq \boldsymbol{x}_{\text{ub}}, \tag{8.5}$$

where $\boldsymbol{x}_{\text{lb}}$ and $\boldsymbol{x}_{\text{ub}}$ are the lower and upper bounding vectors. In this work, we follow the usual definitions for Pareto dominance, i.e. a point $\hat{\boldsymbol{x}}$ is on the Pareto frontier if there exists no point $\boldsymbol{x}$ such that $\boldsymbol{f}(\boldsymbol{x}) \preceq \boldsymbol{f}(\hat{\boldsymbol{x}})$ [116]. Simply put, for a two-objective problem this means that there must be no point to the lower or left of a point on the frontier, considering the objective space.

We solve the multi-objective optimization problem by scalarising the objective function. The 'scalarising' refers to converting the multi-objective problem with a vector-valued objective function into a single-objective problem with a scalar-valued objective function. The method we employ is the well-established linear scalarisation [102] also known as weighted sum method [151]. Additionally, the optimizer also enriches the population by adding the Pareto optimal samples using Pareto sorting.

The optimization process is conducted in two steps to reduce computational costs. As a first step, the bottom actuators are fixed at a particular location (same arrangement as Design-A shown in Fig. 8.6), and the coordinates of the top actuators are used as the design variables. From the first step, we find the optimal locations for the top actuators.

Figure 8.13 shows the design variable space showing all the computed points. The x and the y axes refer to the two design variables, namely the x and the y coordinates of the actuator. The different colors depict clustered regions where the optimizer identifies Pareto optimal solutions. It can be observed from figure 8.13 that the clustered region in red shows the maximum out-of-plane displacement with the leftmost point being equivalent to the point obtained for the single objective optimization shown in figure 8.11 (at point $x_1 = 0.72$ and $x_2 = 0.906$).

Figure 8.14 plots all the sample points in the objective value space, with the value of the two objective functions– snap-through voltages and the out-of-plane displacements. A Pareto front can be visualized in the figure, which consists of the leftmost and the bottom-most points. The front shows the trade-off between the two objective functions. Improving one of the objective functions can deteriorate the other when moving along the Pareto front. By visual inspection, the indicated point at the apex of the Pareto front is found to be the most appropriate solution. At this location of the top actuators, we get an out-of-plane displacement of 4.2 mm and snap-through voltage (968.7 V) which is within the operating limits of the MFC actuators.

The indicated point marked in Figure 8.14 can be better visualized in figure 8.15 a). This depicts the best location of the top actuators obtained from this step. It is located on the Pareto frontier, leading to maximum out-of-plane displacement and minimum snap-through voltages.

As a next step, we fix the position of the top actuators, from the results obtained from the first step, and consider the bottom set of actuators for optimization. The design variables are now the position of the bottom actuators, as shown in figure 8.16. Figure 8.15 b) depicts the optimal location of the bottom actuators. The complete optimization process ends up with the optimal location for the top and the bottom actuators.

In this optimization approach, we require only two design variables (x and y coordinates of a single actuator), in each optimization step. Only one coordinate is needed for the design variable, as we have already fixed the length and width of the MFC actuator from the previous parametric study. A more intricate optimization process involving four design variables at the same time (simultaneously considering the coordinates of both top and bottom actuators as design variables) is not considered in this work. The author found the adopted two-step optimization strategy more computationally efficient, though this might not cover the entire design space.

It must be noted that the optimal Design-B is found for straight fiber laminates, with the layout proposed in Arrieta et al. [7]. A similar approach is carried out to calculate the optimal location of actuators for VS laminates. However, the assumption that the actuators remain straight with respect to the laminate edges (as discussed in Section 8.5) is restricting for the case of VS laminates. The algorithm did not generate any improved results. The author found that the actuators, when aligned

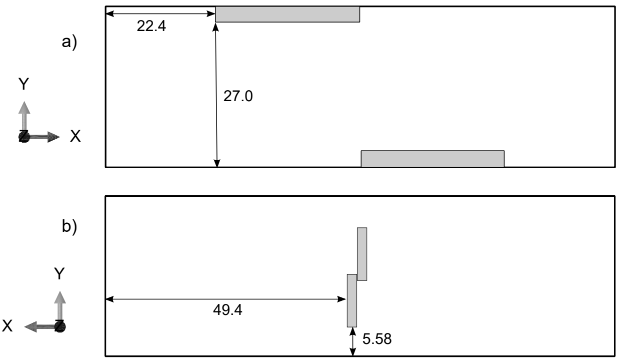

FIGURE 8.15: Optimal position of the MFC patches after carrying out multi-objective optimization in multistable rectangular plate for snap-through and snap-back. The plate comprises here of straight fiber laminates. This is referred as 'Design-B'.

to a certain angle with respect the plate edges, improved the actuation capability of the bistable plate. However, this required an additional design variable to be added in the optimization scheme, which increased the computational effort drastically. No converged optimal solution was found within a reasonable amount of runs.

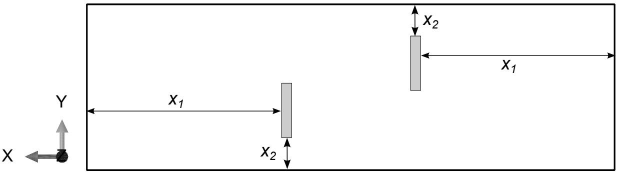

FIGURE 8.16: Design variables for the optimization of the bottom actuators.

8.6 Conclusions

In this chapter, we design a rectangular bistable plate consisting of seven distinct sections. This design was chosen so that the edges remain straight allowing easy integration to a larger structure. The dimensions of the plate are decided based on the morphing trailing edge flap discussed in the next chapter. Two different snapping strategies have been investigated a) using force and b) actuators. The central part of the plate was replaced with VS laminate to compare the difference in the snap-through loads. The VS laminate with layup: $[45^\circ\langle 30^\circ|60^\circ\rangle/45^\circ\langle -30^\circ|-60^\circ\rangle]$, was found to have 15.7% of the snap-through load reduction.

A detailed parametric study was conducted to identify the most appropriate size and location of the actuators on a straight-fiber multistable laminate. The location of the actuators was further improved using an optimization scheme. A two-level optimization procedure was carried out, where first the optimal location of the top actuators were found. Fixing the top actuators, consequently the optimal position of the bottom actuators were located. A significant improvement in the reduction of snap-through voltages was observed with optimal solutions. The optimal location of the actuators could be found only for straight fiber laminates.

9

Design and Analysis of Morphing Trailing Edge Flap

9.1 Introduction

[1] The preceding chapters have focused on different modeling techniques to analyze multistable laminates constructed from straight as well as curvilinear fiber paths. The previous chapter particularly aimed at the design of rectangular bistable plates, keeping in mind the ensuing morphing application for a wind turbine trailing edge flap. It has been observed that using VS laminates, the snapping voltages could be reduced. An improvement in snap-through load reduction was also made when the actuators were placed at an optimal location.

In this chapter, we make a transition from the plate level to a much larger morphing flap. In the first place, a morphing flap with integrated bistable plates is designed. The bistable plates studied in the previous chapter are utilized to realize the morphing of trailing edge flap. The design primarily focused on identifying a suitable location for the placement of the bistable plates, which can successfully deflect the trailing edge flap. It must be noted that the flap used here was taken from the *SmartBlades* project, where originally a servo-motor actuator was used to deflect the trailing edge flap.

By means of a numerical model, the proposed concept and the design is modeled and analyzed. The morphing of the flap was achieved using two different methods a) by applying a concentrated load at the center of the bistable plates b) using actuators on the top and bottom surface of the bistable plates. Upon snap-through of the bistable plates, the trailing edge flap deflects at a particular angle. Once the actuation force/voltage is removed, the flap stays in the deflected position. Thus, eliminating the need of a continuous supply of energy to maintain a particular position which is normally required in conventional actuators.

---

[1] This chapter is based on the conference proceeding: Haldar et al. [89]

A comparison of the flap's response was made between the bistable plates with straight fiber laminate and VS laminate. In this chapter, the employed VS laminates is a result of the investigations from previous chapters.

9.2 Design of morphing trailing edge flap

Different concepts of adaptive structures in large wind turbine blade have already been devised in the last few years. Active flaps are one such concept, that have great potential in reducing fatigue loads in wind turbine blades (Refer to chapter 1). In the German national research project *SmartBlades* (with German Research Alliance FORWIND with several industry partners), different concepts of active control have been studied. Oltmann [160] and later Bartels [15] devised the overall dimension of the flexible trailing edge flap for the reference blade used in the *SmartBlades* project. The design of the trailing edge flap is a result of a specialized wind energy code. The trailing edge flap constituted 25% chord length relative to the reference blade, with a span length of 10 m from 68 m (80.5 % of the blade radius) to 78 m (92.7 % of the blade radius) of the blade. The initial concept of the flap consists of two equal and opposite concentrated forces applied at two different points of a stringer, using servo motors. The gaps between the stringers and the flap spar are covered with elastomers. Further details of the concept can be found in Monner et al. [152]. Figure 9.1 shows the demonstrator having the chord length of 2 meters, which is equal to the mean chord length at outer and inner end of the reference blade (at 78 m and 68 m span of the blade respectively).

FIGURE 9.1: Demonstrator of a morphing trailing edge flap [152].

9.2.1 *Description of the concept*

The plates investigated and designed in the Chapter 8 are integrated in the morphing flap. The adopted composite plate design yields two stable shapes (as depicted previously in figure 8.3), one curved and the other straight. Both configurations have straight edges which makes it easy to integrate into a larger structure. We

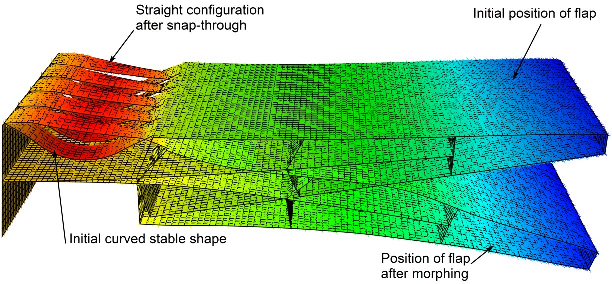

FIGURE 9.2: Morphing trailing edge concept using multistable elements (Exaggerated view).

propose here a design, where the bistable plate is attached to the rotor blade flap in its curved stable state. Figure 9.2 shows the exaggerated view of the morphing flap integrated with the bistable plates. Between the vertical spar which is fixed with the rest of the rotor blade, and the upper part of flexible trailing edge, the multistable elements are accomodated. The modelling and the numerical simulation was conducted employing MATLAB and PYTHON scripts in combination with a standard FE Solver (ABAQUS).

Once attached, the whole system is allowed to come to equilibrium.

The bistable plate snaps to the straight stable configuration as a force is applied or the actuators are activated. This results in an deflection of the flap. The flap returns to its original position when the multistable plate snaps back from the straight stable shape to the curved stable shape.

9.2.2 *Analysis of the morphing concept using numerical approach*

A numerical study has been conducted, and tested for the initial proof of concept. The finite element model of the flap consists of four-noded quadrilateral S4R shell elements with a mesh size of 5 mm. As discussed in the previous chapter, a certain meshing scheme was adopted for the bistable plates. The portion of the curvilinear fiber paths is discretized with a fine mesh, and the edge with a coarser mesh. The section comprising of the unsymmetric laminate is modeled using a finer mesh for better accuracy. As shown in figure 9.3, a transition region is modeled, which comprises of a mesh scheme to connect the finer mesh at the interior of the multistable plate with the coarser mesh near the edges. The element size at the edge is chosen such that it exactly matches the flap mesh size, thus avoiding numerical issues at the contact point. This is well elucidated in the figure 9.3. In the whole process, geometric nonlinearity is considered. For cases where convergence is an issue, appropriate numerical stabilization is also applied.

To induce the residual stresses in the multistable laminate, the fabrication process is carried out in a separate FE analysis, following the procedure described in 5.2.2

and 8.4. The curved stable shape attained after the cool-down process is imported in the flap model such that it fits at a desired location of the flap. The correct dimension of the initial rectangular plate is found by a parametric study such that its curved stable shape fits in the particular location of the trailing edge flap. The residual stress field of the bistable plate is imported as well, which is applied to the bistable as initial stresses. This step is crucial as it is the residual stress that imparts bistability in the plates. As seen from previous analyses conducted in Chapter-8, the rectangular multistable plate cools down in its curved stable shape. The multistable plates in its curved stable form is imported into the flap section. The bistable elements are attached to the flap section using the kinematic coupling of all degrees of freedom, except allowing rotation in the direction of the curvature of one of the stable shapes. It is important to note that the initial state is followed by a relaxation step so that the whole system comes into equilibrium once the bistable plate is attached to the flap.

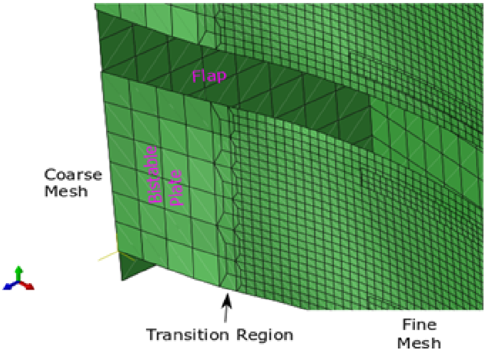

FIGURE 9.3: Scaled view near the contact point of the flap and the bistable plate. It also shows the adopted mesh scheme for the plates and the flap.

9.3 Snapping mechanisms of embedded multistable elements

As observed in the previous chapters, shapes of the bistable laminates can be changed either using mechanical forces or by applying voltages in actuators. There are certain advantages and disadvantages for both the mechanisms. Applying mechanical force does not have any effect on the stable shapes of the plates, and therefore advantageous in retaining the actual bistable shapes of the plate. However, mechanisms involving mechanical force could be cumbersome to adopt on the bistable plates integrated in a flap.

Actuators, on the other hand, can be easily integrated into the bistable plates and accomplish morphing. However, as discussed in chapter-7, due to the added stiffness, they can significantly reduce the curvature of the bistable plates. This can have a depreciating effect on the net deflection of the trailing edge flap.

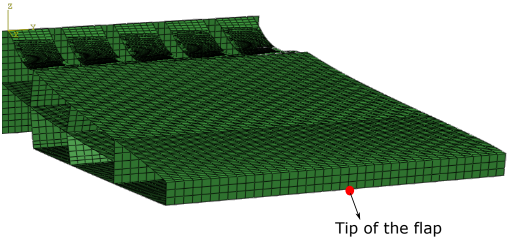

FIGURE 9.4: Tip of the morphing trailing edge flap.

9.3.1 *Applying mechanical force*

A concentrated load is applied at the center of all bistable rectangular plates. The load applied on the bistable plate versus the deflection of the morphing flap tip is plotted in Figure 9.5. For reference, the tip of the flap is illustrated in figure 9.4. The path A–B–C–D–E depicts the snap-through behavior of rectangular plate with straight fibers, whereas the path A'–B'–C'–D'–E' depicts that for a rectangular plate corresponding to VS laminate with layup:$[45^\circ\langle 30^\circ|60^\circ\rangle/45^\circ\langle -30^\circ|-60^\circ\rangle]_T$. This particular VS was found to reduce the snap-through loads in Chapter-8 (figure 8.5)

The point A/A' depicts the initial equilibrium state of the flap with the embedded bistable plates. Once the forces are applied, the bistable plates snap to the straight stable shape. This point can be observed at B–C/B'–C'. On subsequent application of the forces, the flap now moves in the other direction, to the direction of the force to reach point D/D'. At this point, the applied forces are removed. On removal of the forces, the bistable plates rest in the straight-stable shape, which is at the point E/E'. This shows the distinct advantage of using bistable elements embedded in the morphing trailing edge in an active manner, where a continuous supply of force/energy is not required. The distance A–E/A'–E' refers to the tip deflection due to the change in the stable shapes of the bistable rectangular plate. It can be clearly observed that the use of a VS laminate can lead to reduced snap-through forces, with some difference in the tip deflection.

9.3.2 *Using MFC actuators*

For a more practically feasible snapping mechanism, bistable rectangular plates with MFC actuators are used. In the previous chapter, we devised two designs: Design A, as an outcome of initial parametric study, and Design B, as a result of the multi-objective optimization. In the section, we integrate the bistable plates with both the designs and compare their individual performances.

The applied voltage on the actuators of the straight fiber rectangular plate, versus the tip defection of the trailing edge is plotted in Figure 9.6. The curve follows the path A-B-C-D-E-F. In Figure 9.6, point A refers to the initial state. Once the

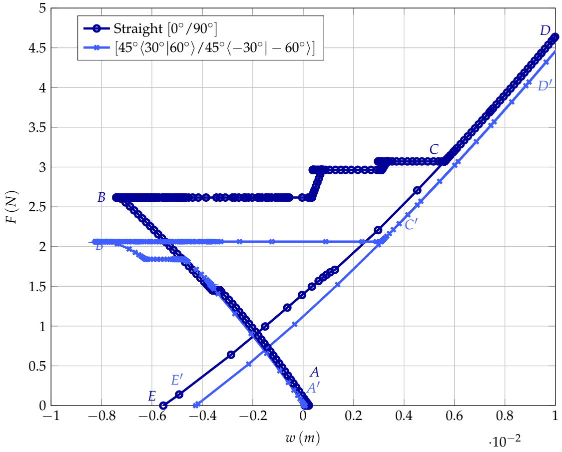

FIGURE 9.5: Load-displacement of the designed morphing trailing edge flap. The load F is applied at the center of a bistable plate, and the maximum tip displacement of the trailing edge flap is shown. A comparison between the load-displacement curve corresponding to bistable plates with a VS laminate and a straight fiber laminate is depicted.

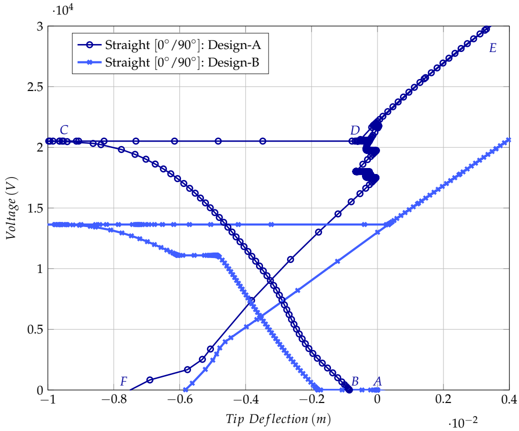

FIGURE 9.6: Voltage-displacement plot of the designed morphing trailing edge flap. The plot depicts the voltage V applied on the longitudinal MFC actuators v/s the maximum tip displacement of the trailing edge flap. A comparison is made between the voltage - tip displacement response of actuators placed at the center of the plate (Design A) and that of actuators placed at the optimal location (Design-B).

bistable plates are integrated to the flap, the MFC actuators are added and the residual stresses emanating from the curing process are allowed to redistribute

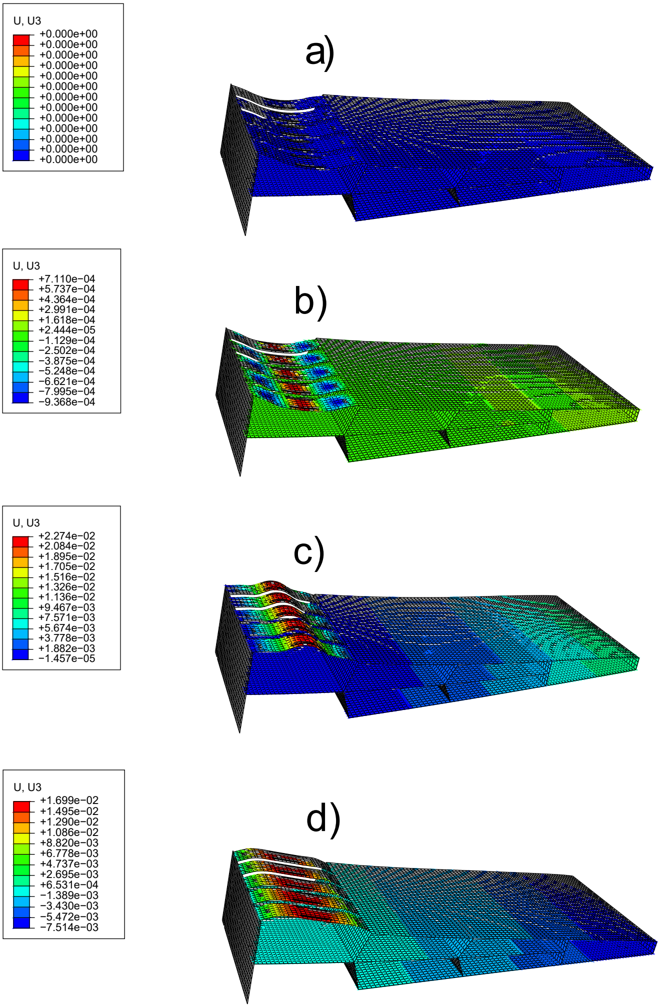

FIGURE 9.7: Contour plot of the out-of-plane displacement of the morphing trailing edge flap on the application of voltage on the longitudinal MFC actuators. The actuators on the rectangular multistable plates are placed according to Design-A a) The initial state of the trailing edge with the attached curved bistable plates b) The equilibrium state after attaching the bistable plates c) Application of voltage on the MFCs leading to snap-through d) Removal of the voltages and the bistable plates now remain in the straight stable configuration.

until the whole system comes to an equilibrium state. Due to this phenomenon, there is a small defection at the tip of the flap, which can be seen at point B. Once the voltages are applied on the longitudinal MFC patches, strains are developed, which in turn results in a curvature. Due to the difference in the layer properties, a curvature develops which subsequently causes the bistable plate to snap (Point C). This leads to a deflection in the trailing edge flap as seen in Figure 9.7. The corresponding voltage applied on the MFCs and the resulting tip deflection of the flap is depicted in Figure 9.6. As the voltage is switched off, the bistable plates remain in the second stable shape, thus maintaining the deflected state of the flap (point F). All the steps described have been visualized in Fig. 9.7. It must be noted that the intermediate jumps and plateaus are due to the local snapping phenomenon (can be perceived as local buckling) occurring especially in rectangular plates. An improved behaviour in regard to reduction of snap-through (37%) voltage can be observed for Design-B as shown in Fig. 9.6. Design-B has also lead to reduction in the out-of-plane displacement. The more out-of-plane displacements the multistable elements can display, the larger is the flap deflection.

Bistable plates with different VS laminates are also integrated in the flap. Figure 9.8 shows a comparison between the morphing flap with straight fibers and VS laminates, constructed using Design-A. Using certain VS laminates as expected, the snap-through voltage is decreased. It is also observed that the tip deflection of the flap also decreases as seen in figure 9.8. The investigated VS laminates, show significant improvement over the straight fiber laminate.

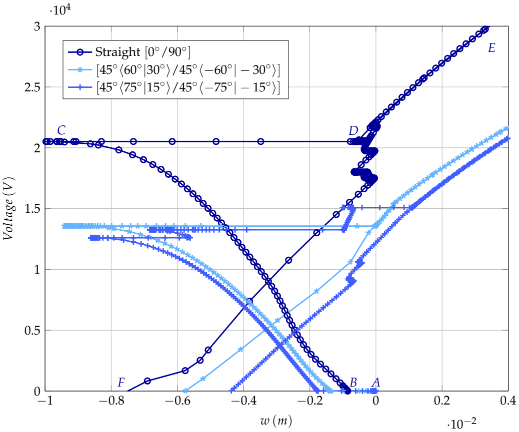

FIGURE 9.8: Voltage-displacement plot of the designed morphing trailing edge. The plot depicts the voltage V applied on the longitudinal MFC actuators placed according to Design-A v/s the maximum tip displacement of the trailing edge flap. A comparison is made between the straight fiber laminate and the VS laminate.

Several VS laminates are investigated with both Design-A and B, as shown in Table 9.1. Although Design-B was a result of multi-objective optimization for straight fibers, it was also used to investigate with VS laminates. The table shows a brief summary of the investigations carried out.

Laminate Layup	**Design-A**	**Design-B**
Straight fiber $[0^\circ/90^\circ]$	✓	✓
$[45^\circ\langle 15^\circ\vert 75^\circ\rangle/45^\circ\langle -15^\circ\vert -75^\circ\rangle]$	✓	*
$[45^\circ\langle 30^\circ\vert 60^\circ\rangle/45^\circ\langle -30^\circ\vert -60^\circ\rangle]$	✗	✓
$[45^\circ\langle 60^\circ\vert 30^\circ\rangle/45^\circ\langle -60^\circ\vert -30^\circ\rangle]$	✓	✓
$[45^\circ\langle 75^\circ\vert 15^\circ\rangle/45^\circ\langle -75^\circ\vert -15^\circ\rangle]$	✓	*

✓ Bistable
✗ Bistability is lost
* Converged solution not found

Table 9.1: Study on the bistability of different VS laminates and straight fiber laminate constructed using Design-A and Design-B, when integrated into the flap.

As the flap used was not particularly designed to incorporate the bistable plates. It could be observed that the voltage requirement in both straight fiber laminate and VS laminates for the current flap is much outside the operating limits of the actuators

9.3.3 *Morphing with reduced thickness*

In an attempt to trigger snap-through in the bistable plates within the operating range of the actuators, a redesign of the flap has been considered. In this design, the thickness of the flap is suitably reduced. This design does not account for critical parameters such as aerodynamic loadings required for designing a flap. However, in practice such structure is designed such that it is not activated by aerodynamic loading. Due to the flexible nature of the flap, calculation of aerodynamic pressure on it will require a coupled aeroelastic analysis. Such analysis is beyond the objective of the study. In this work, the proof of the proposed design concept is demonstrated using numerical tools.

A complete snap-through and snap-back have been manifested, leading to morphing of the flap and then returning back to the neutral position.

Using the reduced thickness of the flap, it is shown in figure 9.9 that both snap-through and snap-back can be accomplished using the designed bistable plate. The flap starts with the neutral position 'N' (as shown in figure 9.9). , where the bistable plates are in its the curved stable shape (with some initial deflection due to the added actuators). As the voltage is increased, at point 'ST' (around 1300 V), the snap-through occurs. Once the voltage is removed, the flap rests in the straight stable state, which can be seen at point P1. In the snap-back process, the other set of actuators are activated. Now, the flap at P1 position is actuated to reach at the point 'SB' (around -330 V), where the bistable plate is snapped back from the straight stable shape to the curved stable shape. Once the voltage is removed, the

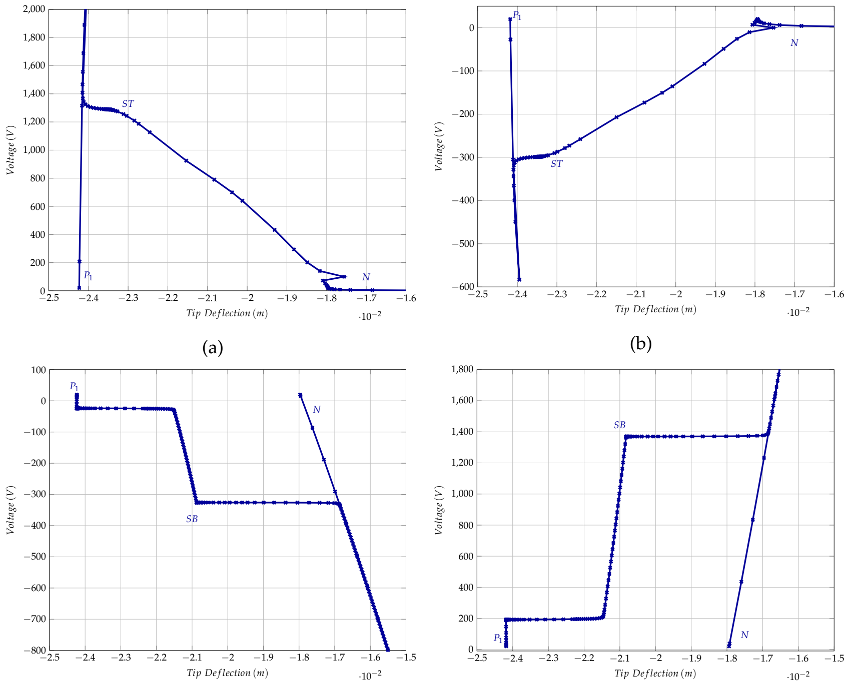

(a)

(b)

(c)

(d)

FIGURE 9.9: Voltage on the actuators v/s tip deflection of the flap as the multistable plate snaps from one stable shape to another. a), b) voltage on the top and bottom actuators respectively as the multistable plates snap from curved to straight shape, morphing the flap to a deflected shape; c),d) voltage on the top and bottom actuators respectively as the multistable plates snap from straight to curved shape, returning the flap back to the initial position. All the required snapping voltages are within the operating limits of +1500 to -500 V.

flap returns to the initial neutral position. Both the voltages are within the operating range of the MFC, which is from +1500V to -500V.

The FE analysis lead to successfully display of the morphing mechanism. However, the Design-B with VS laminates was not shown in this section, as no converged solution was found.

9.4 Conclusions

In this work, the design of a morphing trailing edge flap for a wind rotor blade is proposed using multistable laminates. A numerical model is developed to verify the proposed concept. In this design, bistable plates are used with both straight fiber and VS laminates.

Using mechanical force as an actuation method, the load required to snap the bistable plates v/s the tip deflection of the flap is plotted. It was found that certain VS laminates required lower loads to trigger snap-through and thereby morphing the flap at a particular deflection.

A similar analysis was carried out to snap the bistable plates using actuators. Two different designs for the placement of actuators were used (as described in the previous chapters: Design-A and Design-B). With Design-B, a significant reduction in the voltage requirement to snap the plates was observed. In addition, using design-A the results for straight fiber and the VS laminate were compared. As expected, certain VS laminates required lower snap-through voltages. However, the tip deflections were also reduced in the case of VS laminates, for both the actuation mechanisms.

On conducting a complete parametric study using Design-A and Design-B on the straight fiber and the VS laminate, it was found that certain VS laminates lost bistability when integrated into the flap.

From these numerical investigations, it is interesting to see that the proof of the concept is well verified. However, with this current design, the voltage requirement of the actuators to trigger snap-through was much outside its operating range. The design could be improved by including the bistable plates at other locations, which would involve redesigning the flap as a whole.

10

Summary, Conclusions and Future Work

10.1 Summary and Conclusions

To put it succinctly, this work can be largely divided into four different parts, with different objectives but in a mutually inclusive way. The following summarizes the work as wells concludes with essential findings.

- The first part comprises of a detailed state of art, motivation and theoretical background.

  An in-depth literature review of the different concepts used in load alleviation of wind-turbine blades was presented. An overview of the major EU and US projects on smart wind turbine blades was presented. Apart from that, a literature review on bistable plates (Chapter 2), with recent works of analytical and numerical treatment; and different actuation mechanism were presented as well. A theoretical background on the mechanics of unsymmetrical bistable laminates and how gauss egregium principal links geometry and mechanics is briefly addressed in Chapter 3. The introduction to equilibrium paths, VS laminates, and the DQM is also covered in this chapter.

- For the second part, VS laminates were systematically investigated using both semi-analytical and numerical tools (Chapter 4). The formulation was approximate, as uniform curvatures were assumed. The fibers in the VS laminates were varied linearly, from T_0 at the center to T_1 at the end of the plate. The bistable shapes predicted using the semi-analytical tools agreed well with FE results. There were however, some discrepancies at the edges of certain VS laminates. A parametric study was conducted for VS angle parameter $\phi = 0^\circ$ and $\phi = 45^\circ$, which revealed its rich design space, with the possibility of wide range of shapes. It was the first time that the family of VS laminates was recognized which yielded similar stable shapes as straight fiber laminates. For example, unsymmetric VS laminates with $\phi = 45^\circ$ and

$T_0 + T_1 = 90°$ resulted in bistable shapes similar to unsymmetric cross-ply laminates. This classification of VS laminate provides an additional possibility to any designer aiming for certain bistable shapes, to choose VS laminate configurations as an alternative to straight fiber laminates.

- Once the VS laminate configurations were recognized as bespoke to desired bistable shapes (with the morphing flap in mind), the next step was to model the snapping phenomenon, which is essential in the design of morphing structures with bistable laminates. This comprises the third part of the dissertation, where snapping loads (for Chapter 4 and Chapter 5) and snapping voltages (for Chapter 6) were predicted using semi-analytical formulations and numerical tools. The analytical framework introduced in Chapter 4, was extended to calculate the snapping loads of the VS laminates. Due to the inherent nonlinearity near limit point, UC assumption was quite restrictive leading to high discrepancies with respect to FE results.

  However, what emerged interesting from the numerical investigations, was the load tailoring capability of VS laminates. It was found that certain VS laminate lead to 45% reduction in the snap-through force as compared to straight cross-ply laminate, with 14% reduction in out-of-plane displacement. This property of tailoring snap-through loads is quite attractive for design of any morphing structure.

  To investigate further the snapping process for a large number of VS laminates, a fast yet accurate tool was required. Such a tool could help designers to map the entire design space easily, selecting favorable designs.

  It was previously demonstrated that the importance of solving the membrane problem for an accurate prediction of the behavior of bistable laminates [128, 213]. In chapter 6, the formulation used in Lamacchia et al. [128] was extended for VS laminates. Higher order Legendre polynomials were used, to predict the snap-through loads which were verified using FE tools. A good agreement with the FE results was achieved. With the development of this analytical model, the snap-through could be determined using a fast yet accurate tool.

  To get a better insight into the snap-through process, the deformation modes were investigated near the limit point. It was interesting to observe that different VS laminates have a different preferential mode of snapping. It is not just the difference in the stiffnesses in different VS laminates, but also the presence of location undulations on the surface, (as a result of the cool-down process) that leads to differences in the snap-through loads.

  In terms of practicability, applying force might not be a viable option in a larger structure, due to space constraints. The model used in Chapter 6 was extended in Chapter-7 to allow morphing using MFC actuators. The model comprised of three steps, crucial for determining the snap-through and snap-back voltages. This refined model showed significant improvement in the prediction of the snapping voltages with experimental and the FE results, when compared to the current available models in literature. A parametric study was conducted for exploring the potential design space, where VS laminates were identified exhibiting higher out-of-plane displacement but with the requirement of lower snapping voltages.

- The fourth part of the dissertation connected the concepts addressed in the last two parts and exemplified the technology in a morphing trailing edge flap of a wind turbine. A design was proposed, where several bistable rectangular plates were integrated into the morphing flap. A rectangular bistable plate was designed with several sections comprising of $[0^\circ/90^\circ]$ layup, and a VS laminate layup (Chapter 8). A multi-objective derivative-free optimization algorithm was used to find the optimal location of the actuators for straight fiber laminates, leading to lower snap-through voltages and large out-of-plane displacements.

  The designed bistable plates were then integrated into the morphing flap. Proof of the proposed concept was demonstrated using a nonlinear FE model. As the bistable plates were snapped from the curved to straight stable shape, it resulted in a deflection of the flap. However, as the flap used was not specifically designed for integrating bistable plates, the snapping voltages were found outside the operating limit. Therefore, the flap was redesigned by reducing the thickness at individual sections. With this design, we were able to demonstrate the deflection of the trailing edge flap as the bistable plates snapped. The trailing edge remained in the deflected position, without the need of a continuous supply of force/energy to hold it, making it unique when compared to other morphing concepts.

10.2 Scope of Future Work

EXPERIMENTAL STUDIES With the advent of advanced fiber placement technology, it is possible to manufacture bistable VS laminates. Experimental verification of the bistable shapes of VS laminates would certainly be interesting and the next step forward. Furthermore, the effectiveness of MFC actuators for morphing VS laminates could be studied experimentally.

DYNAMIC ACTUATION Few works in the past have highlighted the potential of using dynamic actuation for load reduction. The combination of exploiting VS laminates, with dynamic actuation is certainly an interesting topic to explore. The semi-analytical method proposed in this work could be easily extended to include the inertial effects of a dynamic problem. A systematic parametric study of the complete design space, could lead to design with the potential of even further reduction in snap-through loads.

AUGMENTED OPTIMIZATION STUDIES As mentioned in Chapter 8, the optimization algorithm used was limited to only two design variables. Increasing the number design variables, by uplifting the generalizations made could lead to improved solutions, covering a broader design space. However, a gradient-free optimization approach for this problem is inherently computationally expensive. The semi-analytical approach can be used to formulate an optimization problem with gradient-based algorithms. The sensitivity of the design variable could be determined using the semi-analytical formulation.

MULTISTABLE VS COMPOSITE SHELL It has been previously shown that the combination of initial curvature and the material anisotropy can lead to interesting regimes of design like tristability. The tristable design regions previously determined by Vidoli and Maurini [212], were limited to a narrow range of material parameters. Certainly, using VS laminates to design such structures gives the possibility to extend the previously obtained material parameter range.

ENSEMBLE DESIGN OF FLAP AND INTEGRATED BISTABLE COMPONENTS In this work, a trailing edge flap was used to demonstrate the proposed morphing concept with bistable elements. An ensemble design of the flap with bistable plates would be the next logical design step. This would require a redesign of the internal section of the flap. A systematic parametric study, exploring increased number of layers, would reveal suitable locations for embedding the bistable elements with actuators.

A

Stiffness Invariants

The invariants U_i relate to the single ply stiffness properties as:

$$\begin{aligned}
U_1 &= \frac{1}{8}\left(3\bar{Q}_{11} + 3\bar{Q}_{22} + 2\bar{Q}_{12} + 4\bar{Q}_{66}\right) \\
U_2 &= \frac{1}{2}\left(\bar{Q}_{11} - \bar{Q}_{22}\right) \\
U_3 &= \frac{1}{8}\left(\bar{Q}_{11} + \bar{Q}_{22} - 2\bar{Q}_{12} - 4\bar{Q}_{66}\right) \\
U_4 &= \frac{1}{8}\left(\bar{Q}_{11} + \bar{Q}_{22} + 6\bar{Q}_{12} - 4\bar{Q}_{66}\right) \\
U_5 &= \frac{1}{8}\left(\bar{Q}_{11} + \bar{Q}_{22} - 2\bar{Q}_{12} + 4\bar{Q}_{66}\right)
\end{aligned} \tag{A.1}$$

Using Equation 4.6 and 4.7, the ABD matrix yields:

$$\begin{aligned}
\left[A_{11}, B_{11}, D_{11}\right] &= U_1\left[t, 0, t^3/12\right] + U_2\left[V_1^A, V_1^B, V_1^D\right] + U_3\left[V_2^A, V_2^B, V_2^D\right] \\
\left[A_{22}, B_{22}, D_{22}\right] &= U_1\left[t, 0, t^3/12\right] - U_2\left[V_1^A, V_1^B, V_1^D\right] + U_3\left[V_2^A, V_2^B, V_2^D\right] \\
\left[A_{12}, B_{12}, D_{12}\right] &= U_4\left[t, 0, t^3/12\right] - U_3\left[V_2^A, V_2^B, V_2^D\right] \\
\left[A_{66}, B_{66}, D_{66}\right] &= U_5\left[t, 0, t^3/12\right] - U_3\left[V_2^A, V_2^B, V_2^D\right] \\
\left[A_{16}, B_{16}, D_{16}\right] &= \frac{1}{2}U_2\left[V_3^A, V_3^B, V_3^D\right] + U_3\left[V_4^A, V_4^B, V_4^D\right] \\
\left[A_{26}, B_{26}, D_{26}\right] &= \frac{1}{2}U_2\left[V_3^A, V_3^B, V_3^D\right] - U_3\left[V_4^A, V_4^B, V_4^D\right]
\end{aligned} \tag{A.2}$$

where V is defined as:

$$\begin{aligned}
V_1^{(A,B,D)} &= \int_{-t/2}^{t/2} \cos(2\theta) \left[1, z, z^2\right] \mathrm{d}z \\
V_2^{(A,B,D)} &= \int_{-t/2}^{t/2} \sin(2\theta) \left[1, z, z^2\right] \mathrm{d}z \\
V_3^{(A,B,D)} &= \int_{-t/2}^{t/2} \cos(4\theta) \left[1, z, z^2\right] \mathrm{d}z \\
V_4^{(A,B,D)} &= \int_{-t/2}^{t/2} \sin(2\theta) \left[1, z, z^2\right] \mathrm{d}z
\end{aligned} \tag{A.3}$$

where θ is the function of the spatial coordinates and t is the total thickness of the plate.

B

Expansion of the energy terms for the reduced analytical model

---

If $\boldsymbol{A}$ and $\boldsymbol{B}$ are matrices of size $m\times$n, where $[\mathbf{A}] = a_{ij}$ and $[\mathbf{B}] = b_{ij}$ the Hadamard product is given as:

$$(\mathbf{A} \circ \mathbf{B}) = [a_{ij} b_{ij}] \tag{B.1}$$

The Kronecker delta product of a matrix $\mathbf{A}$ of size $m \times n$ where $[\mathbf{A}] = a_{ij}$ and matrix $\mathbf{B}$ of size $p \times q$ is defined as:

$$\mathbf{A} \otimes \mathbf{B} = \begin{bmatrix} a_{11}B & \dots & a_{1n}B \\ \vdots & \ddots & \vdots \\ a_{m1}B & & a_{mn}B \end{bmatrix}$$

The value of $\mathbf{P}, \mathbf{Q}, \mathbf{R}, \mathbf{S}$ and $\mathbf{T}$ from Eq. 6.43 is given as follows:

$$\begin{aligned} \mathbf{P} = \int_{-1}^{1} \int_{-1}^{1} \frac{1}{2} \big(& A_{11} \circ (N_1)_{xx} \circ (N_1)_{xx} + A_{12} \circ (N_1)_{xx} \circ (N_1)_{yy} + \\ & A_{13} \circ (N_1)_{xx} \circ (N_1)_{xy} + A_{21} \circ (N_1)_{yy} \circ (N_1)_{xx} + \\ & A_{22} \circ (N_1)_{x} \circ (N_1)_{xx} + A_{23} \circ (N_1)_{yy} \circ (N_1)_{xy} + \\ & A_{31} \circ (N_1)_{xy} \circ (N_1)_{xx} + A_{32} \circ (N_1)_{xy} \circ (N_1)_{yy} + \\ & A_{33} \circ (N_1)_{xy} \circ (N_1)_{xy} \big) \, d\tilde{x} d\tilde{y} \end{aligned} \tag{B.2}$$

$$
\begin{aligned}
\mathbf{Q} = \int_{-1}^{1}\int_{-1}^{1} \big(& A_{11} \circ (N_1)_{xx} \circ (N_2)_{xx} + A_{12} \circ (N_1)_{xx} \circ (N_2)_{yy} + \\
& A_{13} \circ (N_1)_{xx} \circ (N_2)_{xy} + A_{21} \circ (N_1)_{yy} \circ (N_2)_{xx} + \\
& A_{22} \circ (N_1)_{yy} \circ (N_2)_{yy} + A_{23} \circ (N_1)_{yy} \circ (N_2)_{xy} + \\
& A_{31} \circ (N_1)_{xy} \circ (N_2)_{xx} + A_{32} \circ (N_1)_{xy} \circ (N_2)_{yy} + \\
& A_{33} \circ (N_1)_{xy} \circ (N_2)_{xy} \big) \, d\tilde{x} d\tilde{y}
\end{aligned} \tag{B.3}
$$

$$
\begin{aligned}
\mathbf{R} = \int_{-1}^{1}\int_{-1}^{1} \frac{1}{2} \big(& A_{11} \circ (N_2)_{xx} \circ (N_2)_{xx} + A_{12} \circ (N_2)_{xx} \circ (N_2)_{yy} + \\
& A_{13} \circ (N_2)_{xx} \circ (N_2)_{xy} + A_{21} \circ (N_2)_{yy} \circ (N_2)_{xx} + \\
& A_{22} \circ (N_2)_{x} \circ (N_2)_{xx} + A_{23} \circ (N_2)_{yy} \circ (N_2)_{xy} \\
& + A_{31} \circ (N_2)_{xy} \circ (N_2)_{xx} + A_{32} \circ (N_2)_{xy} \circ (N_2)_{yy} + \\
& A_{33} \circ (N_2)_{xy} \circ (N_2)_{xy} \big) + \big(A_{11} \circ (N_1)_{xx} \circ (N_3)_{xx} + \\
& A_{12} \circ (N_1)_{xx} \circ (N_3)_{yy} + A_{13} \circ (N_1)_{xx} \circ (N_3)_{xy} + \\
& A_{21} \circ (N_1)_{yy} \circ (N_3)_{xx} + A_{22} \circ (N_1)_{yy} \circ (N_3)_{yy} + \\
& A_{23} \circ (N_1)_{yy} \circ (N_3)_{xy} + A_{31} \circ (N_1)_{xy} \circ (N_3)_{xx} + \\
& A_{32} \circ (N_1)_{xy} \circ (N_3)_{yy} + A_{33} \circ (N_1)_{xy} \circ (N_3)_{xy} \big) \, d\tilde{x} d\tilde{y}
\end{aligned} \tag{B.4}
$$

$$
\begin{aligned}
\mathbf{S} = \int_{-1}^{1}\int_{-1}^{1} \big(& A_{11} \circ (N_2)_{xx} \circ (N_3)_{xx} + A_{12} \circ (N_2)_{xx} \circ (N_3)_{yy} + \\
& A_{13} \circ (N_2)_{xx} \circ (N_3)_{xy} + A_{21} \circ (N_2)_{yy} \circ (N_3)_{xx} + \\
& A_{22} \circ (N_2)_{yy} \circ (N_3)_{yy} + A_{23} \circ (N_2)_{yy} \circ (N_3)_{xy} + \\
& A_{31} \circ (N_2)_{xy} \circ (N_3)_{xx} + A_{32} \circ (N_2)_{xy} \circ (N_3)_{yy} + \\
& A_{33} \circ (N_2)_{xy} \circ (N_3)_{xy} \big) \, d\tilde{x} d\tilde{y}
\end{aligned} \tag{B.5}
$$

$$
\begin{aligned}
\mathbf{T} = \int_{-1}^{1}\int_{-1}^{1} \frac{1}{2} \big(& A_{11} \circ (N_3)_{xx} \circ (N_3)_{xx} + A_{12} \circ (N_3)_{xx} \circ (N_3)_{yy} + \\
& A_{13} \circ (N_3)_{xx} \circ (N_3)_{xy} + A_{21} \circ (N_3)_{yy} \circ (N_3)_{xx} + \\
& A_{22} \circ (N_3)_{x} \circ (N_3)_{xx} + A_{23} \circ (N_3)_{yy} \circ (N_3)_{xy} \\
& + A_{31} \circ (N_3)_{xy} \circ (N_3)_{xx} + A_{32} \circ (N_3)_{xy} \circ (N_3)_{yy} + \\
& A_{33} \circ (N_3)_{xy} \circ (N_3)_{xy} \big) \, d\tilde{x} d\tilde{y}
\end{aligned} \tag{B.6}
$$

C

Investigation of complete design space of VS laminate

In this work, we have primarily focused on generating bistable shapes from VS laminate similar to cross-ply laminates. This was particularly because of the envisaged morphing concept. However, a complete design map might be required for designers seeking other bistable shapes, and utilizing the VS tailoring capabilities. The figure below shows the snap-through loads of different VS laminates as a result of a parametric study conducted at an angle interval of 5°. The material and geometrical properties as given in Chapter-4 is adopted.

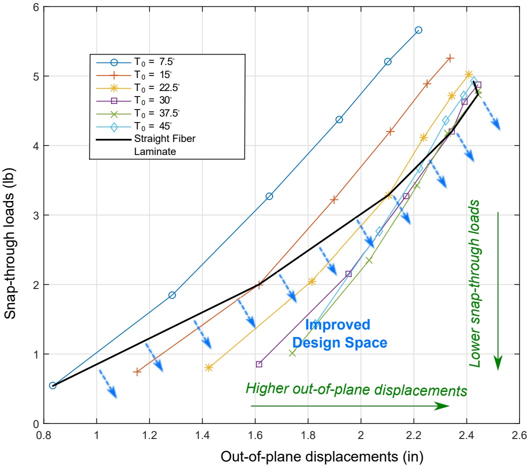

Figure C.1: Extended design space of VS laminates. The indicated regions shows the design space where the lower snap-through loads are required to achieve higher maximum out-of-plane displacements. This design space includes different bistable shapes, as might not have equal out-of-plane displacements at each corners.

Bibliography

1. Abbott, I. H. & Von Doenhoff, A. E. *Theory of wing sections, including a summary of airfoil data* (Courier Corporation, 1959).
2. Ai, Q., Weaver, P. M., Barlas, T. K., Olsen, A. S., Madsen, H. A. & Andersen, T. L. Field testing of morphing flaps on a wind turbine blade using an outdoor rotating rig. *Renewable Energy* **133**, 53 (2019).
3. Alhajahmad, A., Abdalla, M. M. & Gürdal, Z. Design tailoring for pressure pillowing using tow-placed steered fibers. *Journal of Aircraft* **45**, 630 (2008).
4. Anilkumar, P. M., Haldar, A., Jansen, E., Rao, B. N. & Rolfes, R. Design optimization of multistable variable-stiffness laminates. *Mechanics of Advanced Materials and Structures* **26**, 48 (2019).
5. Arrieta, A. F., Kuder, I. K., Rist, M., Waeber, T. & Ermanni, P. Passive load alleviation aerofoil concept with variable stiffness multi-stable composites. *Composite Structures* **116**, 235 (2014).
6. Arrieta, A. F., Kuder, I. K., Waeber, T. & Ermanni, P. Variable stiffness characteristics of embeddable multi-stable composites. *Composites Science and Technology* **97**, 12 (2014).
7. Arrieta, A. F., Kuder, I. K., Waeber, T. & Ermanni, P. Variable stiffness characteristics of embeddable multi-stable composites. *Composites Science and Technology* **97**, 12 (2014).
8. Ashwill, T. *Passive Load Control for Large Wind Turbines* in *51st AIAA/ASME/ASCE /AHS/ASC Structures, Structural Dynamics, and Materials Conference* (2010), 2577.
9. Bak, C., Gaunaa, M., Andersen, P., Buhl, T., Hansen, P., Clemmensen, K. & Møller, R. *Wind tunnel test on wind turbine airfoil with adaptive trailing edge geometry* in *45th AIAA Aerospace Sciences Meeting and Exhibit* (2007), 1016.
10. Bak, C., Gaunaa, M., Andersen, P. B., Buhl, T., Hansen, P. & Clemmensen, K. Wind tunnel test on airfoil Risø-B1-18 with an Active Trailing Edge Flap. *Wind Energy: An International Journal for Progress and Applications in Wind Power Conversion Technology* **13**, 207 (2010).
11. Barlas, T., Lutz, T., Bak, C., Hulskamp, A. & Apinaniz, S. *Requirements for smart rotor technology* tech. rep. (Technical Report Upwind Project, 2010).
12. Barlas, T. K., Olsen, A. S., Madsen, H. A., Andersen, T. L., Ai, Q. & Weaver, P. M. Aerodynamic and load control performance testing of a morphing trailing edge flap system on an outdoor rotating test rig. *Journal of Physics: Conference Series* **1037** (2018).

13. Barlas, T. & van Kuik, G. Review of state of the art in smart rotor control research for wind turbines. *Progress in Aerospace Sciences* **46**, 1 (2010).

14. Barlas, T. K., Madsen, H. A., Klemmensen, K., En, D. T. U. V.-e., Barlas, A. T. K. & Madsen, H. A. Flap testing on the rotating test rig in the INDUFLAP project Wind Energy E Report 2015. **0064** (2014).

15. Bartels, R. *Active Trailing Edge Flap Configurations for Load Reduction of Wind Turbines* in *SmartBlades Conference, Stade, Germany* (2016).

16. Bellman, R. & Casti, J. Differential quadrature and long-term integration. *Journal of Mathematical Analysis and Applications* **34**, 235 (1971).

17. Bellomo, N. Nonlinear models and problems in applied sciences from differential quadrature to generalized collocation methods. *Mathematical and Computer Modelling* **26**, 13 (1997).

18. Berg, J., Resor, B., Paquette, J. & White, J. SMART wind turbine rotor: Design and field test (Tech. Rep.) *SAND2014-0681* (2014).

19. Berg, J., Berg, D. & White, J. Fabrication, Integration and Initial Testing of a SMART Rotor, 1 (2014).

20. Berg, J. C., Barone, M. F. & Yoder, N. SMART Wind Turbine Rotor: Data Analysis and Conclusions. *SAND2014-0712, Sandia National Laboratories* (2014).

21. Berg, J. C., Barone, M. F. & Yoder, N. C. SMART wind turbine rotor: data analysis and conclusions. *SAND2014-0712, Sandia National Laboratories, Albuquerque, NM* (2014).

22. Berg, J. C., Resor, B. R., Paquette, J. A. & White, J. R. SMART Wind Turbine Rotor : Design and Field Test (2014).

23. Bernhammer, L. *Smart Wind Turbine: analysis and autonomous flap* PhD thesis (TU Delft, Netherlands, 2015).

24. Bert, C. W. & Malik, M. Differential quadrature method in computational mechanics: a review. *Applied mechanics reviews* **49**, 1 (1996).

25. Betts, D. N., Kim, H. A. & Bowen, C. R. Modeling and optimization of bistable composite laminates for piezoelectric actuation. *Journal of Intelligent Material Systems and Structures* **22**, 2181 (2011).

26. Betts, D. N., Kim, H. A., Bowen, C. R. & Inman, D. Optimal configurations of bistable piezo-composites for energy harvesting. *Applied Physics Letters* **100**, 114104 (2012).

27. Betts, D. N., Kim, H. A. & Bowen, C. R. Modeling and optimization of bistable composite laminates for piezoelectric actuation. *Journal of Intelligent Material Systems and Structures* **22**, 2181 (2011).

28. Betts, D. N., Salo, A. I., Bowen, C. R. & Kim, H. A. Characterisation and modelling of the cured shapes of arbitrary layup bistable composite laminates. *Composite Structures* **92**, 1694 (2010).

29. Blazquez, A., Reinoso, J., Paris, F. & Canas, J. Analysis in the postbuckling regime of a pressurized stiffened panel. Part II: Numerical analysis and effect of the geometric imperfections. *Compos Struct* **94**, 1544 (2012).
30. Blom, A. *Structural Performance of Fiber-Placed, Variable-Stiffness Composite Conical and Cylindrical Shells* PhD thesis (Technische Universiteit Delft, 2010).
31. Bowen, C., Butler, R., Jervis, R., Kim, H. & Salo, A. Morphing and shape control using unsymmetrical composites. *Journal of Intelligent Material Systems and Structures* **18**, 89 (2007).
32. Brooks, T. R. & Martins, J. R. On manufacturing constraints for tow-steered composite design optimization. *Composite Structures* **204**, 548 (2018).
33. Buermann, P., Rolfes, R., Tessmer, J. & Schagerl, M. A semi-analytical model for local post-buckling analysis of stringer- and frame-stiffened cylindrical panels. *Thin-Walled Structures* **44**, 102 (2006).
34. Buhl, T., Bak, C., Gaunaa, M. & Andersen, P. B. Load Alleviation through Adaptive Trailing Edge Control Surfaces: ADAPWING Overview Abstract : (2013).
35. Bye, D. R. & McClure, P. D. *Design of a morphing vehicle* in *48th AIAA Structures, Structural Dynamics, and Materials Conference* **23** (2007), 2007.
36. Calladine, C. R. *Theory of Shell Structures* Cambridge Books Online (Cambridge University Press, 1983).
37. Calladine, C. The theory of thin shell structures 1888–1988. *Proceedings of the Institution of Mechanical Engineers, Part A: Journal of Power and Energy* **202**, 141 (1988).
38. Cantera, M., Romera, J., Adarraga, I. & Mujika, F. Modelling and testing of the snap-through process of bi-stable cross-ply composites. *Composite Structures* **120**, 41 (2015).
39. Capellaro, M. *Bend twist coupled blades—Redux* in *Proceedings of the IEA topical expert meeting on the application of smart structures for large wind turbine rotor blades, Sandia National Labs, Alberquerque, USA* (2008).
40. Capuzzi, M., Pirrera, A. & Weaver, P. A novel adaptive blade concept for large-scale wind turbines. Part I: Aeroelastic behaviour. *Energy* **73**, 15 (2014).
41. Ceyhan, J. S. O., Boorsma, K., Gonzalez, A., Munduate, X., Pires, O., Sørensen, N., Ferreira, C., Sieros, G., Madsen, J., Voutsinas, S., *et al. Latest results from the EU project AVATAR: Aerodynamic modelling of 10 MW wind turbines* in *Journal of Physics: Conference Series* **753** (2016), 022017.
42. Ceyhan, O., Pires, O., Munduate, X., Sorensen, N. N., Schaffarczyk, A. P., Reichstein, T., Diakakis, K., Papadakis, G., Daniele, E., Schwarz, M., Lutz, T. & Prieto, R. in *35th Wind Energy Symposium* (American Institute of Aeronautics and Astronautics, 2017).

43. Chillara, V. S. & Dapino, M. J. Stability considerations and actuation requirements in bistable laminated composites. *Composite Structures* **184**, 1062 (2018).

44. Chillara, V. S. C., Headings, L. M., Tsuruta, R., Itakura, E., Gandhi, U. & Dapino, M. J. Shape memory alloy–actuated prestressed composites with application to morphing automotive fender skirts. *Journal of Intelligent Material Systems and Structures* **30**, 479 (2019).

45. Coburn, B. H., Pirrera, A., Weaver, P. M. & Vidoli, S. Tristability of an orthotropic doubly curved shell. *Composite Structures* **96**, 446 (2013).

46. Coburn, B. H., Wu, Z. & Weaver, P. M. Buckling analysis of stiffened variable angle tow panels. *Composite Structures* **111**, 259 (2014).

47. Collis, S. S., Joslin, R. D., Seifert, A. & Theofilis, V. Issues in active flow control: theory, control, simulation, and experiment. *Progress in Aerospace Sciences* **40**, 237 (2004).

48. Cui, Y. & Santer, M. Characterisation of tessellated bistable composite laminates. *Composite Structures* **137**, 93 (2016).

49. Dai, F., Li, H. & Du, S. Design and analysis of a tri-stable structure based on bi-stable laminates. *Composites Part A: Applied Science and Manufacturing* **43**, 1497 (2012).

50. Dai, F., Li, H. & Du, S. A multi-stable wavy skin based on bi-stable laminates. *Composites Part A: Applied Science and Manufacturing* **45**, 102 (2013).

51. Dano, M.-L. & Hyer, M. W. Snap-through of unsymmetric fiber-reinforced composite laminates. *International Journal of Solids and Structures* **39**, 175 (2002).

52. Dano, M.-L. & Hyer, M. SMA-induced snap-through of unsymmetric fiber-reinforced composite laminates. *International Journal of Solids and Structures* **40**, 5949 (2003).

53. Dano, M. L., Jean-St-Laurent, M. & Fecteau, A. Morphing of Bistable Composite Laminates Using Distributed Piezoelectric Actuators. *Smart Materials Research* **2012**, 1 (2012).

54. Dano, M.-L. *SMA-Induced Deformations in General Unsymmetric Laminates* PhD thesis (Citeseer, 1997).

55. Dano, M.-L. & Hyer, M. W. the Response of Unsymmetric Laminates To Simple Applied Forces. *Mechanics of Advanced Materials and Structures* **3**, 65 (1996).

56. Dano, M.-L. & Hyer, M. W. Thermally-induced deformation behavior of unsymmetric laminates. *International Journal of Solids and Structures* **35**, 2101 (1998).

57. Daynes, S., Potter, K. & Weaver, P. Bistable prestressed buckled laminates. *Composites Science and Technology* **68**, 3431 (2008).

58. Daynes, S., Diaconu, C., Potter, K. & Weaver, P. Bistable Prestressed Symmetric Laminates. *Journal of Composite Materials* **44**, 1119 (2010).
59. Daynes, S., Nall, S., Weaver, P., Potter, K., Margaris, P. & Mellor, P. in *50th AIAA/ASME/ASCE/AHS/ASC Structures, Structural Dynamics, and Materials Conference* (American Institute of Aeronautics and Astronautics, 2009).
60. Daynes, S., Trask, R. S. & Weaver, P. M. Bio-inspired structural bistability employing elastomeric origami for morphing applications. *Smart Materials and Structures* **23**, 125011 (2014).
61. Daynes, S., Weaver, P. & Potter, K. Aeroelastic study of bistable composite airfoils. *Journal of Aircraft* **46**, 2169 (2009).
62. De Vries, H. *On synthetic jet actuation for aerodynamic load control* PhD thesis (University of Twente, Netherlands, 2013).
63. Diaconu, C. G., Weaver, P. M. & Arrieta, A. F. Dynamic analysis of bi-stable composite plates. *Journal of Sound and Vibration* **322**, 987 (2009).
64. Diaconu, C. G., Weaver, P. M. & Mattioni, F. Concepts for morphing airfoil sections using bi-stable laminated composite structures. *Thin-Walled Structures* **46**, 689 (2008).
65. Dudte, L. H., Vouga, E., Tachi, T. & Mahadevan, L. Programming curvature using origami tessellations. *Nature materials* **15**, 583 (2016).
66. Duran, A., Fasanella, N., Sundararaghavan, V. & Waas, A. Thermal buckling of composite plates with spatial varying fiber orientations. *Composite Structures* **124**, 228 (2015).
67. ECN, N. Project final report:Advanced aerodynamic modelling, design and testing for large rotor blades, 1 (2017).
68. Fedorov, V. *Bend-Twist Coupling Effects in Wind Turbine Blades* The project was equivalently funded by the Department of Wind Energy, by Vestas Wind Systems A/S and by the Danish Energy Authority through the EFP-project titled "Anisotropic beam model for analysis and design of passive controlled wind turbine blades" with journal no. 33033-0075. PhD thesis (Denmark, 2012).
69. Ferede, E. *Static aeroelastic optimization of composite wind turbine blades using variable stiffness laminates: Exploring twist coupled composite blades in stall control,* PhD thesis (TU Delft, 2016).
70. Fernandes, A., Maurini, C. & Vidoli, S. Multiparameter actuation for shape control of bistable composite plates. *International Journal of Solids and Structures* **47**, 1449 (2010).
71. Fichaux, N., Beurskens, J., Jensen, P. H., Wilkes, J., Frandsen, S., Sorensen, J. & Eecen, P. Upwind: Design limits and solutions for very large wind turbines. *Sixth Framework Programme* (2011).

72. Forterre, Y., Skotheim, J. M., Dumais, J. & Mahadevan, L. How the Venus flytrap snaps. *Nature* **433**, 421 (2005).
73. Galletly, D. A. & Guest, S. D. Bistable composite slit tubes. II. A shell model. *International Journal of Solids and Structures* **41**, 4503 (2004).
74. Galletly, D. A. & Guest, S. D. Bistable composite slit tubes. I. A beam model. *International Journal of Solids and Structures* **41**, 4517 (2004).
75. Giddings, P. F., Bowen, C. R., Salo, A. I., Kim, H. A. & Ive, A. Bistable composite laminates: Effects of laminate composition on cured shape and response to thermal load. *Composite Structures* **92**. Fifteenth International Conference on Composite Structures, 2220 (2010).
76. Gigliotti, M., Wisnom, M. R. & Potter, K. D. Loss of bifurcation and multiple shapes of thin [0/90] unsymmetric composite plates subject to thermal stress. *Composites Science and Technology* **64**, 109 (2004).
77. Gliesche, K. & Feltin, D. Beanspruchungsgerechte Textilkonstruktionen fuer Composites-Bauteile. *TECHNISCHE TEXTILIEN* **38**, 209 (1995).
78. GOLABCHI, M. R. & Simon, D. *Morphing multiscale textured shells* in *Symposium of the International Association for Shell and Spatial Structures (50th. 2009. Valencia). Evolution and Trends in Design, Analysis and Construction of Shell and Spatial Structures: Proceedings* (2009).
79. Groh, R., Avitabile, D. & Pirrera, A. Generalised path-following for well-behaved nonlinear structures. *Computer Methods in Applied Mechanics and Engineering* **331**, 394 (2018).
80. Groh, R. & Pirrera, A. Orthotropy as a driver for complex stability phenomena in cylindrical shell structures. *Composite Structures* **198**, 63 (2018).
81. Gude, M. & Hufenbach, W. Design of novel morphing structures based on bistable composites with piezoceramic actuators. *Mechanics of Composite Materials* **42**, 339 (2006).
82. Gude, M., Hufenbach, W. & Kirvel, C. Piezoelectrically driven morphing structures based on bistable unsymmetric laminates. *Composite Structures* **93**, 377 (2011).
83. Gude, M., Hufenbach, W. & Kirvel, C. Piezoelectrically driven morphing structures based on bistable unsymmetric laminates. *Composite Structures* **93**, 377 (2011).
84. Guest, S. & Pellegrino, S. Analytical models for bistable cylindrical shells. *Proceedings of the Royal Society A: Mathematical, Physical and Engineering Sciences* **462**, 839 (2006).
85. Guimarães, T. A., Rade, D. A. & Cesnik, C. E. *Active Flutter Suppression on Composite Tow Steered Panels based on Piezoelectric Actuation* in *2018 AIAA/ASCE/AHS/ASC Structures, Structural Dynamics, and Materials Conference* (2018), 0188.

86. Gurdal, Z. & Olmedo, R. In-plane response of laminates with spatially varying fiber orientations-variable stiffness concept. *AIAA journal* **31**, 751 (1993).
87. Gurdal, Z., Tatting, B. & Wu, K. in *46th AIAA/ASME/ASCE/AHS/ASC Structures, Structural Dynamics and Materials Conference* (American Institute of Aeronautics and Astronautics, Austin,TX, 2005).
88. Gürdal, Z., Tatting, B. & Wu, C. Variable stiffness composite panels: Effects of stiffness variation on the in-plane and buckling response. *Composites Part A: Applied Science and Manufacturing* **39**, 911 (2008).
89. Haldar, A., Jansen, E. & Rolfes, R. *Analysis of Morphing Trailing Edge Flap with Embedded Multistable Variable Stiffness Laminates* in *AIAA Scitech 2019 Forum* (2019).
90. Haldar, A., Jansen, E., Rolfes, R. & Weaver, P. *Tailoring Snap-through Loads in Variable Stiffness Composites* in *2018 AIAA/ASCE/AHS/ASC Structures, Structural Dynamics, and Materials Conference* (2018).
91. Haldar, A., Reinoso, J., Jansen, E. & Rolfes, R. in *Multiscale Modeling of Heterogeneous Structures* 61 (Springer, 2018).
92. Haldar, A., Reinoso, J., Jansen, E. & Rolfes, R. Thermally induced multistable configurations of variable stiffness composite plates: Semi-analytical and finite element investigation. *Composite Structures* **183**, 161 (2018).
93. *Haliade-X offshore windturbine platform* `https://www.ge.com/renewableenergy/wind-energy/offshore-wind/haliade-x-offshore-turbine`.
94. Hamouche, W., Maurini, C., Vincenti, A. & Vidoli, S. Basic criteria to design and produce multistable shells. *Meccanica* (2016).
95. Hau, E. *Wind turbines: fundamentals, technologies, application, economics* (Springer-Verlag Berlin Heidelberg, 2006).
96. Herath, M. T., Lee, A. K. & Prusty, B. G. Design of shape-adaptive wind turbine blades using Differential Stiffness Bend–Twist coupling. *Ocean Engineering* **95**, 157 (2015).
97. Hofmeister, B., Bruns, M. & Rolfes, R. Finite element model updating using deterministic optimisation: A global pattern search approach. *Engineering Structures* **195**, 373 (2019).
98. Holmes, D. P. Elasticity and Stability of Shape Changing Structures. *Current Opinion in Colloid & Interface Science* (2019).
99. Holmes, D. P., Roché, M., Sinha, T. & Stone, H. A. Bending and twisting of soft materials by non-homogenous swelling. *Soft Matter* **7**, 5188 (11 2011).
100. Hufenbach, W. & Gude, M. Analysis and optimisation of multistable composites under residual stresses. *Composite Structures* **55**, 319 (2002).

101. Hufenbach, W., Gude, M. & Kroll, L. Design of multistable composites for application in adaptive structures. *Composites Science and Technology* **62**, 2201 (2002).
102. Hwang, C. & Masud, A. *Multiple objective decision making, methods and applications: a state-of-the-art survey* (Springer-Verlag, 1979).
103. Hyer, M. W. Calculations of the room-temperature shapes of unsymmetric laminates. *Journal of Composite Materials* **15**, 296 (1981).
104. Hyer, M. W. Some Observations on the Cured Shape of Thin Unsymmetric Laminates. *Journal of Composite Materials* **15**, 175 (1981).
105. Hyer, M. W. The Room-Temperature Shapes of Four-Layer Unsymmetric Cross-Ply Laminates. *Journal of Composite Materials* **16**, 318 (1982).
106. Hyer, M. W. & Charette, R. F. Use of curvilinear fiber format in composite structure design. *AIAA Journal* **29**, 1011 (1991).
107. Hyer, M. & Lee, H. The use of curvilinear fiber format to improve buckling resistance of composite plates with central circular holes. *Composite Structures* **18**, 239 (1991).
108. Iqbal, K., Pellegrino, S. & Daton-Lovett, A. *Bi-stable composite slit tubes* in *IUTAM-IASS symposium on deployable structures: theory and applications* (2000), 153.
109. Iqbal, K. & Pellegrino, S. in *41st Structures, Structural Dynamics, and Materials Conference and Exhibit* (2000).
110. Jansen, E., Abramovich, H. & Rolfes, R. *The direct prediction of buckling loads of shells under axial compression using VCT-towards an upgraded approach* in *29th congress on the International Council of the Aeronutical Science* (2014), 1.
111. Jansen, E. *Nonlinear vibration analysis of composite cylindrical shells using a semi-analytical formulation* in *19th AIAA Applied Aerodynamics Conference* (2001).
112. Johnson, S. J., Baker, J. P., Van Dam, C. & Berg, D. An overview of active load control techniques for wind turbines with an emphasis on microtabs. *Wind Energy: An International Journal for Progress and Applications in Wind Power Conversion Technology* **13**, 239 (2010).
113. Jones, R. M. *Mechanics of Composite Materials* (Mc Graw Hill, New York, 1975).
114. Jones, R. M. *Buckling of bars, plates, and shells* (Bull Ridge Corporation, 2006).
115. Jun, W. & Hong, C. Cured Shape of Unsymmetric Laminates with Arbitrary Lay-Up Angles. *Journal of Reinforced Plastics and Composites* **11**, 1352 (1992).
116. Kalyanmoy, D. *Multi objective optimization using evolutionary algorithms* (John Wiley and Sons, 2001).
117. Kebadze, E., Guest, S. D. & Pellegrino, S. Bistable prestressed shell structures. *International Journal of Solids and Structures* **41**, 2801 (2004).

118. Kim, B., Potter, K. & Weaver, P. *Multi-tow shearing mechanism for high-speed manufacturing of variable angle tow composites* in *ECCM15–15th European Conference on Composite Materials* (2012).

119. Kim, B. C., Potter, K. & Weaver, P. M. Continuous tow shearing for manufacturing variable angle tow composites. *Composites Part A: Applied Science and Manufacturing* **43**, 1347 (2012).

120. Kim, H. A., Betts, D. N., T. Salo, A. I. & Bowen, C. R. Shape memory alloy-piezoelectric active structures for reversible actuation of bistable composites. *AIAA Journal* **48**, 1265 (2010).

121. Kim, S.-W., Koh, J.-S., Lee, J.-G., Ryu, J., Cho, M. & Cho, K.-J. Flytrap-inspired robot using structurally integrated actuation based on bistability and a developable surface. *Bioinspiration & biomimetics* **9**, 036004 (2014).

122. Kota, S., Hetrick, J. A., Osborn, R., Paul, D., Pendleton, E., Flick, P. & Tilmann, C. *Design and application of compliant mechanisms for morphing aircraft structures* in *Smart Structures and Materials* (2003), 24.

123. Kriegesmann, B., Jansen, E. L. & Rolfes, R. Semi-analytic probabilistic analysis of axially compressed stiffened composite panels. *Composite Structures* **94**, 654 (2012).

124. Kuder, I. K., Arrieta, A. F., Rist, M. & Ermanni, P. Aeroelastic response of a selectively compliant morphing aerofoil featuring integrated variable stiffness bi-stable laminates. *Journal of Intelligent Material Systems and Structures* **27**, 1949 (2016).

125. Kuder, I. K., Arrieta, A. F. & Ermanni, P. Design space of embeddable variable stiffness bi-stable elements for morphing applications. *Composite Structures* **122**, 445 (2015).

126. L. Giomi, L. M. Multi-stability of free spontaneously curved anisotropic strips. *Proceedings: Mathematical, Physical and Engineering Sciences* **468**, 511 (2012).

127. Lachenal, X., Daynes, S. & Weaver, P. M. Review of morphing concepts and materials for wind turbine blade applications. *Wind Energy* **16**, 283 (2013).

128. Lamacchia, E., Pirrera, A., Chenchiah, I. & Weaver, P. Morphing shell structures: A generalised modelling approach. *Composite Structures* **131**, 1017 (2015).

129. Larwood, S. & Zuteck, M. Swept Wind Turbine Blade Aeroelastic Modeling for Loads and Dynamic Behavior. *AWEA Windpower* (2006).

130. Lee, J.-G., Ryu, J., Kim, S.-W., Koh, J.-S., Cho, K.-J. & Cho, M. Effect of initial tool-plate curvature on snap-through load of unsymmetric laminated cross-ply bistable composites. *Composite Structures* **122**, 82 (2015).

131. Li, H., Dai, F., Weaver, P. & Du, S. Bistable hybrid symmetric laminates. *Composite Structures* **116**, 782 (2014).

132. Li, J. & Yu, X. B. *Fatigue analysis of an innovative extensible wind turbine blade* in *ASME 2016 International Mechanical Engineering Congress and Exposition* (2016), V06BT08A059.
133. Li, S. & Wang, K. Plant-inspired adaptive structures and materials for morphing and actuation: a review. *Bioinspiration & biomimetics* **12**, 011001 (2016).
134. Liebst, B. S. Wind turbine gust load alleviation utilizing curved blades. *Journal of Propulsion and Power* **2**, 371 (1986).
135. Lobitz, D. W. & Veers, P. S. Load Mitigation with Bending/Twist-coupled Blades on Rotors using Modern Control Strategies. *Wind Energy* **6**, 105 (2003).
136. Loukaides, E. & Seffen, K. Multistable grid and honeycomb shells. *International Journal of Solids and Structures* **59**, 46 (2015).
137. Loukaides, E., Smoukov, S. & Seffen, K. Magnetic actuation and transition shapes of a bistable spherical cap. *International Journal of Smart and Nano Materials* **5**, 270 (2014).
138. Lozano, G. G., Tiwari, A. & Turner, C. A design algorithm to model fibre paths for manufacturing of structurally optimised composite laminates. *Composite Structures* **204**, 882 (2018).
139. Lozano, G. G., Tiwari, A., Turner, C. & Astwood, S. A review on design for manufacture of variable stiffness composite laminates. *Proceedings of the Institution of Mechanical Engineers, Part B: Journal of Engineering Manufacture* **230**, 981 (2016).
140. *Macro Fibre Composite* `https://www.smart-material.com/MFC-product-main.html` (2019).
141. Madsen, H. A., Barlas, A. & Andersen, T. L. *A morphing trailing edge flap system for wind turbine blades* in *Proceedings of the 7th ECCOMAS Thematic Conference on Smart Structures and Materials (SMART 2015)* **7** (2015).
142. MANSFIELD, E. H. The inextensional theory of thin flat plates. *The Quarterly Journal of Mechanics and Applied Mathematics* **8**, 338 (1955).
143. Mansfield, E. H. Large-deflexion torsion and flexure of initially curved strips. *Proceedings of the Royal Society of London. A. Mathematical and Physical Sciences* **334**, 279 (1973).
144. Mansfield, E. H. & Küchemann, D. Bending, buckling and curling of a heated elliptical plate. *Proceedings of the Royal Society of London. Series A. Mathematical and Physical Sciences* **288**, 396 (1965).
145. Mao, H., Ganga, P. L., Ghiozzi, M., Ivchenko, N. & Tibert, G. Deployment of Bistable Self-Deployable Tape Spring Booms Using a Gravity Offloading System. *Journal of Aerospace Engineering* **30**, 04017007 (2017).
146. Mattheij, P., Gliesche, K. & Feltin, D. 3D reinforced stitched carbon/epoxy laminates made by tailored fibre placement. *Composites Part A: Applied Science and Manufacturing* **31**, 571 (2000).

147. Mattioni, F., Weaver, P. M., Potter, K. D. & Friswell, M. I. Analysis of thermally induced multistable composites. *International Journal of Solids and Structures* **45**, 657 (2008).

148. Mattioni, F., Weaver, P. M. & Friswell, M. Multistable composite plates with piecewise variation of lay-up in the planform. *International Journal of Solids and Structures* **46**, 151 (2009).

149. Mattioni, F., Weaver, P. M., Potter, K. D. & Friswell, M. I. *The application of thermally induced multistable composites to morphing aircraft structures* in *The 15th International Symposium on: Smart Structures and Materials and Nondestructive Evaluation and Health Monitoring* (2008), 693012.

150. McWilliam, M. K., Barlas, T. K., Madsen, H. A. & Zahle, F. Aero-elastic wind turbine design with active flaps for AEP maximization. *Wind Energy Science* **3**, 231 (2018).

151. Messac, A. *Optimization in practice with MATLAB®: for engineering students and professionals* (Cambridge University Press, 2015).

152. Monner, H. P., Huxdorf, O., Pohl, M., Riemenschneider, J., Homeyer, T. & Hölling, M. *Smart structures for wind energy turbines* in *25th AIAA/AHS Adaptive Structures Conference* (2017), 0295.

153. Montemurro, M. & Catapano, A. On the effective integration of manufacturability constraints within the multi-scale methodology for designing variable angle-tow laminates. *Composite Structures* **161**, 145 (2017).

154. Murray, D. V. & Myers, O. J. Modeling bistable composite laminates for piezoelectric morphing structures. *ISRN Materials Science* **2013**, 1 (2013).

155. Nagendra, S., Kodiyalam, S., Davis, J. & Parthasarathy, V. *Optimization of tow fiber paths for composite design* in *36th Structures, Structural Dynamics and Materials Conference* (1995), 1275.

156. Neuhaus, L., Singh, P., Homeyer, T., Huxdorf, O., Riemenschneider, J., Wild, J., Peinke, J. & Hölling, M. Mitigating loads by means of an active slat. *Journal of Physics: Conference Series* **1037** (2018).

157. Norman, A., Seffen, K. & Guest, S. Multistable corrugated shells. *Proceedings of the Royal Society A: Mathematical, Physical and Engineering Sciences* **464**, 1653 (2008).

158. Norman, A., Seffen, K. & Guest, S. Morphing of curved corrugated shells. *International Journal of Solids and Structures* **46**, 1624 (2009).

159. Ochinero, T. T. *Deformations of unsymmetric composite panels* PhD thesis (Virginia Polytechnic Institute and State University, 2001).

160. Oltmann, N. *Active Trailing Edge Flap Design for Load Reduction of Wind Turbines* in *Smart Blades Conference, Oldenburg, Germany* (2015).

161. Panesar, A. S. *Multistable morphing composites using variable angle tows (VAT)* PhD thesis (University of Bristol, 2012).

162. Panesar, A. S., Hazra, K. & Weaver, P. M. Investigation of thermally induced bistable behaviour for tow-steered laminates. *Composites Part A: Applied Science and Manufacturing* **43**, 926 (2012).

163. Panesar, A. S. & Weaver, P. M. Optimisation of blended bistable laminates for a morphing flap. *Composite Structures* **94**, 3092 (2012).

164. Parnas, L., Oral, S. & Ceyhan, Ü. Optimum design of composite structures with curved fiber courses. *Composites Science and Technology* **63**, 1071 (2003).

165. Peeters, D. M., Lozano, G. G. & Abdalla, M. M. Effect of steering limit constraints on the performance of variable stiffness laminates. *Computers & Structures* **196**, 94 (2018).

166. Petroski, H. Deployable Structures. *Am. Sci.* **92**, 122 (2014).

167. Pezzulla, M., Stoop, N., Jiang, X. & Holmes, D. P. Curvature-driven morphing of non-Euclidean shells. *Proceedings of the Royal Society of London A: Mathematical, Physical and Engineering Sciences* **473** (2017).

168. Pirrera, A., Avitabile, D. & Weaver, P. M. Bistable plates for morphing structures: A refined analytical approach with high-order polynomials. *International Journal of Solids and Structures* **47**, 3412 (2010).

169. Pirrera, a., Avitabile, D. & Weaver, P. M. On the thermally induced bistability of composite cylindrical shells for morphing structures. *International Journal of Solids and Structures* **49**, 685 (2012).

170. Pohl, M. & Riemenschneider, J. *Designing and testing a flexible trailing edge for wind energy turbine blades* in *2018 AIAA/AHS Adaptive Structures Conference* (2018), 1066.

171. Portela, P., Camanho, P., Weaver, P. M. & Bond, I. Analysis of morphing, multi stable structures actuated by piezoelectric patches. *Computers & Structures* **86**, 347 (2008).

172. Potter, K., Weaver, P., Seman, A. A. & Shah, S. Phenomena in the bifurcation of unsymmetric composite plates. *Composites Part A: Applied Science and Manufacturing* **38**, 100 (2007).

173. Quan, J. & Chang, C. New insights in solving distributed system equations by the quadrature method—I. Analysis. *Computers and Chemical Engineering* **13**, 779 (1989).

174. Rahman, T., Ijsselmuiden, S. T., Abdalla, M. M. & Jansen, E. L. Postbuckling Analysis Of Variable Stiffness Composite Plates Using A Finite Element-Based Perturbation Method. *International Journal of Structural Stability and Dynamics* **11**, 735 (2011).

175. Raju, G., Wu, Z. & Weaver, P. M. Buckling and postbuckling of variable angle tow composite plates under in-plane shear loading. *International Journal of Solids and Structures* **58**, 270 (2015).

176. Raviv, D., Zhao, W., McKnelly, C., Papadopoulou, A., Kadambi, A., Shi, B., Hirsch, S., Dikovsky, D., Zyracki, M., Olguin, C., *et al.* Active printed materials for complex self-evolving deformations. *Scientific reports* **4**, 7422 (2014).

177. Reis, P. M. A perspective on the revival of structural (in) stability with novel opportunities for function: from buckliphobia to buckliphilia. *Journal of Applied Mechanics* **82**, 111001 (2015).

178. Ren, L. A Model for Shape Control of Cross-ply Laminated Shells using a Piezoelectric Actuator. *Journal of Composite Materials* **40**, 1271 (2005).

179. Ren, L. A theoretical study on shape control of arbitrary lay-up laminates using piezoelectric actuators. *Composite Structures* **83**, 110 (2008).

180. *Smart Trailing Edges for Wind Turbines* V001T04A001 (2018).

181. Rimrott, F. Storable tubular extendible member: a unique machine element. *Machine Design* **37**, 156 (1965).

182. Rolfes, R., Teßmer, J., Degenhardt, R., Temmen, H., Bürmann, P. & Juhasz, J. *New design tools for lightweight aerospace structures* in (2004).

183. Runge, C. Über empirische Funktionen und die Interpolation zwischen äquidistanten Ordinaten. *Zeitschrift für Mathematik und Physik* **46**, 20 (1901).

184. Ryu, J., Lee, J., Cho, M., Kim, S.-W., Koh, J.-S. & Cho, K.-J. *Snap-through behavior of bi-stable composite structure using SMA spring actuator* in *Proceedings of the 52nd AIAA/ASME/ASCE/AHS/ASC Structures, Structural Dynamics, and Material Conference, CO, USA* (2011).

185. Schlecht, M. & Schulte, K. Advanced Calculation of the Room-Temperature Shapes of Unsymmetric Laminates. *Journal of Composite Materials* **33**, 1472 (1999).

186. Schlecht, M., Schulte, K. & Hyer, M. W. A comparative study for the calculation of the temperature dependent shapes of unsymmetric laminates based on finite element analysis and extended classical lamination theory. *Mechanics of Composite Materials* **31**, 247 (1995).

187. *A Morphing Concept Based on Unsymmetric Composite Laminates and Piezoceramic MFC Actuators* (2004).

188. Schultz, M. R., Wilkie, W. K. & Bryant, R. G. Investigation of self-resetting active multistable laminates. *Journal of aircraft* **44**, 1069 (2007).

189. Schultz, M. R. & Hyer, M. W. Snap-Through of Unsymmetric Cross-Ply Laminates Using Piezoceramic Actuators. *Journal of Intelligent Material Systems and Structures* **14**, 795 (2003).

190. Schultz, M. R., Hyer, M. W., Williams, R. B., Wilkie, W. K. & Inman, D. J. Snap-through of unsymmetric laminates using piezocomposite actuators. *Composites Science and Technology* **66**. Special Issue in Honour of Professor C.T. Sun, 2442 (2006).
191. Schultz, M. R. *Use of piezoelectric actuators to effect snap-through behavior of unsymmetric composite laminates* PhD thesis (Virginia Tech, 2003).
192. Scott Collis, S., Joslin, R. D., Seifert, A. & Theofilis, V. Issues in active flow control: theory, control, simulation, and experiment. *Progress in Aerospace Sciences* **40**, 237 (2004).
193. Seffen, K. 'Morphing' bistable orthotropic elliptical shallow shells. *Proceedings of the Royal Society of London A: Mathematical, Physical and Engineering Sciences* **463**, 67 (2007).
194. Seffen, K. Mechanical memory metal: a novel material for developing morphing engineering structures. *Scripta Materialia* **55**, 411 (2006).
195. Seffen, K. A. & Vidoli, S. Eversion of bistable shells under magnetic actuation: a model of nonlinear shapes. *Smart Materials and Structures* **25**, 065010 (2016).
196. Seffen, K. A. & Guest, S. D. Prestressed Morphing Bistable and Neutrally Stable Shells. *Journal of Applied Mechanics* **78**, 011002 (2011).
197. *Generating Curvilinear Fiber Paths from Lamination Parameters Distribution* (American Institute of Aeronautics and Astronautics, 2006).
198. Shu, C. *Differential Quadrature and Its Application in Engineering* (Springer-Verlag, London, 2000).
199. Sieros, G., Bulder, B. H., Chaviaropoulos, P., Jamieson, P. & Sørensen, J. D. Upscaling wind turbines: theoretical and practical aspects and their impact on the cost of energy. *Wind Energy* **15**, 3 (2012).
200. Sobel, D. *Longitude: The True Story of a Lone Genius Who Solved the Greatest Scientific Problem of His Time* (Bloomsbury Publishing, 2010).
201. Sousa, C., Camanho, P. & Suleman, a. Analysis of multistable variable stiffness composite plates. *Composite Structures* **98**, 34 (2013).
202. Spickenheuer, A., Schulz, M., Gliesche, K. & Heinrich, G. Using tailored fibre placement technology for stress adapted design of composite structures. *Plastics, Rubber and Composites* **37**, 227 (2008).
203. Stäblein, A. R., Hansen, M. H. & Pirrung, G. Fundamental aeroelastic properties of a bend–twist coupled blade section. *Journal of Fluids and Structures* **68**, 72 (2017).
204. Tawfik, S. *Stability and morphing characteristics of bistable composite laminates* PhD thesis (Georgia Institute of Technology, 2008).
205. Tawfik, S., Tan, X., Ozbay, S. & Armanios, E. Anticlastic Stability Modeling for Cross-ply Composites. *Journal of Composite Materials* **41**, 1325 (2006).

206. Tawfik, S. A., Stefan Dancila, D. & Armanios, E. Unsymmetric composite laminates morphing via piezoelectric actuators. *Composites Part A: Applied Science and Manufacturing* **42**, 748 (2011).

207. Thresher, R. & Laxson, A. *Advanced wind technology: new challenges for a new century* tech. rep. (National Renewable Energy Lab.(NREL), Golden, CO (United States), 2006).

208. Tibbits, S. 4D printing: multi-material shape change. *Architectural Design* **84**, 116 (2014).

209. Tibbits, S. *Active Matter* (MIT Press, 2017).

210. Van den Broek, S., Minera, S., Jansen, E., Pirrera, A., Weaver, P. M. & Rolfes, R. in *Advances in Predictive Models and Methodologies for Numerically Efficient Linear and Nonlinear Analysis of Composites* (ed Petrolo, M.) 143 (Springer International Publishing, Cham, 2019).

211. Van Dam, C. P., Chow, R., Zayas, J. R. & Berg, D. E. Computational Investigations of Small Deploying Tabs and Flaps for Aerodynamic Load Control. *Journal of Physics: Conference Series* **75**, 012027 (2007).

212. Vidoli, S. & Maurini, C. Tristability of thin orthotropic shells with uniform initial curvature. *Proceedings of the Royal Society A: Mathematical, Physical and Engineering Sciences* **464**, 2949 (2008).

213. Vidoli, S. Discrete approximations of the Föppl–Von Kármán shell model: From coarse to more refined models. *International Journal of Solids and Structures* **50**, 1241 (2013).

214. Waitukaitis, S., Menaut, R., Chen, B. G.-g. & van Hecke, M. Origami Multistability: From Single Vertices to Metasheets. *Phys. Rev. Lett.* **114**, 055503 (5 2015).

215. Waldhart, C. *Analysis of tow-placed variable-stiffness laminates* PhD thesis (Virginia Polytechnic Institute and State University, 1996).

216. White, S., Raju, G. & Weaver, P. Initial post-buckling of variable-stiffness curved panels. *Journal of the Mechanics and Physics of Solids* **71**, 132 (2014).

217. Wilkie, W. K., Bryant, R. G., High, J. W., Fox, R. L., Hellbaum, R. F., Jalink, A., Little, B. D. & Mirick, P. H. *Low-cost piezocomposite actuator for structural control applications* in *Smart structures and materials 2000: industrial and commercial applications of smart structures technologies* **3991** (2000), 323.

218. Williams, R. B., Grimsley, B. W., Inman, D. J. & Wilkie, W. K. *Manufacturing and mechanics-based characterization of macro fiber composite actuators* in *ASME 2002: International mechanical engineering congress and exposition* (2002), 79.

219. Williams, R. B., Park, G., Inman, D. J. & Wilkie, W. K. *An overview of composite actuators with piezoceramic fibers* in *20th International Modal Analysis Conference. Los Angeles* (2002), 421.

220. Wilson, S. A., Jourdain, R. P., Zhang, Q., Dorey, R. A., Bowen, C. R., Willander, M., Wahab, Q. U., Willander, M., Al-hilli, S. M., Nur, O., Quandt, E., Johansson, C., Pagounis, E., Kohl, M., Matovic, J., Samel, B., van der Wijngaart, W., Jager, E. W., Carlsson, D., Djinovic, Z., Wegener, M., Moldovan, C., Iosub, R., Abad, E., Wendlandt, M., Rusu, C. & Persson, K. New materials for micro-scale sensors and actuators: An engineering review. *Materials Science and Engineering: R: Reports* **56**, 1 (2007).

221. *Wind Energy in Europe in 2018* tech. rep. (Wind Europe, 2019).

222. Wu, K. C. *Thermal and Structural Performance of Tow-Placed, Variable Stiffness Panels* (IOS Press, 2006).

223. Wu, Z., Raju, G. & Weaver, P. M. Postbuckling analysis of variable angle tow composite plates. *International Journal of Solids and Structures* **50**, 1770 (2013).

224. Yang, Y., Dias, M. A. & Holmes, D. P. Multistable kirigami for tunable architected materials. *Physical Review Materials* **2**, 110601 (2018).

225. Yasuda, H. & Yang, J. Reentrant Origami-Based Metamaterials with Negative Poisson Ratio and Bistability. *Phys. Rev. Lett.* **114**, 185502 (18 2015).

226. Zhang, Z., Wu, H., Ye, G., Wu, H., He, X. & Chai, G. Systematic experimental and numerical study of bistable snap processes for anti-symmetric cylindrical shells. *Composite Structures* **112**, 368 (2014).

227. Zuteck, M. D. *Adaptive blade concept assessment: curved planform induced twist investigation* (Sandia National Laboratories Clear Lake Shore, Texas, USA, 2002).